ON THE ORIGIN, MORPHOLOGY AND KINEMATICS OF MOLECULAR GAS IN EARLY-TYPE GALAXIES

Timothy A. Davis
Wadham College

A thesis submitted in candidature for the degree of Doctor of Philosophy
Michaelmas Term 2011

ON THE ORIGIN, MORPHOLOGY AND KINEMATICS OF MOLECULAR GAS IN EARLY-TYPE GALAXIES

Timothy A. Davis
Wadham College

A thesis submitted in candidature for the degree of Doctor of Philosophy
Michaelmas Term 2011

ABSTRACT

In this thesis I present new interferometric ^{12}CO observations of 30 early-type galaxies (ETGs). These galaxies were the brightest $\sim$2/3 of CO detected ETGs from the complete, volume limited ATLAS^{3D} survey. By including literature data I construct the largest ever sample of mapped ETGs, containing 41 objects, and use this sample to analyse the morphology, kinematics and origin of the molecular gas.

Many of the galaxies in this sample have relaxed molecular discs, but polar structures, rings, bars and disturbed gas distributions are also present. Around half of the galaxies have molecular gas that follows the stellar light profile, similar to molecular gas in spirals, while others have molecular gas excesses, truncations, rings or composite profiles. The molecular gas extent is smaller in absolute terms in ETGs than in late-type galaxies, but the size distributions are similar once scaled by the galaxies optical/stellar characteristic scalelengths. Cluster environments, however, lead to systems having denser, more compact molecular reservoirs.

I find that molecular gas is an excellent kinematic tracer, even in high-mass ETGs, and thus molecules may be the kinematic tracer of choice for probing the M/L evolution of galaxies over cosmic-time. I use this knowledge to construct the first ever early-type CO Tully-Fisher relation, and show that it is offset from the Tully-Fisher relation of spirals by 0.98 ± 0.22 magnitudes at K_s-band.

I find that a third of my sample galaxies have their molecular and ionised gas kinematically misaligned with respect to the stars, setting a strong lower limit on the importance of externally acquired gas (e.g. from mergers and cold accretion). The origin of the molecular gas seems to depend strongly on environment, with externally acquired material being common in the field but nearly completely absent in Virgo. Furthermore, my results suggest that galaxy mass may be an important independent factor associated with the origin of the gas, with the most massive fast-rotating galaxies in our sample always having kinematically aligned gas.

DECLARATION

I declare that no part of this thesis has been accepted, or is currently being submitted, for any degree or diploma or certificate or any other qualification in this University or elsewhere. This thesis is the result of my own work unless otherwise stated below.

The data reduction described in Chapter 2 was done in collaboration with Katherine Alatalo, and will be published in Alatalo, Davis et al., in preparation. All of the work presented in this thesis was completed under the supervision of Martin Bureau, and in collaboration with Katherine Alatalo, Lisa Young, Leo Blitz and the members of the ATLAS^{3D} team. The JAM models used in Chapters 3, 4 and 5 were the work of Michele Cappellari and Nicholas Scott.

The material in Chapter 4 is to be submitted to Monthly Notices of the Royal Astronomical Society (MNRAS), while Chapters 3 and 5 were published in Davis et al. 2011b, MNRAS, Volume 414, Issue 2, pp. 968-984 and Davis et al. 2011a, MNRAS, in press, respectively.

ACKNOWLEDGMENTS

I would firstly like to thank my supervisor, Martin Bureau, for all his help and encouragement during the course of my DPhil. In addition, thanks for the many in-depth comments: I hate to think how many red pens have been used up over my three years at Oxford! Thanks for involving me in such an interesting project, and inducting me into the world of mm-interferometry at an exciting time for the field.

On a similar note, many thanks to Lisa Young, Katey Alatalo and Leo Blitz for being my guides around all the pitfalls and idiosyncrasies of mm-astronomy. Thank you all for the comments, encouragement and scientific discussion. Many thanks also to Alison Crocker for her help while I learned the ropes in the first year (and as a collaborator since), and Estelle Bayet for sharing her knowledge of astrochemistry.

Thanks are also due to Leo Blitz for hosting me during my enjoyable four month visit to UC Berkeley and observing runs on CARMA, and to Professor Yasuo Fukui for hosting me for a month in Nagoya. I should also thank N. Scott, M. Cappellari, M. Sarzi, D. Krajnović, R. L. Davies, R. McDermid, E. Emsellem, and all of the ATLAS^{3D} team. I have learned so much from attending team meetings, and having scientific discussions with you all. Thank you also to all the people who have participated in Black Hole Lunch over the years: the instant feedback, ideas and help you were able to give me helped shape the course of my PhD.

My three short years in Oxford have been highly enjoyable, thanks in large part to my workmates- thank you to all the astrograds for being such great fun! Special thanks must go to the Tower, the best office in the world! Thanks too to everyone in Wadham MCR, for all the parties, meals and trips. Special thanks must go to the poor people who helped me by reading drafts of this manuscript: J. Davis, L. Morabito, M. Scott and A. Crocker – thanks so much!

Finally, thanks to my family for all your love, help and support!

CONTENTS

LIST OF FIGURES

LIST OF TABLES

1

INTRODUCTION

"Mortal as I am, I know that I am born for a day. But when I follow at my pleasure the serried multitude of the stars in their circular course, my feet no longer touch the earth" - Ptolemy, c.150 AD

Galaxies are one of the most basic building blocks of the universe. These vast gravitationally-bound collections of stars, gas and dark matter are ubiquitous, tracing the cosmic web out to the highest redshifts we can observe. Almost every star, planet and moon that has ever existed has done so within the confines of a galaxy. Understanding these complex, beautiful and enigmatic objects is therefore of utmost importance if we want to understand the make-up of the cosmos.

In this thesis I concentrate on understanding early-type galaxies (ETGs), the most massive stellar systems in our universe. ETGs are at the end point of hierarchical evolution, and their properties hide a whole raft of information on the build-up of the universe which we would like to decode. Specifically I attempt here to increase our understanding of the cold gas present at the heart of some ETGs. I do this through studying the morphology and kinematics of the gas, and using these as tools to understand its origin, fate, and effect on the host galaxy.

I use Chapter 1 to introduce this subject, focusing on the formation and evolution of ETGs. In Section 1.1, I discuss the general properties of ETGs and how they compare to the other galaxy types, and provide some pertinent history on the classification of

galaxies. I then go on in Section 1.2 to highlight the problems that arise from these morphological classification schemes, and discuss previous attempts to provide a more physical classification for ETGs. Section 1.3 discusses the current state of knowledge about the different phases of the inter-stellar medium (ISM) in ETGs. Then in the last part of this chapter (Section 1.4) I introduce the ATLAS^{3D} survey, its physical classification for ETGs, and introduce the galaxy sample used throughout this thesis.

Subsequently, in Chapter 2, I present the data upon which this work is based, discuss data-reduction techniques and present a study of the gas morphology. I go on in Chapter 3 to investigate the Tully-Fisher relation of early-type galaxies, using both single-dish and interferometric CO data. In Chapter 4, I use the interferometric data to investigate the extent and kinematics of the gas, and compare these with better-studied spiral galaxy samples. Finally in Chapter 5, I use the kinematics of the gas to constrain its origin. Each chapter has its own introduction, in which I review the literature, identify gaps in the current understanding of the subject, and discuss the specific techniques I use to tackle open questions. This introduction is therefore limited in scope to exploring the current state of our understanding of ETGs, and discussing the survey which forms the foundation of this thesis.

1.1 GALAXY CLASSIFICATION AND EVOLUTION

In the paradigm of cold dark matter with a non-zero cosmological constant (ΛCDM), galaxies are built up through hierarchical merging. Dark matter begins to collapse into small structures, in which the first stars and galaxies are born. Under the influence of gravity these small halos then merge to produce larger and larger systems, at the same time as accreting gas from filaments in the cosmic web. More massive structures are formed over time, and at the current epoch clusters and super-clusters of galaxies are still assembling.

Individual galaxies can have very different evolutionary paths, creating the large variety of different galaxy types we see around us today. The morphology of galaxies gives us information about their structure, and the processes shaping their evolution.

The morphological galaxy classification scheme which enjoys the widest usage today dates back to Hubble (1926). In the Hubble 'tuning fork', galaxies are classified by the apparent size of the central bulge with respect to the disk, and the presence or absence of spiral arms and bars in the disk (see Fig. 1.1).

In this scheme galaxies that have no obvious stellar disk are called *ellipticals*. Galaxies whose disks have no sign of spiral arms, and do not have dust lanes covering the entire disk, are called *S0s* (or lenticulars). Galaxies with spiral arms are called *spiral* galaxies, and are further sub-classified by the presence or absence of a stellar bar. Finally, galaxies which do not show rotational symmetry about dominating nuclei are classified as *irregular*.

Within each class, the galaxies are further sub-divided. Un-barred spiral galaxies are arranged along the upper prong of the tuning fork in a continuum, from Sa galaxies that have large bulges and/or smooth, tightly wound spiral arms (located closest to S0s in the tuning fork diagram), to Sc galaxies with the smallest bulges and flocculent spiral arms. Each type is duplicated on the lower prong of the tuning fork by its barred contemporaries (SBa-c). Of course, all of these classes are not discrete, but in actuality form a continuous sequence, as suggested by the layout of Fig. 1.1.

Taken together, ellipticals and S0s are known as *early-type* galaxies and spirals and irregulars as *late-type* galaxies. This early- and late-type naming convention is also sometimes applied to spirals, with Sa galaxies referred to as "early-type spirals" and Sc galaxies as "late-type spirals". This nomenclature was originally intended to reflect Hubble's proposed evolutionary sequence, where elliptical galaxies collapsed over time to form spiral disks. In current hierarchical scenarios this sequence is reversed, with lower mass spirals merging to form ellipticals - the naming convention, however, remains.

ETGs are thought to have experienced multiple mergers and bear the scars of this violent past (e.g. Toomre, 1977). Spiral galaxies, on the other hand, have followed a more secular evolution, driven by the effect of bars and spiral structure (e.g. Kormendy, 1979; Kormendy & Kennicutt, 2004). These evolutionary pathways lead to galaxies with vastly different morphologies and properties.

For instance, ETGs have been shown to be much more common in cluster environ-

ments than in the field (e.g. Oemler, 1974; Davis & Geller, 1976; Dressler, 1980), i.e. their fraction increases as the environmental density increases. This correlation, often known as the morphology-density relation, suggests that dense environments cause the transformation of spirals into ETGs. The mechanism behind such a transformation is still hotly debated.

ETGs also follow a tight colour-magnitude relation, where brighter galaxies have redder optical colours (the 'red sequence'; e.g. Baum, 1959; Visvanathan & Sandage, 1977; Baldry et al., 2004). The small scatter in this relation requires the stellar content of the galaxies to be fairly uniform and predominantly old (e.g. Bower, Lucey & Ellis, 1992). Spiral galaxies on the other hand lie in a 'blue-cloud', separated from the ETGs by a region with few galaxies (the 'green valley'; e.g. Baldry et al., 2004). The existence of the green valley suggests that galaxies must transit quickly between the blue-cloud and the red-sequence. The observed high alpha-element enhancement of ETGs also requires star formation to be shut down quickly, faster than can be accomplished by just letting a galaxy exhaust its gas reservoir (e.g. Peletier, 1989; Thomas, Greggio & Bender, 1999; Bell et al., 2004). The exact mechanism quenching star formation in ETGs is still hotly debated, with feedback from an active galactic nucleus, starburst winds, merging activity and the effect of cluster environments all potentially contributing (e.g. Silk & Rees 1998; Barnes 2002; Birnboim & Dekel 2003; Hopkins et al. 2005; See Chapter 5).

In general, the stellar populations of ETGs are indeed found to be old when studied in optical bands via broadband colours and/or line indices. For example Thomas et al. (2005) showed that star formation activity in early-type galaxies is expected to have peaked between redshifts of $\approx$3 and 5 in high-density environments and between redshifts $\approx$1 and 2 in low-density environments. At least 50% of the total stellar mass density in ETGs must already have formed by a redshift of $\sim$1. They also find evidence for 'downsizing', where the star formation activity is quenched in the most massive galaxies first, and continues for a much longer period in lower mass ETGs. Spirals, on the other hand, still have ongoing star-formation in the present era, fuelled by large atomic and molecular gas reservoirs (e.g. McGaugh & de Blok, 1997).

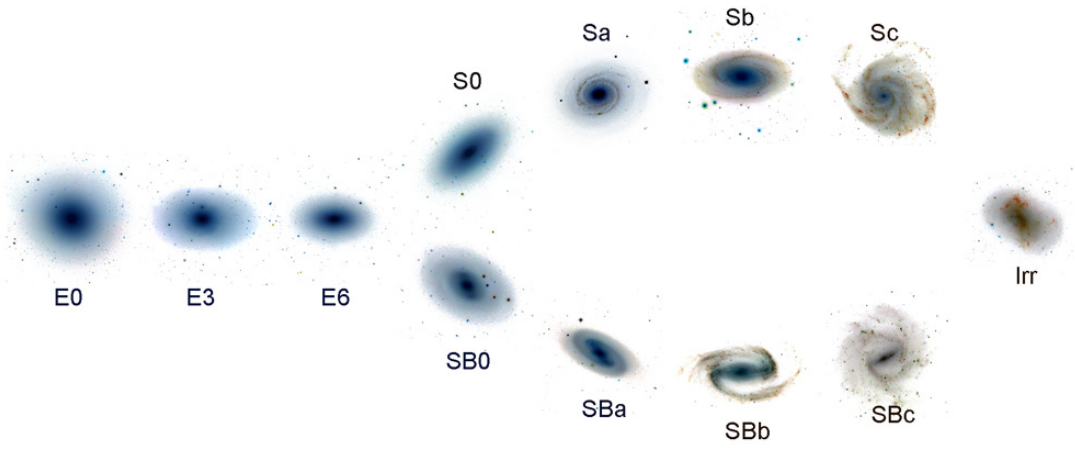

Figure 1.1: Hubble (1936) 'tuning fork' morphological classification scheme

1.1.1 *Early-type galaxy properties*

Since the advent of deep optical imaging, it has become apparent that ETGs are not purely amorphous stellar systems, but do have some structural features, including dust lanes, bars and shells (e.g. Malin & Carter, 1980; Ebneter, Davis & Djorgovski, 1988). These features do not appear to change the underlying stellar structure of the galaxy too dramatically, and hence ETGs are still considered a single family.

The surface brightness profiles of ETGs can usually be well fit with either a de Vaucouleurs $R^{1/4}$ law (de Vaucouleurs, 1948) or a Sersic $R^{1/n}$ law (Sersic, 1968). The stellar isophotes are generally ellipsoidal, but have deviations (of the order of a few percent) which reveal boxy or discy shapes (as discussed in Section 1.2.0.1). The profile shape correlates with the luminosity of the galaxy, more massive galaxies being best fitted with Sersic profiles with $n > 4$ and boxy isophotes, while less luminous systems tend to have more disk like ($n \rightarrow 1$) Sersic profiles.

The luminosity of ETGs is found to correlate with the stellar velocity dispersion (Faber & Jackson, 1976), the relative degree of rotational support inherent in the system (Davies et al., 1983), and the age and metallicity of the stellar populations (e.g. Thomas et al., 2005). A relation is also found between the surface brightness and effective radius of ETGs (Kormendy, 1977). The Kormendy and Faber-Jackson relations are

actually two projections of a three-dimensional relation between the effective radius, mean surface brightness and central velocity dispersion known as the Fundamental Plane (e.g. Faber et al., 1987; Dressler et al., 1987; Djorgovski & Davis, 1987).

UV data from the Galaxy Evolution Explorer (GALEX) satellite, which is very sensitive to young stellar populations, has revealed that in addition to a dominant old stellar population (discussed above), some ETGs have residual ongoing star formation. Kaviraj et al. (2007) and Schawinski et al. (2007) concluded that about 30% of massive ETGs at low redshift have experienced some star formation in the last Gyr. In Section 1.3, I will discuss in detail the ISM of early-type galaxies, and its role in fuelling this residual star formation. First however I return to the problem of finding a galaxy classification that correlates with the intrinsic properties of ETGs.

1.2 TOWARDS A PHYSICAL CLASSIFICATION FOR EARLY-TYPE GALAXIES

The delineation and sub-division of the spiral sector in Hubbles tuning fork stems from morphological characteristics (spiral arms) that are directly related to the internal structure of the galaxy. Unfortunately, Hubble was forced to sub-classify early-type galaxies, not by some visible indicator of the internal structure but instead by the *apparent* axis ratio. ETGs are placed in a sequence of increasing apparent ellipticity from E0 (roundest) to E7 (flattest). This has the drawback that the classification scheme depends not only on the intrinsic shape of ETGs, but also on their inclination.

The limitations of a scheme based on the apparent ellipticity were emphasised by van den Bergh (1990, 2009). He showed that there is a dearth of S0 galaxies with face-on inclinations and that flatter ellipticals are, like lenticular galaxies, fainter than rounder ellipticals. This suggests some of the flatter elliptical galaxies are actually lenticular, but happen to be viewed at an angle which makes detecting the disk difficult. Various authors have attempted to provide a more physical classification for early-type galaxies, and I present a brief synopsis of these efforts below.

1.2.0.1 *Discy/boxiness & excess/deficit*

Kormendy & Bender (1996) made an attempt to classify early-type galaxies by splitting them according to their surface brightness profiles. Early-type systems in this classification range from those with boxy isophotes to S0-like systems with discy isophotes (see Fig. 1.2). This classification has the advantage that it correlates to some extent with the degree of rotation in the system, and thus presumably also with different formation and evolutionary pathways. Discy systems tend to have significant rotational support, while boxy systems have little net rotation. Boxy galaxies are also radio-loud, have X-ray halos, and have older stellar populations than discy systems (Bender et al., 1989). Unfortunately the classification of individual galaxies still depends on the observed inclination of the galaxy, and discy/boxiness usually varies with radius.

With the availability of high spatial resolution Hubble Space Telescope (HST) imaging, a new dichotomy between these types of ellipticals was uncovered. Kormendy et al. (2009) report that boxy ETGs tend to have a deficit of light in the centre, below the usual de Vaucouleurs (1948) profile expected for this type of galaxy. Discy galaxies have a corresponding excess of light in the very central parts. This can be understood if the galaxies have different evolutionary pathways.

Systems with a deficit of light could have undergone dry mergers, which caused core scouring due to the action of binary supermassive black holes (e.g. Begelman, Blandford & Rees, 1980; Merritt, Mikkola & Szell, 2007). Excess systems have undergone recent wet mergers which, through the dissipation of gas, grow extra disk-like components in the centre (these can then hide any signature of core scouring if present).

1.2.0.2 *The SAURON project*

Another way to classify early-type galaxies is to directly analyze their stellar kinematics. Although observationally more demanding, such a method has the advantage of

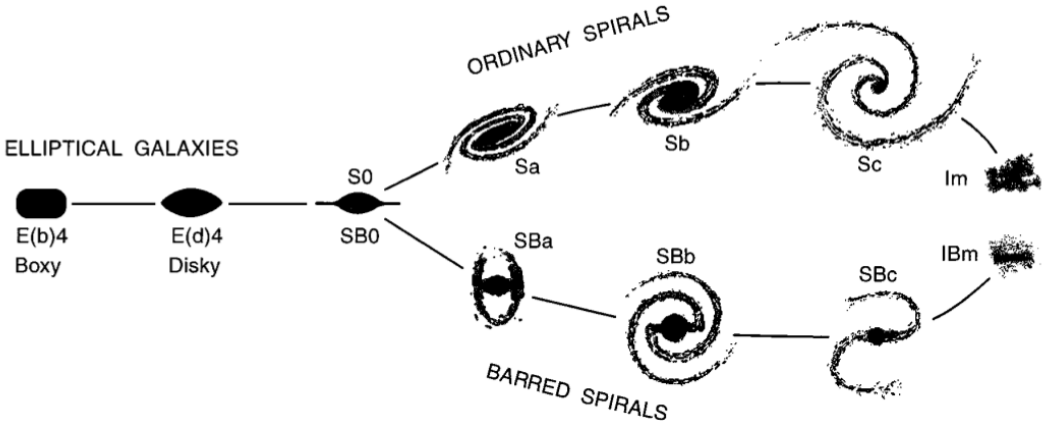

Figure 1.2: The revised classification scheme of Kormendy & Bender (1996) as presented in that work.

directly shedding light on the dynamics of the objects. Integral field units (IFUs), where one obtains a grid of spectra over the target, can be used to provide a two dimensional picture of the internal structures of ETGs. The SAURON project built a custom-designed IFU for this purpose (Bacon et al., 2001), and used it to observe a representative sample of early-type galaxies (de Zeeuw et al., 2002).

Based on a sample of 48 ETGs, the SAURON team showed that the properties of ETGs depend strongly on their degree of rotational support. Emsellem et al. (2007) reported that λ_R, the observed projected total stellar angular momentum per unit mass, naturally separates ETGs into two classes - slow and fast rotators.

Slow rotators are massive, nearly round, triaxial systems, often with large kinematically-decoupled cores (KDCs) and kinematic misalignments between the photometric and kinematic axes. Fast rotators tend to have a low mass, well-aligned photometric and kinematic axes, are axisymmetric, and some have small young KDCs. These differences led the authors to suggest that the two are physically-distinct classes of galaxies and, most importantly, they prove that this classification is reasonably insensitive to viewing angle.

However tantalizing the results of the SAURON project, it was clear that understanding the physical classification of ETGs using λ_R would require a larger sample of galaxies, as free as possible from selection effects. The ATLAS^{3D} survey was created to fill such a role, and is described in detail in Section 1.4.

As part of the SAURON project various authors investigated the inter-stellar medium (ISM) present in ETGs (e.g. Sarzi et al., 2006; Morganti et al., 2006; Combes, Young & Bureau, 2007; Shapiro et al., 2010). ETGs are not ISM free systems, as once assumed, and I now turn to describing the various components of the ISM present in ETGs.

1.3 THE ISM OF EARLY-TYPE GALAXIES

The ISM is a catch all term for the gaseous (and solid) products that inhabit the space between the stars in galaxies. The ISM has various phases, each residing at a characteristic temperature and density. Although the constituents of the ISM are similar across galaxy types, the relative importance of each constituent can vary strongly between galaxies of different morphological types, and even between different locations within a single galaxy. In this Section, I will briefly introduce the components of the ISM in ETGs, and discuss their relative abundances.

1.3.1 Hot gas

X-ray-emitting hot gas was first detected in ETGs by Forman et al. (1979). Typically found at the virial temperature of the galaxy halo ($\sim 10^6$-10^7 K), this gas is observed in almost all optically-luminous ellipticals ($L_B \gtrsim 10^{10}$ $L_\odot$), often in sizeable quantities (up to 10^9-10^{10} $M_\odot$). The gas is usually in a halo centred on the galaxy, but extending beyond the stellar body. Very large ellipticals may have halos of up to 100 kpc in radius, but most do not exceed 50 kpc (O'Sullivan, 2002).

Unlike most components of the ISM found in ETGs (discussed below), the X-ray luminosity does correlate (positively) with the luminosity of early-type galaxies (O'Sullivan, Forbes & Ponman, 2001). The gas comes from two main sources: mass loss from red giant stars and shocked accretion from the galaxy's surroundings (e.g. Mathews & Brighenti, 2003).

The presence of hot gas can have a significant influence on the other phases of the ISM. Thermal evaporation of cold gas by the hotter X-ray gas (e.g. Nipoti & Binney, 2007), both as it enters galactic halos and *in situ* in the disk of galaxies, can suppress star formation and decrease the detection rate of cold gas (Braine, Henkel & Wiklind, 1997). Grain sputtering can also be very effective at destroying dust reservoirs in passive ETGs over short timescales (<50 Myr; Clemens et al., 2010).

1.3.2 Ionised gas

A large proportion of ETGs (50-75%) have been shown to contain ionised gas reservoirs (10^4-10^6 $M_\odot$) at a temperature of $\sim 10^4$K (Caldwell, 1984). The optical nebular emission of hydrogen recombination lines and the forbidden transitions of oxygen, nitrogen and sulphur are commonly used to trace this gas, which is usually rotating, and coincides spatially with dust lanes (Sadler & Gerhard, 1985).

Ratios of optical emission lines (such as those mentioned above) can be used to diagnose the mechanism ionising the gas. Some galaxies contain nuclear emission only, likely to be powered by an active galactic nucleus (Ho, Filippenko & Sargent, 1997b), but a large fraction have more extended gas. Not all of the mechanisms powering this extended gas emission are not fully understood (e.g. Sarzi et al., 2010), but leading candidates include star formation (Ho, Filippenko & Sargent, 1997a), shocks (Dopita & Sutherland, 1995), photoionisation by old stars (Binette et al., 1994; di Serego Alighieri, Trinchieri & Brocato, 1990), and interaction with the hot phase of the ISM (Sparks, Macchetto & Golombek, 1989).

Sarzi et al. (2006) showed that ionised gas is much more common in field ETGs than those found in the Virgo cluster. Furthermore, in ≈50% of these objects the gas kinematics are decoupled from the stellar kinematics, implying a recent acquisition of gaseous material. I will return to this method for determining the origin of the gas in ETGs in Chapter 5.

1.3.3 *H I*

Early-type galaxies can contain significant amounts of neutral hydrogen (H I; Bottinelli & Gouguenheim, 1977; Knapp, Turner & Cunniffe, 1985). The surveys of Morganti et al. (2006), Grossi et al. (2009) and Oosterloo et al. (2010) show that between 44 and 66% of field ETGs have detectable neutral hydrogen reservoirs. This gas is distributed in a wide variety of structures including centrally-concentrated disks, large disks, extended disturbed distributions and free-floating clouds. These have H I masses ranging from 10^6 to 10^{10} $M_\odot$, and the amount of H I present is independent of the luminosity of the galaxy, suggesting much of it comes from external sources (e.g Knapp, Turner & Cunniffe, 1985). Deep H I observations (e.g. Morganti et al., 2006) have confirmed that almost all H I-detected field ETGs show signs of accretion, indicating an average H I accretion rate of 0.1 $M_\odot$ yr^{-1} (Oosterloo et al., 2010). Neutral gas has a much lower detection rate in cluster environments (di Serego Alighieri et al., 2007; Oosterloo et al., 2010), and interferometric H I observations suggest that this material is being stripped by ram pressure from the hot intra-cluster medium.

1.3.4 *Dust*

Dust is the umbrella term for carbonaceous and silicate particles in space which range from a few molecules to 0.1 μm in size. Dust has been detected in ETGs both from obscuration in optical images and by its emission in the far infrared (FIR; Hawarden et al., 1981; Ebneter, Davis & Djorgovski, 1988). Colbert, Mulchaey & Zabludoff (2001) have shown that over 75% of early-types contain dust features in optical images, and Knapp et al. (1989) detected a similar fraction in the FIR. More sensitive Spitzer space telescope observations have yielded even higher detection rates in the MIR (38/43 for ellipticals; Temi, Brighenti & Mathews, 2007), and thus it seems clear that dust is present in most if not all early-types, even if cold gas is not detected. As discussed above, hot gas can destroy dust through grain sputtering, and thus how one balances the dust sources within a galaxy with its destruction rate remains an unanswered

question (e.g. Merluzzi, 1998). In this thesis I attempt to increase our understanding of the relationship between dust and molecular gas in ETGs.

1.3.5 Molecular gas

Molecules were first detected in the ISM by Swings & Rosenfeld (1937), who detected the methylidyne radical (CH) in interstellar sight lines. Molecules in the ISM are usually highly clumped in molecular clouds and larger giant molecular clouds (GMCs). This allows the optical depth to increase sufficiently for the gas to self-shield, protecting itself from the interstellar radiation field. Temperatures in molecular clouds range from 10 to 50 K, with volume densities ranging from 10^3 to 10^7 cm^{-3}.

The most abundant molecular species is H_2. Unfortunately, H_2 lacks a permanent dipole moment, most molecular gas is found under conditions too cold to excite quadrupole emission, and the high opacity of molecular clouds prevents UV absorption studies from probing the bulk of the gas. Thus molecular gas is most commonly traced by the second most abundant molecule, carbon monoxide (CO). CO was first detected in space by Wilson, Jefferts & Penzias (1970), who detected the 1-0 transition in the Orion Nebula. CO has several easily-observed rotational transitions in the millimetre regime, starting with the 1-0 transition at 2.6 mm, with further lines spaced every $\approx$115 GHz.

The critical density for CO(1-0) emission is low ($\approx 10^3$ cm^{-3}) and therefore it is thought to be a good tracer of the total molecular gas mass. However, in order to use CO to trace the total mass, one must rely on the conversion from CO-integrated intensities to H_2 column densities. This conversion factor (X_{CO}) is usually determined through observations of Galactic giant molecular clouds (GMCs) and very local galaxies such as the Magellanic clouds, where estimates of the H_2 column densities can be made using the virial theorem for individual GMCs (e.g. Young & Scoville, 1991), or line ratios of different CO isotopes (Wild et al., 1992). X_{CO} can also be estimated by equating observed FIR dust masses with HI and CO measurements, and assuming a fixed dust-to-gas ratio (as in Bloemen, Deul & Thaddeus, 1990; Leroy

et al., 2011), or alternatively by studying the diffuse γ-ray emission caused by inverse Compton scattering from H_2 nuclei (e.g. Strong & Mattox, 1996). The value of X_{CO} has been found to vary by at least an order of magnitude between giant spirals and dwarf irregulars, and is heavily dependent on metallicity and/or the strength of the UV radiation field (Boselli, Lequeux & Gavazzi, 2002; Leroy et al., 2011). Throughout this work, however, I adopt a single X_{CO} factor of 3.0×10^{20} cm^{-2} (K km s^{-1})$^{-1}$, as estimated for Milky Way GMC's by Dickman, Snell & Schloerb (1986) and Young & Scoville (1991).

Molecular gas was first detected in ETGs (the dwarf elliptical NGC185 and the unusual elliptical Cen A) by Wiklind & Rydbeck (1986) and Phillips et al. (1987). Since then, various surveys have detected molecular gas in samples of ETGs selected to be bright in the infrared (e.g. Wiklind & Henkel, 1989; Sage & Wrobel, 1989), or which have dust obscuration in optical images (Wang, Kenney & Ishizuki, 1992). Such surveys were unable to shed much light on the abundance of molecular gas in the total ETG population, both due to small-number statistics and the biases introduced by different selection methods. Knapp & Rupen (1996), for instance, report a molecular gas detection rate of 80% for ETGs brighter than 1 Jy at 100 μm, while Sage & Wrobel (1989) report $\approx$45% and Wang, Kenney & Ishizuki (1992) $\approx$65%.

Combes, Young & Bureau (2007) performed one of the first studies of molecular gas in a representative sample of ETGs that were not infrared-selected. They observed the SAURON sample of galaxies (discussed in Section 1.2.0.2) and reported a molecular gas detection rate of 28%. The survey of Welch, Sage & Young 2010 (which combined and added to the results of Welch & Sage 2003; Sage & Welch 2006 and Sage, Welch & Young 2007) was the first volume-limited sample published, and found a detection rate of 26% for ETGs within 20 Mpc. I discuss single-dish CO observations of the larger ATLAS^{3D} complete volume-limited sample of ETGs in Sections 1.4.6 and 1.4.7.4.

The picture emerging from these observations is that $\approx$1/4 of early-type galaxies have a molecular gas reservoir containing 10^6 to 10^9 M$_\odot$ of molecular gas. ETGs have molecular gas to stellar mass fractions which can vary widely. Some systems have a minuscule amount of gas, unlikely to affect the galaxy's evolution (0.0001%), while some ETGs have 10% of the stellar galaxy mass in molecular form. The molecular

gas masses are not found to correlate with the luminosity of the host galaxy, but do correlate well with the FIR flux, suggesting that star formation in ETGs proceeds similarly to that in spirals.

One of the main rationales for studying CO in external galaxies is because molecular gas it is believed to be required for star formation. Schmidt (1959) reported that the relation between star formation rate surface density and molecular gas surface density on global scales is a power law, and Kennicutt (1998) report that this has an index of $\approx$1.4. Bigiel et al. (2008) studied the same relation on smaller scales within galaxy discs, and instead found a linear dependence between star formation rate density and molecular gas surface density. Several studies of this global star formation law in ETGs have been conducted, and the data are found to be consistent with either relation (Temi, Brighenti & Mathews, 2009; Shapiro et al., 2010; Wei et al., 2010; Crocker et al., 2011). Larger samples of galaxies and spatially-resolved studies will be required to determine if the star formation law is different in ETGs.

Until recently only small numbers of ETGs had been mapped with millimetre interferometers (e.g. Wrobel & Kenney, 1992; Young, 2002; Schinnerer & Scoville, 2002; Young, Bureau & Cappellari, 2008; Crocker et al., 2008, 2009; Wei et al., 2010; Crocker et al., 2011). These studies have found that the molecular gas is usually centrally concentrated, and distributed in disks and rings. The gas is often relaxed, but asymmetries have been occasionally observed within the gas distributions, indicative of ongoing disturbances and/or accretion.

In this thesis I aim to increase the number of galaxies with mapped molecular gas, to better understand the trends and correlations highlighted by previous authors, and uncover the variety of structures present in these galaxies. This work has been undertaken as part of the multi-wavelength ATLAS^{3D} project, which I describe in the next section.

1.4 THE ATLAS^{3D} PROJECT

The ATLAS^{3D} project is a multi-wavelength survey of a carefully-selected, complete volume-limited (1.16×10^5 Mpc^3) sample of 260 ETGs (Cappellari et al., 2011a, hereafter Paper I). The observations include multicolour optical and near-infrared imaging, two-dimensional kinematics of the atomic (H I), molecular (CO) and ionized (Hβ, [O III] and [N I]) gas, and the kinematics and properties of the stellar populations (from the Hβ, Fe5015 and Mg b absorption line indices). Unlike SAURON, the project also includes a coordinated suite of semi-analytic, N-body binary merger and cosmological simulations of galaxy formation. This thesis is drawn from work done as part of this survey.

1.4.1 Sample selection criteria

The galaxies selected to form the ATLAS^{3D} parent sample have a distance $<$42 Mpc, and a K_s-band absolute total magnitude of $\lesssim$-21.5. The volume was chosen to be observable from the William Herschel Telescope (WHT) on La Palma ($|\delta$ - 29°$| < 35°$; where δ is the sky declination), but excluding the dusty region near the Galactic equatorial plane ($|b| < 15°$; where b is the Galactic latitude). This leads to a parent sample of 871 galaxies of all types. The ETGs were then selected by visual inspection of optical images, to form the core ATLAS^{3D} sample of 260 galaxies. This sample is complete down to its limiting magnitude (Fig. 1.3) and forms a tight red sequence in a colour-magnitude diagram, with only a few ETGs in the blue cloud (Fig. 1.4).

1.4.2 Data

This thesis reports on aspects of the molecular gas observations of the ATLAS^{3D} sample, and makes extensive use of the other multi-wavelength data available from other parts of ATLAS^{3D}. The main observations that I make use of in this thesis are

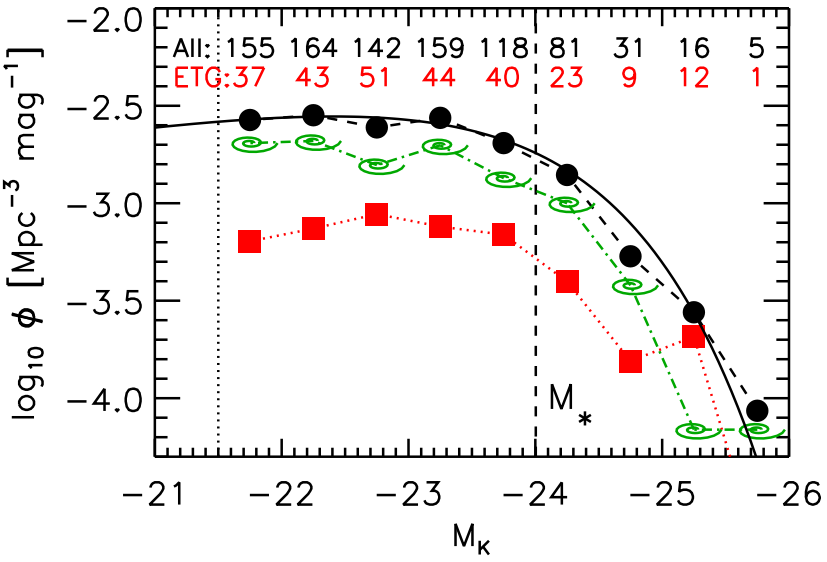

Figure 1.3: K_s-band luminosity function (LF) of the ATLAS^{3D} *parent* sample of 871 galaxies (black filled circles). The LF for the spiral galaxies (green spirals) and the 260 ETGs which constitute the ATLAS^{3D} sample (red squares) are also shown separately. The solid curve shows the Schechter 1976 function derived by Bell et al. 2003 from a fit to 6,282 galaxies. It was not fitted to the data. The black numbers above the symbols indicate the total number of galaxies included in each 0.5 mag bin, while the red ones are the corresponding numbers for the ETGs of the ATLAS^{3D} sample. There is no evidence of incompleteness down to the magnitude limit of the survey (vertical dotted line), which is ≈ 2.5 mag below M_* (vertical dashed line). This figure is taken directly from Paper I.

introduced here, while others will be introduced as and when necessary.

1.4.3 *SAURON IFU data*

As mentioned in the previous section, all of the ATLAS^{3D} galaxies have SAURON IFU data available (Emsellem et al., 2011, hereafter Paper III). SAURON was built at Lyon Observatory and mounted at the WHT Cassegrain focus. It is based on the TIGER concept (Bacon et al., 1995), using a microlens array to sample the field of view. Details of the instrument can be found in Bacon et al. (2001). All galaxies were observed with the low-resolution mode of SAURON, covering a field of view of about $33'' \times 41''$ with $0\farcs94 \times 0\farcs94$ lenslets. Mosaicking was used to reach up to one effective radius (the radius encompassing half the light) when necessary.

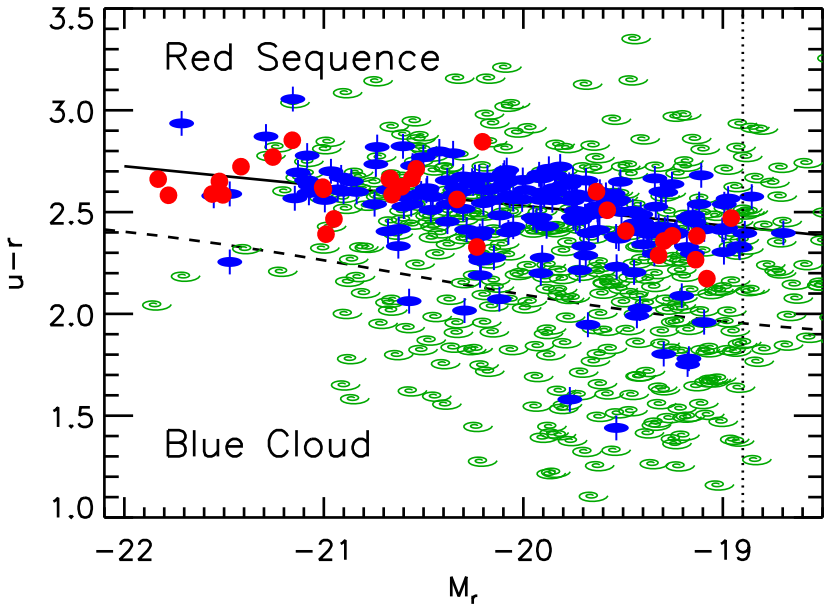

Figure 1.4: *u-r* versus M_r colour-magnitude diagram of the morphologically-selected ATLAS^{3D} parent sample with SDSS photometry. The blue ellipses with an axis are fast-rotators, the red filled circles are slow rotators, and the green spirals are spiral galaxies. The dashed line indicates the separation between the red sequence and blue cloud established by Baldry et al. (2004, 2006), from a sample of 151,642 galaxies. The vertical dotted line indicates our approximate survey completeness limit in *r*-band, $M_r \lesssim -18.9$ mag. The solid line is a linear fit to the ETGs only, minimising the sum of the absolute value of the residuals. This figure is taken directly from Paper I.

The SAURON observations of the ATLAS^{3D} galaxies, and the extraction of the stellar and ionised gas kinematics, are described in detail in Paper I. In brief, for each target, individual datacubes were merged and analysed as described in Emsellem et al. (2004), ensuring a minimum signal-to-noise ratio of 40 per spatial and spectral pixel using the binning scheme developed by Cappellari & Copin (2003). The SAURON stellar kinematics were derived using a penalized pixel fitting routine (Cappellari & Emsellem, 2004), providing parametric estimates of the line-of-sight velocity distribution for each spaxel. During the extraction of the stellar kinematics, the GANDALF code (Sarzi et al., 2006) was used to simultaneously extract the ionised gas line fluxes and kinematics. The mean stellar velocity maps for the ATLAS^{3D} galaxies are presented in Krajnović et al. (2011, hereafter Paper II.).

1.4.4 *Photometric data and optical imaging*

The ATLAS^{3D} survey has collected together optical and near-infrared imaging of each of the 260 galaxies. Optical images in the u,g,r,i and z-bands are taken from the Sloan Digital Sky Survey (SDSS; Abazajian et al., 2009) or our own Isaac Newton Telescope (INT) imaging (Scott et al., in preparation).

The K_s-band magnitudes (and images) are taken from the Two-Micron All Sky Survey (2MASS; Jarrett et al., 2000; Skrutskie et al., 2006). The $K_{s,total}$ magnitudes are measured over large apertures in the K_s-band images, to include the total flux from the galaxy using the techniques developed in Kron (1980) and curves-of-growth (see Jarrett et al. 2000 for further details). They have been widely used in the astronomical community and are found to be robust to $\approx$0.1 mag (Noordermeer & Verheijen, 2007).

1.4.5 *Jeans models*

In this thesis I utilise axisymmetric Jeans anisotropic dynamical models (JAM; Cappellari, 2008) of the ATLAS^{3D} galaxies. Some examples of the approach, using SAURON integral-field kinematics, are presented in Scott et al. (2009). For the ATLAS^{3D} survey a multi-Gaussian expansion (MGE; Emsellem, Monnet & Bacon, 1994) model was fitted to the optical photometry (Scott et al. in preparation). The MGEs were then used to construct JAM models for all the 260 ATLAS^{3D} galaxies (see Cappellari et al., 2010) which were fitted to the SAURON stellar kinematics (Paper II). The models have three free parameters: the inclination (i_{JAM}); the mass-to-light ratio (M/L) and the anisotropy, which are assumed to be spatially constant. From each mass model the predicted circular velocity curve in the plane of the galaxy was calculated.

1.4.6 CO single-dish data

As reported in Young et al. (2011), hereafter Paper IV, the Institut de Radioastronomie Millimétrique (IRAM) 30m telescope at Pico Veleta, Spain, was used for simultaneous observations of CO(1-0) and CO(2-1) in all of the ATLAS^{3D} galaxies.

The beam full width at half maximum (FWHM) is 21.″6 and 10.″8 at 115 GHz and 230GHz, respectively. The SIS receivers were used for observations in the wobbler switching mode, with reference positions offset by $\pm$ 100″ in azimuth. The 1 MHz filterbank back-end gave an effective total bandwidth of 512 MHz (1330 km s^{-1}) and a raw spectral resolution of 2.6 km s^{-1} at CO(1-0). The 4 MHz filterbank gave an effective total bandwidth of 1024 MHz (also 1330 km s^{-1}) and a raw spectral resolution of 5.2 km s^{-1} at CO(2-1). The system temperatures ranged from 190 to 420 K at 2.6 mm and 240 to 600 K at 1.3 mm. The time on source was interactively adjusted so that the final, co-added CO(1-0) spectrum of each galaxy had a rms noise level of $\approx$3.0 mK T_a^* ($\approx$19 mJy) per binned 31 km s^{-1} channel.

At this sensitivity, the minimum detectable H_2 masses range from $\sim 1 \times 10^7$ $M_\odot$ for nearby galaxies to $\sim 1 \times 10^8$ $M_\odot$ for the most distant sample members (over a 300 km s^{-1} linewidth). The results of this survey are presented in Section 1.4.7.4.

1.4.7 First results from ATLAS^{3D}

In this section I summarise some of the initial results of the ATLAS^{3D} survey, which aid understanding of the material presented in this thesis.

1.4.7.1 Fast and slow rotators

In Paper III the SAURON analysis of the stellar angular momentum of ETGs (Section 1.2.0.2) has been repeated, with the much larger ATLAS^{3D} sample. They show that 86 $\pm$ 2% (224/260) of all ETGs in the ATLAS^{3D} volume are fast rotators: these have

the regular stellar rotation, with aligned photometric and kinematic axes (Paper II), and often have embedded stellar discs and bars. Fast rotators span the full range of apparent ellipticities (from 0 to 0.85), but likely have intrinsic ellipticities from about 0.35 to 0.85. The most flattened fast-rotators thus have morphologies consistent with spiral galaxies. Edge-on fast rotators appear morphologically equivalent to S0s, or to flat ellipticals with discy isophotes. Many of the apparently-round fast-rotators have bars or dusty disks, indicating that they are viewed face-on. All the galaxies classified as 'discy' ellipticals E(d) by Bender, Saglia & Gerhard (1994) belong to the fast-rotators class. Contrary to E(d) and S0 galaxies, the fast-rotators can be robustly recognised from integral-field kinematics even when they are nearly face-on.

Only a small fraction ($14 \pm 2\%$) of ETGs are slow rotators. Of all slow rotators, 11 per cent (4/36) have two counter-rotating stellar disc-like components and a rather low-mass ($< 10^{10.5}$ $M_\odot$). All other slow rotators (32/36) appear relatively round on the sky ($\epsilon < 0.4$), tend to be massive ($M_{dyn} > 10^{10.5}$ $M_\odot$), and many have a kinematically decoupled core. Slow rotators dominate the high-mass end of the ATLAS^{3D} sample, with only about a quarter of galaxies with masses above $10^{11.5}$ $M_\odot$ being fast rotators.

Importantly, the classification of ETGs into ellipticals and lenticulars is misleading. Slow rotators tend to be classified as ellipticals and fast rotators as lenticulars, but the contamination between classes is strong enough to bias studies based purely on these classical morphologies. Paper III shows that 20% of all fast rotators are classified as ellipticals, and more importantly 66% of ellipticals in the ATLAS^{3D} sample are fast rotators.

Cappellari et al. (2011b, hearafter Paper VII) thus suggest a new "comb" classification scheme for galaxies, illustrated in Figure 1.5. As in previously proposed revisions (van den Bergh, 1976; Kormendy & Bender, 1996) of Hubble's tuning-fork classification scheme, this diagram represents *intrinsic* galaxy properties. Fast-rotators form a parallel sequence to spiral galaxies, as already emphasised for S0 galaxies by van den Bergh (1976) who proposed a distinction into S0a–S0c. Together with spiral galaxies (Sa–Sc) and early-type galaxies, anemic spirals (Aa–Ac) are also included, as suggested by van den Bergh (1976). These represent transition objects (examples of which are often observed in clusters) between the genuine spirals, with obvious

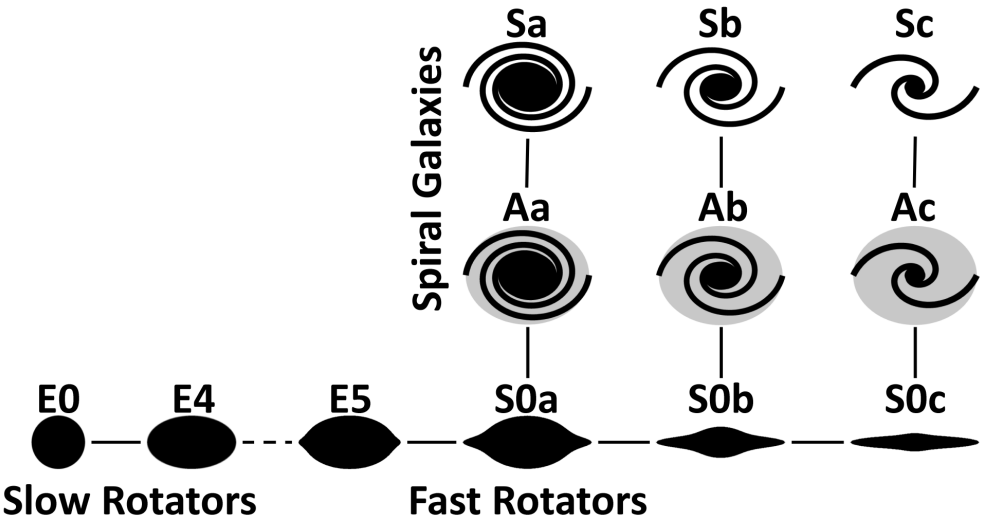

Figure 1.5: Proposed ATLAS^{3D} "comb" classification scheme in schematic form. Slow-rotator (E0–E4) and fast-rotator (E5–S0c) early-type galaxies are visualized as edge-on. This figure is taken directly from Paper VII.

large-scale spiral arms, and the fast rotators with no evidence of spiral structure in optical images.

1.4.7.2 The kinematic morphology density relation

Paper VII studied the *kinematic* morphology-density relation using fast and slow rotators to replace lenticulars and ellipticals (as used in the classical morphology-density relation; Dressler, 1980). The authors report that the relation is cleaner than using classical morphologies. Slow rotators are nearly absent in the lowest density environments and generally make up a small fraction ($\approx$4%) of the total galaxy population in the relatively low-density environments explored by the ATLAS^{3D} survey, with the exception of the dense core of the Virgo cluster where they make up $\approx$20% of the galaxy population. This contrasts with the classic studies that invariably find significant fractions of (misclassified) ellipticals down to low-density environments (e.g. Oemler, 1974; Davis & Geller, 1976; Dressler, 1980).

Figure 1.6 shows a clean log-linear relation exists between the fraction of spiral galaxies and the local galaxy number surface density within a cylinder enclosing the three nearest galaxies (Σ_3). This holds for nearly four orders of magnitude in

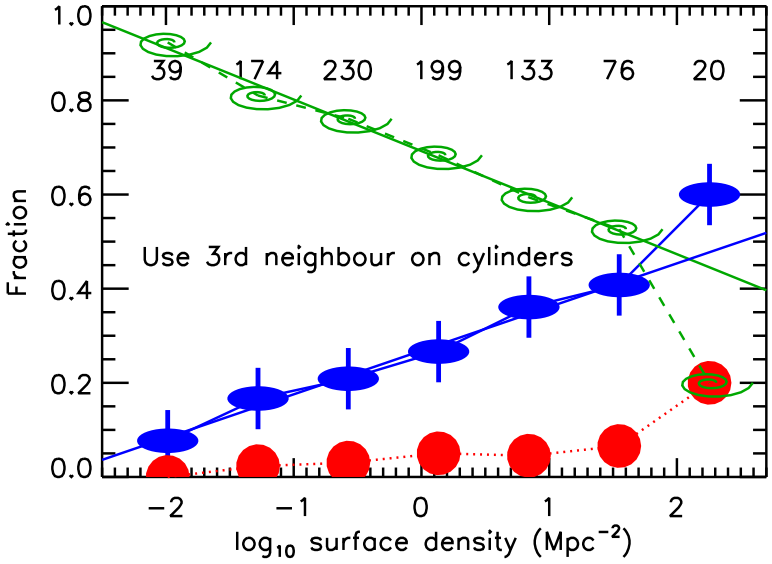

Figure 1.6: Morphology-density relation for fast rotators (blue ellipses with vertical axes), slow rotators (red filled circles) and spiral galaxies (green spirals). The solid blue and green lines are best fit to the first six values. The numbers above the symbols represent the number of galaxies included in each of the seven density bins. This figure is taken directly from Paper VII.

the surface density down to $\Sigma_3 \approx 0.01$ Mpc^{-2}, the fraction of spirals decreasing by 10% per dex in Σ_3 while the fraction of fast-rotators increases at a similar rate. The existence of a smooth kinematic morphology-density relation in the field excludes processes related to the cluster environment (e.g. ram-pressure stripping) as main drivers of the apparent conversion of spirals into fast-rotators. Instead it suggests that the segregation is driven by local effects at the small-group scale. Only at the highest densities in the Virgo core does the log-linear relationship break down, where the fraction of slow-rotators also starts to increase. This suggests that a different mechanism is at work there, possibly linked to the stripping of gas from spirals by the hot intergalactic medium in the cluster core and/or the corresponding lack of cold accretion.

1.4.7.3 H I in ATLAS^{3D} ETGs

Serra et al. (in preparation) present the ATLAS^{3D} H I survey of a volume-limited, complete sample of 166 ETGs (all of the ATLAS^{3D} galaxies above a declination of -2°

due to source observability constraints).

The observations, taken at the Westerbork radio telescope (WSRT), enable detection and mapping of H I down to 5×10^6 - 5×10^7 $M_\odot$ within the survey volume. Serra et al. report a detection rate of 39% for ETGs outside the Virgo cluster, and 10% for those inside it. When compared to suitable spiral galaxy surveys, they find that as a population, ETGs have much less H I than spiral galaxies. However, a significant fraction of detected ETGs are as H I-rich as spiral galaxies. ETGs, however, usually lack the high-column-density H I typically found in the bright stellar disc of spiral galaxies.

The majority of detected ETGs have their H I distributed in a rotating disc or ring, while the rest have H I in unsettled configurations or scattered clouds. H I discs/rings can be divided into two classes based on their size. Large discs/rings extend out to tens of kpc from the galaxy centre and have between 10^8 and 10^{10} $M_\odot$ of H I. Small discs are strongly coupled to the host galaxy, confined within the stellar body and have H I masses $\lesssim 10^8$ $M_\odot$. This class of galaxies is often detected in CO, and exhibits dust or blue features, demonstrating that the cold ISM is providing fuel for star formation.

The properties of the H I do not depend strongly on the galaxy luminosity, but they do depend on the environment density. The low detection rate in Virgo is driven by galaxies within 1 Mpc from the cluster centre. Further out, the H I properties are consistent with those of ETGs outside of Virgo. This is also the cluster-centric radius where spiral galaxies start being affected by the cluster environment. Consequently Serra et al. suggest that ETGs located in the outskirts of Virgo may be falling into the cluster for the first time. The H I in isolated ETGs is typically distributed in large regular gas discs or rings, while in richer environments the fraction of galaxies with a disturbed H I morphology increases. This effect appears to be correlated to the presence of nearby neighbours.

1.4.7.4 *ATLAS^{3D} single-dish CO survey*

Paper IV reported on the observation of all of the ATLAS^{3D} sample galaxies with the IRAM-30m telescope (see Section 1.4.6 for details of these observations). The authors report an overall CO detection rate of $22 \pm 3\%$, with no dependence on galaxy luminosity and only a modest dependence on the dynamical mass of the galaxy. The detection rate and molecular gas mass fractions of the sample galaxies are almost identical inside and outside of the Virgo cluster, even though the ETGs (unlike spirals) seem to be virialized within the cluster. Thus the cluster members must have retained their molecular gas over several Gyr in the cluster. The most CO-rich early-type galaxies (with H_2 masses $> 10^9$ $M_\odot$) all exist in low-density environments.

Very few slow rotators are detected in molecular gas, suggesting that the mechanism forming these galaxies is more effective at destroying molecular gas, and/or that these galaxies are unable to re-generate or re-accrete molecular gas.

The CO-detected galaxies from the ATLAS^{3D} single-dish survey form the basis for the interferometric follow-up presented in this thesis. Details of the observations of these galaxies follow in Chapter 2.

2

CARMA ATLAS^{3D} MOLECULAR GAS MAPPING

"The universe is simmering down, like a giant stew left to cook for billions of years. Sooner or later we won't be able to tell the carrots from the onions' - Arthur Bloch

2.1 THE CARMA SAMPLE

In order to understand the cold gas present at the heart of some of the ATLAS^{3D} galaxies (see Sections 1.3.5 and 1.4.7.4) it is important to investigate the morphology and kinematics of the gas in a spatially resolved manner. Aperture synthesis arrays have recently become sensitive enough to map these relatively gas poor systems, however before the start of this doctoral thesis only $\sim$10 ETGs had been interferometrically mapped (as discussed in Section 1.3.5).

In order to gain a more complete picture of the molecular gas in these systems we selected the brightest $\sim$2/3 of the ATLAS^{3D} galaxies detected in CO(1-0) by Paper IV (see Sections 1.4.6 and 1.4.7.4 for full details), which do not have interferometric maps available in the literature. These 30 galaxies were observed as part of the ATLAS^{3D} Combined Array for Research in Millimeter-wave Astronomy (CARMA) survey. In the rest of this Section, I present the details of the data reduction and analysis for these objects. When I discuss the interferometric sample in the rest of

this thesis, I also include the 11 galaxies from the ATLAS^{3D} sample for which data is already available from the literature, mostly from SAURON survey (de Zeeuw et al., 2002) follow-ups. These are NGC 0524, NGC 2685, NGC 2768, NGC 3032, NGC 3489, NGC 4150, NGC 4459, NGC 4477 and NGC 4526 (see Table 2.3 for full details). This leads to a total sample of 41 mapped ETGs. This sample of galaxies is complete down to a flux limit of 18.5 Jy km s^{-1} (the 34 brightest objects). Because these galaxies are drawn from the complete, volume limited ATLAS^{3D} sample this allows us to make strong statements about the molecular gas in ETGs as a class.

Five galaxies with fluxes below this threshold also have CO images, either from the literature (NGC 2685, NGC 2768, NGC 3489, NGC 4477), or imaged as part of this CARMA survey (UGC 05408). Two of the galaxies imaged as part of the CARMA survey were later removed from the ATLAS^{3D} sample (NGC 2697 and NGC 4292), either due to showing some evidence of spiral structure in deeper optical imaging, or because of a change in magnitude cuts applied to the sample. Because these objects were already imaged with CARMA, I still present their maps in this thesis. However, NGC 2697, which has visible spiral structure in new optical imaging, will not be used for analysis in later chapters.

As the mapped galaxies were flux selected, they are biased towards higher molecular gas masses, but are statistically indistinguishable (using a Kolmogorov-Smirnov test) from the full sample of CO-detected systems in terms of their molecular gas mass to stellar mass fraction, local environment, and host galaxy properties (e.g. velocity dispersion, luminosity, effective radius and λ_R; Emsellem et al. 2011, hearafter Paper III). The mapped galaxies also follow the same CO Tully-Fisher relation (Paper V). Other than molecular gas mass, the only parameter in which our sample may have some bias is cluster membership. Because the Virgo cluster is nearby, its members are relatively bright in CO(1-0), and we have mapped a greater percentage of cluster members than field galaxies. However, we do not expect this to affect our conclusions. Overall, we thus consider that our CO-rich ETG sample is reasonably free of biases, although it is worth remembering that we do not fully sample the parameter space at small molecular gas masses ($<10^8$ M$_\odot$).

The galaxies observed as part of the ATLAS^{3D} CARMA sample have absolute K-

band magnitudes that span the whole range covered by the ATLAS^{3D} sample, between $M_k = -21.57$ mag (PGC 058114) and $M_K = -25.09$ mag (NGC 4753). All but three galaxies mapped with CARMA (IC 719, NGC 1222, and NGC 7465) are regular rotators (meaning they have a regular stellar velocity field; Paper II). NGC 1222, classified as a non-regular rotator, is a strong starburst, known to be undergoing a three way merger (Beck, Turner & Kloosterman, 2007). NGC 7465 is in a small interacting group (with NGC 7464 and 7463), and has a kinematically decoupled core. IC 719 does show ordered rotation in its stellar component, but has two counter-rotating disk components (one likely formed from the misaligned molecular gas I map here). Properties of each galaxy in the sample are listed in Table 2.1.

2.2 OBSERVATIONS, DATA REDUCTION AND CALIBRATION

Observations for this survey were taken at CARMA over the course of five semesters, beginning in the autumn of 2008. Galaxies were observed in the CARMA D–array, with 11–150m baselines, corresponding to resolutions of 3.″5–4.″8 at CO(1–0). Two galaxies that appeared to have significant flux resolved out were then followed up in the lower resolution CARMA E–array (8–66m baselines). The observations presented here were the result of ≈467 hours of CARMA data. Observational parameters are listed in Table 2.2. The CARMA correlator and receivers were upgraded during the course of ATLAS^{3D} observations, so data taken later has a larger available bandwidth.

2.2.1 Reduction and calibration

Raw CARMA visibility data were reduced using the `MIRIAD` package. Raw data were first Hanning smoothed, and observations of the calibrator inspected in order to search for decorrelations in time and over baselines. Any identified bad time periods, or antennas were then flagged. Next, the unflagged data were corrected for the differences in the length of the fibre-optic lines between the antennas and the correlator. After flagging and linelength correction, the observations then were

Table 2.1: CARMA ATLAS^{3D} galaxy sample

Name	α (J2000)	δ (J2000)	v_{sys} (km s^{-1})	d (Mpc)	Virgo
(1)	(2)	(3)	(4)	(5)	(6)
IC 0676	11 12 39.84	+09 03 20.7	1429	24.6	0
IC 0719	11 40 18.52	+09 00 35.6	1833	29.4	0
IC 1024	14 31 27.07	+03 00 30.0	1479	24.2	0
NGC 1222	03 08 56.76	-02 57 19.3	2422	33.3	0
NGC 1266	03 16 00.79	-02 25 38.6	2170	29.9	0
NGC 2697*	08 54 59.40	-02 59 15.2	1814	22.0	0
NGC 2764	09 08 17.44	+21 26 35.8	2706	39.6	0
NGC 2824	09 19 02.22	+26 16 12.3	2758	40.7	0
NGC 3182	10 19 33.02	+58 12 21.0	2118	34.0	0
NGC 3607	11 16 54.54	+18 03 07.1	942	22.2	0
NGC 3619	11 19 21.60	+57 45 28.3	1560	26.8	0
NGC 3626	11 20 03.78	+18 21 25.6	1486	19.5	0
NGC 3665	11 24 43.64	+38 45 46.2	2069	33.1	0
NGC 4119	12 08 09.60	+10 22 44.7	1656	16.5	1
NGC 4292*	12 21 16.49	+04 35 44.3	2258	29.8	0
NGC 4324	12 23 06.17	+05 15 02.8	1665	16.5	1
NGC 4429	12 27 26.56	+11 06 27.3	1104	16.5	1
NGC 4435	12 27 40.49	+13 04 44.3	791	16.7	1
NGC 4694	12 48 15.10	+10 59 01.3	1171	16.5	1
NGC 4710	12 49 39.36	+15 10 11.7	1102	16.5	1
NGC 4753	12 52 22.07	-01 11 57.9	1163	22.9	0
NGC 5379	13 55 34.35	+59 44 34.3	1774	30.0	0
NGC 5866	15 06 29.60	+55 45 48.0	755	14.9	0
NGC 6014	15 55 57.39	+05 55 54.7	2381	35.8	0
NGC 7465	23 02 00.96	+15 57 53.3	1960	29.3	0
PGC 029321	10 05 51.18	+12 57 40.7	2816	40.9	0
PGC 058114	16 26 04.29	+02 54 23.6	1507	23.8	0
UGC 05408	10 03 51.86	+59 26 10.2	2998	45.8	0
UGC 06176	11 07 24.68	+21 39 25.6	2677	40.1	0
UGC 09519	14 46 21.12	+34 22 14.2	1631	27.6	0

Notes: Column 1 lists each galaxy observed by CARMA as part of the ATLAS^{3D} survey. Columns 2, 3 and 4 detail the coordinates of the optical centre of the galaxy, and its optical heliocentric velocity. Column 5 lists the distance to the galaxy, and Column 6 shows if this galaxy is a Virgo cluster member (defined in Paper I as existing within a sphere of radius 3.5 Mpc centered on the cluster centre) All of these quantities are taken directly from Table 5 in Paper I. Galaxies with stars next their name were removed from the ATLAS^{3D} survey, as discussed in Section 2.1.

passband calibrated, using a bright calibrator source, to eliminate instrumental spectral fluctuations. The data products were then phase corrected using a bright quasar within 20° of the source. Any large fluctuations in phase which remained after phase calibration were also flagged, and the process was repeated with the inclusion of the new flags. After the data were satisfactory, the gain solutions derived from a planetary calibrator were applied to the science source.

MIRIAD was used to convert all visibility files to 3-dimensional data cubes. Where available, a zeroth order continuum fit to the *uv*-data was made using channels uncontaminated by line emission. Only data taken with the upgraded correlator had sufficient bandwidth for a reliable continuum fit. The continuum-free combined *uv*-data were then inverted in velocity space using the MIRIAD task INVERT. Channel widths were initially chosen to be 10km s^{-1} ($\approx$3 raw channels from the *uv*-data), but were then iteratively adjusted to achieve at least 3σ detections in all channels where flux was present, while giving the best resolution possible. Pixels of $1'' \times 1''$ were chosen as a compromise between sampling and resolution, giving approximately 4 resolution elements per beam, and ensuring data products were reasonably uniform across the sample. This pixel size corresponds to a physical scale of between 75 and 220 parsecs, depending on the distance of the source. We imaged out to the half-power beam radius, which for CARMA's combination of 10m and 6m antennas is $\approx 72''$.

Robust weighting was used to optimally minimise side-lobes and achieve a low noise level. The MIRIAD task CLEAN was used to deconvolve the source emission from the beam, in the region of interest within the dirty cubes. CLEAN was iterated until little improvement was seen in the residuals (up to a maximum of 600 times). Deconvolution with the maximum entropy method was also attempted, producing very similar results, but the maps we present here are based on CLEAN. The resulting clean component map was then convolved with the beam FWHM (estimated at the centre of the map) using the MIRIAD task RESTOR. This produced the final, reduced 3-dimensional data cube for each galaxy. The units for each channel map are intensity : Janskys per beam (Jy $beam^{-1}$), per channel.

A zeroth moment (integrated intensity map), and a first moment (integrated velocity map) were created from the final clean cube. These are presented in Section

2.A of this chapter, along with channel maps of detected emission. The integrated intensity and mean velocity maps were produced by the masking method: the deconvolved image cube was smoothed along both spatial and velocity axes, and the smoothed cube was clipped at ≈2.5 times the rms noise in a channel (as listed in Table 2.2). The clipped version of the smoothed cube was then used as a mask to define a three-dimensional volume in the original, unsmoothed cube, over which I take the zeroth and first moment (as in Regan et al., 2001; Young, Bureau & Cappellari, 2008). The final units for the moment zero map are Jy beam^{-1} km s^{-1}, and $<$ km s^{-1} $>$ for the first moment.

2.2.2 *Comparison to single-dish data*

In Section 2.A I show the spectra derived both from my CARMA observations, and single-dish observations from the IRAM-30m telescope (Section 1.4.6). Overall, the single dish spectra agree well with the spectra extracted from the CARMA observations. In the cases where CARMA derives more flux than the 30m, it is clear that the source extends much farther than the ≈21″single dish beam (e.g. NGC 4710, NGC 5866, NGC 7465). In the couple of cases where CARMA does not recover as much flux as the single dish, either the sources are close to the detection limit of CARMA (NGC 3182, NGC 5173, UGC 05408) or it appears that there could be larger scale structure that CARMA has resolved out. IC 1024 shows an asymmetry in the CARMA data, viewed both in the spectrum as well as in the channel maps, that is not seen by the single dish. This could be caused by pointing errors at the IRAM-30m, causing us to miss much of the flux from one horn of the distribution.

Overall, the good agreement seen between the single dish and the CARMA spectra means that the majority of molecular gas is in structures that vary on small scales, i.e. in the form of dense clumps and clouds. One would expect if the molecular gas were more diffuse in nature, that many of the CARMA maps would have a significant portion of the flux resolved out. It is, however, possible that there is a diffuse molecular component that neither the single dish, nor the interferometer were

Table 2.2: Details of the ATLAS^{3D} CARMA observations

Name	Semester	ΔV (km s^{-1})	BW (km s^{-1})	$\sigma_{\rm rms}$ (mJy bm^{-1})	Continuum (mJy bm^{-1})	Morph. Class
(1)	(2)	(3)	(4)	(5)	(6)	(7)
IC 0676	09B	10	410	24.0	< 2.70	D
IC 0719	10A	20	580	5.3	< 0.26	D
IC 1024	08B	10	420	16.5	< 1.80	M
NGC 1222	08B	5	420	20.2	< 1.60	X
NGC 2697	08B+09A	20	380	7.4	< 1.20	R
NGC 2764	09B	10	410	11.4	< 1.30	D
NGC 2824	08B	25	400	8.6	< 1.50	D
NGC 3182	09A	30	390	7.2	< 1.40	R
NGC 3607	10B	20	900	5.3	< 0.26	D
NGC 3619	10B	30	900	3.2	$= 1.44 \pm 0.41$	M
NGC 3626	09B	25	400	4.9	< 0.87	R
NGC 3665	10B	10	910	7.2	$= 9.60 \pm 0.75$	D
NGC 4119	08B	10	410	16.2	< 1.80	R
NGC 4292	08B	10	410	8.3	< 0.92	R
NGC 4324	09A	20	400	3.2	< 0.50	R
NGC 4429	10B	10	840	8.1	< 0.27	D
NGC 4435	10B	10	920	9.3	< 0.32	D
NGC 4694	10A	10	390	7.5	< 0.26	X
NGC 4710	09A	10	410	9.8	< 1.10	B
NGC 4753	10B	15	735	7.4	< 0.31	D
NGC 5379	10A	10	410	7.9	< 0.21	R
NGC 5866	10B	10	920	12.9	< 0.44	B
NGC 6014	08B	10	350	19.6	< 2.30	S
NGC 7465	08B+09A	10	410	10.6	< 1.20	D
PGC 029321	09B	10	410	11.0	< 1.20	D
PGC 058114	09A	10	410	13.2	< 1.50	D
UGC 05408	09A	25	200	10.5	< 2.60	D
UGC 06176	09A	15	735	8.3	< 0.35	D
UGC 09519	08B	10	410	16.6	< 1.80	D

Notes: Column 1 lists each galaxy observed by CARMA as part of the ATLAS^{3D} survey. Column 2 details the semester(s) in which the galaxy was observed. Column 3 lists the channel spacing used to create the maps shown in Section 2.A. Column 4 details the bandwidth used to observe the CO(1-0) line at the time of observation. Column 5 lists the root mean square noise per velocity channel, measured in regions devoid of line emission. Column 6 lists the 3mm continuum flux, or corresponding upper limit. Column 7 shows the morphological class I assign to the gas in this galaxy. D = disk, R = ring, B = bar, X = majorly disturbed, M = minor disturbance, S = spiral.

Table 2.3: Details of the literature data used for ATLAS^{3D} sample galaxies

Name	Telescope	Reference	Morph. Class
(1)	(2)	(3)	(4)
NGC 0524	PdBI	Crocker et al. (2011)	D
NGC 1266	CARMA	Alatalo et al. (2011)	X
NGC 2685	OVRO	Schinnerer & Scoville (2002)	R
NGC 2768	PdBI	Crocker et al. (2008)	D
NGC 3032	BIMA	Young, Bureau & Cappellari (2008)	D
NGC 3489	PdBI	Crocker et al. (2011)	S
NGC 4150	BIMA	Young, Bureau & Cappellari (2008)	M
NGC 4459	BIMA	Young, Bureau & Cappellari (2008)	D
NGC 4476	BIMA	Young (2002)	D
NGC 4477	PdBI	Crocker et al. (2011)	D
NGC 4526	BIMA	Young, Bureau & Cappellari (2008)	D
NGC 4550	PdBI	Crocker et al. (2009)	X

Notes: Column 1 lists the ATLAS^{3D} sample galaxy name. Column 2 contains the name of the telescope the data was taken with. PdBI is the Plateau de Bure Interferometer, BIMA is the Berkeley-Illinois-Maryland Association millimeter interferometer, OVRO is the Owens Valley Radio Observatory millimeter interferometer, and CARMA is the Combined Array for Research in Millimeter-wave Astronomy. Column 3 lists the data reference, while Column 4 contains my morphological class, as in Table 2.2.

sufficiently sensitive to detect.

2.2.3 *Millimeter continuum*

3mm continuum emission was detected in two sources, NGC 3619 and NGC 3665. In both galaxies this emission is from a central unresolved point source (at our resolution; $\approx 4\farcs5$).

NGC 3619 was detected as an unresolved point source in the NRAO VLA Sky Survey (NVSS; Condon et al., 1998), with a 1.4 GHz flux of 6.1$\pm$0.6 mJy. My data reveal that this flux drops to 1.44 mJy beam^{-1} at 3mm. A maximum of 0.2 mJy at 3mm can be explained by dust, based on the Infrared Astronomical Satellite (IRAS) 100 and 60 μm, and Infrared Satellite Observatory (ISO) 170 μm observed fluxes. As the molecular gas in this system is also barely resolved (see Appendix 2.A) this continuum flux could potentially come from star-formation, or an embedded AGN. I suggest here that an AGN explanation is more likely, given that the maximum predicted flux at 3mm from free-free emission in the central 5$''$ of this galaxy is 0.02 mJy (based on

the SAURON Hβ fluxes, as in Crocker et al., 2008)

NGC3665 is a twin-jet radio source, and X-ray point source, clearly indicating the presence of an AGN. It has been detected at 408 MHz, 1.4 Ghz, 4.85 Ghz and 5 Ghz (Ficarra, Grueff & Tomassetti, 1985; Gregory & Condon, 1991; Condon et al., 1998), and shown to have a power law profile, typical of synchrotron emission from a jet (Sramek, 1975). My 3mm continuum flux measurement of 9.6 mJy beam^{-1} however, is found to be inconsistent with a continued monatomic power law decrease in the radio flux. A maximum of 0.2 mJy at 3mm can be explained by dust, based on the IRAS 100 and 60 μm observed fluxes, and 0.04 mJy by free-free emission (calculated from the SAURON Hβ fluxes, as above). I hence suggest the continuum emission is AGN powered, and speculate that perhaps self-absorption flattens the synchrotron emission spectrum at low frequencies, but that the 3mm continuum emission is optically thin (e.g. Krips et al., 2007).

2.3 MORPHOLOGICAL CLASSIFICATION

From visual inspection of the integrated intensity maps, along with the average integrated velocity and channel maps presented in Section 2.A I can identify five rough morphological categories into which the galaxies fall.

1. Discs: 22/40 galaxies (55%) have their gas distributed in a relaxed disc.

2. Rings and Bars: 7/40 galaxies (17.5%) have their gas distributed in a ring which is obvious in the moment zero map. In NGC 5379, which appears to be close to edge on, the molecular gas displays solid body rotation. This could be due to either the effects of a bar, or the projection of an edge on ring. 2/40 galaxies (14%) appear to have their gas in the X2 orbits within bars, as revealed by an X-shaped position velocity diagram (see Chapter 4). These galaxies sometimes also have structures in the integrated intensity maps which support the assumption that one arm of the "X" is due to a ring at the end of the bar.

3. Weakly disturbed gas: 3/40 galaxies (7.5%) show signs of minor disturbances. These include tails of emission, and asymmetric gas distributions. The gas however appear to be regularly rotating.

4. Strongly disturbed gas: 4/40 galaxies (10%) of the sample galaxies show morphological and kinematic disturbances that suggest the gas is not relaxed.

5. Spiral structure: 2/40 galaxies (5%) have single or double spiral arm structures in the molecular gas, that are not obvious in optical images.

Figure 2.1 shows the *Ks*-band magnitude distribution for the mapped ATLAS^{3D} galaxies as a function of these molecular gas morphologies. Galaxies with molecular disks are present at all magnitudes, making up 50% of the total population at low magnitudes. However, all galaxies brighter than -24.5 mag have their molecular gas distributed in a relaxed disk. Galaxies with molecular rings tend to be at lower magnitudes, and those with bars seem to be at intermediate magnitudes. Galaxies with disturbances, and spiral structure also tend to be at lower magnitudes. The lack of galaxies with non disk-like morphology at high magnitudes is interesting; however due to the small number of such systems I am unable to draw strong conclusions, although I discuss potential causes in Section 2.4.1.

Galaxies with strong morphological disturbances that reside in the field have the largest molecular gas reservoirs present in any of the sample galaxies. These systems are either undergoing mergers (NGC 1222) or are expelling their gas via AGN feedback (NGC 1266), and hence have been caught at special times in their evolution. Galaxies with large molecular gas masses that are not strongly disturbed tend to have this gas distributed in relaxed disks, or within bars. Rings and minor disturbances are more commonly found in galaxies with lower molecular gas masses. Once again these trends are tentative due to low number statistics, but I briefly discuss them in Section 2.4.1.

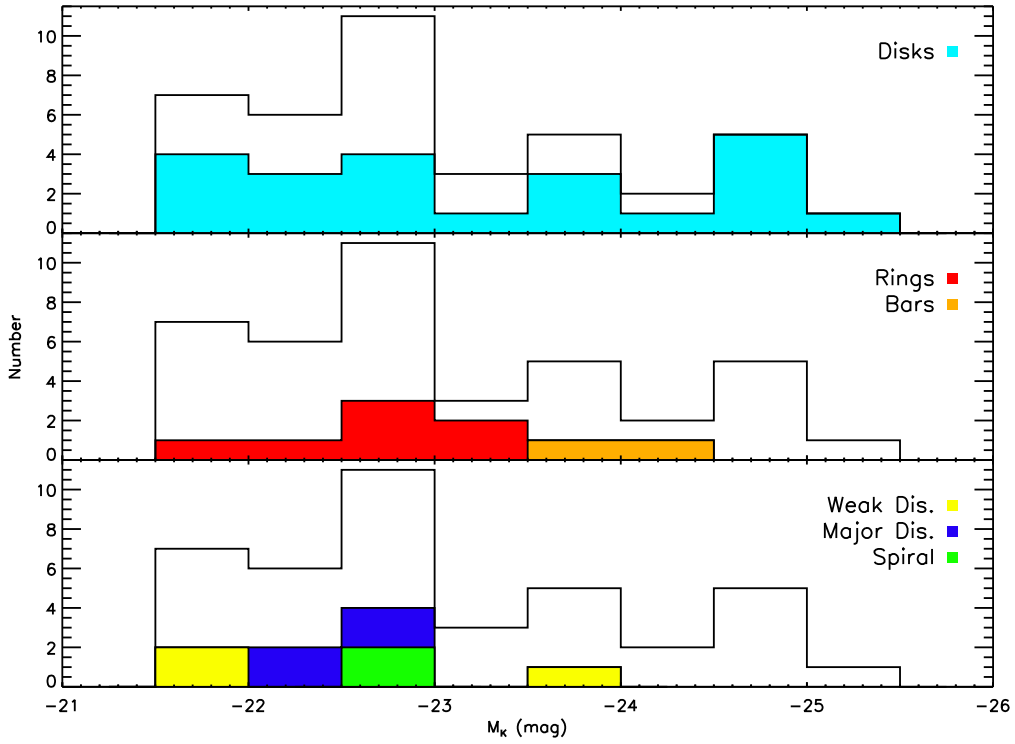

Figure 2.1: The *Ks*-band magnitude distribution for the CARMA ATLAS^{3D} galaxies as a function of molecular gas morphology. The white histogram shows the total distribution of *Ks*-band magnitudes for the CARMA sample of galaxies. The area coloured in each histogram shows the contribution of each morphological class towards the total. The top panel shows the *Ks*-band magnitudes of galaxies with molecular disks. The middle panel shows the distribution for galaxies with rings and bars, and the bottom the individual contributions for galaxies with some form of disturbance, and molecular spirals.

2.3.1 *Comparison to dust*

Molecular gas and dust are thought to be closely linked within the ISM. For instance, H_2 molecules form most efficiently on the surface of dust grains (e.g. Duley & Williams, 1993). Dust is also thought to play an important role in shielding molecular clouds from the interstellar radiation field. It is thus unsurprising that previous studies of molecular gas in ETGs have found that the gas and dust are almost always spatially coincident (e.g. Crocker et al., 2011; Young, Bureau & Cappellari, 2008). The morphology of the dust varies however, some galaxies having nuclear dust rings and disks, while others show large scale spiral dust patterns. There are some signs that

the dust morphology correlates with the mass of molecular gas present. For instance, Crocker et al. (2011) report that galaxies with over 10^8 $M_\odot$ of molecular gas have clear flocculent spiral patterns in the dust disks, while galaxies with less molecular mass have less obscuring dust and the dust structures are less ordered.

Figure 2.2 shows the CO integrated intensity maps of the galaxies mapped at CARMA, overlaid on unsharp-masked SDSS or INT *g*-band images. Similarly to other studies, I find that the CO is generally spatially coincident with obscuring dust. It is clear, however, that the dust often extends further than the molecular gas. This could be because dust obscuration is able to trace to fainter gas surface densities than the CO observations, and/or that the dust is mixed with ionised gas or H I which prevent it from being destroyed by grain sputtering. Galaxies with large molecular masses either have disturbed dust distributions (generally in galaxies where the gas is classified as disturbed), or have large discy dust lanes (often with associated dusty spiral arms). Galaxies at lower molecular masses tend to have more flocculent dust structures, or small central dust rings. These trends are very loose however, and examples of all dust morphologies exist at all molecular masses, suggesting other factors are important in determining the dust morphology.

2.4 DISCUSSION

2.4.1 *Molecular gas morphologies*

In Section 2.3 I presented the different molecular gas morphologies seen in the ATLAS^{3D} ETGs. This is the first time that the morphology of the gas in a large sample of ETGs has been analysed. I find that mostly commonly the molecular gas is in a relaxed disc or ring. Less commonly the gas appears to be disturbed and out of equilibrium.

Nearly all ETGs that have molecular gas maps (either presented here or in the literature) have centrally concentrated gas distributions. This is expected, as galaxy mergers and close interactions are thought to funnel gas into the centre of galaxies (e.g. Combes, 1994; Mihos & Hernquist, 1996); mass loss from stars will also have

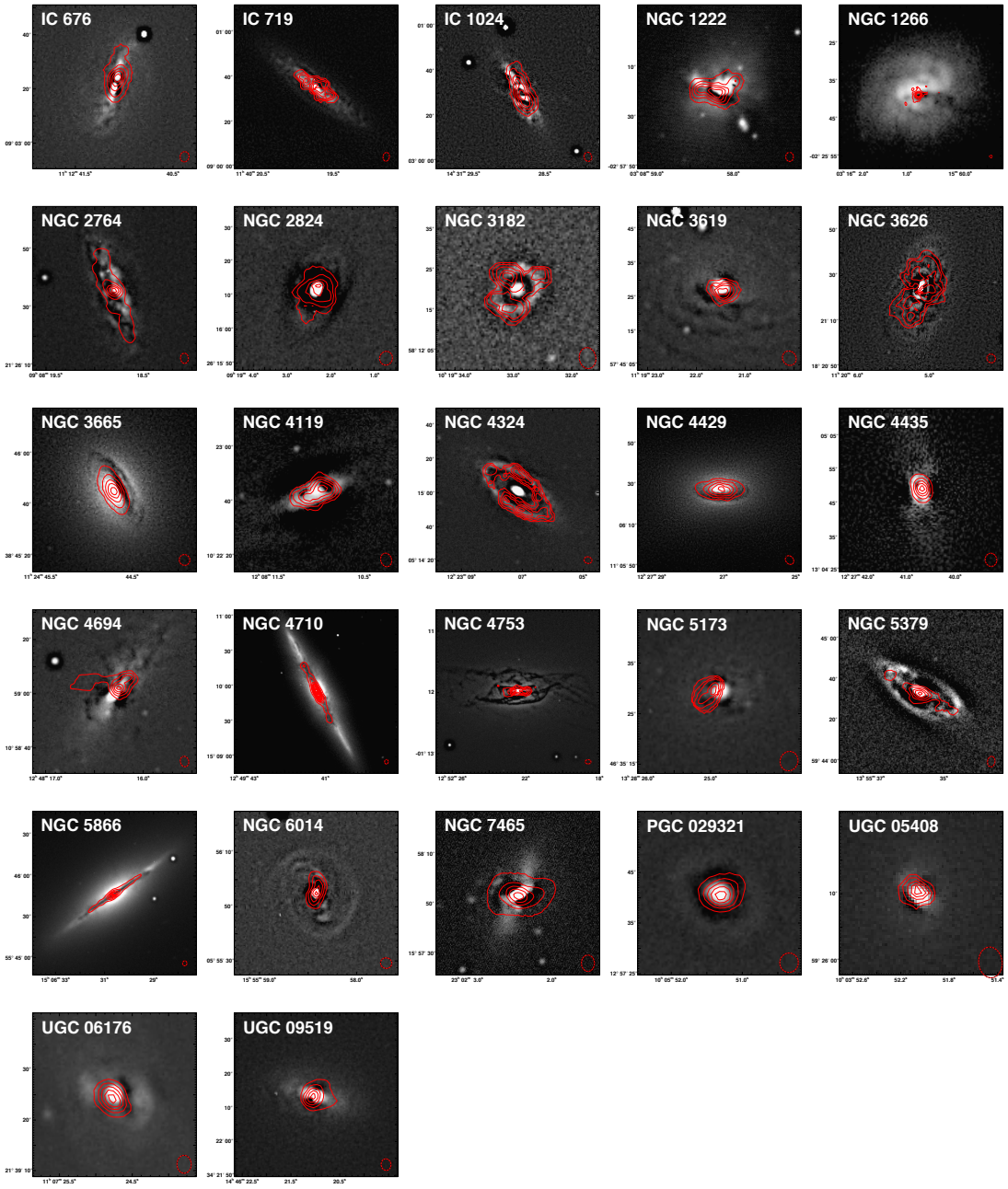

Figure 2.2: CARMA integrated intensity maps (red contours), overlaid on optically obscuring dust made visible by unsharp-masking SDSS or INT *g*-band images. This figure does not include the two non-ATLAS^{3D} galaxies and PGC 058114 due to a lack of suitable photometry.

more chance to become dense in the centres of galaxies, because of the larger volume density stars loosing mass. Caution must be exercised in concluding that all the molecular gas in ETGs is centrally concentrated, however. Almost all of the mapped ETGs were selected via single-dish observations of their central regions. In the sample discussed here, gas rings or disturbed gas distributions outside of the central 23″ (1.6 - 4.6 Kpc) would be missed by our IRAM-30m observations. For instance, the CO polar ring in NGC2685 has a radius of 9.4 Kpc (Schinnerer & Scoville, 2002) and as such would not have been detected by our survey. Although outside the scope of this thesis, combining large field H I-interferometry with UV imaging would be a potent way to identify further ETGs with extended rings and disturbed gas, and obtain an estimate of their prevalence.

2.4.1.1 *The effect of galaxy mass*

In Figure 2.1, I presented evidence that the most luminous ETGs with $M_{Ks} \lesssim$ -24.5 mag (which are also presumably those with the highest masses) all have molecular gas in relaxed discs, while at lower masses some galaxies have rings, bars, spirals or disturbed gas. There are many reasons that one might expect such a difference. Massive galaxies have deeper potentials, which would cause disturbed gas to relax faster (however see Section 2.4.1.2). Massive ETGs have also been shown to host hot X-ray halos, which can suppress the accretion of cold gas (Forman, Jones & Tucker, 1985). Furthermore, in massive galaxies, virial shocks (such as those discussed by Birnboim & Dekel, 2003) can also create a halo mass threshold, above which incoming gas will always shock to the virial temperature, which again stops the accretion of further cold gas. I return to the effect that galaxy mass has on the morphology and kinematics of the molecular gas throughout this thesis.

2.4.1.2 *Disturbed systems*

The relatively large number of disturbed systems (7/41 when one includes galaxies with major and minor signs of disturbance) is quite puzzling. Dynamical times are short in the centre of massive ETGs (T_{dyn} ≈10 Myr for gas orbiting at 1 kpc in an ETG with a mass of 10^{11} $M_{\odot}$) and hence it is expected that gas would relax quickly. The fraction of galaxies one would expect to observe as disturbed ($f_{\rm disturbed}$) if mergers happen randomly, and gas is constantly used up by star formation would be:

$$f_{\rm disturbed} = \frac{a \times T_{\rm dyn}}{\tau_{SF}} \tag{2.1}$$

where $T_{\rm dyn}$ is the dynamical time, τ_{SF} is the time taken to deplete the molecular gas reservoir via star-formation (typically ≈1 Gyr) and a is the number of dynamical times the gas takes to relax.

If one makes the assumption that molecular gas is used up by star-formation in 1 Gyr, and the typical dynamical time in these galaxies is 10 Myr, then in order to match the observed fraction of disturbed galaxies ($f_{\rm disturbed}$ ≈0.17±0.06) the molecular gas is required to take ≈17±6 dynamical times to relax completely. This relaxation timescale is larger than that canonically assumed (≈3$T_{\rm dyn}$).

This analysis suggests that it could take molecular gas a long time to relax in these systems. Alternatively, our sample could be biased towards including more disturbed galaxies. It is possible that the morphological selection (and lack of a colour cut) used in selected the ATLAS^{3D} galaxies biases us towards including more recent mergers. Galaxies undergoing mergers will appear more elliptical on the sky, even if they had disk like progenitors. With the exception of NGC 1222, however, the galaxies with gas classified as disturbed are reasonably discy, without clear signs of merging activity, suggesting that such a bias is unlikely to play a large role. I thus conclude that there is some conflict between the canonically assumed relaxation times and our observations, however a more thorough study will be required to rule out population biases, and the effect of radial variations of $T_{\rm dyn}$.

I am able to use the gas morphology to place a lower limit on the amount of

molecular gas that has come from external sources, such as tidal stripping and accretion events. I include all galaxies with disturbed morphologies (7 systems), and an additional 5 systems where the molecular gas is rotating along a different axis than the stars (see Chapter 5). Assuming the masses provided in Paper IV, these 12 sources have 6×10^9 $M_\odot$, or 41% of the total molecular mass present in the sample galaxies. If we assume that this gas has fallen in over a galaxy's virial time ($\approx 10^8$ yr), then this would mean a minimum external gas accretion rate of ≈ 60 $M_\odot$ yr^{-1} on ETGs as a population, or an average accretion rate onto the 260 ATLAS^{3D} galaxies of ≈ 1.5 $M_\odot$ yr^{-1} per galaxy (around the level of gas accretion observed onto local spiral galaxies, e.g. Fraternali & Binney, 2008).

2.4.1.3 *Dust and the effect of resolution*

The resolution of the interferometric observations ($\approx$4.″5) means that complex molecular gas distributions may be smoothed by the large synthesised beam, and appear to be more disky and regular. Galaxies at the edge of the sample volume suffer more from this effect than nearer systems, as the size of the beam increases by a factor of four over the sample volume. If we assume that dust is a good tracer of molecular gas we can achieve much higher spatial resolutions (especially if Hubble Space telescope imaging is available). Figure 2.2 shows that many of the galaxies may have tightly wound dust spirals, which are smoothed out in the molecular gas maps to look discy. Higher spatial resolution CO maps could provide a better understanding of the degree of substructure present in these galaxies, and even potentially allow an estimate of the density variations in these galaxies, and its relation to star-formation.

2.5 CONCLUSIONS

In this chapter I have introduced the ATLAS^{3D} CARMA survey, and presented new interferometric CO observations for 30 ETGs. Combined with data available in the literature I construct the largest ever sample of mapped ETGs, containing 41 objects.

I use this sample to analyse the morphology of the molecular gas in ETGs. As found by previous authors with smaller samples, many of the galaxies have relaxed molecular disks (55%). Rings and bars are present in 17.5% of the ATLAS^{3D} ETGs, while a further 17.5% show some form of disturbance. A small proportion (5%) of the sample galaxies have clear single or doubled armed spiral morphologies. This is the first time the relative abundance of different gas morphologies has been measured in a large sample; however clearly larger numbers of galaxies are required if one wants to understand the abundance of some of the rarer subclasses. I acknowledge that our survey is biased towards galaxies with centrally concentrated molecular gas, and suggest ways in which this bias could be overcome.

High luminosity galaxies almost always have their molecular gas distributed in a relaxed disk, perhaps because disturbed gas relaxes faster in a deep stellar potential, or because a hot halo or halo-mass threshold is suppressing the accretion of new cold gas.

The CO emission is generally spatially coincident with obscuring dust, and the two are likely strongly coupled. However dust often extends further than the molecular gas we detect, either because it is associated with neutral or ionised gas, or because we do not have the sensitivity to detect its molecular counterpart. Inspecting the morphology of the dust leads us to conclude that flocculent dust spirals are common, especially in galaxies with high molecular masses. These may be present in the molecular gas, however we lack sufficient resolution to detect such features at this time.

The data presented in this chapter form the basis for the analysis conducted in the rest of this thesis. In Chapter 3 I use the gas kinematics to investigate the CO Tully-Fisher relation of ETGs. In Chapter 4 I go on to investigate the morphology and kinematics of the molecular gas in more detail. Finally in Chapter 5, I consider the origin of this gas, and thus the fate of ETGs as a class.

APPENDIX 2.A ATLAS^{3D} CO MAPS

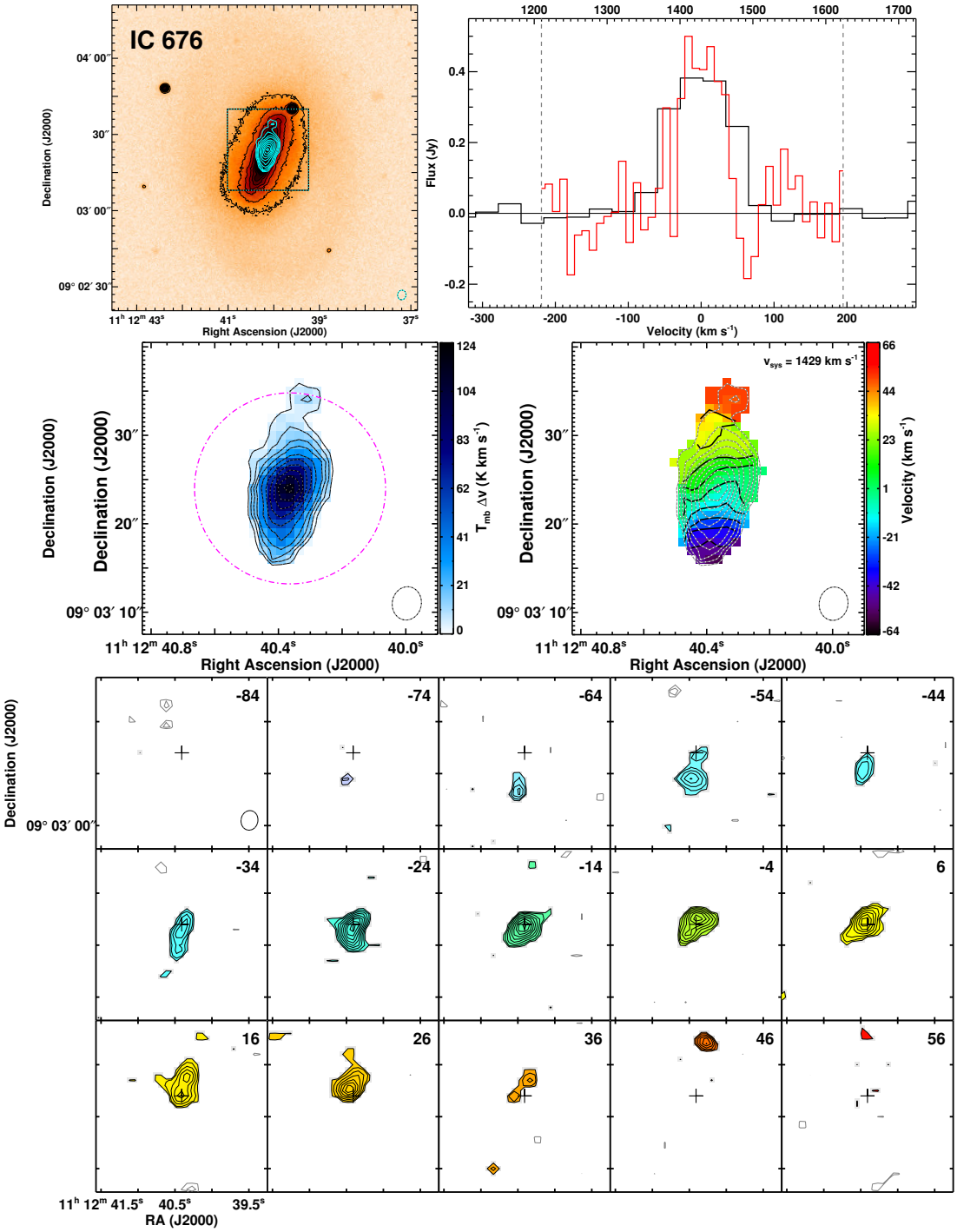

Figure 2.3: *Top left:* CO (blue contours) overlaid on SDSS (or INT) *r* band-image (top left). The square indicates the region zoomed into in the other images. *Top right:* IRAM-30m (black) and CARMA spectra (red) overlaid (top right), dashed lines indicate the CARMA correlator bandwidth. *Middle row:* CO integrated intensity with IRAM-30m beam overlaid (dashed circle), and CO velocity field. *Bottom:* CO channel maps, colour coded by velocity.

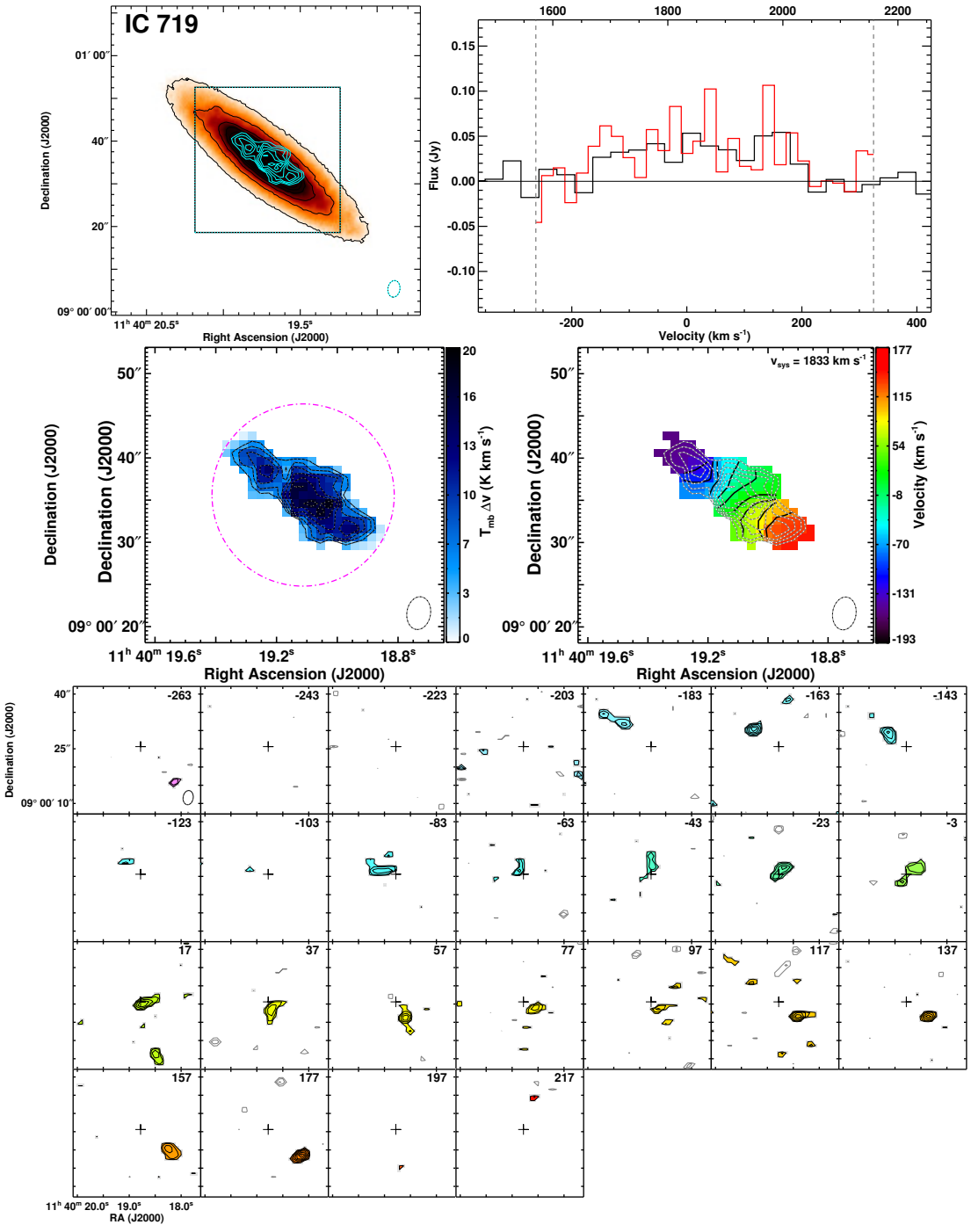

Figure 2.3: continued

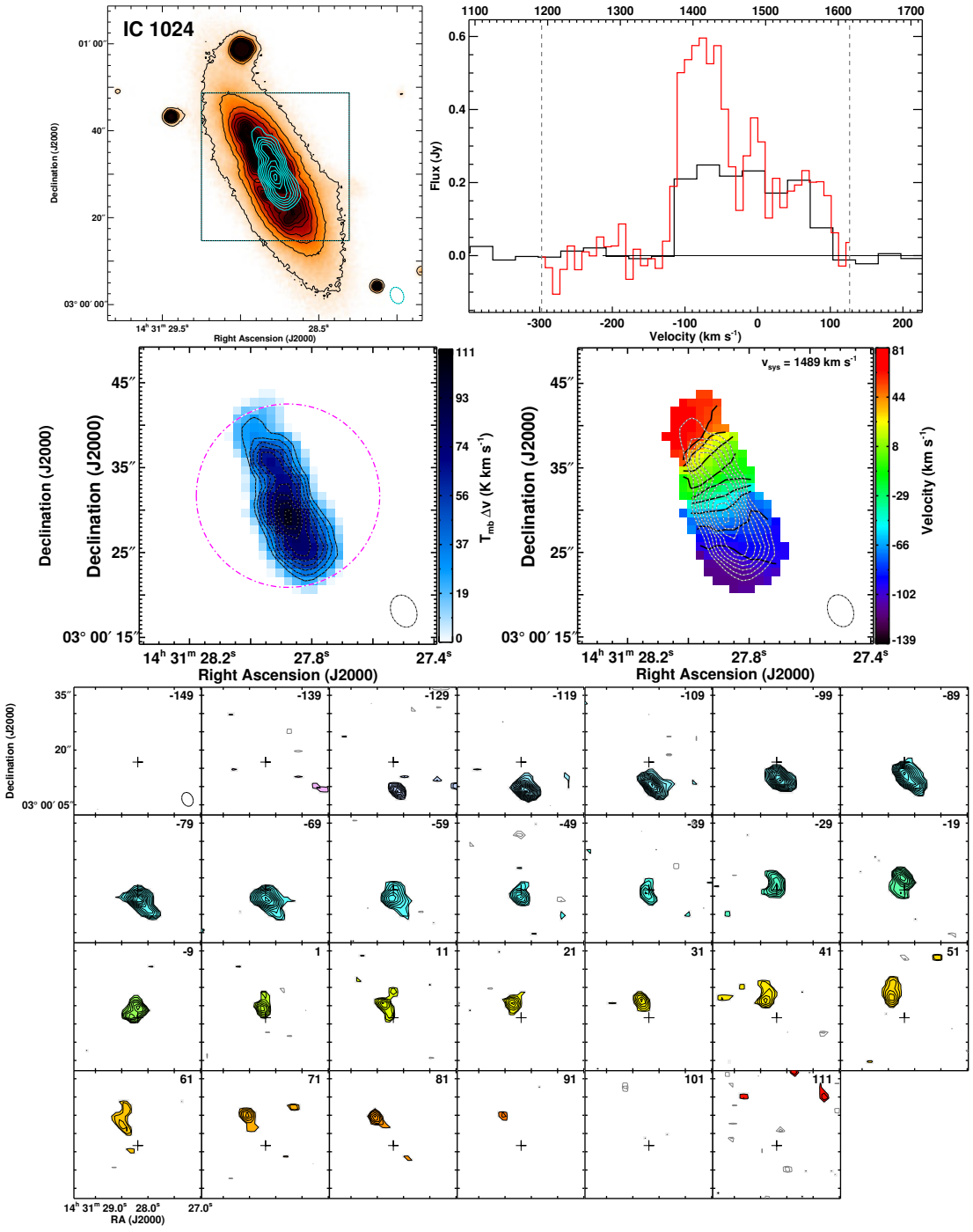

Figure 2.3: continued

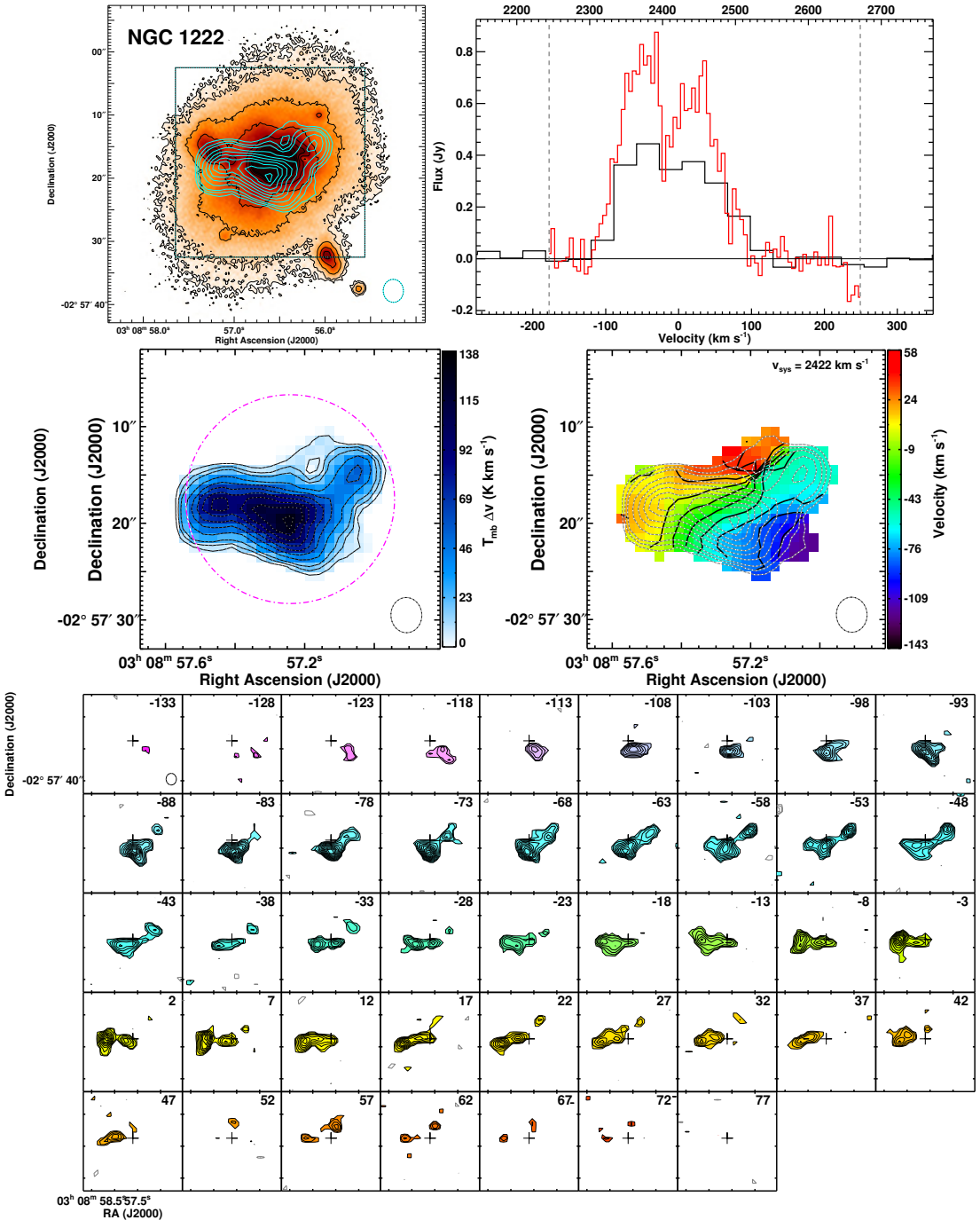

Figure 2.3: continued

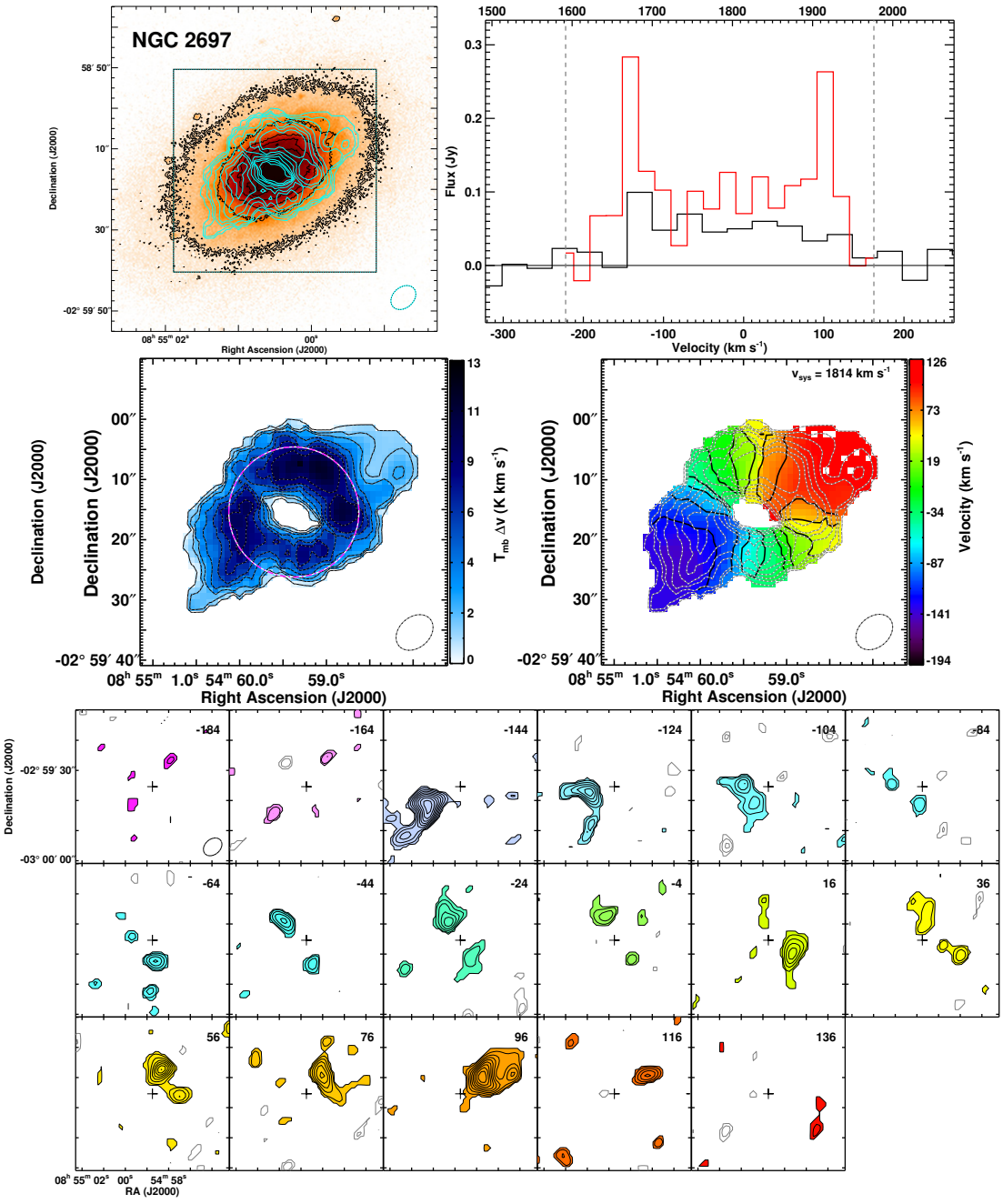

Figure 2.3: continued

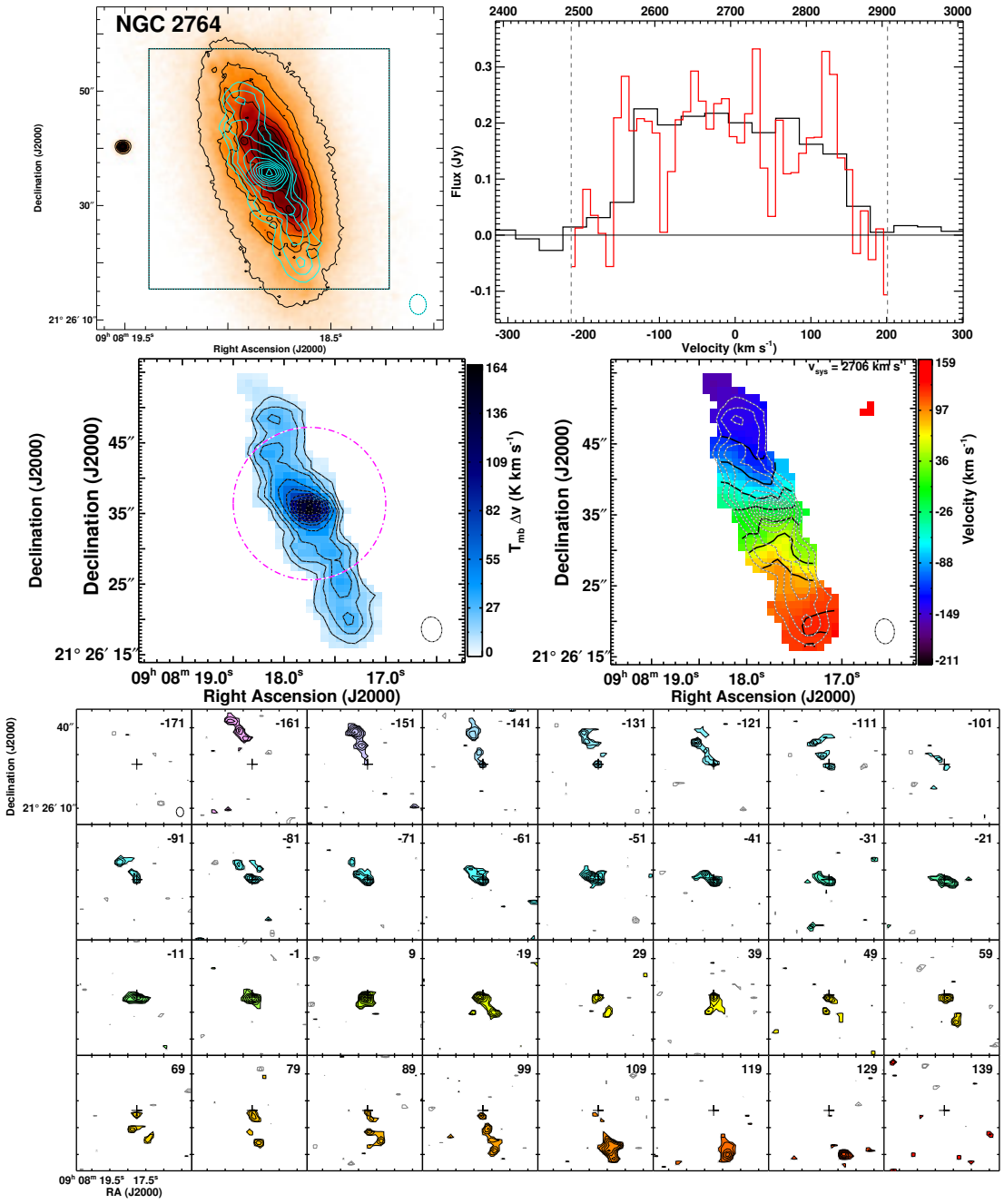

Figure 2.3: continued

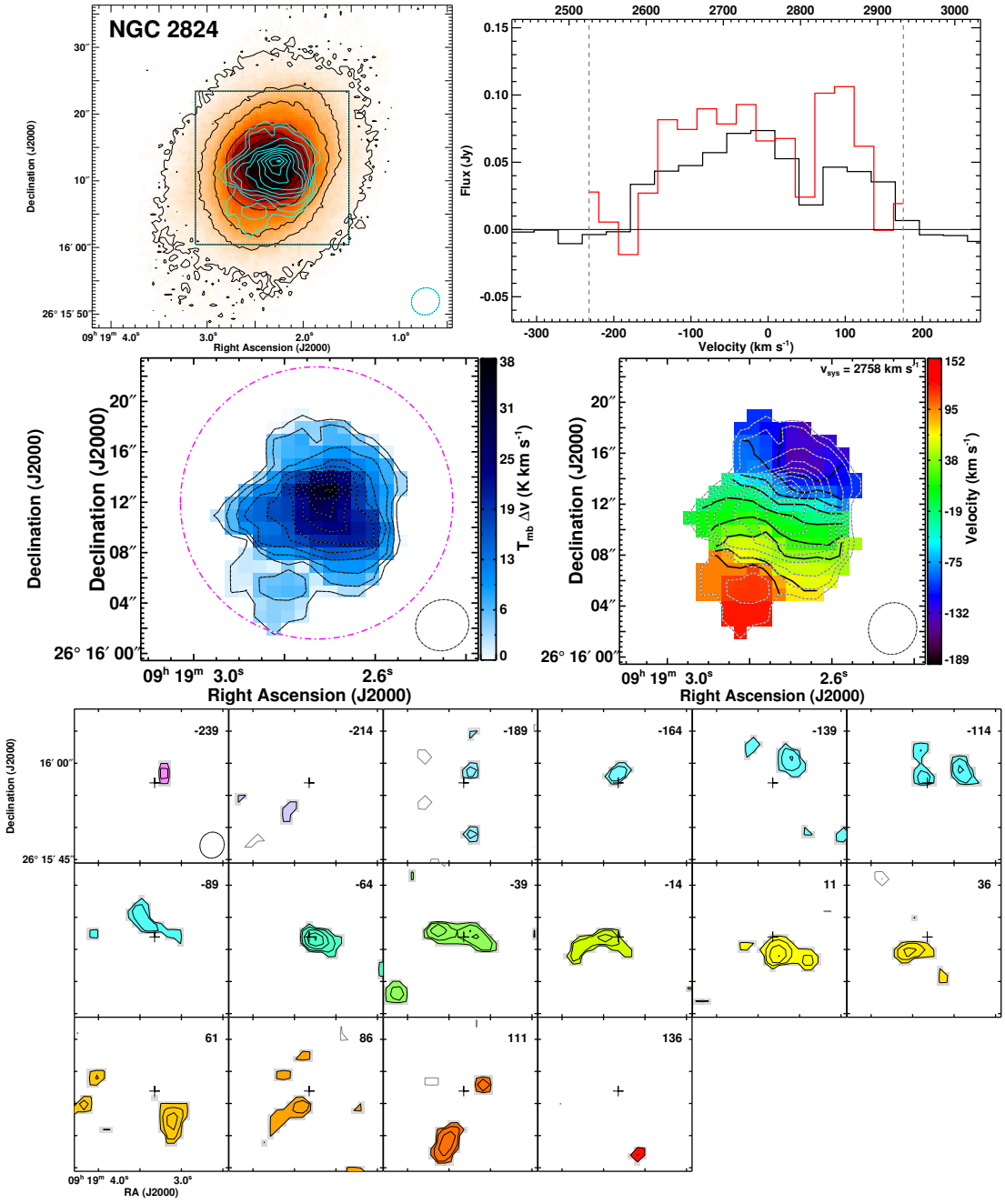

Figure 2.3: continued

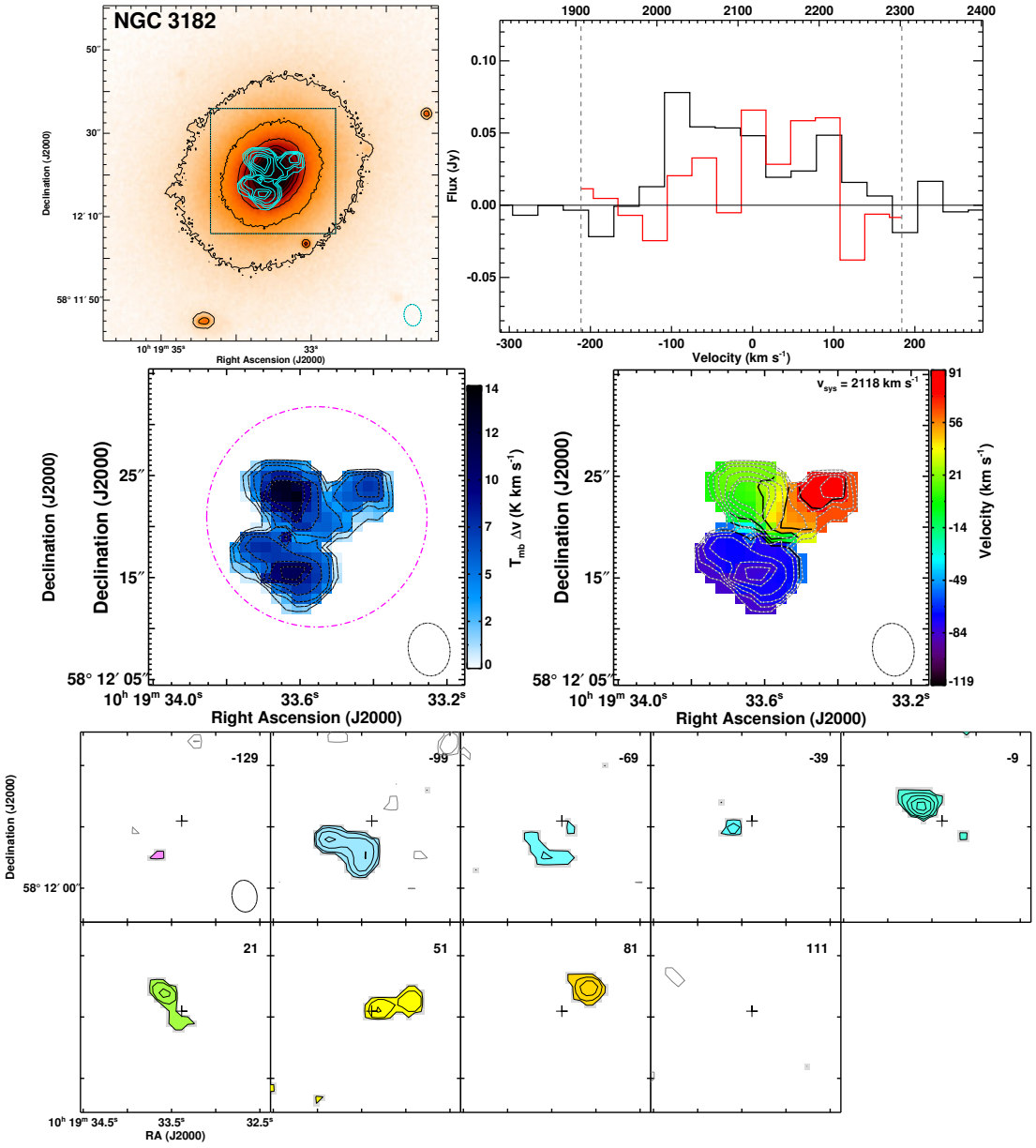

Figure 2.3: continued

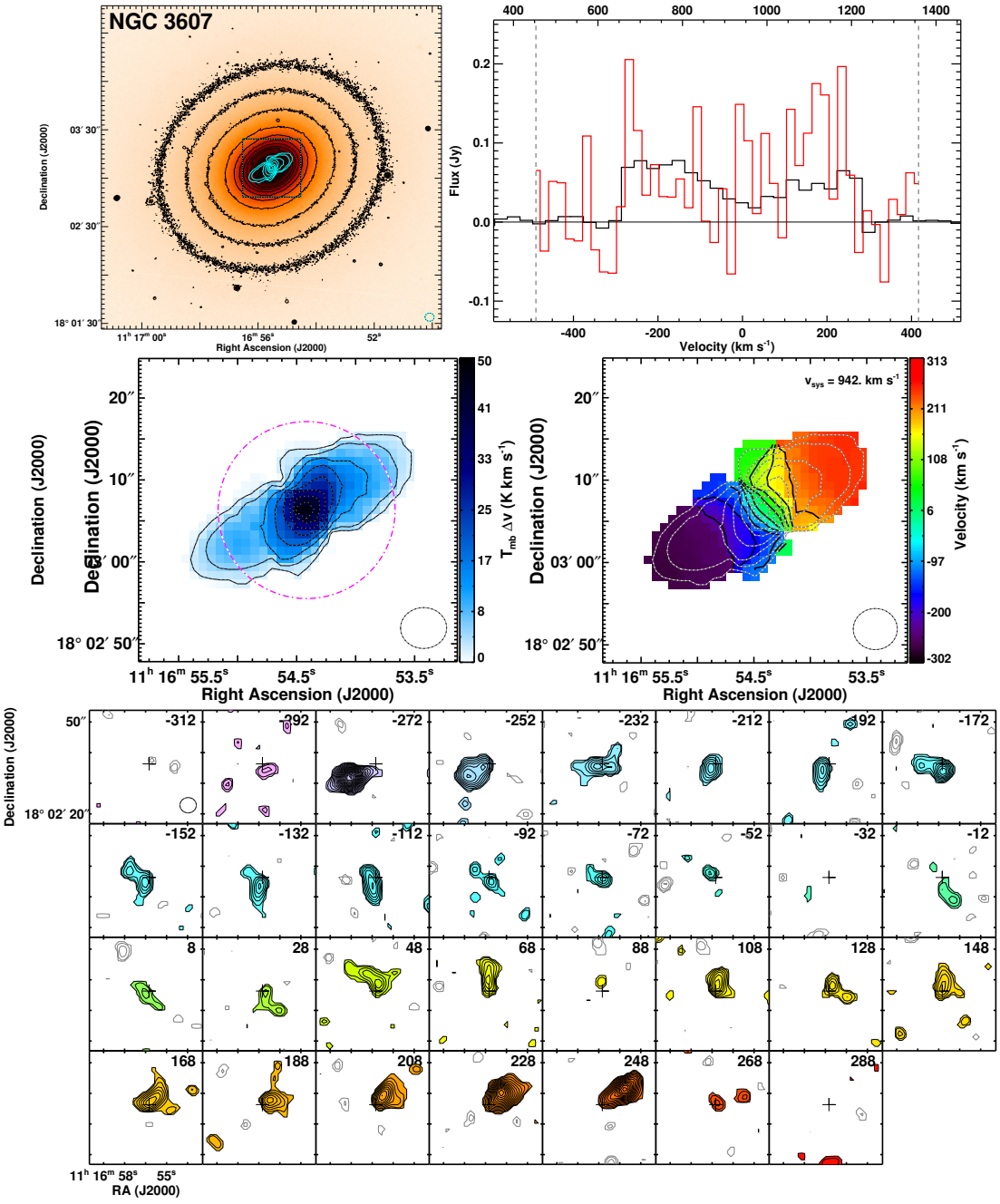

Figure 2.3: continued

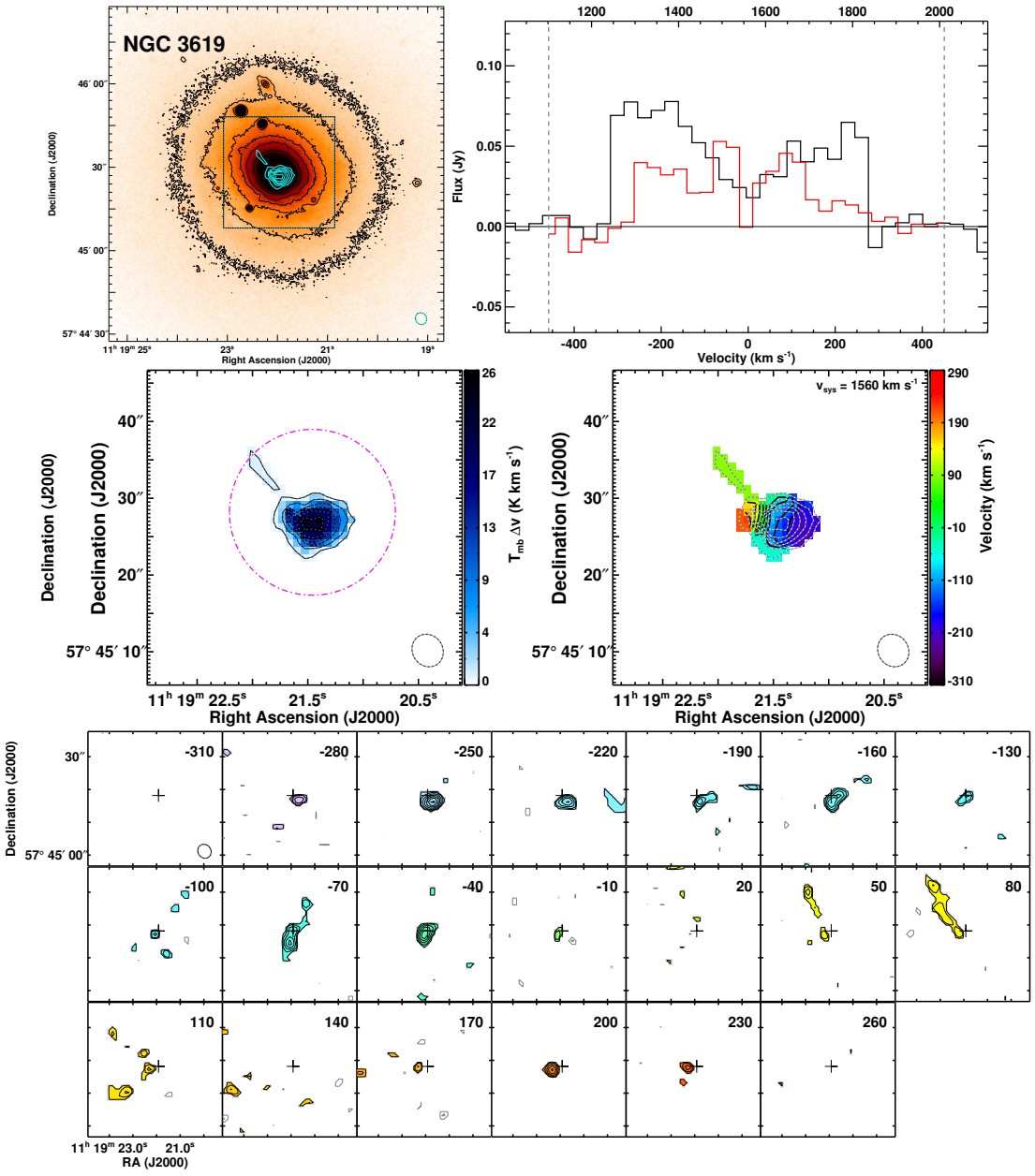

Figure 2.3: continued

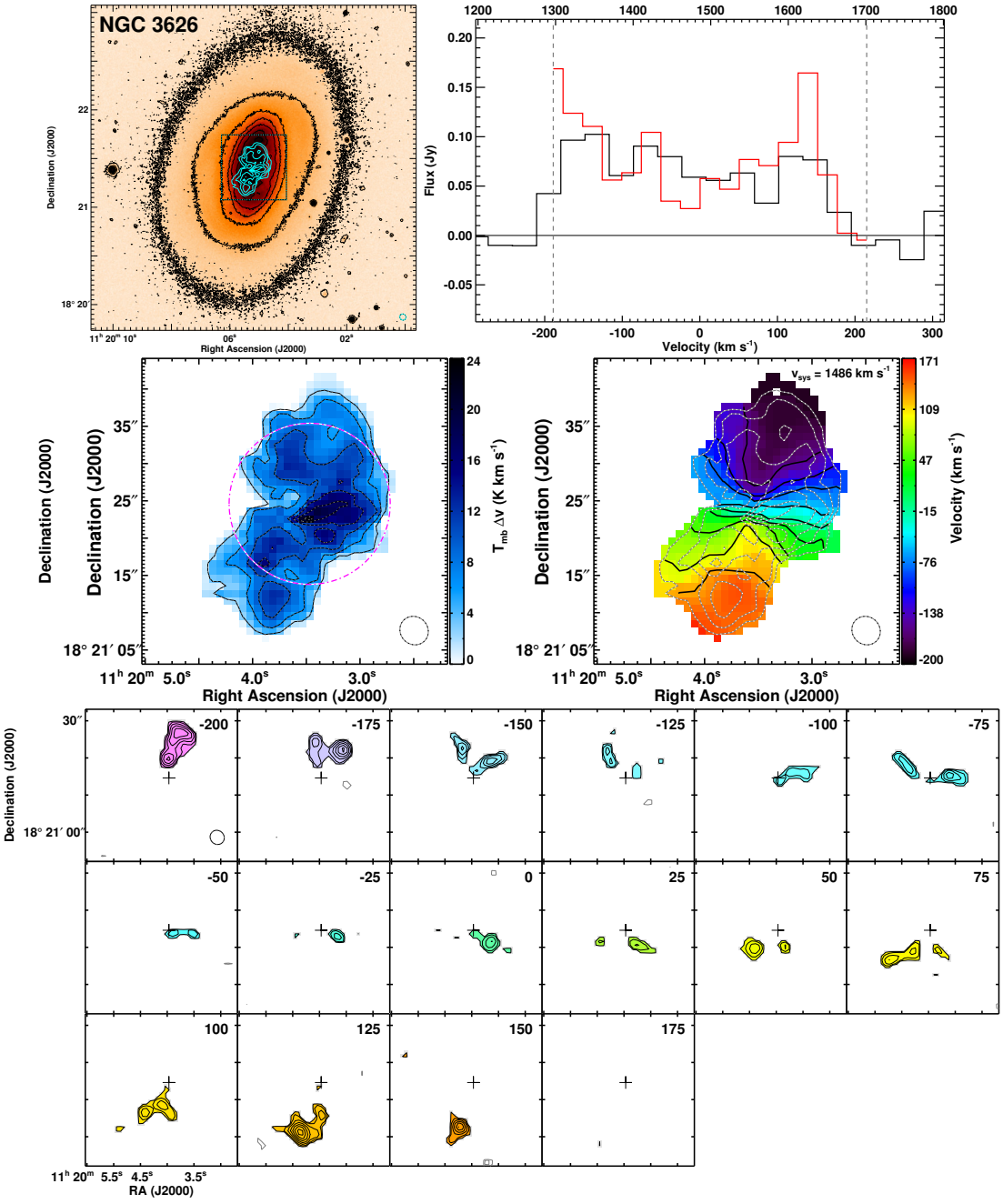

Figure 2.3: continued

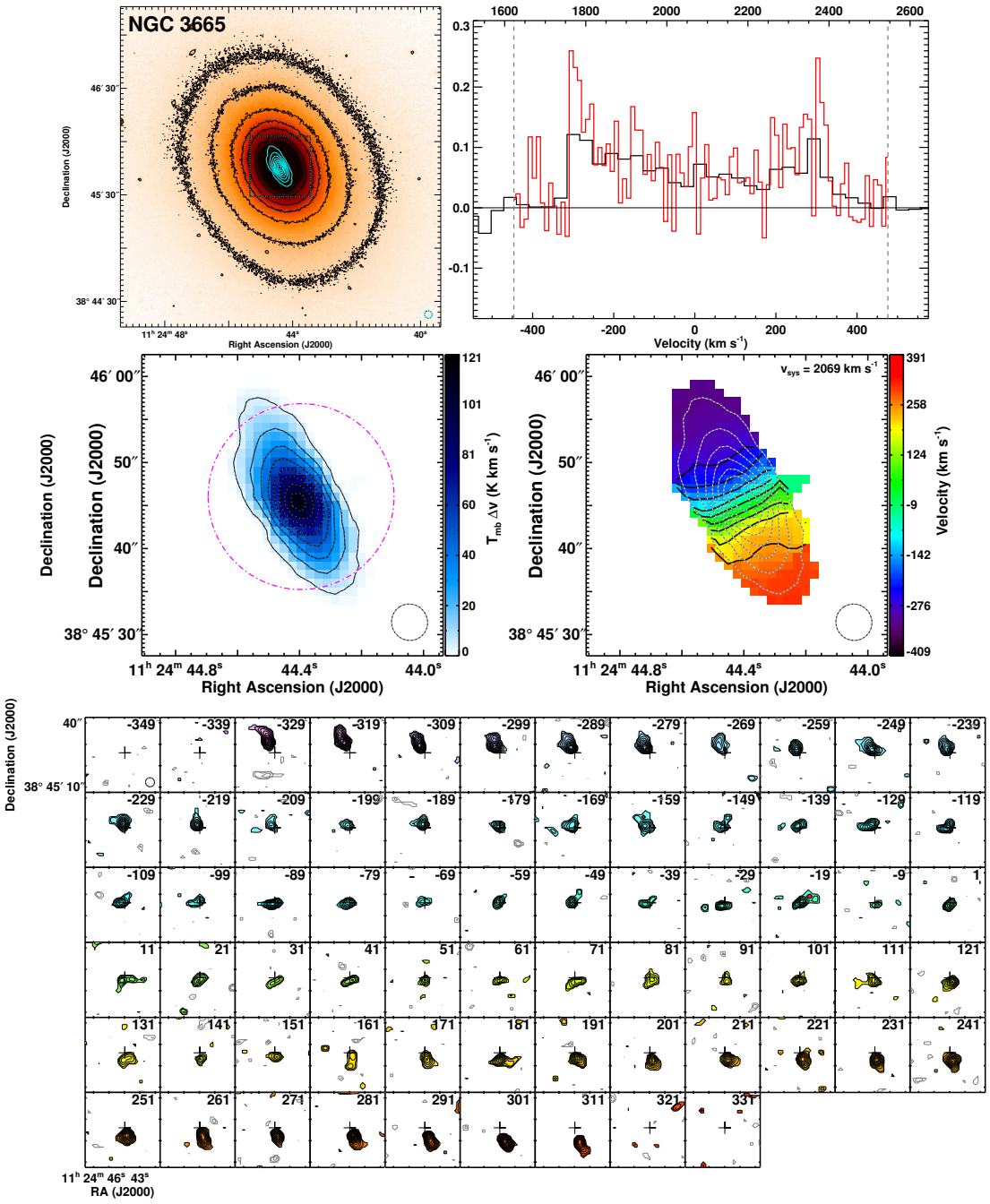

Figure 2.3: continued

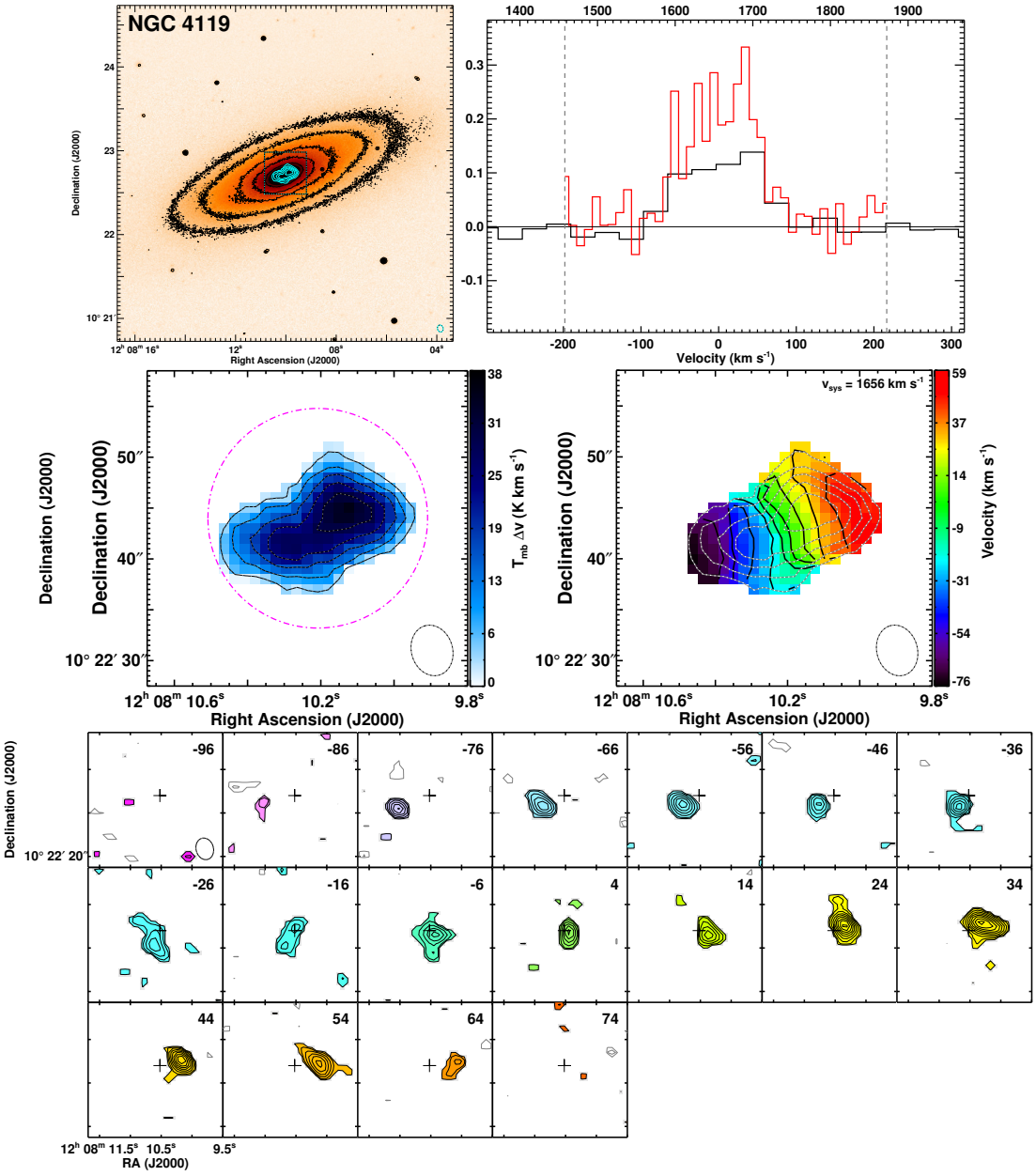

Figure 2.3: continued

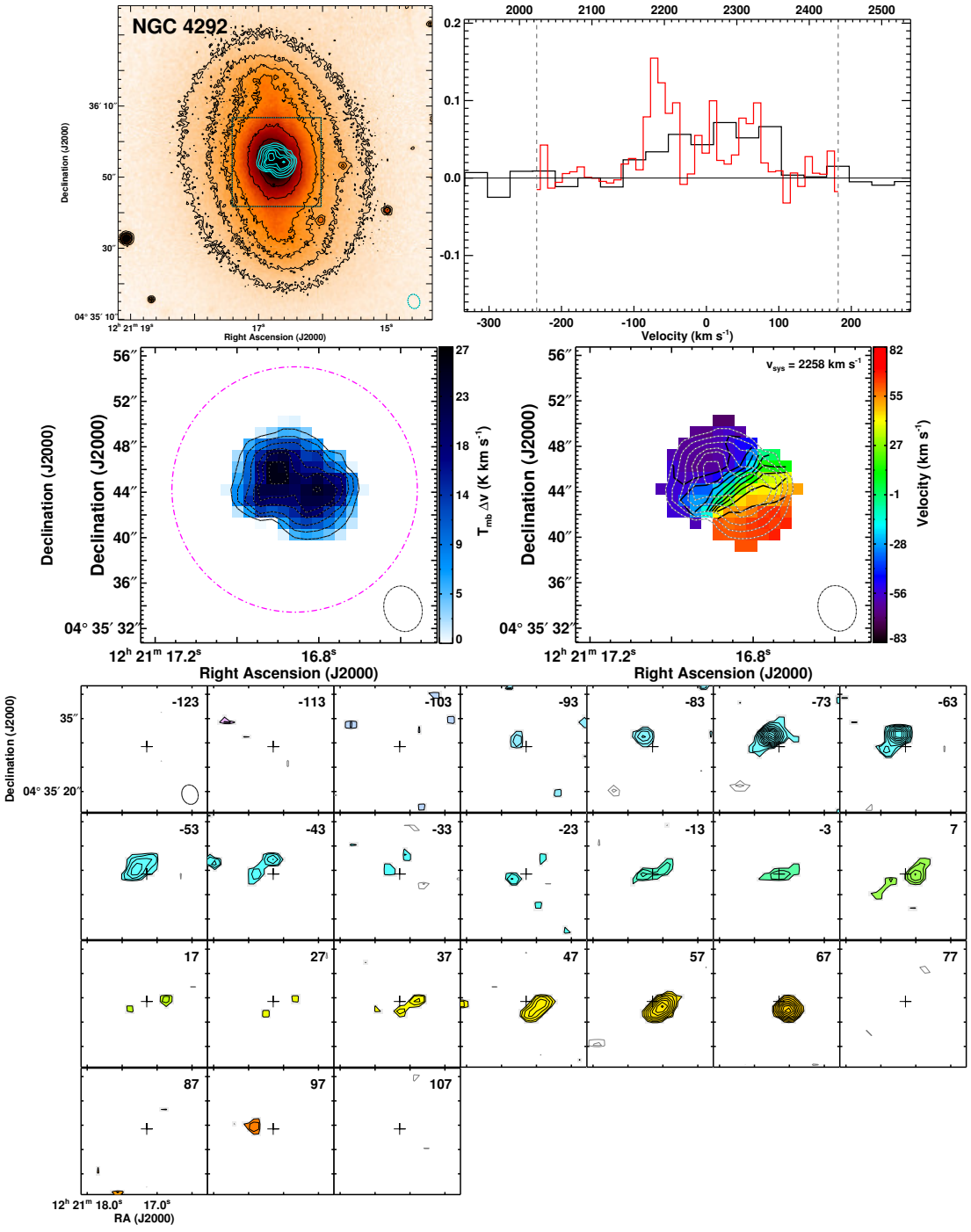

Figure 2.3: continued

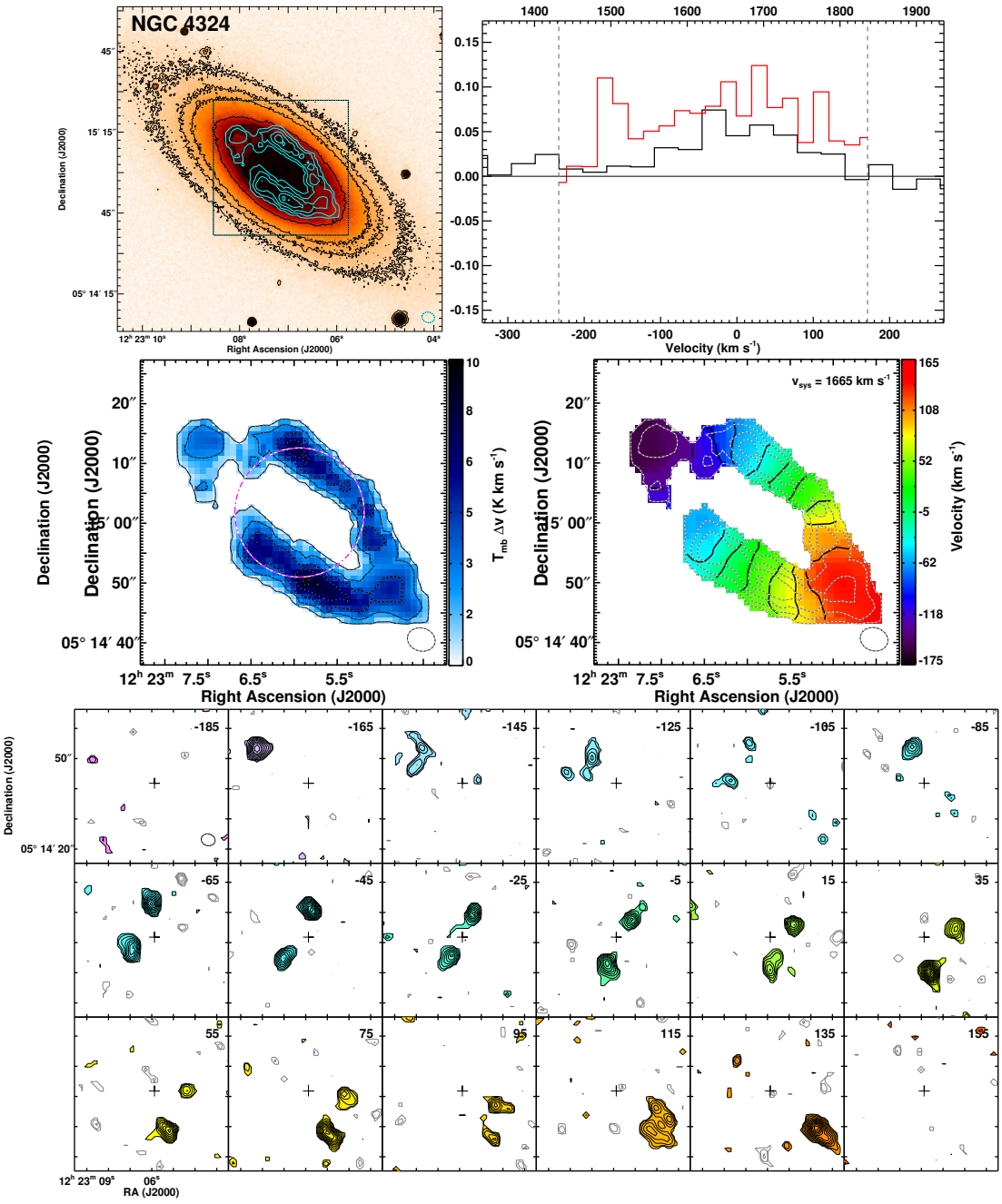

Figure 2.3: continued

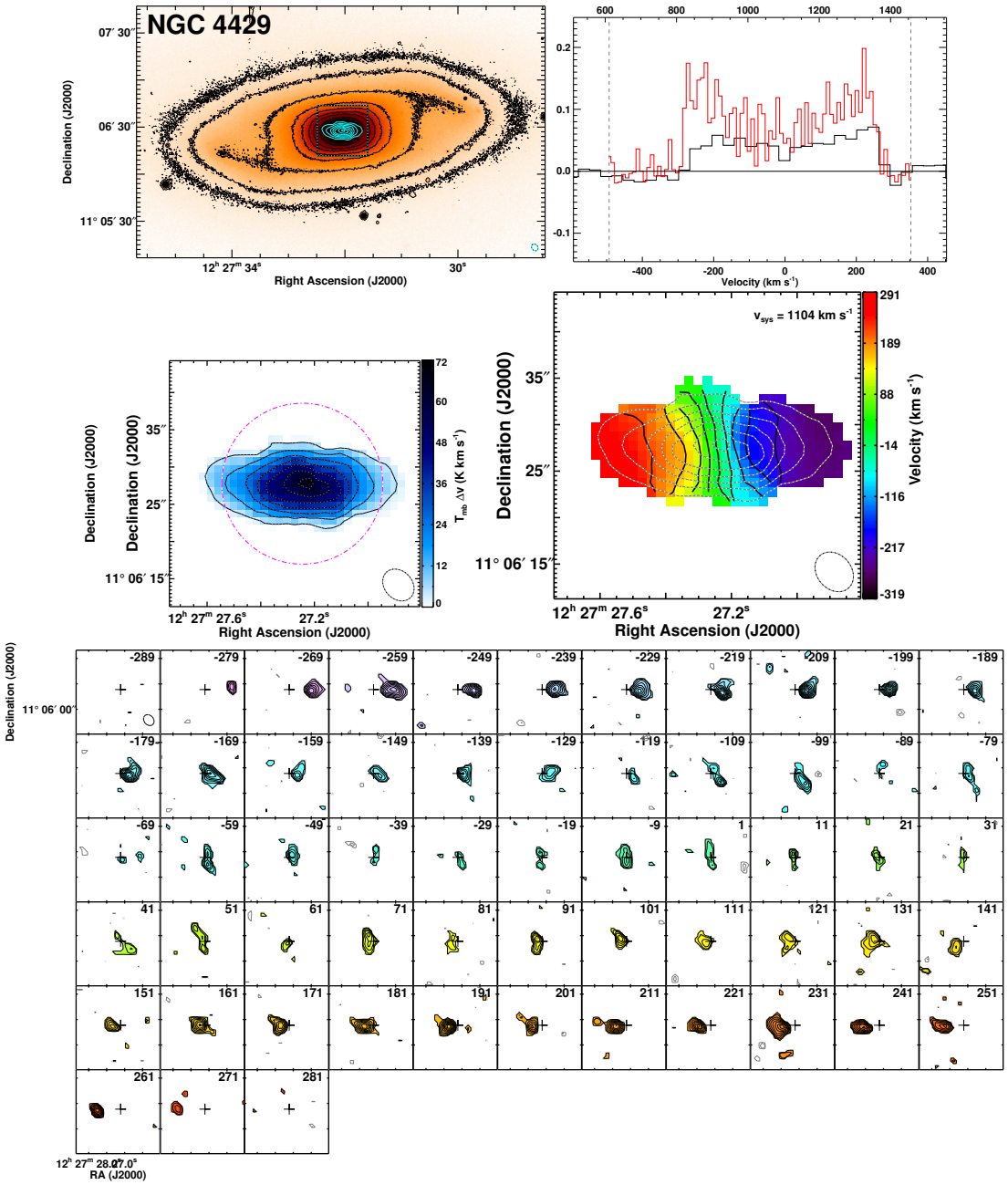

Figure 2.3: continued

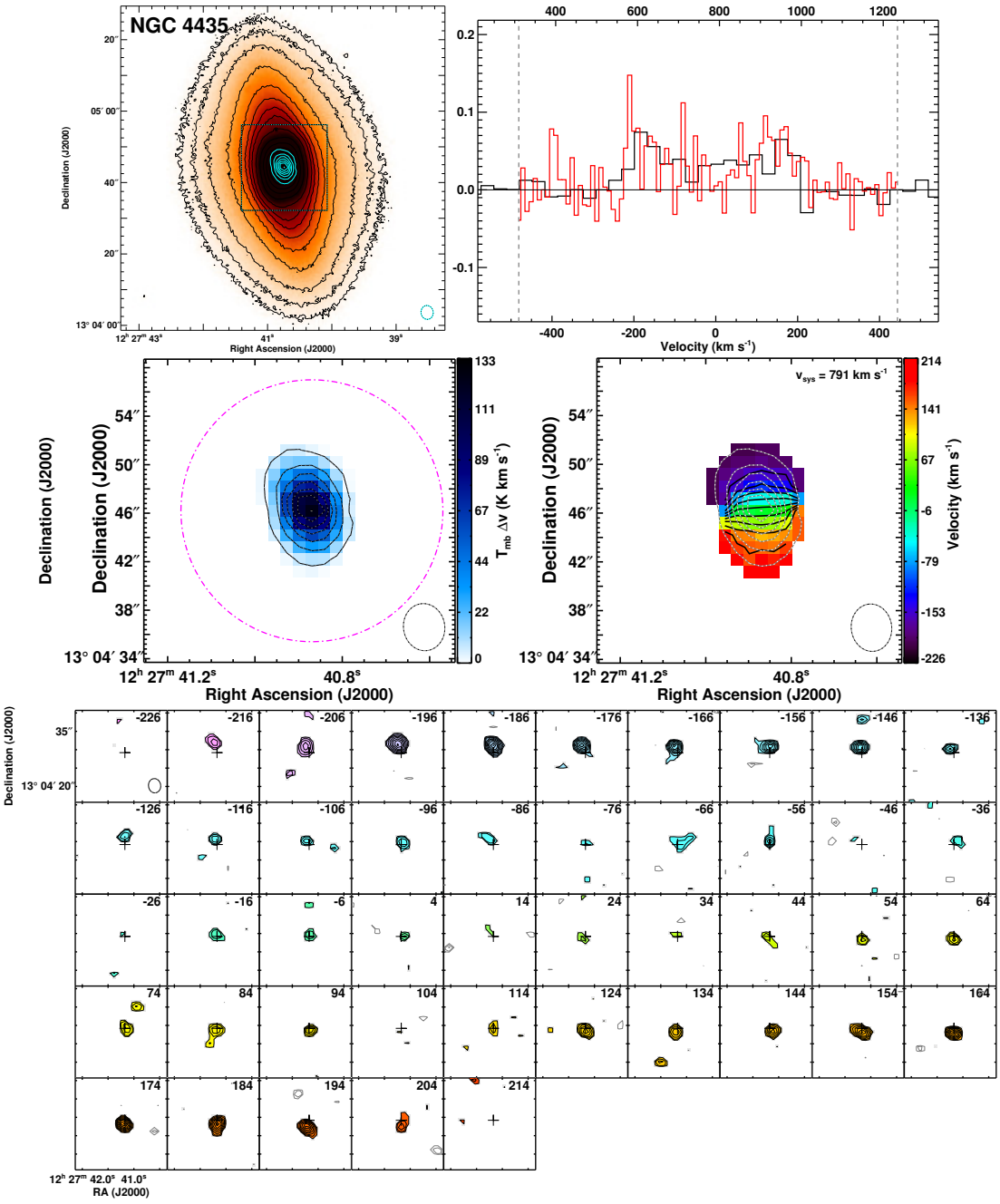

Figure 2.3: continued

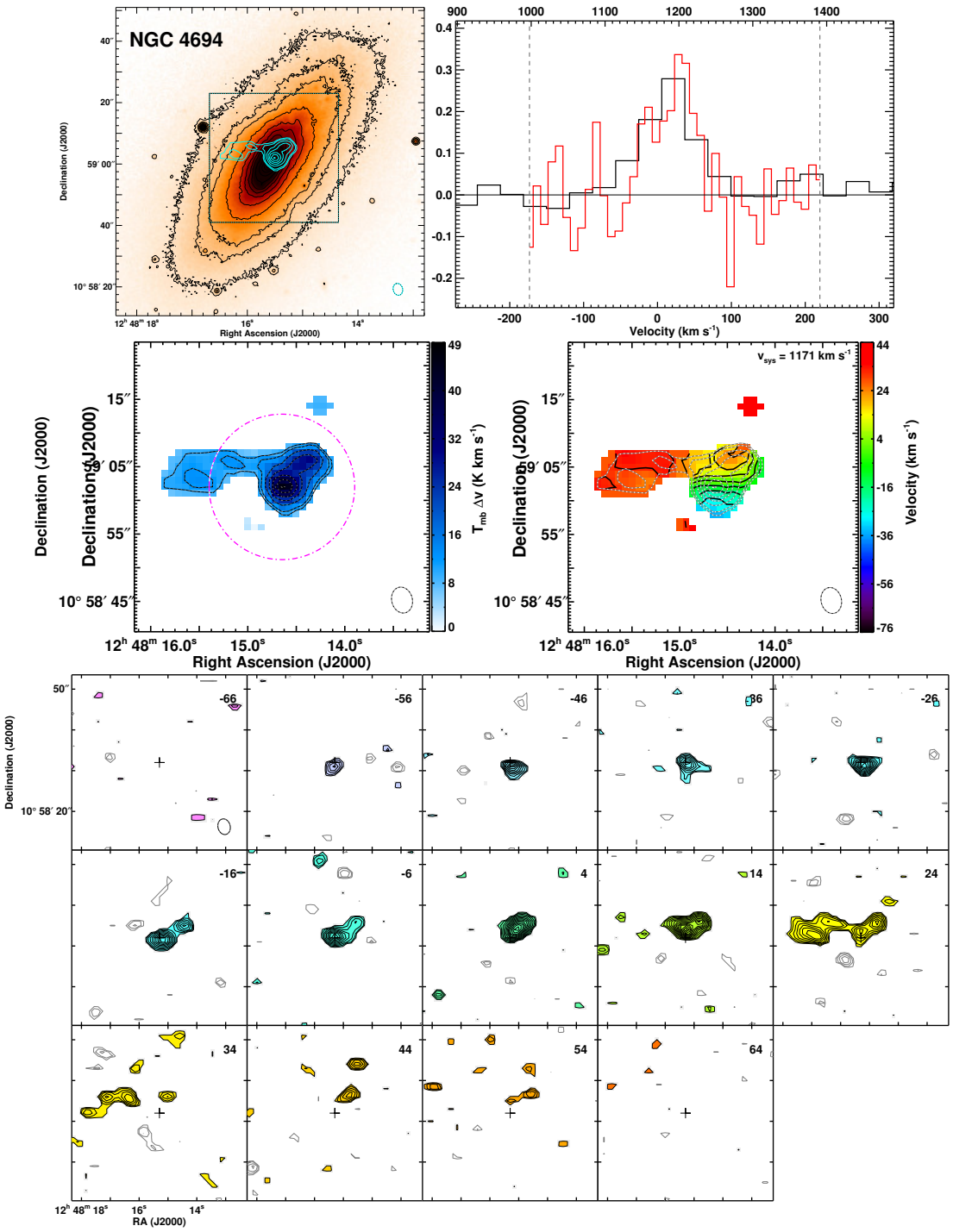

Figure 2.3: continued

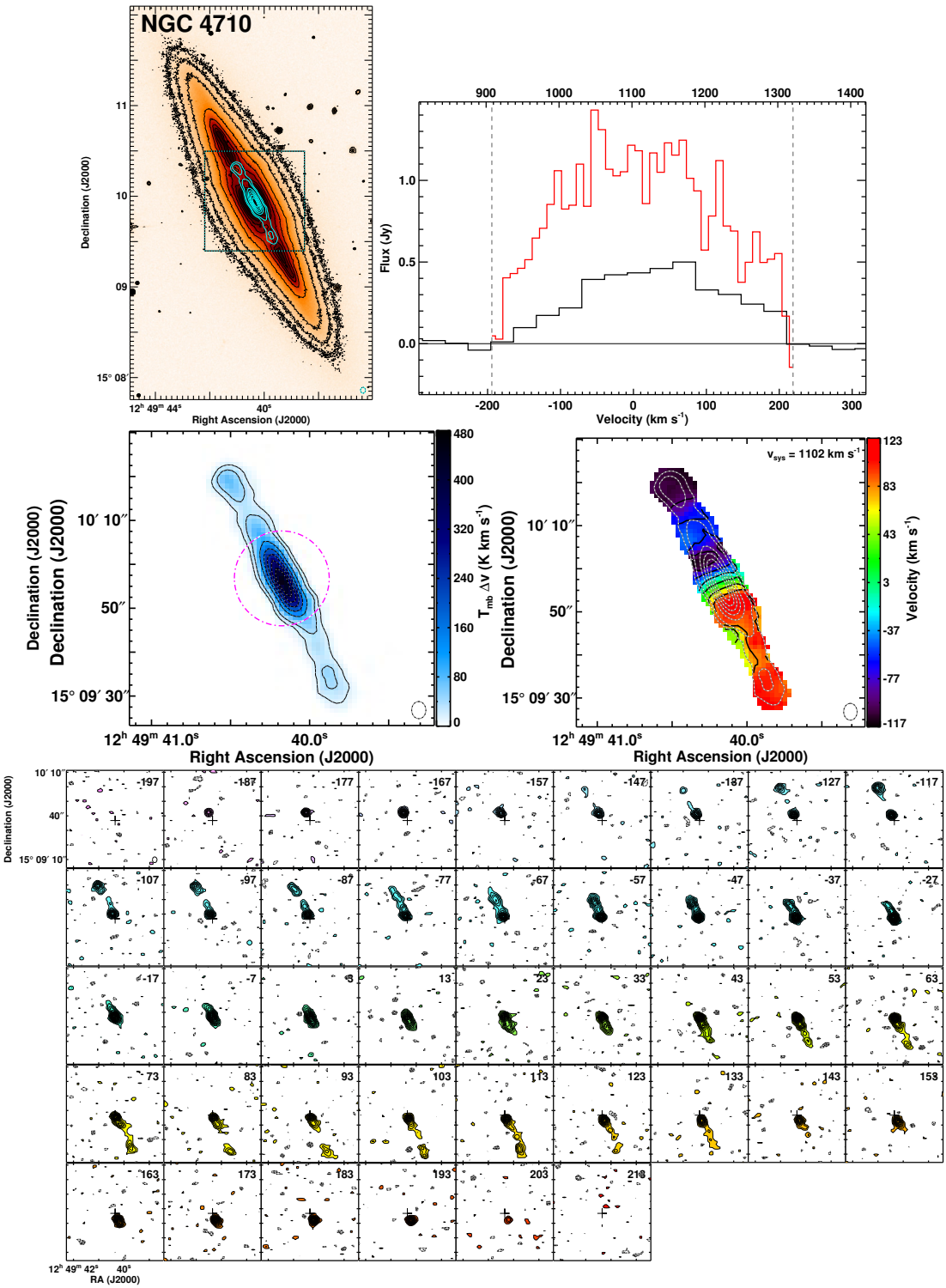

Figure 2.3: continued

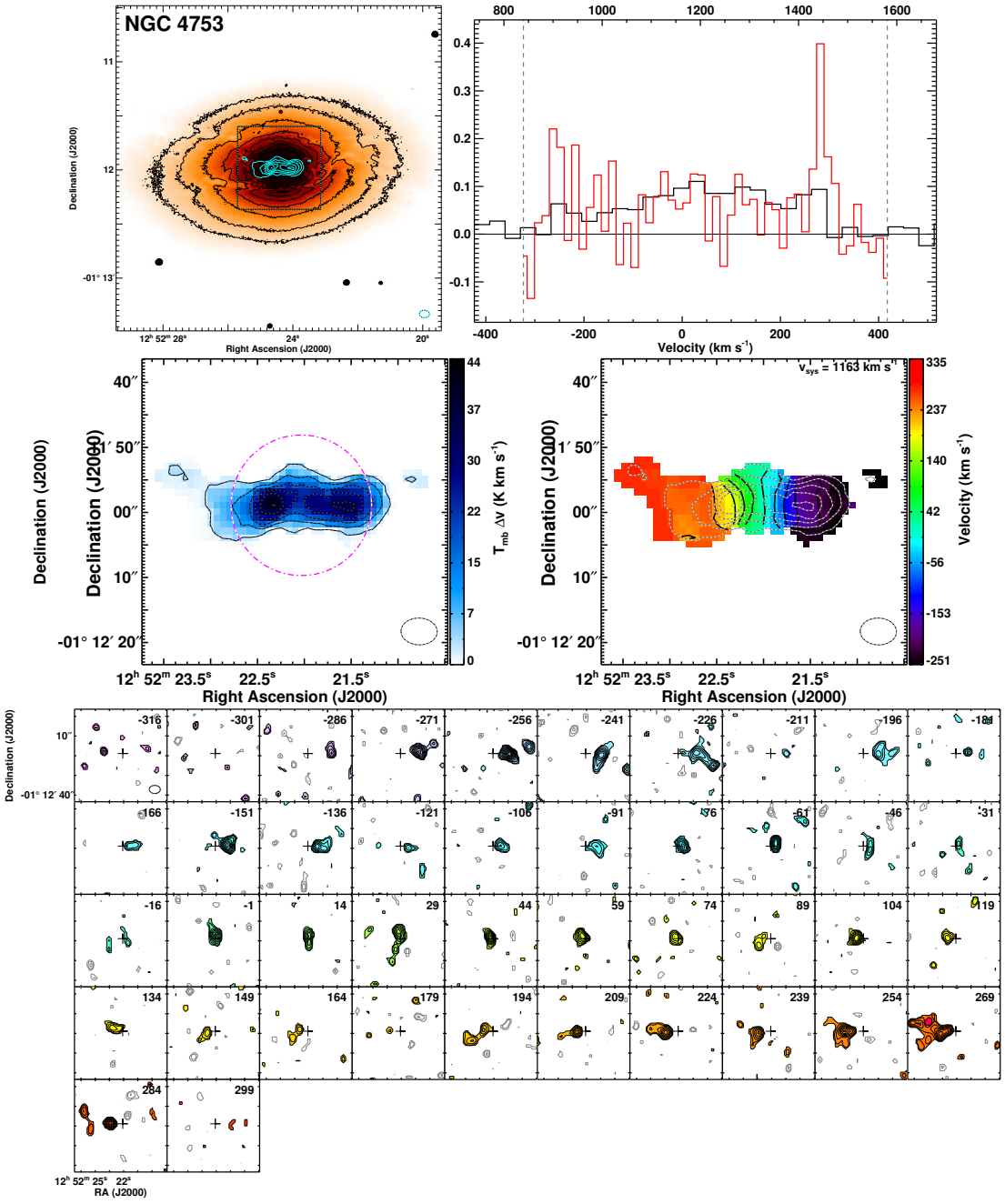

Figure 2.3: continued

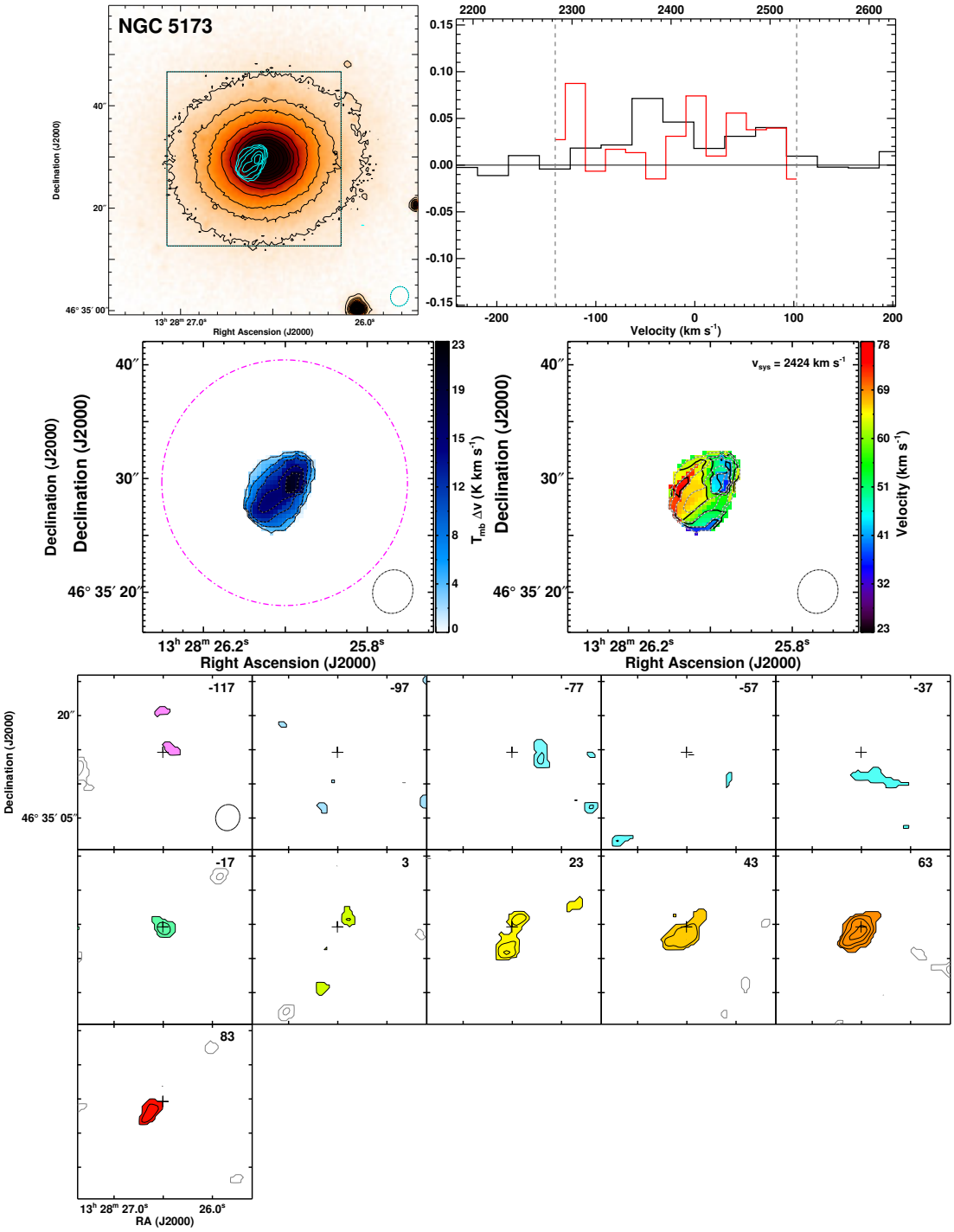

Figure 2.3: continued

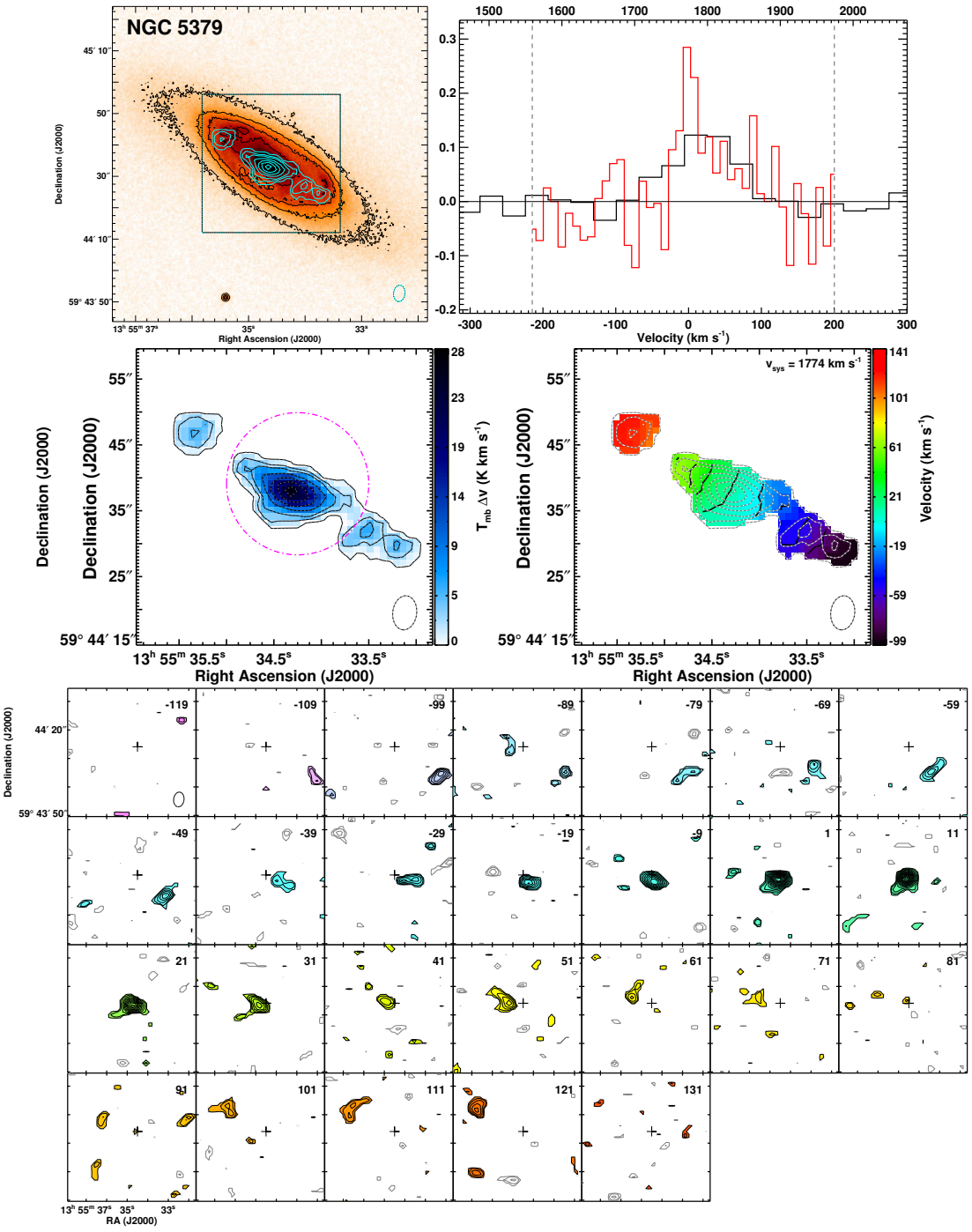

Figure 2.3: continued

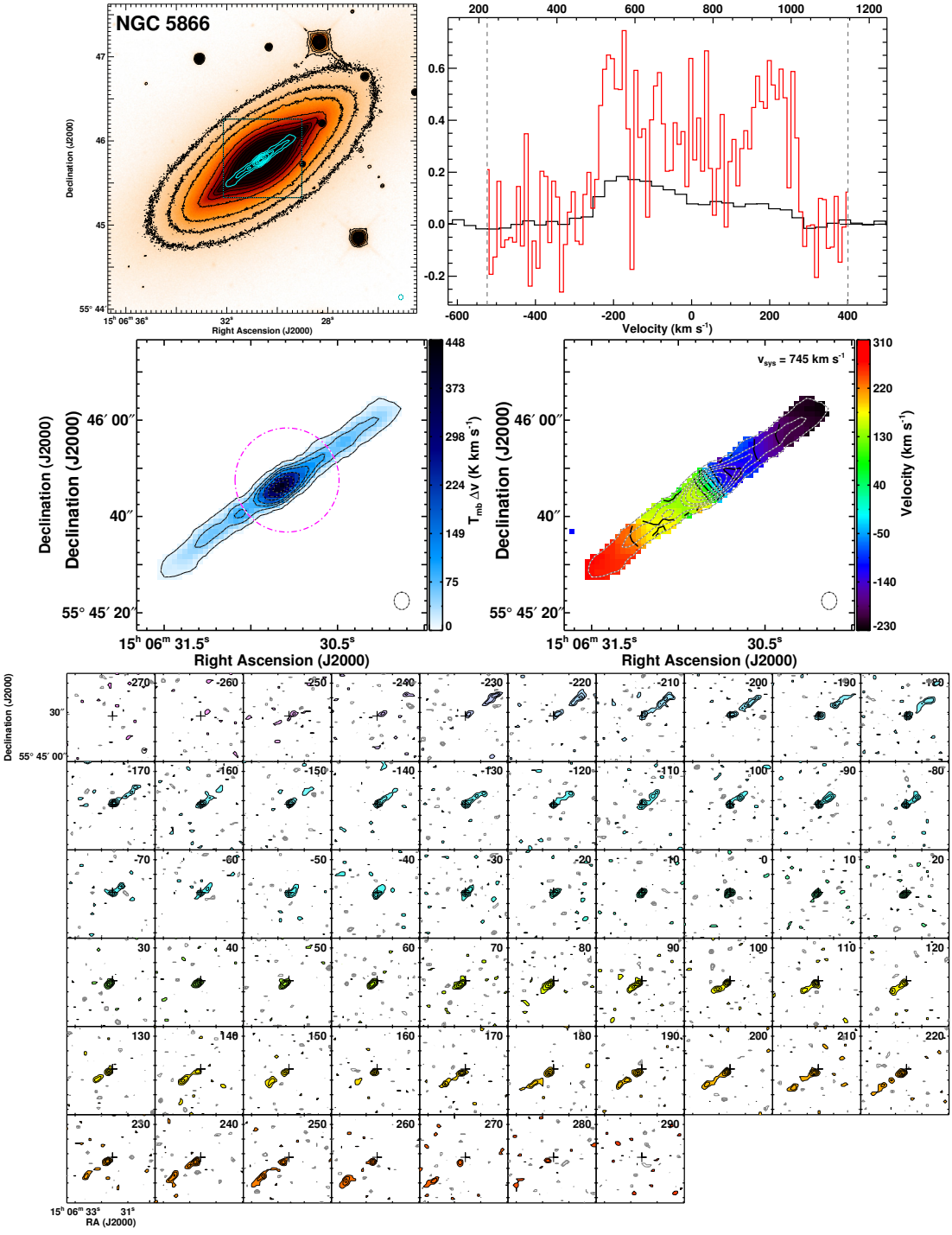

Figure 2.3: continued

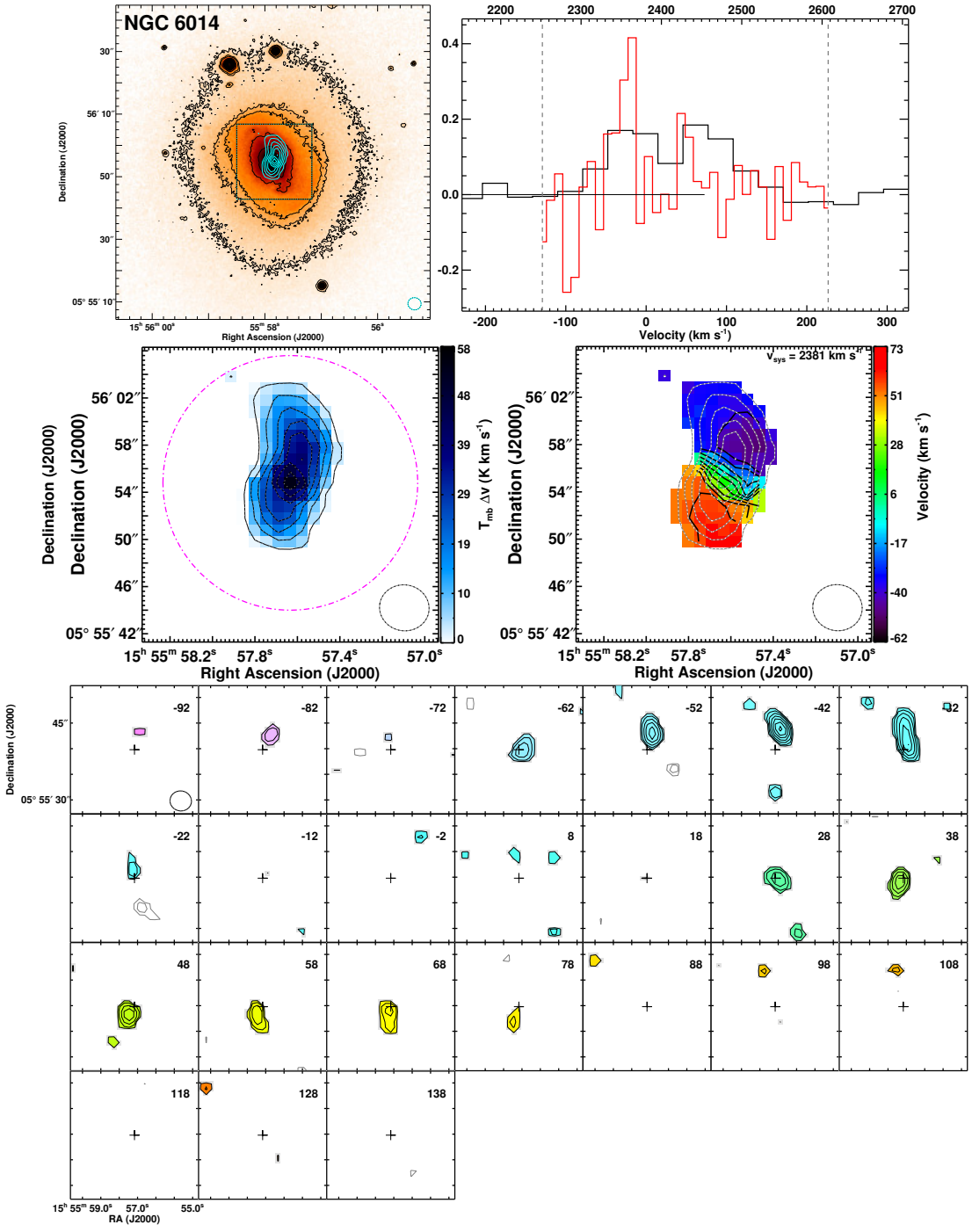

Figure 2.3: continued

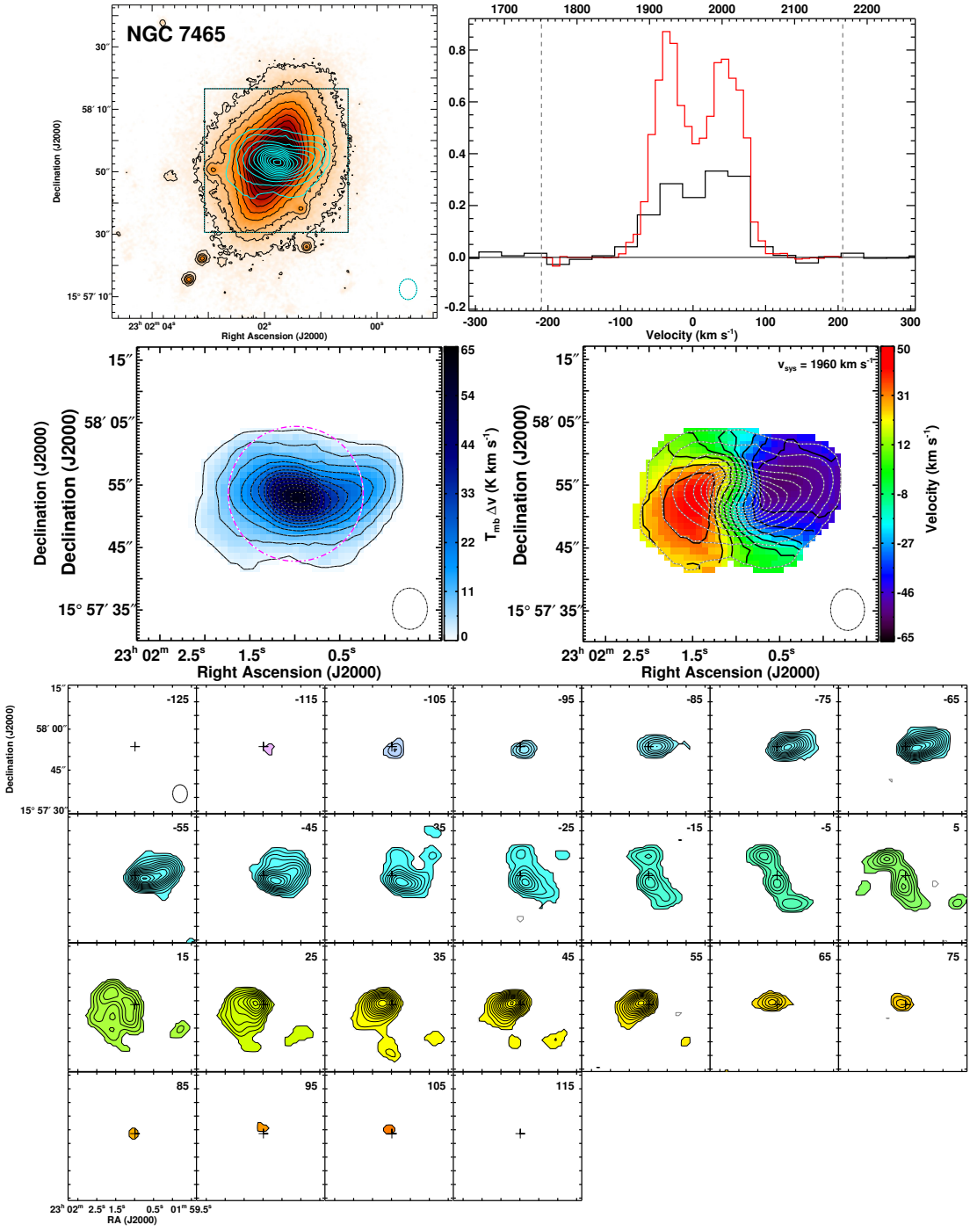

Figure 2.3: continued

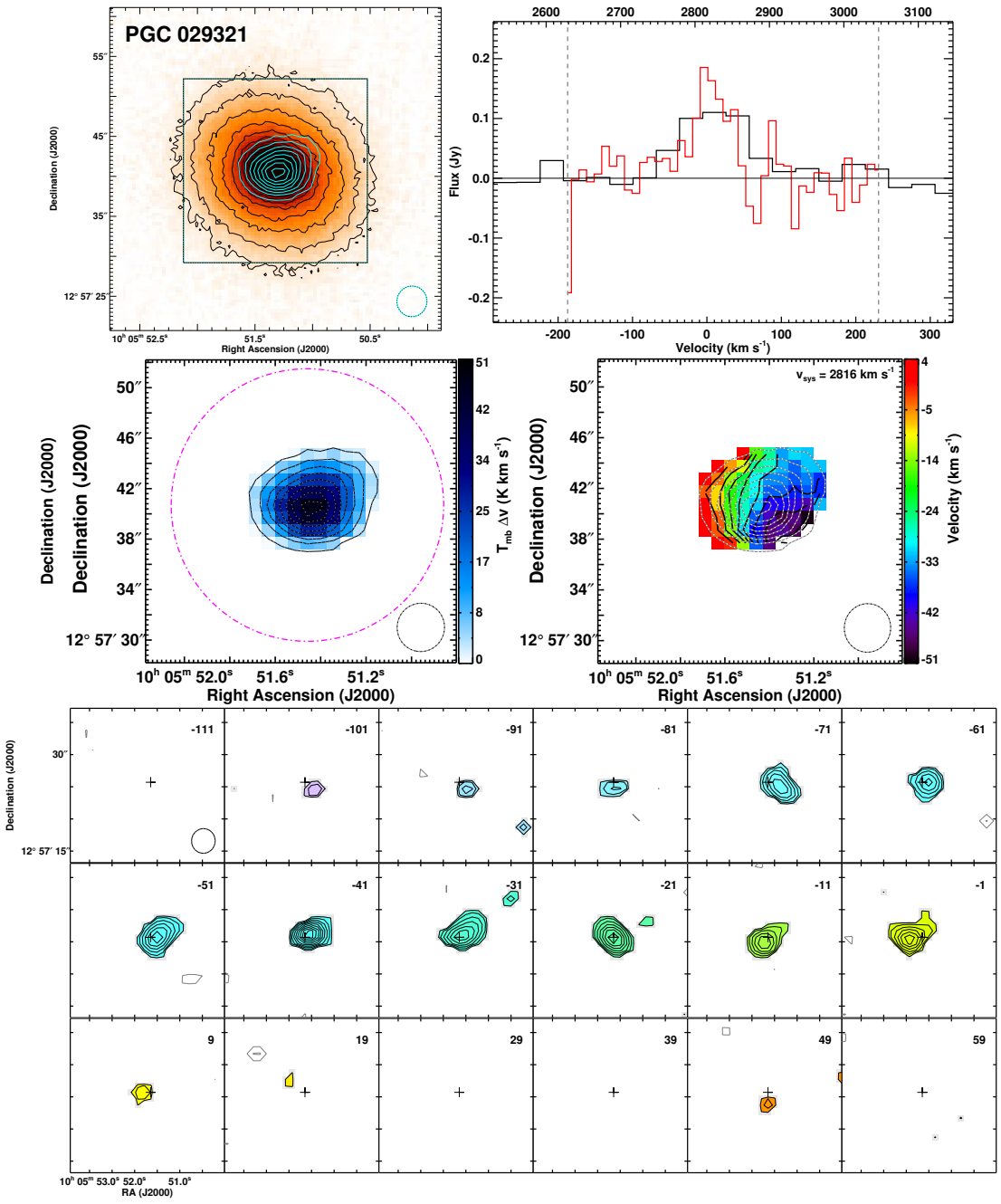

Figure 2.3: continued

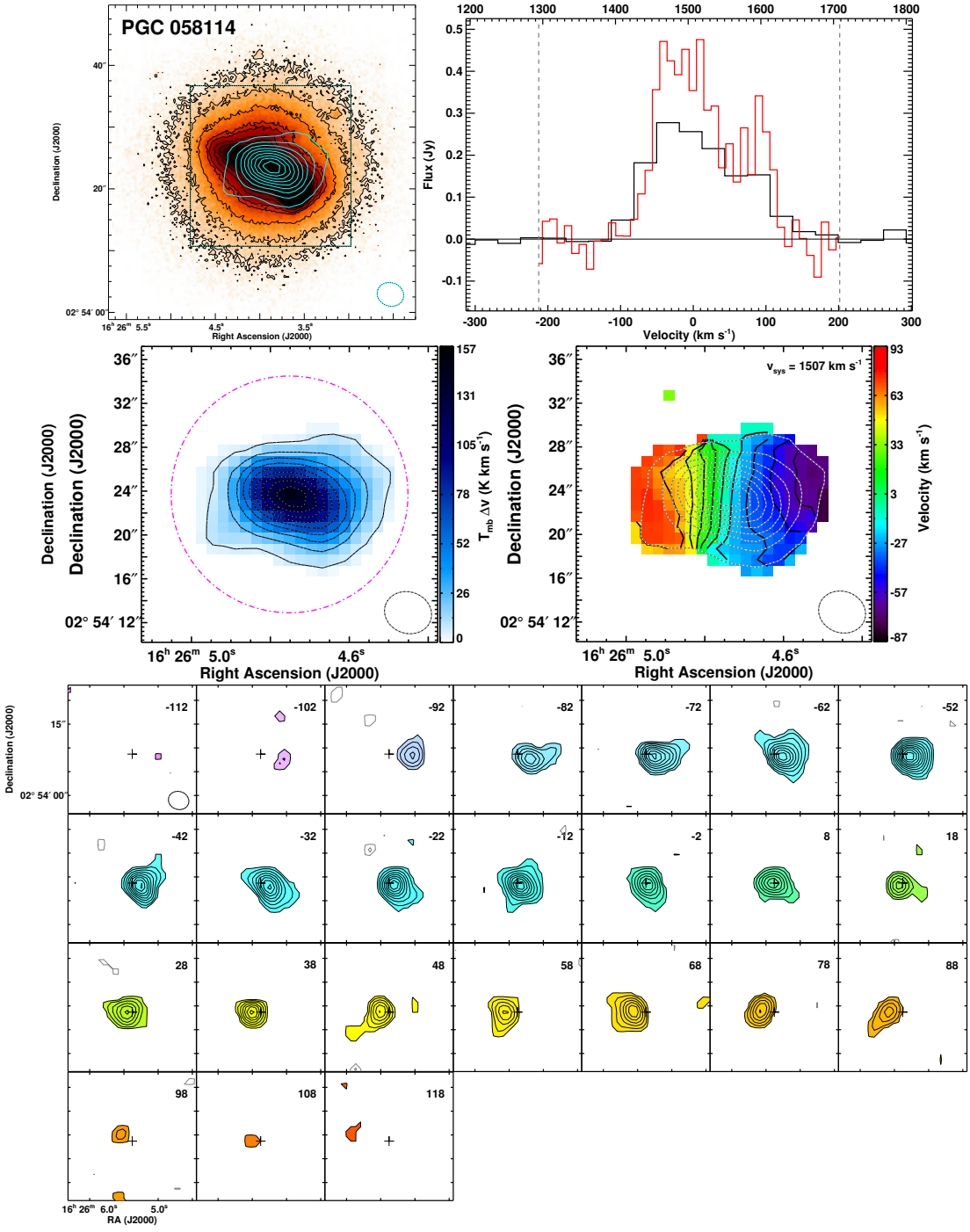

Figure 2.3: continued

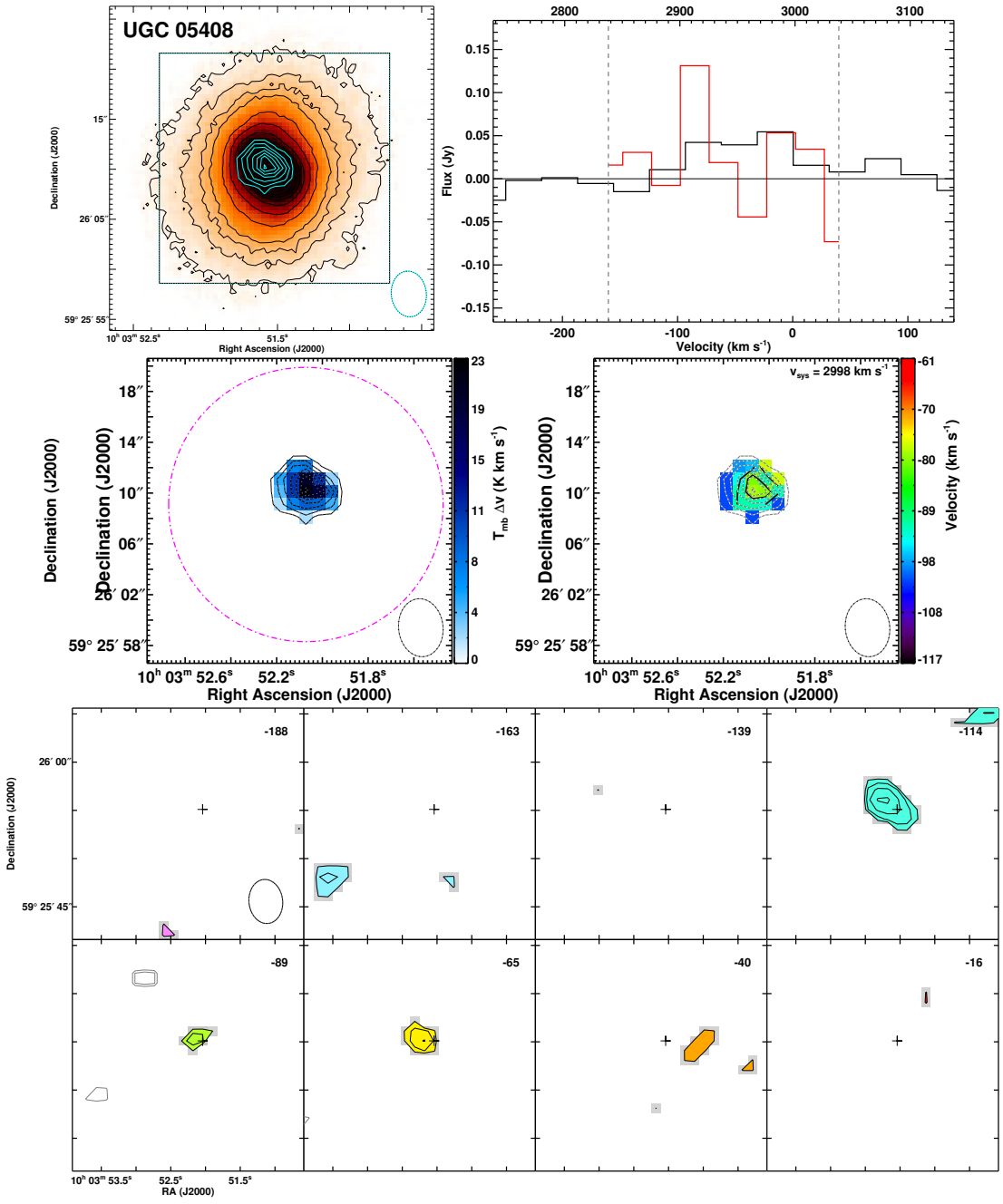

Figure 2.3: continued

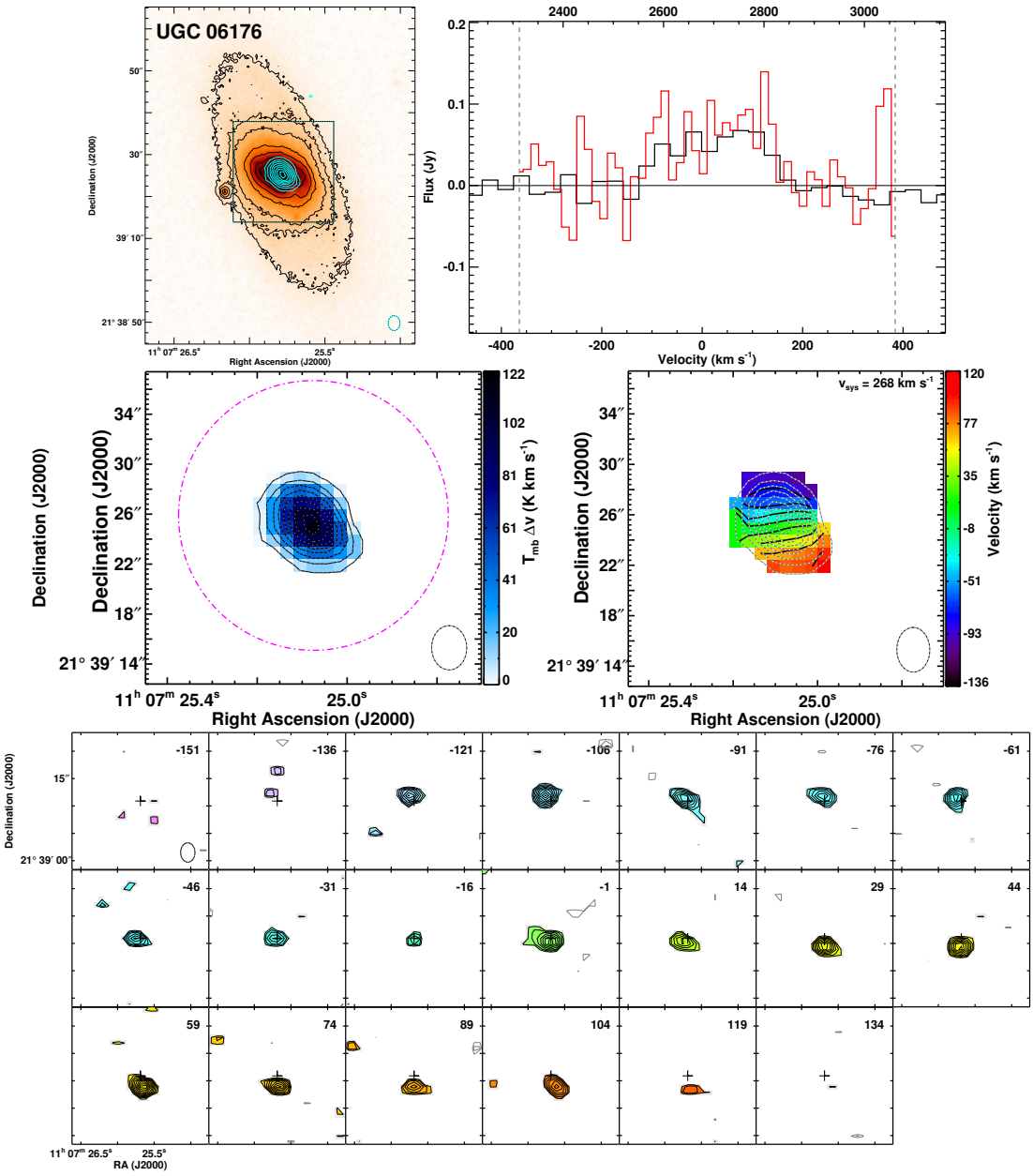

Figure 2.3: continued

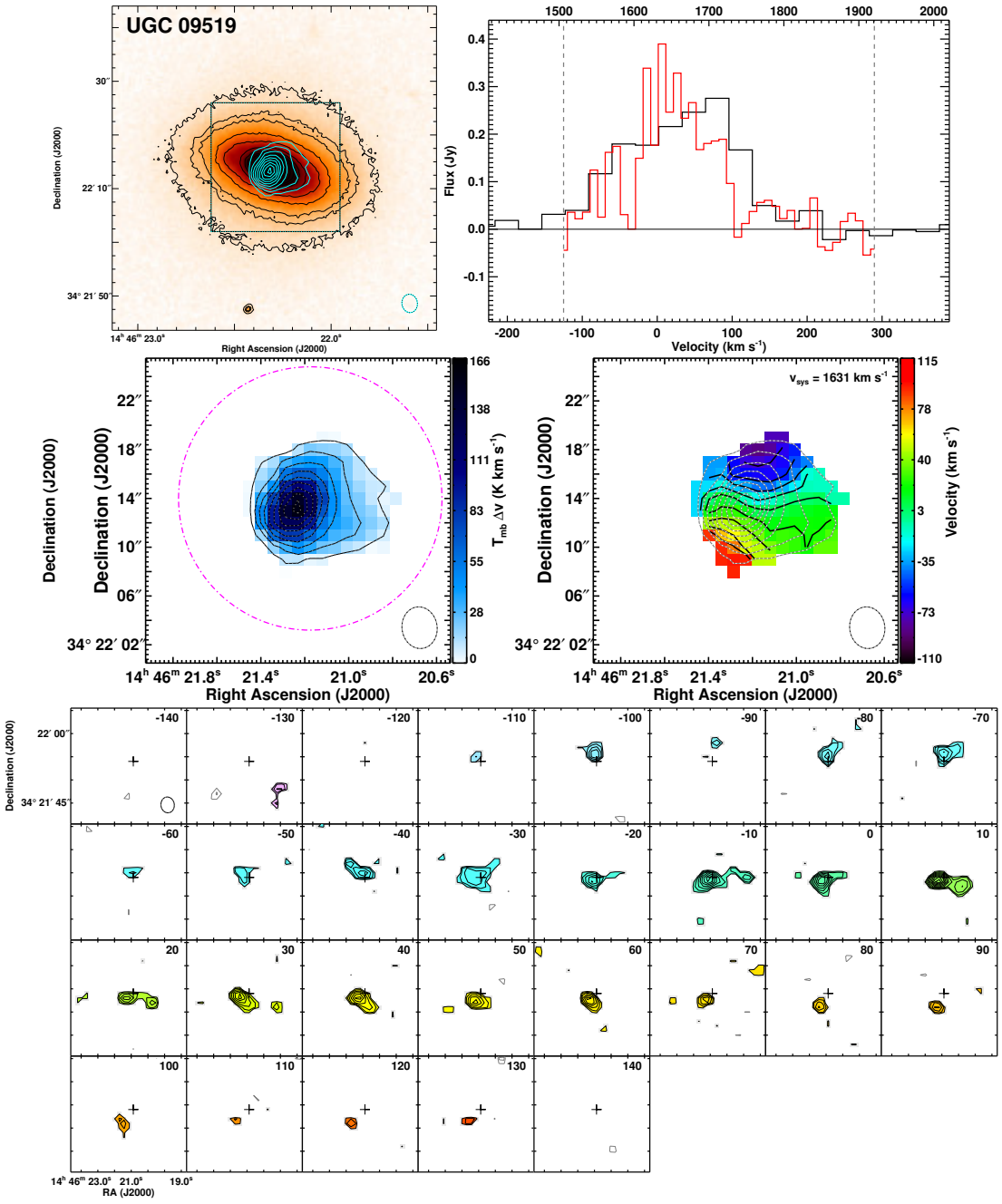

Figure 2.3: continued

3

THE CO TULLY-FISHER RELATION OF EARLY-TYPE GALAXIES

"swept away with the swirling of galaxies, clockwise and counterclockwise, ticking with light..."
- Gene Wolfe, 1983

The material in this chapter has been published as 'The ATLAS^{3D} project – V. The CO Tully-Fisher relation of early-type galaxies', Timothy A. Davis, Martin Bureau, Lisa M. Young, Katherine Alatalo, Leo Blitz, Michele Cappellari, Nicholas Scott, Maxime Bois, Frederic Bournaud, Roger L. Davies, P. Tim de Zeeuw, Eric Emsellem, Sadegh Khochfar, Davor Krajnovic, Harald Kuntschner, Pierre-Yves Lablanche, Richard M. McDermid, Raffaella Morganti, Thorsten Naab, Tom Oosterloo, Marc Sarzi, Paolo Serra and Anne-Marie Weijmans, MNRAS, Volume 414, Issue 2, pp. 968-984

3.1 INTRODUCTION

The Tully-Fisher relation (TFR; Tully & Fisher, 1977) of spiral galaxies has proved itself to be one of the most important correlations in extragalactic astrophysics. For example, its use as a distance measure is vital in extending the cosmic distance ladder, allowing the scale of structures in the nearby universe to be determined and studied. The underlying cause of this relation between luminosity and rotational velocity is usually interpreted as the product of a relatively constant total (luminous plus dark)

mass-to-light ratio (M/L) in the local spiral galaxy population (Gavazzi, 1993; Zwaan et al., 1995), and hence a strong coupling between dark and luminous mass. Studying the slope and zero-point of the TFR is thus also a powerful probe of the M/L evolution of galaxies (e.g. Phillipps, 1989; Sprayberry et al., 1995; Bell & de Jong, 2001).

The TFR as introduced by Tully & Fisher (1977) uses rotation velocities derived from H I line-widths in spiral galaxies, which should approximate the true projected circular velocity of the galaxies as long as the H I distributions are relaxed and reach into the flat parts of the galaxy rotation curves. Over the years, however, the TFR has gradually been recognised as denoting the empirical relationship between the luminosity and rotation velocity of galaxies (generally disc galaxies) as measured with a variety of kinematic tracers, using differing techniques at various wavelengths.

Studying the TFR in lenticular and elliptical galaxies (collectively referred to as early-type galaxies; ETGs) is problematic, as they do not all possess extended relaxed atomic gas distributions. Indeed, it has been shown that even where H I is present in early-type galaxies it can be disturbed, and hence the measured line-widths are in some cases unrelated to galaxy properties (e.g. Morganti et al., 2006; Williams, Bureau & Cappellari, 2010). Although widespread, the ionised gas is generally faint, with significant pressure support; and is thus not ideal either (Bertola et al., 1995). The TFR of early-type galaxies is nevertheless important, as these galaxies are believed to have turbulent formation histories and the TFR may give clues about their assembly and evolution. For example, many authors have suggested that S0 galaxies have avoided violent interactions, and are the faded descendants of high-redshift spirals (e.g. Dressler, 1980; Dressler et al., 1997). In this scenario, S0 galaxies become dimmer whilst keeping the same dynamical mass, leading to an offset TFR.

Due to the problems listed above, stellar tracers of galactic rotation are generally used in ETGs. Due to the importance of pressure support in these systems, however, stellar dynamical modeling or an asymmetric drift correction is required to extract the true circular velocities. This adds additional systematic uncertainties to the already challenging stellar kinematic observations (which must reach sufficiently large radii). Recent analyses of ETGs have suggested that S0 galaxies do indeed have a measurable offset from the spiral TFR, of around 0.5 - 1.0 mag at *K*-band (Neistein et al., 1999;

Bedregal, Aragón-Salamanca & Merrifield, 2006; Williams, Bureau & Cappellari, 2010). Magorrian & Ballantyne (2001), Gerhard et al. (2001) and Rijcke et al. (2007) have all considered extending this approach to construct TFRs that include elliptical galaxies, and find that these are also offset from the spiral TFR, by 0.5 to 1.5 mag at optical wavelengths.

In this Chapter I consider the use of CO as a tracer of the circular velocity of fast-rotating early-type galaxies. CO is thought to be free of many of the problems that beset H I in early-types. As discussed earlier in this thesis, molecular gas is reasonably abundant in early-type galaxies, with ≈22% of early-type galaxies in the local volume (<42 Mpc distant) containing a substantial molecular gas reservoir. The detection rate of molecular gas is also independent of galaxy luminosity and mass (the two most important TFR parameters), providing a direct and unbiased probe of the potential in high-mass galaxies, which are often H I poor (see Section 1.4.7.3). Furthermore, in Chapter 2 we showed that the molecular gas is relaxed in 82.5% of the ETGs in our sample. Therefore CO provides a powerful, directly observable measure of the circular velocity of galaxies of all masses and morphological types, irrespective of environment. Additionally, the small beamsizes of the mm-wave single-dish telescopes used to detect CO eliminate source confusion, at least in nearby galaxies, while current interferometers routinely yield arcsecond angular resolutions.

The possibility of using CO line-widths to investigate the Tully-Fisher relation was first explored by Dickey & Kazes (1992), and this method has since been used by various authors to investigate the CO TFR of spiral and irregular galaxies (e.g. Schoniger & Sofue, 1994; Schoeniger & Sofue, 1997; Tutui & Sofue, 1997; Lavezzi & Dickey, 1998; Tutui et al., 2001) and quasars (Ho, 2007). In spiral galaxies, the CO velocity widths obtained are directly comparable to those found in H I (Lavezzi, 1997).

One possible complication introduced when using CO as a dynamical tracer is that the molecular gas in early-types is usually confined to the inner regions. This means that it is only possible to probe the kinematics where dark matter does not yet play a significant role. This is the opposite of H I TF analyses, which are generally probing H I at large radii, in the dark matter-dominated part of the rotation curve. As such, a TFR measured in the central region could be considered more similar to

the Faber-Jackson (central velocity dispersion - luminosity) relation (Faber & Jackson, 1976). The ETG CO TFR will therefore only be directly comparable to TF results from H I if the 'disc-halo conspiracy' , where dark matter flattens the rotation curve at a similar velocity to that found (from luminous material) in the inner regions, also holds for early-type galaxies (Kent, 1987; Sancisi, 2004; Gavazzi et al., 2007).

Some authors have suggested that there is a change in the slope of the TFR for high-mass disc galaxies, brighter than an absolute *K*-band magnitude of ≈-23.75 (Peletier & Willner, 1993; Verheijen, 2001; Noordermeer & Verheijen, 2007). A break in the TFR at a similar position is also found for elliptical galaxies (Gerhard et al., 2001; Rijcke et al., 2007). It has been suggested that this break occurs because many massive galaxies have declining circular velocity profiles, whereas low mass galaxies have relatively flat circular velocity curves. In other words, the aforementioned disc-halo conspiracy is not perfect in ETGs, and many have a local rotation velocity peak at small radii. The radius where one measures the velocity hence becomes important (see Noordermeer & Verheijen, 2007). Measures of maximal rotation produce a much larger break than measures of the asymptotic rotation velocity, supporting this interpretation. Clearly, the existence of a break in the TFR could lead to systematic biases when deriving distances or probing galaxy evolution. Fortunately, however, I show in this chapter that the CO velocities are consistent with measures of the rotation beyond the peak of the galaxy circular velocity curves.

This chapter (and the associated paper) represents the first attempt to create a CO TFR for early-type galaxies. One can identify two major pitfalls that need to be overcome for this approach to be successful. Firstly, as discussed above, it has been shown that the CO in ETGs is often very centrally concentrated, and hence in some galaxies it may not reach beyond the peak of the rotation curve. Identifying such cases is critical to obtain a useful TFR. Secondly, it has been shown that the molecular gas in early-type galaxies is often misaligned with respect to the stars (e.g. Young 2002; Schinnerer & Scoville 2002; Young, Bureau & Cappellari 2008; Crocker et al. 2009a; Crocker et al. 2008b). In these cases the inclination of the stars is not useful, and an estimate of the inclination of the molecular gas itself is required in order to de-project its observed rotation velocity.

Our goal in this chapter is therefore to explore and demonstrate that, despite the potential pitfalls highlighted above, ETGs do appear to follow a robust luminosity-rotational velocity relation, consistent with that measured using other tracers at the same radii. Although technical aspects will certainly be improved and the interpretation of this relation remains uncertain, an ETG CO TFR is a tantalising and promising tool for galaxy evolution studies, worthy of further consideration. In Section 3.2 of this chapter I discuss the data used in this work, outline methods for estimating the inclination of the galaxy and the gas, and my method for extracting the circular velocity from observed CO line-widths. In Section 3.3, I compare these velocities with other measures such as circular velocities derived from dynamical models, and show that it is possible to use simple criteria to select galaxies where CO is a good tracer of the circular velocity beyond the peak of the galaxy rotation curve. In Section 3.4, I present my ETG CO TFRs, and explore how different data and inclination estimates affect the resulting relations. In Section 3.5, I more fully discuss my results and compare them with previous TFR results derived using other tracers. I summarise my conclusions in Section 3.6.

3.2 DATA

The sample used here contains all of the galaxies with CO spectra avalible from the IRAM-30m telescope (Paper IV). Details of the data acquisition and reduction are presented in Section 1.4.6. Of the 52 detections from Paper IV, 4 are only detected in CO(2-1), and a further 8 had an insufficient signal to noise ratio to perform the analysis required here, leaving 40. In addition to these I include the ETGs IC2099, NGC 4292 and NGC 4309, which were detected in CO as part of the initial ATLAS^{3D} survey, but were later removed from the sample because they are too faint at K_s-band to meet the final sample selection criteria. This should not affect the TFR. This leaves a total of 43 galaxies, the properties of which are listed in Table 3.1. The K-band magnitudes used in this chapter are $K_{s,total}$ from 2MASS, as described in Section 1.4.4.

The CO(1-0) and CO(2-1) single-dish spectra for each detected galaxy, binned to 31 km s^{-1} channels, were analyzed to find the velocities at which the flux drops to 20%

of the peak height. Each spectrum was read into a routine which, working outwards from the galaxy systemic velocity, locates the first channel where the velocity drops to 20% of the peak value. The measurements were inspected by eye to ensure noise peaks and troughs were not affecting the result. This is analogous to the method used by Tully & Fisher (1977) for measuring H I line-widths. The resulting velocity width is henceforth denoted W_{20}. If the molecular gas is a good tracer of the circular velocity in the galaxies, then the line-width should approximate twice the projected rotational velocity, if the molecular gas distribution reaches beyond the peak of the galaxy rotation curve (Dickey & Kazes, 1992).

Figure 3.1 shows a comparison between W_{20} line-widths measured from CO(1-0) and CO(2-1) spectra. One might expect it to be easier to measure line-widths using CO(2-1), as Paper IV have shown that this transition is usually 1–4 times brighter than CO(1-0) (due to beam dilution and/or intrinstic effects), but Figure 3.1 shows that the agreement between the two measurements is generally good. However, almost all the scatter is below the 1:1 line. In these cases, the molecular gas likely extends further than the $\approx$12″ FWHM of the CO(2-1) beam, and the CO(2-1) line-width measurements are systematically biased low. In Section 3.4.1.3, I show that in some cases even the $\approx$23″ CO(1-0) beam is not extended enough to retrieve the full velocity width. The number of galaxies for which this is a concern is small, however, and in the rest of this chapter I will therefore use line-widths measured from the CO(1-0) spectra.

The instrumental dispersion is small compared to the 31 km s^{-1} channels, so I did not correct the line-widths for it. I also chose not to use corrections for turbulence or line-broadening, as these are generally derived by comparison with H I line-widths in spirals (Lavezzi & Dickey, 1998; Tully & Fouque, 1985; Tutui & Sofue, 1999) and hence may not be applicable to early-type galaxies. The velocity dispersion in the gas is expected to be small (e.g. Okuda et al., 2005). In Section 3.3.1, I attempt to quantify any biases introduced by ignoring these corrections. The derived W_{20} velocity widths are estimated to be robust to within half a channel width, $\approx$15 km s^{-1}, and are listed in Table 3.1.

In addition to the single-dish CO data, I also make use of the interferometric data for those galaxies which have been observed. Chapter 2 discusses this data in depth.

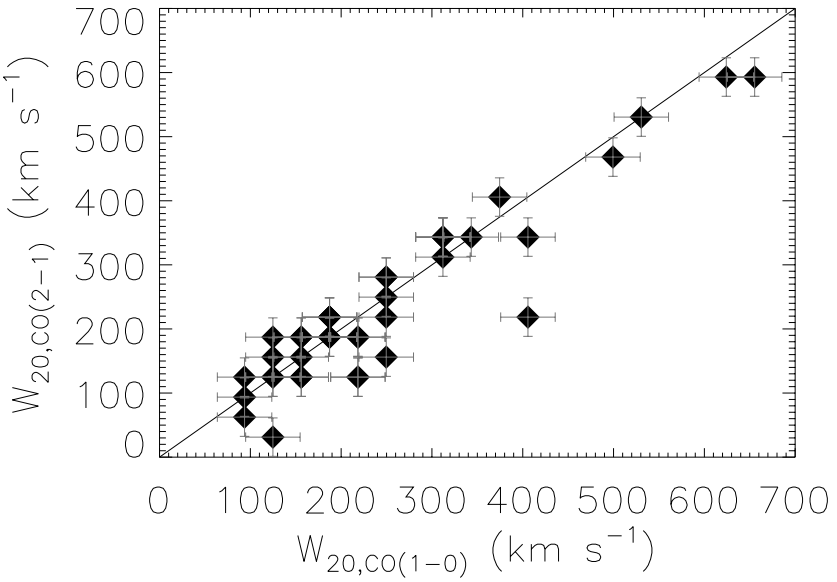

Figure 3.1: A comparison between CO(1-0) and CO(2-1) single-dish line-widths, measured as described in Section 3.2. The solid line shows the one-to-one relation. Linewidths are discretized due to the 30 km s^{-1} channel width.

The CO data cubes were summed spatially to measure total fluxes and revised values for W_{20}, serving as consistency checks on the values derived from the single-dish data. The large primary beam of the arrays also allow us to make better measurements for the small subset of galaxies in which a substantial part of the CO distribution was missed by the 23″ beam of the IRAM 30m telescope, such as in IC676, NGC 4324, NGC 4477, NGC 4710, NGC 7465 and PGC 058114. This can be due to pointing errors or molecular gas distributions that extend beyond the beam. The integration time for the single-dish CO observations was adjusted to obtain a fixed noise level- and as such galaxies which are only detected at $\approx 5\sigma$ will have rather uncertain W_{20} line-widths. The interferometric observations in these cases (NGC 2685, NGC 2768, NGC 3489, NGC 4477) will provide a better constraint on the line-widths. The revised W_{20} values are listed in Table 3.1, but for consistency these velocities are only used in the TFRs presented in Sections 3.4.1.3 and 3.4.1.4.

3.2.1 *Inclination correction*

The measured quantity W_{20} is a projection of the gas velocity into the line-of-sight. If this is to be used for a TF analysis it must be deprojected. Many methods for inclination measurement are available. Starting with the simplest, I compare various method below in order of increasing complexity, to allow future CO TF surveys to select the optimum method for their needs. The methods presented in Sections 3.2.1.1 and 3.2.1.2 use only single-dish molecular data, whilst the method presented in Section 3.2.1.3 requires interferometric maps.

3.2.1.1 *Galaxy axial ratio*

A rough measurement of inclination can be obtained by estimating the axial ratio of the stellar distribution of the host galaxy from imaging data:

$$i_{\mathrm{b/a}} = \cos^{-1}\left(\sqrt{\frac{q^2 - q_0^2}{1 - q_0^2}}\right), \tag{3.1}$$

where q is the ratio of the semi-minor (b) to the semi-major (a) axis of the galaxy, and q_0 is the intrinsic axial ratio when the galaxy is seen edge-on ($q_0 \equiv c/a$). q_0 is often assumed to be 0.2 in disc galaxies (Tully & Fisher, 1977), but early-types can have large bulge-to-disc ratios leading to a large uncertainty in any assumed value of q_0.

Various lines of enquiry suggest a mean q_0 value of $\approx$0.34 for the fast-rotators in the ATLAS^{3D} sample (Weijmans et al., in preparation), which I adopt here. Intrinsic scatter around this value will introduce an artificial increase in the TFR scatter, but the effect is very small. Indeed, I stress that this q_0-related inclination correction is only significant in highly inclined galaxies, where fortunately inclination errors have the smallest effect on the de-projected velocities and thus the derived TFR. For example, assuming $q_0 = 0$ for the current sample would only change the zero-point of the derived TFR by 0.02 dex along the velocity axis, and it does not change the gradient.

It is important to note that using this method to correct the CO velocity widths for a TF analysis implicitly assumes that the CO is distributed in the same plane as the

galaxy major-axis. A sizeable proportion of early-type galaxies have molecular gas misaligned with respect to the stellar kinematic axis (see Chapter 5), so in these cases one expects this method to introduce additional artificial scatter in the TFR.

The value of $i_{b/a}$ obtained by assuming q_0=0.34 for each galaxy is listed in Table 3.1. These values were calculated using Equation 3.1 with the mean galaxy axial ratio reported in the NASA/IPAC Extragalactic Database (NED). These values are the mean of the measurements from the Sloan Digital Sky Survey (SDSS) in the *r* band, 2MASS at K_s band (Skrutskie et al., 2006), and blue and red filters from both the Third Reference Catalogue of Bright Galaxies (RC3; de Vaucouleurs et al., 1991), and the Uppsala General Catalogue of galaxies (UGC/POSS; Nilson, 1973) where available. The exceptions to this are NGC 3665, where the axial ratio is based only on the superior SDSS imaging, and PGC 058114, where the mean value of the axial ratio from the HyperLeda database (Paturel et al., 2003) has been used, due to a larger number of available measurements. When these inclinations are compared to those estimated from the axial ratios of Paper II; derived by calculating the moments of inertia of the surface brightness distribution from the SDSS and INT r-band images) for the galaxies in the ATLAS^{3D} sample they are found to agree well.

3.2.1.2 *Dust axial ratio*

It should be possible to obtain more accurate inclination estimates from fitting ellipses to dust highlighted in unsharp-masked optical images of the galaxies. This method has several advantages over galaxy axial ratios. Dust distributions typically have very small vertical scale-heights, hence Equation 3.1 with q_0=0 should yield a good estimate of their inclinations. As I discussed in Section 2.3.1 the CO and dust in early-type galaxies are usually spatially coincident, and hence the inclination of the dust (i_{dust}) should trace the true inclination of the molecular gas. This is especially useful where the molecular gas and stars are misaligned.

Unsharp-masked dust maps were created for all the galaxies in this work, preferentially from archival Hubble Space Telescope (HST) images, or where these were

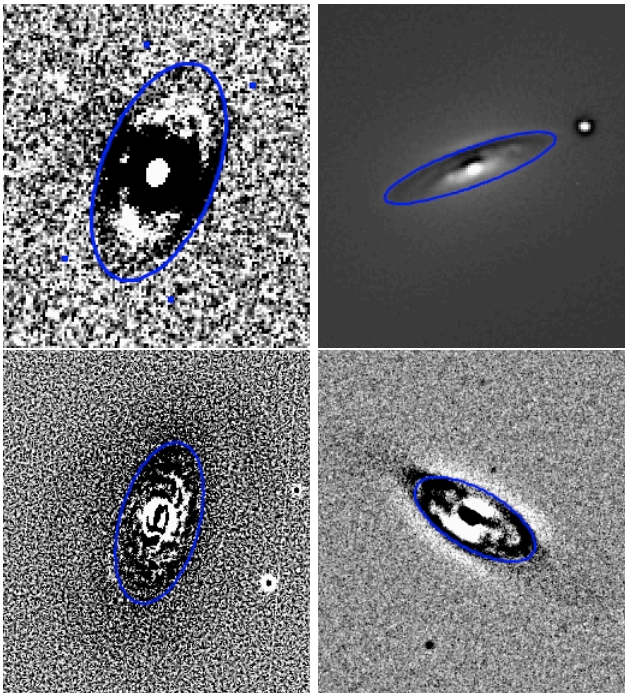

Figure 3.2: Four examples of unsharp-masked images picking up dusty spiral structures and rings. NGC 2824 (top left), NGC 4526 (top right), NGC 3626 (bottom left), NGC 5379 (bottom right). Overlaid in blue are the best fit ellipse from which I estimate the dust inclination.

not available from SDSS g-band (Adelman-McCarthy et al., 2008) or ATLAS^{3D} Isaac Newton Telescope Wide Field Camera (INT-WFC) r-band images (Scott et al., in preparation). Ellipses were then fitted by eye to the resulting maps and the inclination of the dust calculated from Equation 3.1 with q_0=0. Four example galaxies are shown in Figure 3.2.

One of the galaxies (NGC 4753) is well studied in the literature, showing many thin filamentary dust features that are well fitted by a model featuring an inclined disc, twisted by differential precession, with an average $i_{\rm dust}$=75 $\pm 3^{\circ}$ (Steiman-Cameron, Kormendy & Durisen, 1992). I adopt this value here. A full list of $i_{\rm dust}$ values can be found in Table 3.1.

3.2.1.3 *Molecular gas modeling*

Tilted-ring analyses have been used to determine the geometric and kinematic parameters of neutral and molecular gas discs in interferometric data for many years (e.g. Rogstad, Lockhart & Wright, 1974; Christodoulou, Tohline & Steiman-Cameron, 1988; Koribalski et al., 1993). In this work, I have made use of the Groningen Image Processing System (GIPSY) add-on package TiRiFiC, described in Józsa et al. (2007), to fit tilted-ring models to observed data cubes. Due to the small number of independent synthesized beams across a typical sources, an unwarped disc model was fitted where the inclination, position angle, systemic velocity and kinematic centre of the gas were varied globally, and only the velocity and surface brightness were allowed to vary radially (i.e. for each ring). The inclination measures ($i_{\rm mol}$) extracted from these models, and used in this work are listed in Table 3.1. The error quoted for each galaxy is the maximum inclination difference found if each side of the velocity distribution is supplied as an input to the fitting program separately.

We have attempted the analysis described above for all the mapped galaxies in the sample where with have adequate spatial resolution, with one exception where I felt the literature value was sufficient. NGC 2685 has dust lanes which look polar on the north-east side, and are coincident with H I, Hα and CO emission (Schinnerer & Scoville, 2002). This system has been revealed to feature a coherent, extremely warped disk (Józsa et al., 2009), for which I adopt the published average inclination value of $i_{\rm mol}$=69 $\pm$ 9°.

3.2.2 W_{20} *linewidths*

The velocity widths calculated as described in Section 3.2 are an approximation to (twice) the maximum rotation velocity of the CO. To be useful, these CO measurements must reach beyond the peak of the galaxy rotation curves. As molecular gas in early-types is often centrally concentrated this requirement is not trivially fulfilled.

One sign of a tracer having reached a flat part of a galaxy rotation curve is a

classic 'double-horned' velocity profile. Lavezzi & Dickey (1997) discuss in detail the problem of recovering velocity widths from CO observations, given the variety of profile shapes typically seen in millimeter observations. They show that CO profile shapes are affected by the extent of the emitting gas, the beam size of the telescope, pointing errors and the optical depth of the molecular material. CO line-widths are shown to accurately retrieve V_{max} in the majority of cases where the flaring parameter $R_{2,5}$ (the ratio of the velocity widths measured at 20 and 50% of the peak) is less than 1.2 (Lavezzi & Dickey, 1997, 1998). This criterion effectively selects galaxies that show a boxcar, or double-horned, profile shape with sharp edges and rejects those with a more Gaussian profile. I follow this methodology in this work, exclusively using galaxies with double-horned/boxcar/sharp edged profiles, which I call 'boxy' from here on in, assuming that in these systems the measured gas velocity width will approximate the velocity beyond the peak of the circular velocity curve.

The limited signal-to-noise ratio of the spectra, however, means that the value of the flaring parameter discussed above is often rather uncertain. We performed several other tests, attempting to find a good automatic way of classifying boxy velocity profiles. These included fitting single gaussians and selecting those galaxies that shown significant structure in the residuals, and fitting Gauss-Hermite polynomials and looking for a significant kurtosis ($h_4 < 0$). Both of these methods worked well for wide lines and high signal to noise cases, but in the case of narrow lines, or low signal to noise the fits were not well constrained. In these cases the different methods often produced contradictory results, and/or did not agree with a careful classification by eye. In future surveys with better data quality, or large numbers of objects (so one can afford to remove low signal to noise detections) these methods will likely be highly useful, but in this current work, with a limited number of objects I prefer a careful classification by eye.

Even by eye, some cases are hard to classify, especially when the profiles are narrow as the galaxies are fairly face on, or if the signal-to-noise ratio is low. I cautiously use only those galaxies with clear boxy profiles here, flagging the 12 galaxies with uncertain profiles shapes.

Using this profile shape criterion is likely to introduce some uncertainties, for

example galaxies with a molecular ring will have double-horned profiles without the CO necessarily having reached beyond the peak of the rotation curve. Similarly, galaxies that have strong resonances may have their gas distribution truncated at the turnover radius, causing them to not display a classic boxy shape even though the edge of the distribution is rotating at the turnover velocity. In Section 3.3.1, I use the dynamical models available from the ATLAS^{3D} survey to quantify these biases.

3.2.2.1 Combining interferometric and single-dish data

Finally, it is possible to combine the single-dish and interferometric observations, using all available data to increase the number of galaxies with high-quality measurements available. When available, I thus always use interferometric velocity widths and, when well constrained, interferometric inclinations (quantitatively, I select tilted-ring inclinations with errors less than 6°). For the remaining galaxies I preferentially use dust inclinations, or failing this, b/a inclinations. I can also use the interferometric data when available to help ascertain which galaxies have reached beyond the peak of the rotation curve, in conjunction with the usual single-dish boxy criterion. This hybrid measure represents the best estimate of the inclination and velocity width. The adopted best inclinations are listed in Table 3.1.

Table 3.1: Parameters of the ATLAS^{3D} early-type CO-rich galaxies used in this chapter.

Galaxy	T-type	$W_{20,SD}$ (km s^{-1})	$W_{20,inter}$ (km s^{-1})	$i_{b/a}$ (deg)	i_{dust} (deg)	$i_{tilted-ring}$ (deg)	i_{best} (deg)	M_{Ks} (mag)	Dhorn (SD)	Dhorn (best)	Tel.	Ref.
(1)	(2)	(3)	(4)	(5)	(6)	(7)	(8)	(9)	(10)	(11)	(12)	(13)
IC 0676	-1.3	93	170	58 ± 3	-	69 ± 6	69 ± 6	-22.20	-	-	C	1
IC 0719	-2.0	343	353	82 ± 1	79 ± 1	74 ± 5	74 ± 5	-22.70	x	x	C	1
IC 1024	-2.0	221	240	79 ± 1	72 ± 1	-	72 ± 1	-21.70	x	x	C	-
*IC 2099	-1.5	93	-	83 ± 1	-	-	83 ± 1	-21.40	?	?	-	-
NGC 0524	-1.2	312	320	28 ± 8	19 ± 7	44 ± 28	19 ± 7	-24.70	x	x	P	2
NGC 1222	-3.0	156	210	41 ± 5	41 ± 3	-	41 ± 3	-22.70	?	-	C	1

Notes: Column 1 lists the galaxy name. Galaxies with stars next to their name are early-types that were observed by Paper IV but are not included in the ATLAS^{3D} sample. Column 2 contains the morphological T-type from HyperLeda (Paturel et al., 2003). This morphology indicator was not used for the sample selection (see Paper I). Columns 3 and 4 list the velocity widths at 20% of the peak flux, derived from single-dish and interferometric data, respectively. The error in these quantities was estimated as half the velocity width of an individual channel, 15 km s^{-1}. Column 5 contains the inclination derived from galaxy axial ratios. The quoted errors only take into account the error in the measurement of the optical axial ratio, as reported in NED. Column 6 contains the inclination derived from ellipse fitting to unsharp-masked dust images. The error is estimated to be 5% on the measurement of both the minor and major axes. Column 7 contains the inclinations estimated from tilted-ring fits to the interferometric datacubes, the errors on which are calculated as the maximum difference from the best value obtained when using only one half of the galaxy velocity field. Column 8 lists the adopted best inclinations, as described in Section 3.2.2.1. Column 9 contains the K_s-band magnitudes from 2MASS (Skrutskie et al., 2006), converted to absolute magnitudes using the distance to each galaxy adopted for the ATLAS^{3D} survey in Paper I. I assign to the absolute magnitudes an error of ± 0.1 mag, taking into account distance uncertainties, which completely overwhelm errors caused by the lack of an internal extinction correction. Columns 10 and 11 list the galaxies with boxy CO profiles, as determined from visual inspection of the single-dish spectra (Column 9), and a combination of single-dish and interferometric data where available (Column 11). A question mark indicates that with the respective data I am unable to determine if the profile is boxy, and hence do not include it. The telescope used to obtain the interferometric data is indicated in Column 12, where C = CARMA, P = PdBI, B = BIMA and O = OVRO. Column 13 lists the relevant references for the interferometric observations, and in two cases (NGC 2685 and NGC 4753) references for the inclination measurements. (1) this thesis (2) Crocker et al. (2011), (3) Young, Bureau & Cappellari (2008), (4) Józsa et al. (2009) and (5) Steiman-Cameron, Kormendy & Durisen (1992).

Table 3.1: continued

Galaxy	T-type	$W_{20,SD}$ (km s^{-1})	$W_{20,inter}$ (km s^{-1})	$i_{b/a}$ (deg)	i_{dust} (deg)	$i_{tilted-ring}$ (deg)	i_{best} (deg)	M_{Ks} (mag)	Dhorn (SD)	Dhorn (best)	Tel.	Ref.
(1)	(2)	(3)	(4)	(5)	(6)	(7)	(8)	(9)	(10)	(11)	(12)	(13)
NGC 1266	-2.1	187	180	47 ± 4	26 ± 5	-	26 ± 5	-22.90	-	-	C	1
NGC 2685	-1.0	156	220	70 ± 1	61 ± 1	70 ± 10	61 ± 1	-22.80	-	-	O	4
NGC 2764	-2.0	312	310	65 ± 2	65 ± 1	76 ± 15	65 ± 1	-23.20	x	x	C	1
NGC 2768	-4.4	322	360	36 ± 6	-	-	36 ± 6	-24.70	x	x	P	2
NGC 2824	-2.0	312	310	56 ± 3	61 ± 1	-	61 ± 1	-22.90	x	x	C	1
NGC 3032	-1.9	143	150	36 ± 6	35 ± 3	46 ± 11	35 ± 3	-22.00	x	x	B	3
NGC 3182	0.4	218	-	39 ± 5	35 ± 3	-	35 ± 3	-23.20	x	x	-	-
NGC 3489	-1.2	292	240	62 ± 2	-	56 ± 15	62 ± 2	-23.00	?	x	P	2
NGC 3619	-0.9	405	-	44 ± 4	48 ± 2	-	48 ± 2	-23.50	x	x	-	-
NGC 3626	-1.0	374	374	51 ± 3	61 ± 2	67 ± 5	67 ± 5	-23.30	x	x	C	1
NGC 3665	-2.1	624	630	90 ± 1	64 ± 1	74 ± 35	64 ± 1	-24.90	x	x	C	1
NGC 4119	-1.3	156	170	83 ± 1	67 ± 1	69 ± 3	69 ± 3	-22.60	?	-	C	1
NGC 4150	-2.1	234	238	50 ± 3	54 ± 2	54 ± 3	54 ± 3	-21.60	x	x	B	3
*NGC 4292	-1.7	187	190	49 ± 3	50 ± 2	46 ± 14	50 ± 2	-21.54	?	x	C	1
*NGC 4309	-1.5	124	-	69 ± 2	61 ± 1	-	61 ± 1	-20.91	-	-	-	-
NGC 4324	-0.9	218	360	73 ± 1	64 ± 1	62 ± 1	62 ± 1	-22.60	?	x	C	1
NGC 4429	-1.1	499	532	68 ± 2	68 ± 1	60 ± 16	68 ± 1	-24.30	x	x	C	1
NGC 4435	-2.1	405	380	48 ± 4	52 ± 2	-	52 ± 2	-23.80	x	x	C	1
NGC 4459	-1.4	391	400	43 ± 4	46 ± 2	47 ± 2	47 ± 2	-23.90	x	x	B	3
NGC 4477	-1.9	204	260	36 ± 6	26 ± 5	38 ± 3	38 ± 3	-23.70	?	x	P	2
NGC 4526	-1.9	655	663	82 ± 1	78 ± 1	64 ± 8	82 ± 1	-24.60	x	x	B	3
NGC 4684	-1.2	249	-	77 ± 1	-	-	77 ± 1	-22.20	?	?	-	-
NGC 4694	-2.0	93	65	69 ± 2	-	-	69 ± 2	-22.10	-	-	C	1
NGC 4710	-0.9	312	430	78 ± 1	88 ± 1	86 ± 6	86 ± 6	-23.50	x	x	C	1
NGC 4753	-1.4	530	-	61 ± 2	75 ± 1	-	75 ± 1	-25.10	x	x	-	5

Continued from previous page

Table 3.1: continued

Galaxy	T-type	$W_{20,SD}$ (km s^{-1})	$W_{20,inter}$ (km s^{-1})	$i_{b/a}$ (deg)	i_{dust} (deg)	$i_{tilted-ring}$ (deg)	i_{best} (deg)	M_{Ks} (mag)	Dhorn (SD)	Dhorn (best)	Tel.	Ref.
(1)	(2)	(3)	(4)	(5)	(6)	(7)	(8)	(9)	(10)	(11)	(12)	(13)
NGC 5173	-4.9	187	-	24 ± 9	-	-	24 ± 9	-22.90	x	x	-	-
NGC 5273	-1.9	218	-	38 ± 5	38 ± 3	-	38 ± 3	-22.40	x	x	-	-
NGC 5379	-2.0	124	120	80 ± 1	64 ± 1	-	64 ± 1	-22.10	-	-	C	1
NGC 6014	-1.9	156	160	29 ± 7	22 ± 6	22 ± 10	22 ± 6	-23.00	x	x	C	1
NGC 7465	-1.9	158	180	56 ± 3	70 ± 1	58 ± 9	70 ± 1	-22.80	x	-	C	1
PGC 29321	0.0	124	-	31 ± 7	38 ± 3	-	38 ± 3	-21.60	-	-	-	-
PGC 56772	-2.0	249	-	64 ± 2	57 ± 2	-	57 ± 2	-22.00	?	?	-	-
PGC 58114	-2.0	202	240	71 ± 1	-	76 ± 30	71 ± 1	-21.60	-	x	C	1
PGC 61468	0.0	218	-	51 ± 3	-	-	51 ± 3	-21.60	?	?	-	-
UGC 05408	-3.3	156	-	31 ± 7	-	-	31 ± 7	-21.90	x	x	-	-
UGC 06176	-2.0	249	230	70 ± 2	68 ± 1	-	68 ± 1	-22.60	?	-	C	1
UGC 09519	-1.9	187	210	47 ± 4	41 ± 3	63 ± 7	41 ± 3	-22.10	?	x	C	1

Continued from previous page

3.3 COMPARISON WITH OTHER VELOCITY MEASURES

3.3.1 Model circular velocity curves

One would like to test if single-dish CO linewidths provide a good estimate of the circular velocity, and attempt to quantify the biases introduced by using the profile shape as a proxy for reaching beyond the peak of the circular velocity curve. As Williams, Bureau & Cappellari (2010) discuss, one must be careful when comparing velocity measures derived from different methods, as they are likely to have significant systematic differences. However, it is important to ascertain that the CO line-widths vary systematically, in a similar way to other rotation measures.

The gravitational potential of ETGs can also be significantly different from that of spirals. ETGs often have circular velocity profiles with high peaks at small radii that decline before flattening out. The W_{20} line-width is, in general, more sensitive to the peak velocity of the molecular gas, rather than the flat part of the rotation curve, unless the gas disk is sufficiently extended. This would lead to an overestimation of the velocity width. This problem has been discussed in detail by Noordermeer & Verheijen (2007), who find that using the H I peak velocity in massive early-type spirals results in an offset TFR. They report that the asymptotic velocity is a better measure of the total potential, and results in spirals of all masses lying on a single TFR.

An estimate of the amount by which I may be overestimating the velocity widths can be obtained using the circular velocity curves produced by Williams, Bureau & Cappellari (2009) from stellar dynamical modeling of their S0 galaxies. The median value of the circular velocity curve after the peak out to the maximum extent of the data, where the model is well constrained, is adopted as a measure of the velocity of its flat part (in the case of Williams, Bureau & Cappellari (2009) their data extends to $\approx$3 Re). When tested on the S0 circular velocity curves from Williams, Bureau & Cappellari (2009), this median performs well in picking out the velocity of the flat section. The mean ratio of the peak velocity to the flat velocity is 1.15, or 0.06 dex. When transformed to an offset in luminosity (using the parameters of the best-fit S0

TFR of Williams, Bureau & Cappellari 2010), this effect corresponds to an offset of up to 0.5 mag at K_s-band. This is approximately half of the $\approx$1 mag offset observed by various authors between the spiral and ETGs, and is thus significant if not properly accounted for.

In order to test the assumption that the ETGs with boxy profiles have gas distributions that reach beyond the peak of the circular velocity curve, and to see if the line-widths are overly sensitive to the peak velocity, like Williams, Bureau & Cappellari (2009); Williams, Bureau & Cappellari (2010), I utilise the JAM models described in Section 1.4.5. From each mass model the predicted circular velocity curve in the plane of the galaxy was caculated. It is worth bearing in mind that, where the CO is misaligned from the plane of the galaxy, I am thus making implicit assumptions about the symmetry of the matter distribution. As these models include no dark matter, the circular velocity often declines at large radii, and one must be careful to measure the circular velocity at a suitable radius (i.e. where I have constraining data) when comparing to the observations.

Analysis of the ATLAS^{3D} interferometric observations (presented in Chapter 4), suggests that the circular velocity measured at one effective radius (denoted $V_{JAM,Re}$) is a sensible quantity to use for comparison. The effective radii I used here are tabulated in Paper I. For galaxies where interferometric observations are available, I have also calculated the model circular velocity at the maximum extent of the CO, and denote this $V_{JAM,R_{CO}}$. Both values can be found in Table 3.2.

We compare the two model circular velocity measures described above with the measured CO line-widths in Figure 3.3. The line-widths of the galaxies with boxy CO profiles correlate well with the circular velocities measured at both one effective radius (R_e) and the radius of maximum CO extent (R_{CO}). The offset from $V_{JAM,Re}$ is 0.01 ± 0.02 dex, the data points displaying an RMS scatter of 0.1 dex. The galaxies that do not have boxy CO profiles have line-widths systematically smaller than those predicted from the models in most cases, suggesting that their CO has been correctly identified as not reaching beyond the peak of the rotation curve. The comparison with $V_{JAM,Rco}$, albeit with smaller number statistics, shows that the difference between the model and the CO line-widths is again consistent with the models, with a mean offset

of 0.002 $\pm$ 0.02 dex and a RMS scatter of 0.1 dex. There is no systematic behaviour in the residuals for the boxy galaxies in either plot. The galaxies that do not have boxy CO profiles are closer to the JAM model predictions, but do not lie on the one to one relation as expected, with a mean offset of -0.07$\pm$0.05 dex. This offset is likely because the CO is these objects is very compact, and beam effects mean the CO size is overestimated. The JAM model velocities have thus been estimated at the wrong radius (some other possible causes for discrepancies from the JAM are discussed in Chapter 4. The one galaxy which does not have a boxy profile, but has a line-width larger than the predicted circular velocity, is NGC 1266, recently discovered to have a kiloparsec-scale molecular outflow (Alatalo et al., 2011).

To check if the line-widths are overly-sensitive to the peak of the rotation curve, I also extract from the JAM models the maximum of the circular velocity curve, denoted $V_{JAM,max}$, and the median value of the circular velocity curve, measured between the peak and the maximum extent of the SAURON data ($\approx$1R_e), denoted $V_{JAM,>peak}$. As discussed above, defining $V_{JAM,>peak}$ in this way picks out the value of the flat part of the rotation curve well in tests based on the data of Williams, Bureau & Cappellari (2009), which extend to $\approx$3 Re. Our data is only constrained out to around $\approx$1R_e, but the rotation curves do not drop wildly in this region. It should however be noted that this measure may not be the same as the velocity measured at very large radii. The values of $V_{JAM,max}$ and $V_{JAM,>peak}$ can be found in Table 3.2.

The top panel of Figure 3.4 shows a comparison between the observed CO line-widths, de-projected using dust inclinations (as described in Section 3.2.1.2), and $V_{JAM,max}$. The CO line-widths are systematically smaller than the maximum of the circular velocity curve. The median peak of the JAM circular velocity curves is at 8.5″, well within the single-dish beam, and hence I do not expect systematically missed emission to cause this trend. The mean offset from the maximum value is -0.03 $\pm$ 0.02 dex, broadly similar to the offset between the maximum and the flat part of the circular velocity curve expected from the results of Williams, Bureau & Cappellari (2009). The RMS scatter around this value is 0.09 dex. This suggests that the method is not overly sensitive to the peak of the circular velocity curve. The galaxies which do not have boxy profiles are again offset to much lower velocities. The only galaxy

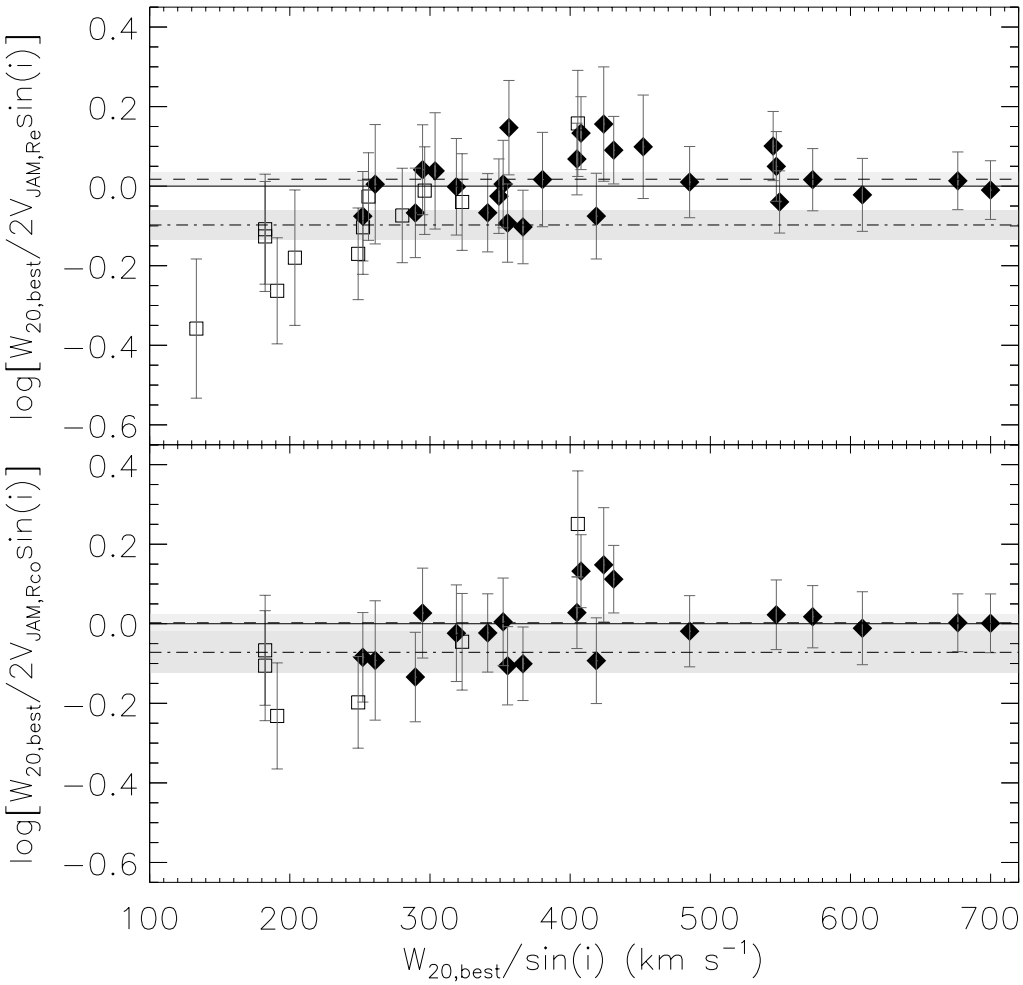

Figure 3.3: Difference between the best CO line-widths de-projected using the best inclinations (as described in Section 3.2.2.1) and twice the JAM model circular velocities, measured at one effective radius (top) and the radius of maximum CO extent, or 12″ whichever is smaller (bottom), plotted against the best inclination de-projected CO velocity width. Galaxies with boxy profiles are plotted as filled diamonds, while the others are shown as open squares. The solid line indicates where the JAM and CO velocities are identical. The dashed line and dot-dashed line are fitted offsets from zero, for the boxy galaxies and the other galaxies, respectively. The errors on the fits are indicated as shaded regions around the best fit lines.

whose line-width is inconsistent with the maximum value of its predicted circular velocity curve is again NGC 1266.

The bottom panel of Figure 3.4 compares the observed CO line-widths, de-projected using dust inclinations, with $V_{JAM,>peak}$. The CO measurements for galaxies with double horned profiles are, within the errors, consistent with the $V_{JAM,>peak}$ measure. The mean offset from this measure is 0.02 ± 0.02 dex, with an RMS deviation of 0.1 dex. The galaxies that were not identified as boxy are on average offset from $V_{JAM,>peak}$ by -0.1±0.04 dex. There are several galaxies that do not have a boxy profile, but are consistent with rotating at $V_{JAM,>peak}$. These galaxies are NGC 4684, PGC 056772 and PGC 061468, all of which have profiles which were hard to classify. If interferometric observations were available I would hence expect to find that the gas does indeed reach beyond the peak of the galaxy rotation curve in these systems.

Figures 3.3 and 3.4 demonstrate that, if one selects galaxies with boxy profiles, W_{20} velocity widths provide an good estimate of the circular velocity after the inner peak of the rotation curve, whether estimated as $V_{JAM,Re}$ or $V_{JAM,>peak}$. It is worth mentioning that, for the sample used here, a simple cut excluding galaxies with CO linewidths $\lesssim$250km s^{-1} would have a similar effect as selecting by profile shape, removing most of the outliers. Applying an arbitrary cut in velocity, the most important TF parameter, could bias the derived TFR, especially for a sample selected in a different way, and hence I prefer selection by profile shape in this work.

3.3.2 *H I line-widths*

Morganti et al. (2006) and Williams, Bureau & Cappellari (2010) have shown that in some cases H I line-widths are not a good measure of the circular velocity for early-type galaxies. I examine this here by retrieving archival H I single-dish line-widths measured at 20% of the peak flux from HyperLEDA (Paturel et al., 2003, denoted $W_{20,HI}$).

In Figure 3.5, I compare the single-dish H I line-widths to twice the projected JAM circular velocities measured at R_e (top panel) and the observed CO line-widths

Table 3.2: Parameters extracted from the JAM model circular velocity curves for the ATLAS^{3D} early-type CO-rich galaxies used in this chapter.

Galaxy	$V_{JAM,Re}$ (km s^{-1})	$V_{JAM,Rco}$ (km s^{-1})	$V_{JAM,max}$ (km s^{-1})	$V_{JAM,>peak}$ (km s^{-1})
(1)	(2)	(3)	(4)	(5)
IC 0676	117	116	118	116
IC 0719	232	232	233	218
IC 1024	150	163	174	157
IC 2099	-	-	-	-
NGC 0524	337	362	368	337
NGC 1222	177	177	236	177
NGC 1266	141	116	144	134
NGC 2685	160	-	186	160
NGC 2764	199	190	207	196
NGC 2768	320	325	342	311
NGC 2824	220	220	278	206
NGC 3032	129	158	238	135
NGC 3182	183	-	198	178
NGC 3489	169	197	198	159
NGC 3619	216	-	277	223
NGC 3626	173	187	256	174
NGC 3665	358	354	362	321
NGC 4150	134	141	163	131
NGC 4270	185	-	193	182
NGC 4292	-	-	-	-
NGC 4309	-	-	-	-
NGC 4324	150	152	169	150
NGC 4429	276	276	294	273
NGC 4435	237	263	266	237
NGC 4459	244	261	273	244
NGC 4477	249	278	295	249
NGC 4526	328	338	348	292
NGC 4684	136	-	137	123
NGC 4694	96	-	99	93
NGC 4710	175	161	202	176
NGC 4753	301	-	302	274
NGC 5173	180	-	202	166
NGC 5273	127	-	148	125
NGC 5379	152	-	158	147
NGC 6014	148	149	185	148

Notes: This table contains the circular velocities derived from the JAM models, extracted at different radii. Galaxies that were removed from the ATLAS^{3D} sample have no JAM model available. Column 2 contains the circular velocities extracted at one effective radius. Column 3 contains the circular velocities extracted at the maximum radial extent of the CO, or 12″, whichever is smaller. Galaxies without interferometric observations are not included. Column 4 contains the maximum circular velocity. Column 5 contains the median of velocities after the peak in the circular velocity curve out to the maximum radius at which the model is constrained by the observational data. Some galaxies had insufficient data to constrain such a median between these two points, and are excluded. The error on these JAM velocities is estimated to be ≈8%. This is a combination of an average 5% error in the observed stellar velocity dispersion constraining the models, and model errors of ≈6% (Cappellari et al., 2006). This does not include errors in inclination, which are harder to quantify.

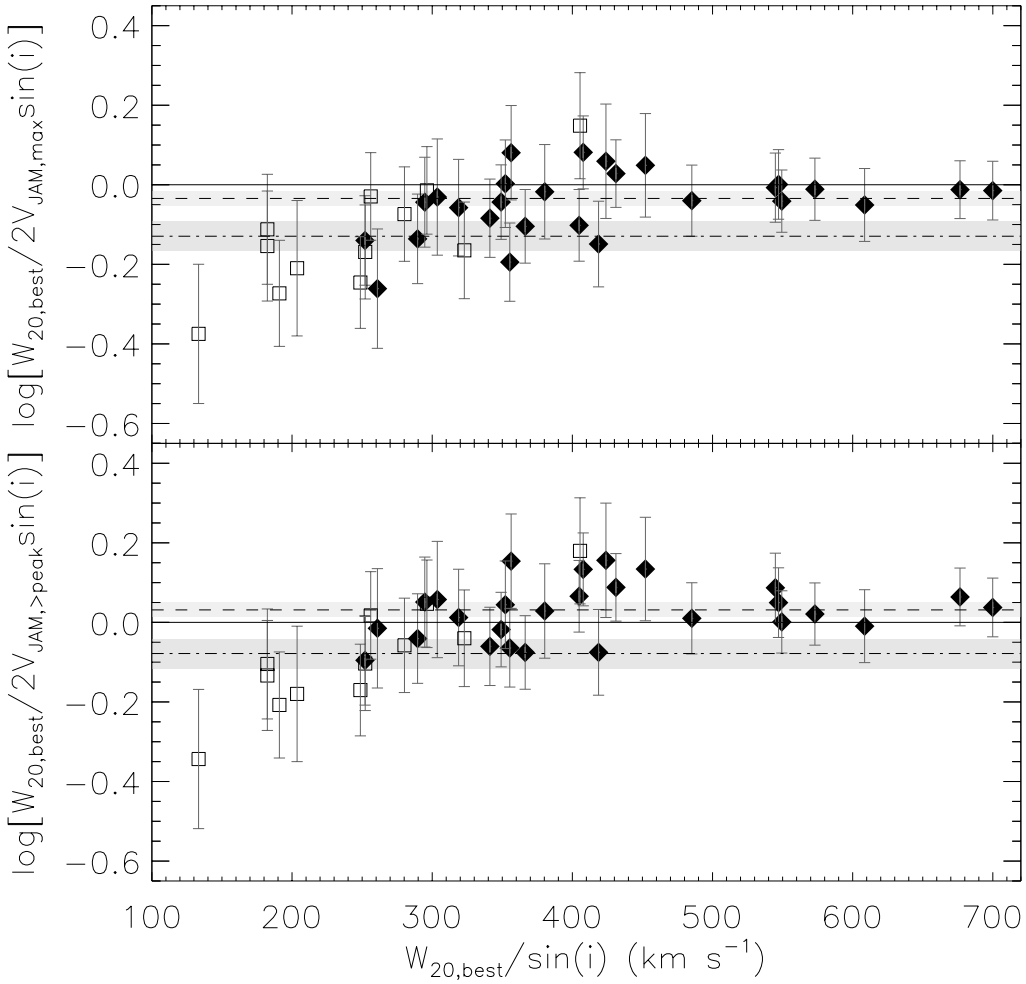

Figure 3.4: Same as Figure 3.3, but for JAM model circular velocities measured at the maximum (top) and using the median velocity after the maximum (bottom).

Table 3.2: continued

Galaxy	$V_{JAM,Re}$ (km s^{-1})	$V_{JAM,Rco}$ (km s^{-1})	$V_{JAM,max}$ (km s^{-1})	$V_{JAM,>peak}$ (km s^{-1})
(1)	(2)	(3)	(4)	(5)
PGC 029321	154	-	165	154
PGC 056772	152	-	153	133
PGC 058114	-	-	-	-
PGC 061468	166	-	166	160
UGC 05408	139	-	163	133
UGC 06176	184	196	219	184
UGC 09519	160	165	182	155

Continued from previous page

(bottom panel). All galaxies from the sample with archival H I data at the time of retrieval are included. We find that although the average difference between the H I line-width and the JAM circular velocities is small (0.02 dex), the scatter is large (RMS scatter of ≈0.11 dex), and the single-dish H I line-widths do not correlate statistically with the galaxy luminosity. The same is true when one compares with observed CO line-widths, with a larger scatter (≈0.15 dex). There is also a systematic trend in the residuals in the bottom panel of Fig. 3.5, where the galaxies with high CO rotation velocities, which are likely of high masses, have systematically smaller H I line-widths.

Figure 3.5 suggests that some of the detected H I sources, at high CO velocities (and hence likely at high mass), are either not related to the galaxy under study or that the H I has been kinematically disturbed. This is consistent with the results of Morganti et al. (2006), Williams, Bureau & Cappellari (2010) and Serra et al., (in preparation).

Single-dish H I Line-widths in the LEDA database are however known to suffer from many issues, including major problems with source confusion. Outer HI disks are also usually warped with respect to the inner regions, and hence a simple inclination estimates from optical images will be insufficient. Interferometric H I data allows one to identify relaxed disks, and in these rotation and the TFR can be studied (e.g. Morganti et al., 2006; Oosterloo et al., 2007; Weijmans et al., 2008; Oosterloo et al., 2010). To further investigate the TFR, and the disk-halo conspiracy in these galaxies, a future paper in the ATLAS^{3D} series will study the H I TFR of ETGs at large radii using superior interferometric H I data.

3.4 RESULTS

Using the data presented in Table 3.1, I construct a series of Tully-Fisher relations to explore the effect of the different inclination and velocity measurements, defined in order of increasing complexity. The results are shown in Figure 3.6. The general form of the K_s band Tully-Fisher relation I have adopted is

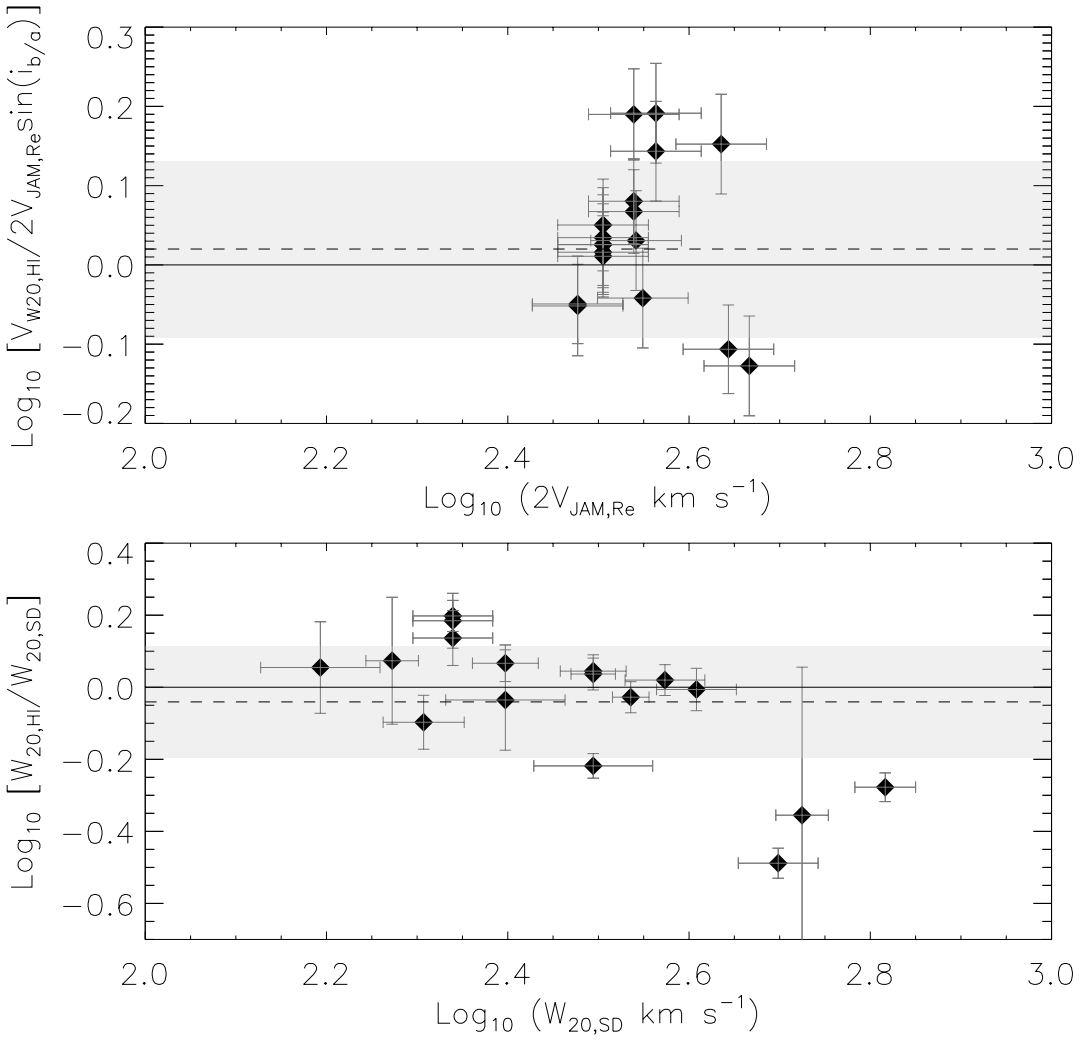

Figure 3.5: *Top:* Difference between the deprojected H I line-width and twice the JAM model circular velocity measured at one effective radius, for galaxies with archival H I data in LEDA, as a function of the model velocities. The solid line indicates where the JAM and H I velocities are identical. The dashed line is the mean difference, with the RMS scatter indicated in grey. *Bottom:* As for the top panel, but comparing observed CO single-dish and H I line-widths, for galaxies with boxy CO profiles only.

$$\mathrm{M}_K = \mathrm{a}\,[\log_{10}\left(\frac{W_{20}}{km\ s^{-1}}\right) - 2.6] + b, \tag{3.2}$$

where a is the slope and b is the zero-point of the relation.

The package `MPFIT` (Markwardt, 2009) was used to fit the inverse of Equation 3.2 (regressing the observed rotation velocities) with the addition of an intrinsic scatter, which I iteratively adjust to ensure a reduced $\chi^2 \approx 1$. Full details of the fitting procedure can be found in Williams, Bureau & Cappellari (2010).

Each plot in Figure 3.6 shows two best-fit lines. For the first I allow both the intercept and slope to vary, while for the second I fix the slope to that found by Tully & Pierce (2000), a = -8.78. For reference I also plot the *K*-band spiral galaxy TFR of Tully & Pierce (2000) (see Equation 3.3), which was constructed using H I line-widths of spiral galaxies in 12 well separated clusters:

$$\mathrm{M}_{K\mathrm{s}} = -8.78\,[\log_{10}\left(\frac{W_{20}}{\mathrm{km\ s^{-1}}}\right) - 2.5] - 23.17, \tag{3.3}$$

and the K_s-band S0 TFR from Williams, Bureau & Cappellari (2010) (see Equation 3.4), which was derived from Jeans modeling of major-axis stellar kinematics from 14 edge-on S0 galaxies:

$$\mathrm{M}_{K\mathrm{s}} = -8.56\,[\log_{10}\left(\frac{W_{20}}{\mathrm{km\ s^{-1}}}\right) - 2.4] - 24.02, \tag{3.4}$$

3.4.1 CO Tully-Fisher relations

3.4.1.1 Inclinations from galaxy axial ratios

The CO TFR de-projected using $i_{\mathrm{b/a}}$ is presented in the top two panels of Figure 3.6. The parameters of the best-fit relations are listed in Table 3.3. The top-left panel shows all galaxies, with open squares for those which do not show a boxy CO profile or where the profile shape is unclear, and solid triangles for those with clear boxy profiles. Only a loose correlation is observed, with clear outliers, almost all of which are galaxies without double horned profiles. A much tighter correlation is observed once one removes galaxies with non-boxy profiles, as shown in the top-right panel. This is physically motivated, as I believe the gas in these galaxies does not reach

beyond the peak of the rotation curve. Once the non-doubled-horned galaxies are removed both best-fit lines agree within the errors with the TFR of Williams, Bureau & Cappellari (2010), providing strong *a posteriori* evidence that the CO in these galaxies does trace the circular velocity in a way that is consistent with dynamical models. The remaining outlier is NGC 7465 which I will discuss in more detail below. If this outlier is removed the best fit relation follows that of Williams, Bureau & Cappellari (2010) even more closely. The intrinsic scatter of the best fit relation with a free, and a constrained, slope is respectively 0.57 and 0.63 mag, with total RMS scatters of 0.69 and 0.78 mag.

3.4.1.2 *Inclinations from dust axial ratios*

In a similar way I can construct a TFR using the inclinations derived from fitting ellipses to the dust distributions highlighted in unsharp-masked images. The CO TFR deprojected using $i_{\rm dust}$ is presented in the middle-left panel of Figure 3.6. Once again, within the quoted errors, the best-fit relations are consistent with the result of Williams, Bureau & Cappellari (2010). The parameters of the best-fit relations are listed in Table 3.3. The intrinsic scatter of the best-fit relation with a free, and a constrained, slope is 0.65 and 0.78 mag respectively, but with a total scatter of 0.75 and 0.94 mag, respectively. The outlier is NGC 7465 - without this galaxies the observed intrinsic scatter in the unconstrained fit decreases to 0.46 mag, with a total scatter of 0.6 mag, confirming the visual impression that the correlation using dust inclinations is tighter. Removing this galaxy also improves the agreement between my best-fit slope with that found by Williams, Bureau & Cappellari (2010).

3.4.1.3 *Inclination from molecular gas modeling*

Using the inclinations from the tilted-ring models and the total velocity widths calculated from the interferometric data, I can construct yet another TFR. First I do this naively, using only the single-dish boxy classifications. This results in the middle-

right panel of Figure 3.6. Some of the interferometric observations have insufficient spatial resolution to strongly constrain the inclination of the molecular gas, and this is reflected in the error bars. As can clearly be seen in this panel, the best-fit relation is only marginally consistent with that of Williams, Bureau & Cappellari (2010). The intrinsic scatter of the best-fit relation with a free, and a constrained, slope is 0.43 and 0.62 mag, with a total scatter of 0.60 and 0.82 mag, respectively.

The interferometric data, at least in some cases, allow us to further refine my technique for identifying galaxies that have reached beyond the peak of the circular velocity curve, by identifying nuclear rings and finding galaxies where a turnover can be seen in the position-velocity diagram (see Chapter 4). Interferometric observations are especially powerful in this regard, as the extent of the CO can be compared to the expected circular velocity curve from dynamical models. For example, NGC 7465, the obvious outlier in the previous plots, features a misaligned circum-nuclear CO distribution, which has a double horned profile, but has no turnover in its velocity field, and is extremely unlikely to reach beyond the peak of the galaxy rotation curve.

Aperture synthesis observations also allow us to identify cases where a galaxy is misclassified using the single-dish data because a pointing error and/or extended molecular gas results in only some smaller portion of the total velocity width being detected. Such cases include NGC 4324, NGC 4477 and PGC 58114. In a few cases where the profile shape was uncertain (due to low signal to noise single dish spectra) the interferometric data reveals that the gas does extend beyond the peak of the rotation curve, allowing us to include them. This is the case for NGC 3489, NGC 4292 and UGC 09519.

The TFR in the middle-right panel of Figure 3.6 can thus be improved using the full knowledge gained from the interferometric data (discussed above), and this results in the TFR shown in the bottom-left panel of Figure 3.6. The best-fit TFR using this additional information agrees with that of Williams, Bureau & Cappellari (2010). The parameters of the best-fit relations are again listed in Table 3.3. The intrinsic scatter of the best-fit relation with a free, and a constrained, slope is 0.32 and 0.33 mag, with a total scatter of 0.54 and 0.58 mag, respectively.

3.4.1.4 *Combining interferometric and single-dish data*

Finally, I can combine the single-dish and interferometric observations, using the hybrid inclinations and velocities described in Section 3.2.2.1. These choices lead to the TFR shown in the bottom-right panel of Figure 3.6. The parameters of the best-fit TF relations are listed in Table 3.3. The best-fit relations closely agree with the result of Williams, Bureau & Cappellari (2010), and the fits with a free and a constrained slope have an intrinsic scatter of 0.36 and 0.37 mag, with a total scatter of 0.54 and 0.57 mag, respectively. The intrinsic scatter found in this relation is similar to that found by a large study of the intrinsic scatter of the spiral galaxy TFR ($\sigma_{\rm int} \approx 0.4$ mag at bands between g and z; Pizagno et al., 2007), and only very slightly larger than that found by Williams, Bureau & Cappellari (2010) ($\sigma_{\rm int} \approx 0.3$ mag at $K_{\rm s}$-band). The small total scatter reflects both the better number statistics and the use of the best possible measures of rotation and inclination.

I find that the residuals from this hybrid relation are statistically uncorrelated with the galaxy $K_{\rm s}$-band luminosity (Skrutskie et al., 2006), optical colour (g-r; Adelman-McCarthy et al., 2008, Scott et al., in preparation), velocity dispersion, galaxy total dynamical mass (Cappellari et al. in preparation) and spin parameter λ_R (Paper III).

3.5 DISCUSSION

3.5.1 *CO as a tracer of galactic potentials*

The results presented in Section 3.3.1 show that CO emission accurately traces the potential of early-type galaxies, if one has a suitable method of identifying which galaxies have extended molecular discs. Our work demonstrates that selecting galaxies via profile shape is robust and does not systematically affect the measured rotation velocity. The main possible contaminant introduced by this selection is galaxies that have molecular rings, which would display a boxy profile without necessarily rotating at $V_{\rm max}$. Circumnuclear rings pose the greatest problem, as they are very unlikely

to rotate at V_{max}, unlike inner and outer rings which are located at resonance points within the flat part of the galaxy circular velocity curve (e.g. Buta, 1986). The number of galaxies with circumnuclear rings in the sample is likely to be small, as their presence in significant numbers would bias the best-fit line in Figure 3.3 to small values. This conclusion is also supported by the interferometric maps presented in Chapter 2, which suggest that only a small percentage of local early-type galaxies have their molecular gas restricted to the circumnuclear region.

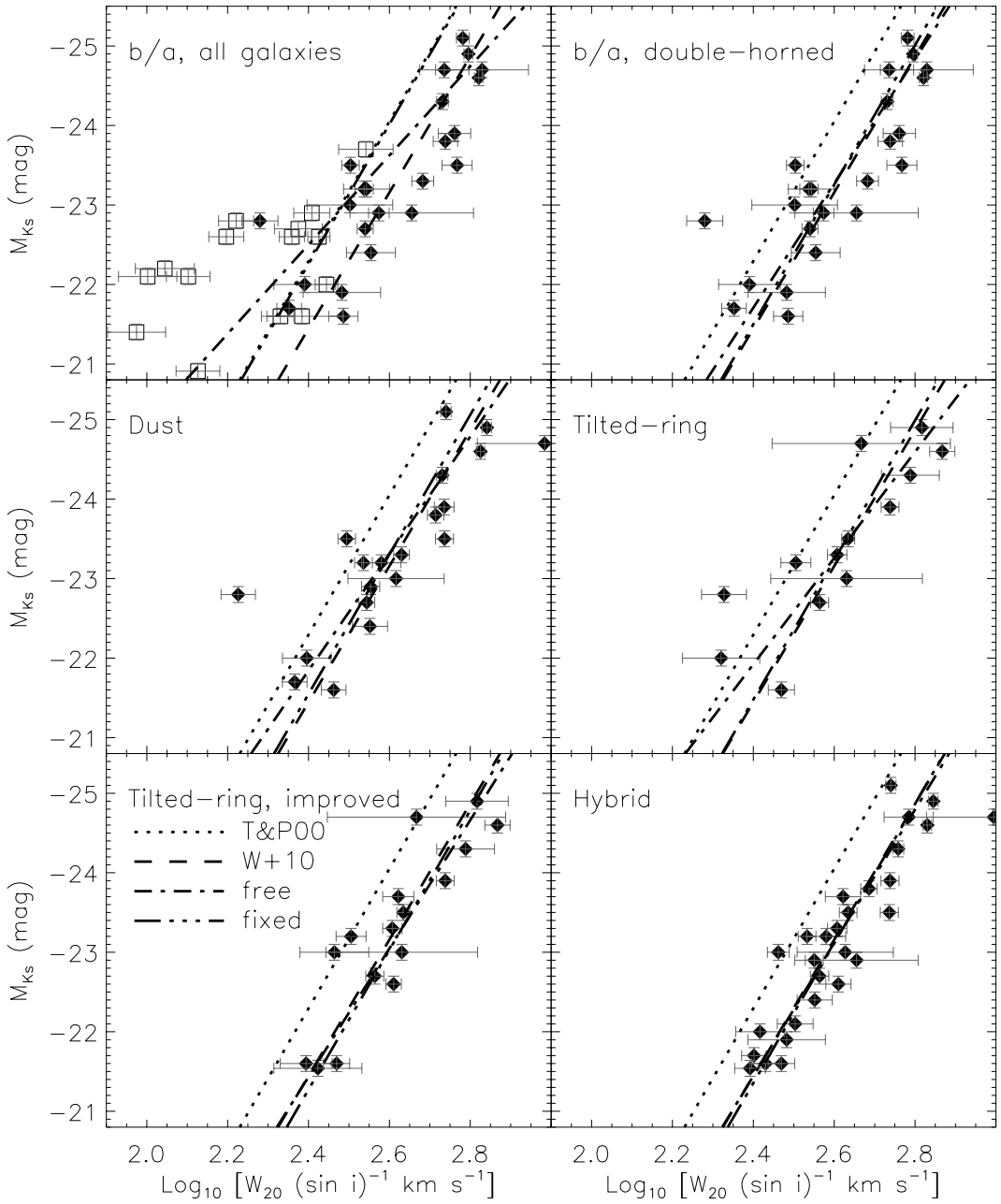

Figure 3.6: CO TFRs constructed using various inclination and line-width measurements. In each plot are the spiral galaxy TFR of Tully & Pierce (2000) (short dashes), and the S0 TFR of Williams, Bureau & Cappellari (2010) (long dashes). Also plotted are the best-fit relations for my data for both an unconstrained fit (dot-dashed) and a fit with slope fixed to that of Tully & Pierce (2000) (triple dot-dashed). The best-fit parameters are listed in Table 3.3. *Top-left:* Inclinations derived from galaxy optical axial ratios (see Section 3.2.1.1). CO detections with boxy profiles are shown as filled diamonds, galaxies with non-boxy profiles and uncertain classifications are shown as open squares. *Top-right:* As top-left, but galaxies with non-boxy profiles are removed. *Middle-left:* As top-right, but using inclinations from unsharp-masked dust images (see Section 3.2.1.2). As top-right, but using interferometric W_{20} values and inclinations derived from tilted-ring fits to the interferometric data (see Section 3.2.1.3). *Bottom-left:* As middle-right, but using the interferometric data to identify galaxies with CO which reaches beyond the peak of the galaxy rotation curve. *Bottom-right:* A hybrid plot using the best inclinations and velocity widths as defined in Section 3.2.2.1.

Table 3.3: Best-fit parameters of the TFRs shown in Figure 3.6.

Inc. method	a (mag)	b (mag)	$\sigma_{\rm int}$ (mag)	$\sigma_{\rm total}$ (mag)	$W_{20,sd}$	$W_{20,inter}$	Selection
(1)	(2)	(3)	(4)	(5)	(6)	(7)	(8)
Stellar b/a	-5.61 $\pm$ 0.71	-23.62 $\pm$ 0.16	0.75	0.82	x	-	none
Stellar b/a	-	-24.01 $\pm$ 0.23	1.30	1.42	x	-	none
Stellar b/a	-7.82 $\pm$ 1.12	-23.27 $\pm$ 0.15	0.60	0.69	x	-	SD
Stellar b/a	-	-23.25 $\pm$ 0.16	0.66	0.78	x	-	SD
Dust	-7.36 $\pm$ 1.19	-23.31 $\pm$ 0.16	0.66	0.76	x	-	SD
Dust	-	-23.30 $\pm$ 0.19	0.79	0.94	x	-	SD
Tilted-ring	-6.68 $\pm$ 1.21	-23.26 $\pm$ 0.17	0.48	0.63	-	x	SD
Tilted-ring	-	-23.23 $\pm$ 0.23	0.65	0.86	-	x	SD
Tilted-ring	-8.07 $\pm$ 1.10	-23.05 $\pm$ 0.12	0.32	0.54	-	x	Inter
Tilted-ring	-	-23.03 $\pm$ 0.13	0.33	0.58	-	x	Inter
Hybrid	-8.38 $\pm$ 0.70	-23.12 $\pm$ 0.09	0.36	0.54	x	x	Inter+SD
Hybrid	-	-23.11 $\pm$ 0.09	0.37	0.57	x	x	Inter+SD

Notes: Column 1 describes the inclination method used to deproject the measured line-width. Columns 2 and 3 show the best-fit slope and zero-point, respectively, of the Tully-Fisher relation of the form $M_{Ks} = \mathrm{a}[\log_{10}(W_{20}/km\,s^{-1}) - 2.6] + b$. Column 2 is blank where the fit was constrained to have the same slope as that found by Tully & Pierce (2000), a=-8.78. Column 4 shows the intrinsic scatter ($\sigma_{\rm int}$) required by the fit to produce a reduced $\chi^2 \approx 1$. Column 5 shows the total RMS scatter around the best-fit relation. A cross in Column 6 denotes that the velocity widths used are from single-dish data, while a cross in Column 7 denotes that interferometric line-widths were used. Column 8 lists the selection method used to find galaxies that have gas beyond the peak of the circular velocity curve. 'SD' means the galaxies single-dish profiles are boxy, while 'Inter' means that interferometric data were used to determine if the gas reaches beyond the peak of the circular velocity curve. The hybrid relations use both single-dish and interferometric data, as described in Section 3.2.2.1.

One should also remember that the circular velocity curves of ETGs rise very quickly, normally peaking within one effective radius (e.g. Williams, Bureau & Cappellari, 2009). This allows the molecular distribution to be compact, but still have enough gas beyond the peak of the galaxy circular velocity curve so that the linewidth is a good proxy of the circular velocity in that region. The good agreement between the derived TFR and that of Williams, Bureau & Cappellari (2010) suggests that the disk-halo conspiracy holds for our early-type galaxies, at least out to $3R_e$. If this conspiracy holds even further out into the dark matter dominated parts of these galaxies (which some authors suggest it does not, e.g. Dutton et al., 2010) will be considered in a future paper in the ATLAS^{3D} series.

3.5.2 *Inclination measures*

The problem of measuring the inclination of early-type galaxies is not new, but it is complicated here as the CO is often not aligned with the stars (e.g. Young, 2002; Schinnerer & Scoville, 2002; Young, Bureau & Cappellari, 2008; Crocker et al., 2008, 2009, 2011), and it is the CO inclination that I require. As I have shown, methods using galaxy optical axis ratios are likely to yield large uncertainties and increase the scatter in the TFR, but they do not seem to significantly affect the determination of its slope or zero-point. This is likely because errors in inclination are most problematic when the galaxy is close to face-on, and the number of nearly face-on galaxies in the sample is small. The profile shape selection criterion also actively selects against face-on galaxies, where the velocity width is less than a few channel widths (no matter how extended the molecular gas is). In many H I TFR papers, galaxies with an inclination less than 45° are discarded (e.g. Tully & Fisher, 1977), so this is not especially worrying. If I apply this cut in inclination to the sample, I retain within the errors the same Tully-Fisher slope and zero-point, and the RMS scatter decreases. Even with a very harsh cut of 65° I retain the same relation. This demonstrates that the results are robust, and the slope and zero-point are minimally affected by the choice of inclination correction.

As hinted above, while the slope and zero-point are robust, the scatter in the relation is affected by the inclination estimation method chosen. Moving from galaxy axial ratios to inclinations derived from dust features decreases the RMS scatter around the best-fit relation by ≈0.15 mag, if one removes the one obvious outlier. My results do reveal a reduction of the total scatter when the inclinations are determined from fitting a thin disc model to interferometric data, despite the limited number statistics. With a larger sample one might expect the scatter to decrease further. In both cases the decrease in scatter is likely due to properly accounting for molecular gas distributions that do not rotate in the same plane as the stars. Unsurprisingly, to obtain the tightest relation one must use measures of inclination (such as unsharp-masked dust images or interferometric imaging of the molecular gas itself) that truly trace the inclination of the gaseous component.

3.5.3 *Intrinsic scatter of the CO TFR*

The intrinsic scatter of my hybrid TFR is 0.36 mag, broadly consistent with typical values found in dedicated studies of the spiral galaxy TFR in the optical, such as those by Pizagno et al. (2007) (0.4 mag at g- and z-band) and Kannappan, Fabricant & Franx (2002) (0.4 mag at r-band). My intrinsic scatter is slightly larger than that found for S0 galaxies by Williams, Bureau & Cappellari (2010) (≈0.3 mag at K_s-band). One reason for the increased scatter may be that Williams, Bureau & Cappellari (2010) considered S0 galaxies only, whereas our sample includes both morphologically classified elliptical and S0 galaxies, that span a wider range in λ_R, the stellar specific angular momentum (Emsellem et al., 2007). This increased scatter may therefore be due to spanning an increased range in internal dynamics.

We do not have sufficient number statistics to constrain an elliptical galaxy TFR separately, but the earliest type galaxies (selected by optical morphology) do lie on average to the faster and/or dimmer side of my relations. There is however no systematic behaviour within the residuals to the fit as a function of λ_R.

3.5.4 *Offset from the spiral TFR*

Exploring changes in the M/L of galaxies as a function of morphological type is one of the main motivations for studying the early-type TFR. Williams, Bureau & Cappellari (2010) have highlighted the importance of comparing TFRs for each morphological type derived using the same tracer and methods, in order to minimize systematic differences. In this spirit I use the spiral galaxy line-widths published by Chung et al. (2009), measured from on-the-fly mapping of 18 Virgo Cluster members, in order to define a spiral CO TFR.

We construct a Tully-Fisher relation for the Chung et al. (2009) spirals in the same way as for the early-type sample, using 2MASS $K_{\rm s,total}$ magnitudes and their W_{20} line-widths corrected for inclination. These inclinations were derived from the galaxy axial ratio and the morphological type using the classical Hubble formula from Hubble (1926). This formula effectively differs from Equation 3.2.1.1 by making q_0 a function of morphological type. For spiral galaxies such as those in the Chung et al. (2009) sample this correction is small, corresponding to a q_0 less than 0.05, and hence this difference is unlikely to systematically effect the comparison of our results. I differ from Chung et al. (2009) however by not assuming a set distance to the Virgo Cluster, which has significant substructure. Instead I use the distance to each galaxy as determined for the ATLAS^{3D} parent sample (Paper I). The resulting TFR is shown in Figure 3.7. The values used to create this figure are listed in Table 3.4.

The best-fit spiral TFR with an unconstrained gradient is

$$\mathrm{M}_{Ks} = (-10.8 \pm 2.5)\,[\log_{10}\left(\frac{W_{20}}{km\ s^{-1}}\right) - 2.6] - (24.1 \pm 0.2)\,, \tag{3.5}$$

where the intrinsic scatter about the correlation is 0.68 mag, with a total scatter of 0.72 mag. The TFR obtained by constraining the fit to have the same slope as that of Tully & Pierce (2000) is

$$\mathrm{M}_{Ks} = -8.78\,[\log_{10}\left(\frac{W_{20}}{km\ s^{-1}}\right) - 2.6] - (24.02 \pm 0.14)\,, \tag{3.6}$$

with an intrinsic scatter of 0.55 mag and a total scatter of 0.59 mag.

Table 3.4: List of the parameters used to create the spiral TFR in Figure 3.7.

Galaxy	Type	Distance (Mpc)	m_{Ks} (mag)	$i_{b/a}$ (deg)	W_{20} (km s^{-1})
(1)	(2)	(3)	(4)	(5)	(6)
NGC 4254	Sc	16.5	6.93	29 ± 7.3	221 ± 1
NGC 4298	Sc	16.5	8.47	59 ± 2.4	270 ± 4
NGC 4302	Sc	14	7.83	90 ± 0.1	353 ± 1
NGC 4303	Sc	16.5	6.84	$19 \pm 12.$	162 ± 2
NGC 4321	Sc	15.85	6.59	38 ± 5.2	239 ± 2
NGC 4402	Sc	16.5	8.49	80 ± 0.7	267 ± 3
NGC 4419	Sa	13.12	7.74	82 ± 0.6	318 ± 2
NGC 4438	Sb	16.5	7.27	87 ± 0.2	272 ± 5
NGC 4501	Sbc	15.3	6.27	60 ± 2.3	518 ± 2
NGC 4527	Sb	14.05	6.93	75 ± 1.1	376 ± 2
NGC 4535	Sc	15.75	7.38	41 ± 4.7	252 ± 5
NGC 4536	Sc	14.09	7.52	59 ± 2.4	318 ± 2
NGC 4548	Sb	18.71	7.12	35 ± 5.8	234 ± 6
NGC 4569	Sab	16.5	6.58	69 ± 1.6	311 ± 1
NGC 4579	Sab	21.3	6.49	39 ± 5.0	329 ± 1
NGC 4647	Sc	16.5	8.05	34 ± 6.0	156 ± 1
NGC 4654	Sc	16.5	7.74	58 ± 2.5	285 ± 1
NGC 4689	Sc	16.5	7.96	39 ± 5.0	182 ± 1

Notes: The galaxy sample listed in Column 1 comes from Chung et al. (2009). Column 2 lists the spiral galaxy type following the Hubble scheme, (RC3; de Vaucouleurs et al., 1991). The distance to the galaxy in Column 3 is from the ATLAS^{3D} parent sample (Paper I). These distances are drawn preferentially from Mei et al. (2007) and Tonry et al. (2001). Column 4 lists the apparent K_s-band magnitudes, taken from 2MASS. Column 5 is the optical galaxy axis ratio, taken from NED, as described in Section 3.2.1.1. The line-widths in Column 6 are taken directly from Chung et al. (2009).

Within observational errors, the best-fit free and constrained spiral CO TFRs are consistent with the relation of Tully & Pierce (2000). The offset between the unconstrained Chung et al. (2009) spiral CO TFR and the hybrid early-type CO TFR (discussed in Section 3.4.1.4) is 0.98 ± 0.22 mag, consistent within errors with the value found by Bedregal, Aragón-Salamanca & Merrifield (2006) and the offset found by Williams, Bureau & Cappellari (2010) between their S0 TFR and the Tully & Pierce (2000) relation.

This result is nevertheless surprising since Williams, Bureau & Cappellari (2010) argue that their offset with Tully & Pierce (2000) is flawed by systematic effects (the tracers and methods being different), and they prefer the much smaller offset (0.5 ± 0.14 mag) from their spiral galaxy sample treated identically to the S0s.

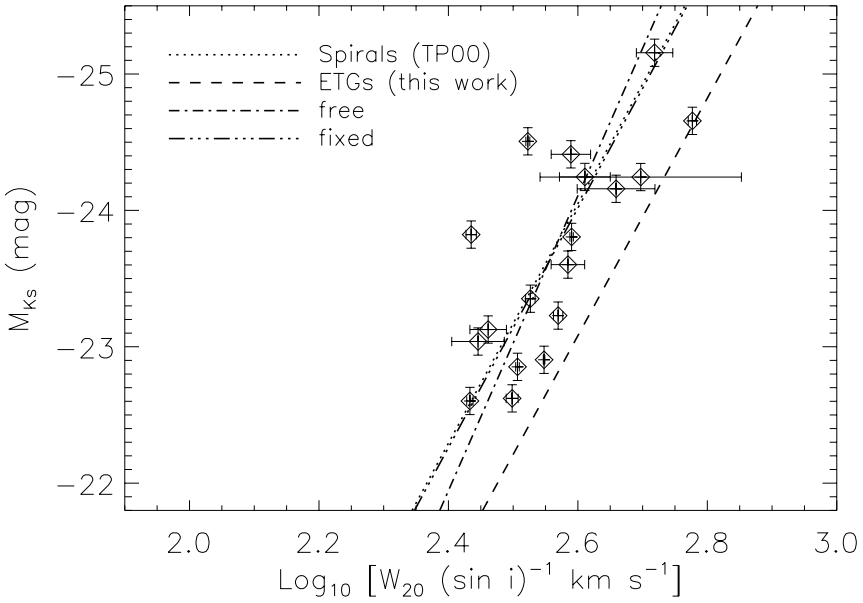

Figure 3.7: Spiral galaxy CO TFR built in the same way as that shown in Fig. 3.6, but using W_{20} values and inclinations from the work of Chung et al. (2009).

It is not immediately clear how my own result can be reconciled with this, as I use identical tracers and methods as Chung et al. (2009). However, I suspect that the different results are due to the mix of morphological types in the spiral samples. Williams, Bureau & Cappellari (2010) use a spiral sample consisting mostly of Sa-Sb spirals, while the sample of Chung et al. (2009) includes a larger fraction of later-type galaxies (mostly Sc), which are known to have a larger zero-point (e.g. Roberts, 1978; Rubin et al., 1985; Masters, Springob & Huchra, 2008; Shen et al., 2009). Separating the Chung et al. (2009) sample more finely into morphological types does not necessarily support this explanation, but the number statistics are very limited.

3.5.5 Origin of the offset TFR for ETGs

In the ETG sample used in this chapter, a few galaxies are consistent with the spiral galaxy relation and many lie between the spiral and early-type relations, consistent with the predictions of passive fading models (e.g. Dressler, 1980; Dressler et al., 1997). The fact that molecular gas is present in all these galaxies, however, suggests

that many must have ongoing star formation (even if weak), and hence evolutionary models relying on a purely passive evolution are ruled out.

The presence of molecular gas mass fractions ranging from <0.1 to 5% in these galaxies perhaps suggests an answer to some of the problems with passive evolution models. Bedregal, Aragón-Salamanca & Merrifield (2006) and Williams, Bureau & Cappellari (2010) both discuss the timescale implied by the ETG-spiral TFR offsets observed, assuming passive fading, and find it uncomfortably short and inconsistent between the B and K_s bands. The presence of low levels of residual star formation would prolong the period it takes for galaxies to fade, and would contribute relatively more light at blue wavelengths than in the infrared. The molecular gas mass fraction in these galaxies is however small , so it is unclear if such a low mass fraction of young stars could extend the fading timescale sufficiently.

An alternative explanation of the TFR offset is that the morphological (and luminosity) evolution is accompanied by a change in the size of the galaxies, affecting the galaxy rotation rather than its luminosity. Williams, Bureau & Cappellari (2010) suggest that a systematic contraction as spirals transform into S0s, consistent with the trend with morphological type of the size-luminosity relation (Courteau et al., 2007), could explain the offset from the spiral TFR. Clearly, a combination of both effects is also possible.

3.5.6 High-mass end of the CO TFR

As discussed in the introduction, one motivation for studying the CO TFR is the ability to probe the full mass range of galaxies, from small disc galaxies to large spheriods, with the same tracer and hence with the same assumptions and systematics. As an example of the power of this approach, I can investigate if the sample shows any evidence of a change in the slope of the TFR at the high-mass end, as reported by some authors (e.g. Peletier & Willner, 1993; Verheijen, 2001; Noordermeer & Verheijen, 2007).

Our sample contains eight galaxies above the luminosity threshold suggested in

previous works ($M_{Ks} \leq$-23.75). As can be seen in the bottom-right panel of Figure 3.6, all but one of these systems are on, or to the right of, the best-fit relation for the whole sample. When one compares the best-fit TFR derived for the whole sample to that for just the fainter galaxies ($M_{Ks} \geq$-23.75), there is a small difference in the gradient and zero-point, in the direction found by other authors. I do not have the number statistics to properly investigate the size of this effect, however, and hence only conclude that my results are consistent with the presence of a different slope at the high-mass end of the TFR.

3.5.7 Single-dish vs aperture synthesis

I have demonstrated here that single-dish spectra are sufficient to construct a robust CO Tully-Fisher relation, and that galaxy inclinations can be taken from optical imaging without noticeably biasing its slope or zero-point (Section 3.5.2). However, one must exercise caution, as the small beams of millimeter telescopes can occasionally underestimate the line-widths of galaxies with extended molecular discs. Barring beam dilution effects, one would expect single-dish profiles to perform even better at higher redshifts, where the angular size of the target galaxies decreases. One caveat to this is that as the angular size of galaxies decreases, source confusion may become a problem.

Naively, interferometric observations should be the best way to obtain an estimate of the true inclination of the molecular gas, and hence reduce the artificial scatter in the TFR. Aperture synthesis observations also tend to have a large field of view, and are thus less likely to face problems with extended gas distributions. Interferometric observations do, however, usually require a larger investment of observing time per source. One must also choose the angular resolution of the data carefully, in order to avoid resolving out the most extended structures, while still having sufficient spatial information to constrain a tilted-ring model. Both single-dish and interferometric studies of the TFR should thus have a bright future.

3.6 CONCLUSIONS AND FUTURE PROSPECTS

In this chapter I have presented the first CO Tully-Fisher relation for early-type galaxies. I have shown that CO line widths are a reliable tracer of the circular velocity in fast-rotating ETGs, and relations derived in this way agree well with ETG TFRs derived by other authors. I showed that my CO TFR relation has a robust slope and zero point, and a comparable scatter to that of TFRs derived with other techniques. The power of the CO Tully-Fisher relation is the ability to perform the same analysis easily for both spiral and early-type galaxies (i.e. identical tracer and method), with purely observable quantities. This technique is therefore particularly suitable for comparing the morphological variations of the zero-point of the Tully-Fisher relation.

The results presented in this chapter show that early-type galaxies follow a TFR that is offset by nearly one magnitude at K_s-band from that of spiral galaxies. This offset is similar to that found by previous authors. An offset ETG TFR is usually thought to be caused by passive evolution of spiral galaxies into lenticulars, after an abrupt cessation of star formation. However, the presence of molecular gas in these ETGs suggests that the majority of this sample must have ongoing residual star-formation, such as that revealed in a subsample of these galaxies (e.g. Temi, Brighenti & Mathews, 2009; Shapiro et al., 2010; Crocker et al., 2011). This should increase the timescale to fade by the required $\approx$1 mag. Some models, such as those that involve a change in the size of galaxies as they transform, do not require star formation to completely cease, providing an alternative explanation that is fully consistent with the data. Unfortunately the low molecular gas fractions in these systems make drawing any firm conclusions difficult.

Another area where the CO TFR (for all spectral types) excels is the ability to extend the technique to higher redshifts, as discussed in Tutui et al. (2001). H I observations are currently limited to $z \lesssim 0.2$ (e.g. Catinella et al., 2008), and stellar kinematics to $z \lesssim 2$ (e.g. van Dokkum, Kriek & Franx, 2009; Cappellari et al., 2009; Cenarro & Trujillo, 2009) whereas CO has already been detected in galaxies at redshifts $z > 6$ (e.g. Walter et al., 2004). The molecular content of galaxies is also expected to increase

with redshift, while the HI content stays approximately constant (Obreschkow & Rawlings, 2009; Bauermeister, Blitz & Ma, 2010; Daddi et al., 2010; Tacconi et al., 2010). CO velocity fields can be resolved, and the rotation (and hence the dynamical mass) estimated even out to high redshift (e.g. Walter et al., 2004; Carilli et al., 2010). This raises the exciting prospect of being able to directly track the mass-to-light ratio evolution of galaxies as a function of both redshift and mophological type, using an easily observable tracer (and without requiring dynamical modeling). New optical/IR instrumentation is just starting to allow surveys of galaxy stellar kinematics out to $z \approx 2$ (e.g. Cappellari et al., 2009; Schreiber et al., 2009), and comparison of these samples to line-widths derived with CO is a promising immediate avenue for future studies of the TFR.

Tutui et al. (2001) showed that constructing a (spiral galaxy) CO TFR is already possible at up to redshifts $z\sim0.1$, but with the next generation of mm-wave telescopes due to enter service over the next few years, we should gain access to CO lines across the redshifted universe for all morphological types. The Redshift Receiver System (RRS) on the Large Millimeter Telescope (LMT), for instance, is optimized for the detection of redshifted transitions of the CO ladder from star-forming galaxies at cosmological distances, and will generate a large database of CO line-widths. If one is able to optically image these galaxies to estimate their inclination and morphology, then this will become an excellent resource for Tully-Fisher analyses. With the ability to detect spectral line emission from CO in a galaxy like the Milky Way at a $z\sim3$ in less than 24 hours, ALMA will also be in an excellent position to study the CO TFR at high redshift. The higher frequency bands that will be available at ALMA also open up the possibility of detecting [CII] emission (rest wavelength 158 μm), which is brighter than CO in many galaxies in the local universe (Crawford et al., 1985) and possibly enhanced further at high redshifts (Maiolino et al., 2009). [CII] may therefore become an important tracer of the circular velocity of high-redshift systems.

Although technical aspects will certainly be improved and the interpretation of this relation remains uncertain, I have shown that the ETG CO TFR is a tantalising and promising tool for galaxy evolution.

4

INVESTIGATING THE EXTENT AND KINEMATICS OF THE MOLECULAR GAS IN EARLY-TYPE GALAXIES

"this brave overhanging firmament, this majestical roof fretted with golden fire..." – Hamlet, Act 2 Scene 2, William Shakespeare

4.1 INTRODUCTION

The molecular gas in ETGs exists in very different conditions than those within the discs of spiral galaxies. For example, ETGs have vastly different gravitational potentials (affecting e.g. the Toomre stability parameter Q; Toomre 1964), different elemental abundances (high metallicity and α-element over-abundance), higher prevalence of hot gas (10^6 K) and active galactic nuclei (AGN). Old stellar populations also create a harder inter-stellar radiation field (e.g. the UV-upturn phenomenon; see Yi 2008 for a review). Furthermore many galaxies can have kinematically misaligned gas with an external origin, rotating very differently than the stars. Spiral galaxies, on the other hand, have had their star-forming gas in situ for many gigayears (even if it is also being topped up externally; e.g. Fraternali & Binney 2008). All these differences may affect the properties of the gas, including its extent, ability to form stars, and kinematics.

To investigate these issues, it is vital to have spatially-resolved data on the distribution and kinematics of the molecular gas. Until recently, only a small number of ETGs had been mapped with mm-interferometers (e.g. Wrobel & Kenney, 1992; Young, 2002; Young, Bureau & Cappellari, 2008; Schinnerer & Scoville, 2002; Crocker et al., 2008, 2009; Wei et al., 2010; Crocker et al., 2011), hence drawing conclusions based on a few objects had been difficult. In this chapter, I attempt to understand the similarities and differences between the extent and distribution of the molecular gas in spirals and ETGs. For this I will use the ATLAS^{3D} ETG sample discussed in Chapter 2. I also follow on from the work presented in the previous Chapter by evaluating the use of molecular gas as a circular velocity tracer in ETGs, in a spatially-resolved manner.

In Section 2 I present a study of the extent of the molecular gas in the sample ETGs, and compare this to the extent of the gas in spirals. In Section 3 I compare the surface brightness profiles of the molecular gas in ETGs, and how they vary with gas origin and environment. In Section 4 I evaluate the use of CO as a tracer of the circular velocity in ETGs, and how the observed CO rotation compares with circular velocity predictions from mass models, and the observed stellar and ionised gas rotation. I discuss these results in Section 5, before concluding in Section 6.

4.2 MOLECULAR GAS EXTENT

In this section I attempt to understand if the radial extent of the molecular gas in ETGs is different from that in spirals. One can imagine mechanisms that would make the gas in ETGs more compact than the gas in spirals. External gas, for instance, will usually fall into the galaxy centre, and create inner discs and rings (Eliche-Moral et al., 2010). Furthermore, the interaction of kinematically-misaligned gas with stellar mass loss from stars could cause the gas to loose angular momentum and become more compact. To look for signatures of these processes, I measured the extent of the gas in my sample of 41 CO-mapped ATLAS^{3D} ETGs presented in Chapter 2, and a comparison sample of 44 spirals from the Berkeley Illinois Maryland Array Survey of Nearby Galaxies (BIMA-SONG; Helfer et al., 2003).

4.2.1 *Redshifting BIMA-SONG*

BIMA-SONG mapped CO(1-0) molecular emission within the centers and discs of 44 nearby spiral galaxies, with a typical spatial resolution of 6″ (360 pc at 12 Mpc, the average distance of the sample galaxies; Helfer et al. 2003). Unfortunately, the ATLAS^{3D} sample galaxies are on average twice as distant (24.5 Mpc), making comparisons difficult. To overcome this problems I artificially 'redshifted' the BIMA-SONG galaxies to the average distance of the ATLAS^{3D} galaxies, using the procedure outlined below.

Firstly, I obtained the clean cubes from the BIMA-SONG archive. The angular size of the beam when observing a distant galaxy appears larger relative to the galaxy size, so each BIMA-SONG cube was convolved with a Gaussian to create the correct relative beam size. The size of the major and minor axes of the convolving gaussian required in order to reach the correct final beam were calculated by assuming that the beams add in quadrature:

$$B^{*}_{\mathrm{min,maj}} = B^{\mathrm{old}}_{\mathrm{min,maj}} \sqrt{\left(\frac{d}{24.5\,\mathrm{Mpc}}\right)^{-2} - 1}, \tag{4.1}$$

where $B^{\mathrm{old}}_{\mathrm{min,maj}}$ is the original beam size, $B^{*}_{\mathrm{min,maj}}$ the convolving beam size, d is the distance to the BIMA-SONG galaxy and 24.5 Mpc is the average distance to the ATLAS-3D galaxies.

Secondly the clean BIMA-SONG cube was scaled to the flux expected at the larger distance, calculated as follows:

$$F^{'} = F\left(\frac{d}{24.5\,\mathrm{Mpc}}\right)^{2}, \tag{4.2}$$

where $F^{'}$ is the new flux and F is the original flux.

Thirdly, a noise cube was created with the Miriad task IMGEN. It was then scaled to the correct level, so that when added to the BIMA-SONG clean cube the resultant cube has the same RMS as a typical CARMA observation of the ATLAS^{3D} galaxies (23 mJy in a 10 km s^{-1} chan). If the BIMA-SONG cube already has an RMS greater than

this level, no additional noise was added. This only applies in some cases, however, and I do not expect this to bias my results.

The required scale (S) for the noise cube was calculated as follows:

$$S = 23\,\mathrm{mJy}\sqrt{1 - \left(\frac{\sigma_{\mathrm{RMS}}}{23\,\mathrm{mJy}}\right)^2 \left(\frac{d}{24.5\,\mathrm{Mpc}}\right)^4}, \tag{4.3}$$

where σ_{RMS} is the original clean cube RMS.

Finally, a moment zero map of the "redshifted" cube was created, clipped at 2σ, and the pixel size was set so the map is Nyquist sampled (3 pixels across the geometric mean of the beam size).

4.2.2 *Measuring gas extents*

The molecular gas extent of each galaxy was estimated from its ATLAS^{3D} or redshifted BIMA-SONG moment zero map. The diameter was measured in the direction of the largest molecular gas extent, a level of approximately twice the RMS noise ($\approx$ 0.046 Jy per 10 km s^{-1} channel on average across the sample), and the position angle along which the diameter was taken was also recorded. This procedure is similar to that followed by Chapman et al. (2004) when measuring CO sizes in sub-millimeter galaxies. The use of a scale radius obtained from a parametric fit to the CO surface density profile would be preferable, but the limited CO spatial extent (compared to the beam) in many objects, and the absence of an obvious suitable parametric form make this impractical at this point.

The beam size of interferometric observations smears the edges of molecular gas distributions, making them appear larger than they truly are. As a first-order attempt to remove this beam smearing, the beam size in the direction of maximum extent was quadratically subtracted from the measured diameter, to give a *'de-convolved'* diameter ($d^{'}$) as follows:

$$d^{'} = \sqrt{d^2 - (2r_{\rm beam})^2}, \tag{4.4}$$

where

$$r_{\rm beam} = \frac{b_{\rm max} b_{\rm min}}{\sqrt{(b_{\rm min}\cos\theta_b)^2 + (b_{\rm max}\sin\theta_b)^2}},$$

and

$$\theta_b = \phi_{\rm GPA} - \theta_{\rm BPA}$$

here d is the measured CO diameter, $b_{\rm max}$ is the beam semi-major axis, $b_{\rm min}$ is the beam semi-minor axis, $\theta_{\rm BPA}$ is the beam position angle in degrees, $\phi_{\rm GPA}$ is the measured position angle along the maximal CO extent in degrees, $r_{\rm beam}$ is the radius of the beam at angle $\phi_{\rm GPA}$, and θ_b is the measured angle from the beam axis, to the molecular gas position angle.

Figure 4.1 shows three examples of the redshifting and CO extent measurement process. In some cases, such as NGC7331 shown in the top panel, the structure and extent of the molecular gas in the original map is preserved. In other cases, like IC342 shown in the middle panels of Figure 4.1, the extent of the molecular gas is similar in the redshifted map, but the structure observed originally has disappeared. Finally, in some cases the spiral galaxies from BIMA-SONG would not be detected at all at the ATLAS^{3D} distance and resolution. Such an example is NGC0628, shown in the bottom panels of Figure 4.1. In total, 25 of the 44 BIMA-SONG late-type galaxies had measurable CO extents after redshifting.

I include 40/41 ETGs here. One ETG, NGC 2685 was removed from this analysis, as it has multiple components making measurement of the extent difficult. The field of view of the ATLAS^{3D} observations is often smaller than that achieved by BIMA-SONG. However, I do not expect this to bias my results, as very few of the ETGs have gas extended enough to reach the edge of the field of view.

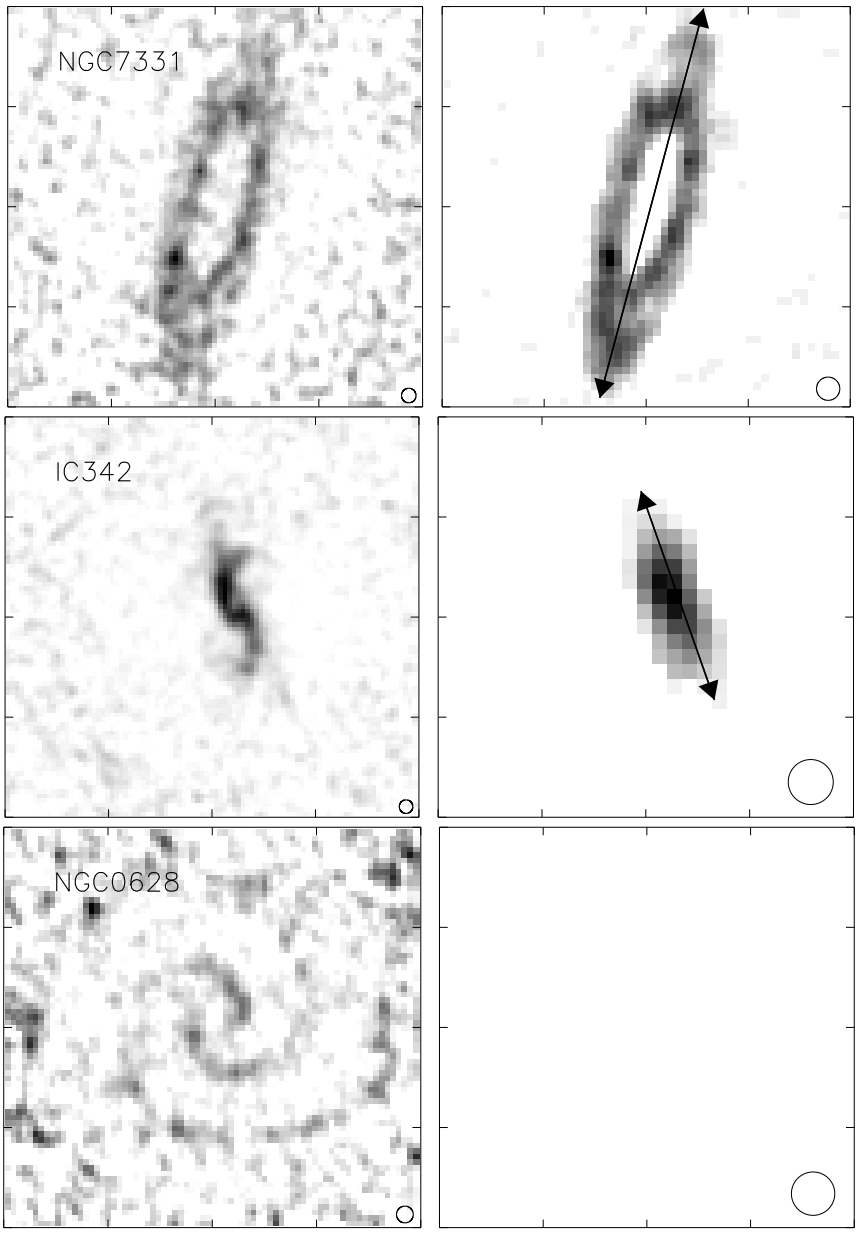

Figure 4.1: Three example CO(1-0) moment zero maps from the BIMA-SONG survey, presented as observed in the left column, and redshifted using the procedure outlined in Section 4.2.1 in the right column. The images in the left column are 85″ square. The angular scale on the right hand images varies dependant on the distance to the object. The difference in beam size (displayed as a black oval in the lower left of each plot) gives an indication of the relative distance, and the new angular scale. The arrow in the upper and middle panels on the right indicate the measurement of maximum extent.

4.2.3 *Comparing spirals and ETGs*

The distribution of absolute molecular gas extents in the redshifted BIMA-SONG and ATLAS^{3D} galaxies are plotted in Figure 4.2. The average BIMA-SONG galaxy CO radial extent is 2.1 kpc, while that for ATLAS^{3D} galaxies is 1.1 kpc. A Mann–Whitney U (MW-U) test gives only a 1.4% chance that they are drawn from the same parent distribution. It is thus clear that molecular gas is much more extended in late-type galaxies than in ETGs. I prefer the Mann–Whitney U test to a Kolmogorov-Smirnov (KS) test here, as it is less sensitive to differences in the shapes of the distributions in the two samples, which are uncertain due to the low number of mapped objects. In all cases below, however, using a KS test would give similar results.

It is also possible to estimate how much more extended the ATLAS^{3D} galaxies would have to be, on average, for the distributions to be consistent. I do this by finding a multiplicative scaling factor that maximizes the statistical similarity between the distributions (as calculated from a MW-U test). Performing this analysis, I find a scaling factor of 1.73.

The top panel of Figure 4.3 shows the molecular gas extent normalized by the effective radius (R_e) of each galaxy. This is the standard scalelength for ellipticals, and represents the radius at which half the light is contained, assuming circular symmetry. The R_e values used here come from Paper I for ATLAS^{3D} galaxies, and for BIMA-SONG I use a combination of the RC3 (de Vaucouleurs et al., 1991) and 2MASS (Jarrett et al., 2000) R_e measurements, combined in the same way as for the ATLAS^{3D} sample (see Paper I for the full justification):

$$R_e = 0.5\,(R_{e,RC3} + 1.7\tilde{R}_{e,2MASS}), \tag{4.5}$$

where $R_{e,RC3}$ is the RC3 value at B-band, and $\tilde{R}_{e,2MASS}$ is the median of the J,H and K_s-band values in the 2MASS catalogue.

The average BIMA-SONG galaxy normalized radial extent is 0.58, while the ATLAS^{3D} galaxy normalized mean is 0.53, suggesting that on average the molecular gas in early- and late-type galaxies covers a similar fraction of the effective radius. A

MW-U test gives a 41% chance that they are drawn from the same parent distribution. A similar analysis to that conducted above suggests that the distributions are close to maximum similarity, with a scaling factor of only 1.04.

In an attempt to verify if the reduction in the average extent difference is down to the normalization radius adopted, I next attempted to normalize the CO diameter by R_{25}, the radius of the 25 mag arcsecond^{-2} isophote in B-band. I use the average R_{25} value from LEDA (Paturel et al., 1991) for each galaxy. The results are shown in the middle panel of Figure 4.3. The average BIMA-SONG galaxy normalized radial extent is 0.22, and the ATLAS^{3D} normalized mean is 0.17. On average, once again, the molecular gas in these systems thus covers a reasonably similar fraction of the 25 mag arcsecond^{-2} isophote. A MW-U test gives a 14% chance that they are drawn from the same parent distribution, and a scaling factor of 1.31 is required to maximise this probability.

The result that the molecular gas distributions cover similar fractions of the scale radii suggests that the molecular gas in larger galaxies is more extended, and that there is little dependence on Hubble type. If this is true, one would expect a similar trend when normalizing by the K_s-band luminosity (bottom panel of Figure 4.3). The L_{K_s} values used for BIMA-SONG galaxies are the average value from the LEDA catalogue (Paturel et al., 1991), and for ATLAS^{3D} galaxies I use the value tabulated in Paper I. These absolute magnitudes are converted into a luminosity assuming that the absolute magnitude of the sun at K_s-band is 3.28 mag (Binney & Merrifield, 1998). The average BIMA-SONG galaxy normalized radial extent is $10^{-10.5}$ kpc $L_{\odot}^{-1}$, while the ATLAS^{3D} galaxies normalized mean is $10^{-10.6}$ kpc $L_{\odot}^{-1}$. A MW-U test gives a 48% chance they are drawn from the same parent distribution, and this distribution is very close to maximal similarity (scaling factor of 0.9985).

The significance of this similarity between the extent of the gas in ETGs and spirals in the context of their evolution will be discussed further in Section 4.5.1.1.

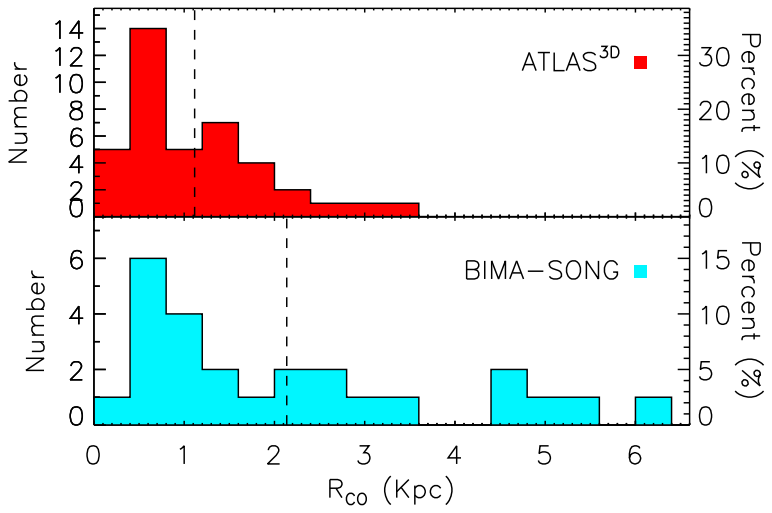

Figure 4.2: Histogram showing the absolute molecular gas extent of the BIMA-SONG (blue) and ATLAS^{3D} (red) sample galaxies. The ATLAS^{3D} histogram contains 40 galaxies, and the BIMA-SONG histogram 25. The dashed lines show the mean extent of the galaxies in that histogram.

4.2.4 *Effect of environment and gas origin*

We can also break down the ATLAS^{3D} sample, in various ways to investigate trends in the molecular gas extent with other parameters. The top panel of Figure 4.4 shows the extent of the molecular gas in the ATLAS^{3D} galaxies normalised by the effective radius, split into those galaxies where the kinematic misalignment between the molecular gas and the stars is greater than 30 degrees (see Chapter 5), and those with kinematically-aligned molecular gas. The aligned galaxies have an average extent of $0.50R_e$ and the misaligned galaxies 0.58 R_e. A MW-U test gives a 26% chance that the kinematically-aligned and misaligned galaxies are drawn from the same parent population (a scaling factor of 1.23 maximizes this probability).

The bottom panel of Figure 4.4 shows a comparison of the extent of the molecular gas, normalised by the effective radius, in the Virgo cluster and field ETGs. The Virgo cluster galaxies have molecular gas distributions that extend on average to 0.39 R_e, while field galaxies have more extended molecular gas distributions, reaching out to 0.60 R_e. A MW-U test gives only a 3% probability that the Virgo and field ETGs are drawn from the same parent distribution, and a scale factor of 1.87 is required

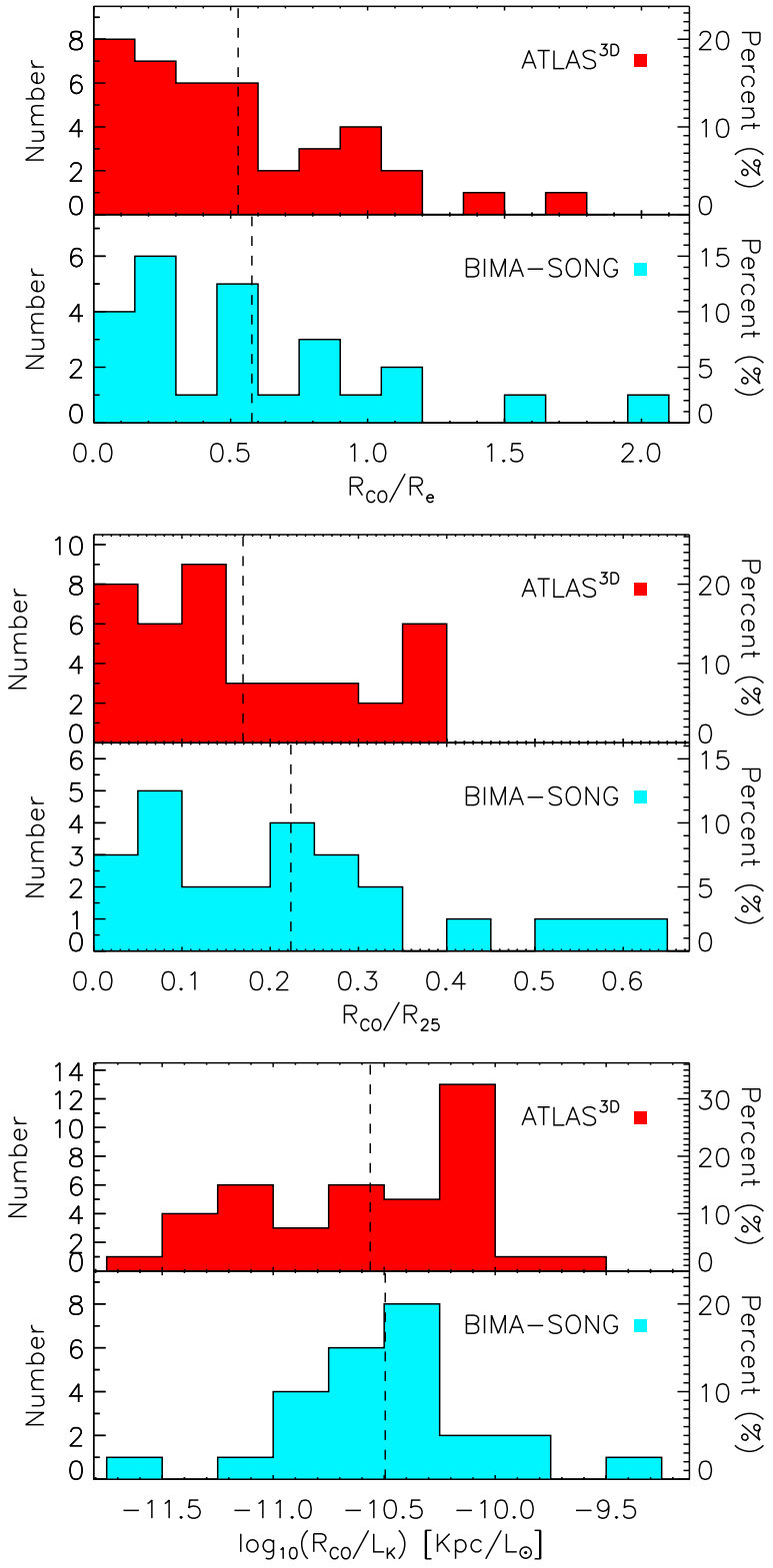

Figure 4.3: As Figure 4.2 but showing the relative molecular gas extent of the BIMA-SONG and ATLAS^{3D} sample galaxies. This has been normalized by the scaled mean of the effective radius of the galaxy at B, H, J and K_s band in the top panel, by the radius to the 25 mag arcsecond^{-2} isophote in B-band in the middle panel, and by the galaxies K_s-band luminosity in the bottom panel. The dashed lines show the mean normalized extent of the galaxies in that histogram.

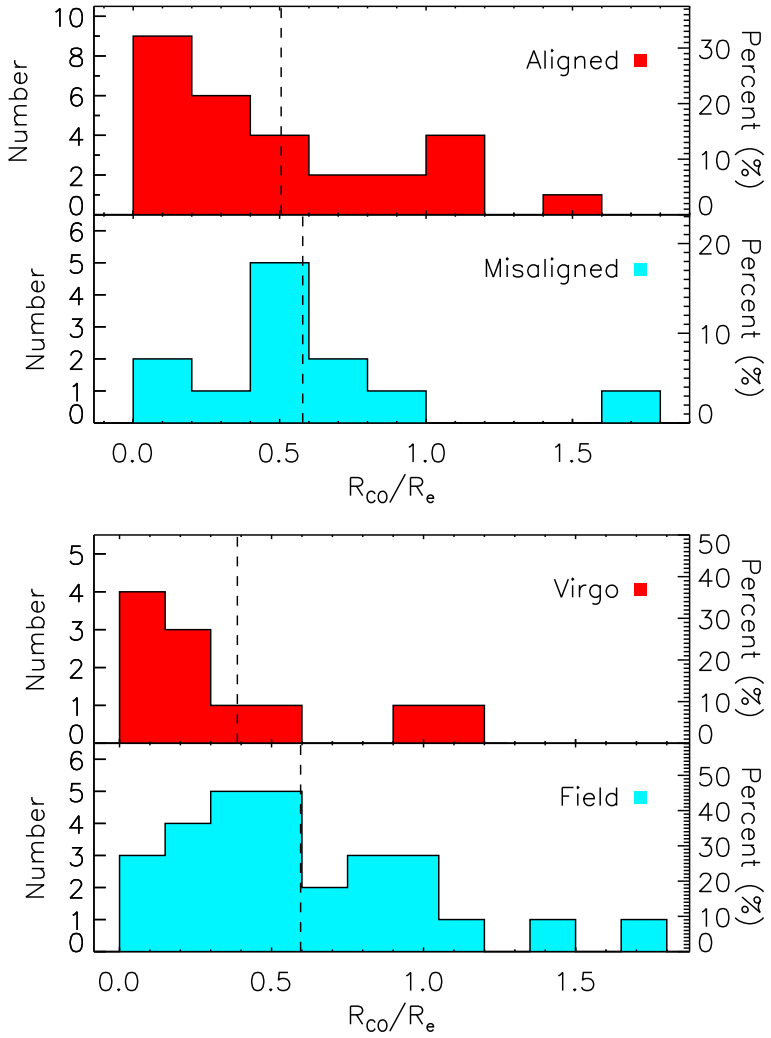

Figure 4.4: The relative molecular gas extent of ATLAS^{3D} sample galaxies, normalized by the galaxies effective radius. In the top panel the ATLAS^{3D} galaxies are split into those with kinematically-aligned molecular gas (top), and misaligned (bottom) with respect to the stars. Kinematic misalignments are taken from Chapter 5. In the bottom panel the ATLAS^{3D} systems are split into Virgo cluster members (top) and field galaxies (bottom). Virgo cluster membership is taken from Paper I.

to maximize this probability.We discuss possible reasons for this environmental difference in Section 4.2.4.

Table 4.1: Parameters used in calculating the maximal extent of the molecular gas in the ATLAS^{3D} early-type sample galaxies.

Galaxy	R_{25} (kpc)	D_{CO} ($''$)	θ_{GPA} (deg)	θ_{BPA} (deg)	B_{maj} ($''$)	B_{maj} ($''$)	R_{CO} (kpc)	$\frac{R_{CO}}{R_e}$	$\frac{R_{CO}}{R_{25}}$	$\log\left(\frac{R_{CO}}{L_{Ks}}\right)$ (kpc/$L_\odot$)	Ref.
(1)	(2)	(3)	(4)	(5)	(6)	(7)	(8)	(9)	(10)	(11)	(12)
IC0676	8.81	22.0	164	0	4.3	4.0	1.22	0.46	0.14	-10.13	1
IC0719	5.39	26.8	50	87	4.0	3.2	1.85	0.48	0.34	-10.13	1
IC1024	3.27	25.0	23	47	4.2	3.6	1.21	1.08	0.37	-9.84	1
NGC0524	9.36	19.4	47	50	2.8	2.6	1.05	0.21	0.11	-11.17	5
NGC1222	5.18	25.0	72	18	5.4	2.3	1.90	1.00	0.37	-10.09	1
NGC1266	5.92	8.9	145	71	4.8	3.2	0.62	0.22	0.10	-10.65	1
NGC2697	8.07	30.0	58	336	5.4	4.6	2.02	0.64	0.25	-10.08	1
NGC2764	8.94	36.5	21	52	4.5	3.7	3.42	1.45	0.38	-10.05	1
NGC2768	23.72	13.0	20	66	2.6	2.3	0.64	0.10	0.03	-11.38	3
NGC2824	4.61	16.0	142	286	3.8	3.4	1.36	1.03	0.29	-10.31	1
NGC3032	4.40	14.0	315	335	6.1	5.0	0.50	0.54	0.11	-10.41	2
NGC3182	9.52	16.5	120	80	5.1	4.1	1.16	0.34	0.12	-10.52	1
NGC3489	6.05	20.0	44	30	3.1	2.9	0.54	0.43	0.09	-10.77	5
NGC3607	14.84	30.0	122	359	5.6	5.0	1.49	0.36	0.10	-11.03	1
NGC3619	10.47	11.1	85	56	4.4	3.9	0.46	0.13	0.04	-11.08	1

Notes: Column 1 lists the names of the galaxies in the ATLAS^{3D} sample considered here. Column 2 lists the radius of the 25 mag arcsec^{-2} isophote at *B*-band, extracted from HyperLEDA and converted into kpc using the distance to the galaxy as tabulated in Paper I. Column 3 contains the maximum CO angular diameter, calculated as described in Section 4.2.2. Columns 4 to 7 contain the galaxy position angle, the beam position angle and the beam major and minor axes, respectively. Column 8 contains the maximum CO extent, beam corrected and converted to a linear size using the distance to the galaxy. Column 9 is the ratio of the CO extent to the effective radius of the galaxy (tabulated in Paper I). Column 10 lists the ratio with respect to R_{25}. Column 11 lists the ratio to the K_s-band luminosity of the galaxy, calculated from the magnitudes listed in Paper I, and converted into a luminosity assuming that the absolute magnitude of the Sun at K_s-band is 3.28 mag (Binney & Merrifield, 1998). Column 12 lists the data reference for the CO interferometry: (1) Alatalo et al. in prep., (2) Young, Bureau & Cappellari (2008), (3) Crocker et al. (2008), (4) Crocker et al. (2009), (5) Crocker et al. (2011).

Table 4.1: continued

Galaxy	R_{25}	D_{CO}	θ_{GPA}	θ_{BPA}	B_{maj}	B_{maj}	R_{CO}	$\frac{R_{CO}}{R_e}$	$\frac{R_{CO}}{R_{25}}$	$\log\left(\frac{R_{CO}}{L_{Ks}}\right)$	Ref.
	(kpc)	($''$)	(deg)	(deg)	($''$)	($''$)	(kpc)			(kpc/$L_\odot$)	
(1)	(2)	(3)	(4)	(5)	(6)	(7)	(8)	(9)	(10)	(11)	(12)
NGC3626	7.65	27.0	148	55	4.1	3.6	1.22	0.50	0.16	-10.55	1
NGC3665	11.85	21.0	65	59	4.2	3.6	1.58	0.32	0.13	-11.08	1
NGC4119	4.90	17.6	107	49	4.7	3.1	0.63	0.20	0.13	-10.55	1
NGC4150	3.98	30.0	161	349	8.5	5.1	0.91	0.78	0.23	-10.01	2
NGC4292	3.72	9.2	44	61	3.3	2.4	0.31	0.15	0.08	-10.44	1
NGC4324	6.63	48.0	48	35	4.6	3.6	1.90	1.19	0.29	-10.08	1
NGC4429	13.53	14.0	90	58	4.4	3.5	0.48	0.14	0.04	-11.36	1
NGC4435	6.71	10.5	23	27	5.3	3.9	0.28	0.11	0.04	-11.39	1
NGC4459	9.59	20.0	113	351	9.0	5.5	0.51	0.19	0.05	-11.16	2
NGC4476	4.41	21.6	24	358	8.3	5.7	0.78	0.60	0.18	-10.13	1
NGC4477	9.15	7.4	47	24	3.3	2.6	0.21	0.07	0.02	-11.50	5
NGC4526	17.52	14.0	111	10	4.3	3.1	0.44	0.13	0.03	-11.51	2
NGC4550	7.48	8.0	1	40	4.7	4.0	0.30	0.26	0.04	-10.74	4
NGC4694	7.61	26.0	97	68	3.9	2.9	1.01	0.43	0.13	-10.17	1
NGC4710	6.25	60.0	30	43	4.3	3.7	2.41	0.96	0.39	-10.34	1
NGC4753	19.13	29.9	92	1	5.5	4.1	1.59	0.29	0.08	-11.15	1
NGC5379	9.57	41.3	57	276	4.9	3.4	2.95	0.97	0.31	-9.67	1
NGC5866	10.16	63.0	144	278	3.8	3.5	2.26	0.86	0.22	-10.56	1
NGC6014	9.18	9.7	128	59	4.1	3.5	0.46	0.12	0.05	-10.83	1
NGC7465	4.36	25.6	71	291	4.7	3.2	1.67	1.75	0.38	-10.17	1
PGC029321	4.26	11.3	125	283	3.8	3.7	0.84	0.55	0.20	-10.05	1
PGC058114	2.07	16.1	91	24	4.4	3.9	0.77	0.72	0.37	-10.05	1
UGC05408	6.80	5.9	120	83	4.4	3.5	0.66	0.43	0.10	-10.31	1
UGC06176	7.88	8.0	36	80	4.0	3.3	0.32	0.16	0.04	-10.87	1
UGC09519	3.10	12.9	145	76	3.6	2.9	0.69	0.77	0.22	-10.21	1

Continued from previous page

Table 4.2: Parameters used in calculating the extent of the molecular gas in the BIMA-SONG late-type galaxies.

Galaxy	Dist.	M_{K_s}	R_e	R_{25}	D_{CO}	θ_{GPA}	θ_{BPA}	B^*_{maj}	B^*_{maj}	R_{CO}	$\frac{R_{CO}}{R_e}$	$\frac{R_{CO}}{R_{25}}$	$\log\left(\frac{R_{CO}}{L_{Ks}}\right)$
	(Mpc)	(mag)	(kpc)	(kpc)	($''$)	(deg)	(deg)	($''$)	($''$)	(kpc)			(kpc/$L_\odot$)
(1)	(2)	(3)	(4)	(5)	(6)	(7)	(8)	(9)	(10)	(11)	(12)	(13)	(14)
IC342	3.9	-23.40	9.80	9.14	11.1	10	33	18.9	17.2	0.57	0.06	0.06	-10.91
NGC2903	6.3	-22.96	3.11	7.11	33.4	30	21	36.5	34.1	1.69	0.54	0.24	-10.27
NGC3184	3.6	-20.57	2.32	3.74	20.7	10	11	16.7	15.2	1.20	0.52	0.32	-9.46
NGC3351	10.1	-23.36	3.68	7.89	14.4	5	6	17.9	12.6	0.60	0.16	0.08	-10.88
NGC3368	10.1	-23.70	3.03	9.93	8.2	40	4	16.9	12.5	0.49	0.16	0.05	-11.10
NGC3521	7.2	-23.50	2.61	5.75	50.0	340	0	30.0	19.3	2.88	1.11	0.50	-10.25
NGC3627	11.1	-24.35	5.01	11.17	77.0	10	80	16.0	12.7	4.50	0.90	0.40	-10.40
NGC3726	11.1	-22.40	5.39	9.25	15.9	10	10	8.7	7.3	0.86	0.16	0.09	-10.34
NGC3938	17.0	-23.34	6.13	10.79	104.1	90	327	8.4	7.7	6.14	1.00	0.57	-9.86
NGC4051	17.0	-23.48	7.65	12.68	20.8	0	358	10.1	7.1	1.09	0.14	0.09	-10.67
NGC4258	8.1	-24.08	6.09	17.03	26.4	340	4	18.5	16.2	1.43	0.23	0.08	-10.79
NGC4303	8.1	-22.70	3.28	7.22	36.4	20	356	11.8	8.8	2.13	0.65	0.29	-10.06
NGC4321	16.1	-24.45	9.81	15.83	46.0	350	9	10.9	7.5	2.66	0.27	0.17	-10.66

Notes: Column 1 lists the names of the galaxies in the BIMA-SONG survey that had measurable extents after undergoing the redshifting procedure outlined in Section 4.2.1. Column 2 contains the distance to the galaxy. Column 3 is the absolute magnitude of the galaxy at K_s-band, extracted from HyperLEDA. Columns 4 and 5 list the effective radius and the radius of the 25 mag arcsec^{-2} isophote at B-band, extracted from HyperLEDA and converted to kpc using the (real) distance to the galaxy. Column 6 contains the maximum CO angular diameter (at the new redshifted distance), calculated as described in Section 4.2.2. Columns 7 to 10 contain the galaxy position angle, the beam position angle and transformed beam major and minor axes, respectively. Column 11 contains the maximum CO extent, beam corrected, and converted to a linear size using the new distance to the galaxy. Column 12 is the ratio of the CO extent to the effective radius of the galaxy (tabulated in Paper I). Column 13 lists the ratio of the CO extent with respect to R_{25}. Column 14 contains the ratio of the CO extent with respect to the K_s-band luminosity of the galaxy, calculated from the absolute magnitudes, which have been converted into a luminosity assuming that the absolute magnitude of the sun at K_s-band is 3.28 mag (Binney & Merrifield, 1998).

Table 4.2: continued

Galaxy	Dist.	M_{K_s}	R_e	R_{25}	D_{CO}	θ_{GPA}	θ_{BPA}	B^*_{maj}	B^*_{maj}	R_{CO}	$\frac{R_{CO}}{R_e}$	$\frac{R_{CO}}{R_{25}}$	$\log\left(\frac{R_{CO}}{L_{Ks}}\right)$
	(Mpc)	(mag)	(kpc)	(kpc)	($''$)	(deg)	(deg)	($''$)	($''$)	(kpc)			(kpc/$L_\odot$)
(1)	(2)	(3)	(4)	(5)	(6)	(7)	(8)	(9)	(10)	(11)	(12)	(13)	(14)
NGC4321	16.1	-24.45	9.81	15.83	46.0	350	9	10.9	7.5	2.66	0.27	0.17	-10.66
NGC4414	19.1	-24.46	2.53	8.20	89.7	340	6	8.2	6.4	5.29	2.09	0.64	-10.37
NGC4535	7.8	-22.08	4.26	7.67	6.4	0	2	11.2	8.7	0.19	0.04	0.02	-10.87
NGC4569	9.7	-23.35	5.33	12.46	45.5	15	358	9.7	8.0	2.68	0.50	0.21	-10.23
NGC4579	16.8	-24.64	5.83	13.18	6.9	90	348	11.8	10.4	0.41	0.07	0.03	-11.56
NGC4736	4.3	-23.06	1.02	4.43	16.7	90	62	39.3	28.6	0.77	0.75	0.17	-10.65
NGC4826	4.1	-22.73	1.94	4.52	10.0	120	2	44.6	31.2	0.60	0.31	0.13	-10.63
NGC5005	4.1	-21.62	0.70	3.10	18.4	80	22	7.1	6.9	1.08	1.55	0.35	-9.93
NGC5033	21.3	-24.69	5.61	21.88	78.2	110	85	8.0	7.1	4.59	0.82	0.21	-10.52
NGC5055	7.2	-23.68	4.22	10.72	38.2	110	17	19.9	18.6	2.16	0.51	0.20	-10.45
NGC5194	8.4	-24.13	5.89	12.79	58.3	10	3	18.5	16.2	3.40	0.58	0.27	-10.43
NGC6946	5.5	-23.33	5.51	8.38	18.0	10	14	26.6	22.0	0.89	0.16	0.11	-10.70
NGC7331	12.5	-24.46	4.46	17.81	86.9	340	5	9.8	8.0	5.14	1.15	0.29	-10.39

Continued from previous page

4.3 GAS SURFACE BRIGHTNESS PROFILES

Various authors (e.g. Young & Scoville, 1982; Regan et al., 2001; Leroy et al., 2009) have studied the correspondence between the radial profile of the molecular gas and that of the stars in spiral galaxies. On small scales ($\sim$100 pc), the clumpy nature of the ISM causes the molecular gas to deviate from a simple exponential profile, but at larger scales (such as those probed by our CARMA observations; $4\farcs5$ at 24.5 Mpc corresponds to $\approx$ 500pc) the molecular gas is found to have a reasonably similar profile to that of the stellar surface density, and has a similar scale-length. Although molecular rings are common in spiral galaxies, they seldom exist in isolation, and thus the over-all surface-brightness profile is still often comparable to the stellar surface brightness. As the overall distribution of extents is similar in spirals and ETGs, one might expect a similar result, with the molecular gas density profiles following those of the stars. However, the observed molecular gas structures in the galaxies vary widely, and include central discs, rings, bars, spirals and disturbed gas. These could therefore have very different surface brightness profiles than the relaxed discs often seen in spiral galaxies.

In order to investigate this issue, I extracted azimuthally averaged radial surface brightness profiles from the CO integrated intensity maps (clipped at 3σ) of all the sample galaxies. I used the CO kinematic position angle (from Chapter 5) and the 'best' inclination for the molecular gas (Chapter 3) to estimate the average CO brightness in concentric elliptical annuli of one beam width (centred at the optical nucleus of the galaxy as tabulated in Paper I). For the galaxies close to edge on (inclination $>80^\circ$), as I do not resolve the molecular gas discs thickness I estimate the surface brightness in rectangular regions one beam width along the major axis of the disc. These CO surface brightness profiles were then compared with the *r*-band stellar luminosity surface density profile, extracted from the MGE model of each galaxy (Scott et al., in prep) as described in Emsellem, Monnet & Bacon (1994) and Cappellari (2002). I used the MGE values rather than those extracted directly from the *r*-band images, as the MGE models have been carefully fitted to remove the effects of foreground stars

and other observational effects. MGE models were not available for NGC 4292 and PGC058114 (due to a lack of suitable *r*-band images), so in these two cases I used the method described above directly on K_s-band images. Using K_s-band images for all sources would not affect my results.

In Figure 4.5, I show four examples of profiles chosen to be representative of the types of radial molecular gas surface density profiles I see. Profiles for all of the ATLAS^{3D} galaxies are shown in Appendix 4.A. Some galaxies (such as NGC 3665, shown in the top-left panel of Figure 4.5) follow the stellar luminosity surface density closely, falling off as an exponential disc with a similar scale length as the stars. I denote such systems as *discy* in this chapter. I find that unlike in spirals where they make up 80% of the population, discy systems make up only half (21/41; 51%) of the ETG sample.

Around a quarter (11/41; 27%) of the galaxies in this work have molecular gas radial profiles that fall off slower than those of the stars, and 7/11 of these appear to be truncated (the CO surface brightness does not smoothly drop to our detection limit, but ends abruptly at large radii). The galaxy (NGC 3489) shown in the upper-right panel of Figure 4.5 is an example of such a profile. I classify such systems as having *excess* emission (with or without truncation) from now on.

Approximately 12% of systems (5/41) have profiles that show a lack of emission in the central regions, with a peak further out before the profile falls off (and is sometimes truncated). I have included the Helix galaxy (NGC 2685) in this category, based on the information available in Schinnerer & Scoville (2002). The width of such features is normally about that of the synthesised beam, suggesting that they are not resolved. NGC 3626 (Figure 4.5, bottom left panel) is an example of such a profile (which I denote as *rings*).

The last major category of profiles I see are like NGC 4710 (bottom-right panel of Figure 4.5). The gas surface density falls quickly from a central peak before peaking again at larger radii. Such systems make up $\approx$5% (2/41) of galaxies in the sample. I denote these systems as *composites*, and discuss their nature (and the nature of the other classes defined above) in Section 4.5.2.

Two galaxies (NGC 1266 and UGC 05408) were not resolved at the resolution of

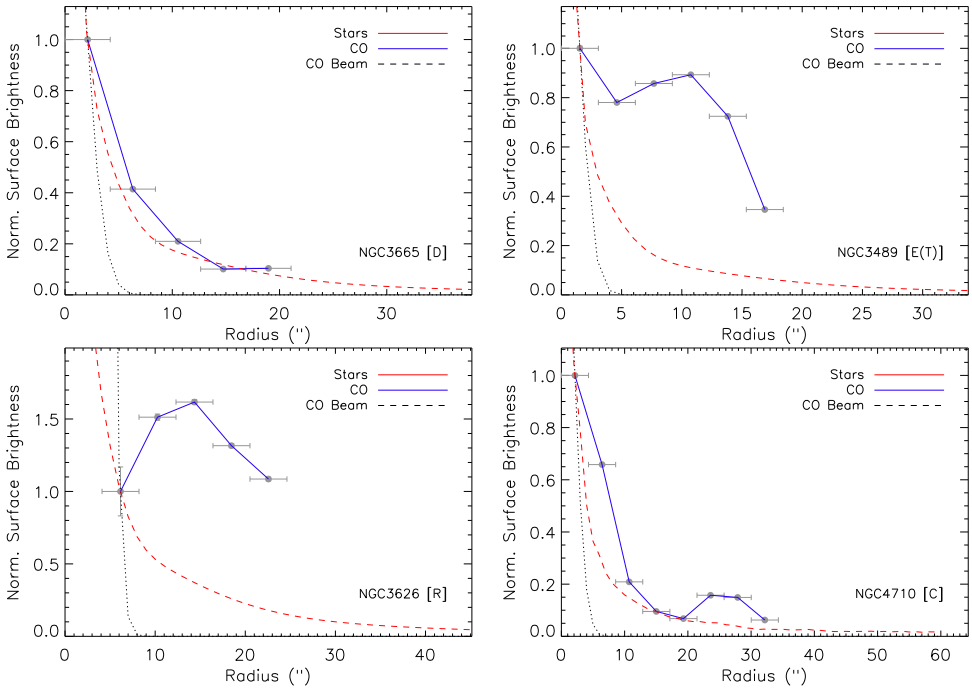

Figure 4.5: Radial surface brightness profiles of the stars (red dashed line; *r*-band) and molecular gas (blue solid line with errors) for four of the ATLAS^{3D} ETGs (normalized at the first CO datapoint). The galaxies shown are NGC 3665 (top-left; classed as a discy galaxy), NGC 3489 (top-right; classed as an excess (truncated) galaxy), NGC 3626 (bottom-left, classed as a ring) and NGC 4710 (bottom-right; classed as a composite system).The CO beamsize is shown as a black dotted gaussian. The error bars on the CO measurements denote the width of the elliptical annuli in the x-direction and the RMS noise in the elliptical annulus in the y-direction. The letter at the bottom-right corner of each plot denotes the profile class.

the D-array CARMA data (but see Alatalo et al. 2011 for a full discussion of the gas in the molecular outflow of NGC 1266). I simply denote these surface-brightness profile as *unresolved*. For a discussion of how these profile types arise see Section 4.5.2.

4.4 GAS KINEMATICS

4.4.1 Comparing CO velocities to circular velocities

In Chapter 3 I compared the CO single-dish and interferometric line-widths with JAM models of the circular velocity of each galaxy. I showed that most of the galaxies with double-peaked or boxy spectra are likely to have relaxed gas reaching beyond the peak of the rotation curve. This allowed me to use these systems to investigate the CO Tully-Fisher relation of ETGs. It is however possible to go beyond this analysis,

and for each galaxy compare the position-velocity diagram (PVD) of the mapped molecular gas with the circular velocity curve derived from the JAM models, as well as the observed stellar and ionised gas velocities (as done for four of these galaxies in Young, Bureau & Cappellari, 2008).

I extracted the CO PVDs from the data cubes along the kinematic position angle determined in Chapter 5. The width of each slice was one spatial pixel, although the PVDs are created by interpolation using a weighted average of the nearest four pixels, so they vary slightly in effective width depending on the position angle (see Gooch 1996 for full details). Two example PVDs are shown in Figure 4.6, while those for the whole of the sample are shown in Appendix 4.B. I do not include the PVDs for the two non-ATLAS^{3D} galaxies (no corresponding IFU data), NGC 2685 (kinematics discussed in Schinnerer & Scoville 2002), NGC 1266 (molecular outflow discussed in Alatalo et al. 2011), PGC058114 (insufficient photometry for a JAM model) and UGC05408 (which is unresolved at the resolution of our data).

The PVDs are overlaid with the JAM circular velocity curves in black (see Section 1.4.5 for details). If the molecular gas is counter-rotating, I also overlay a mirrored version of the circular velocity curve, to allow a direct comparison with the CO, and to investigate if they are in agreement. If the CO tightly follows the circular velocity curve, this suggests that CO is dynamically cold and relaxed, even in ETGs. Substantial disagreement would indicate that the gas is dynamically disturbed, or indicate problems with the JAM models (e.g. invalid assumption of a constant mass-to-light ratio (M/L); see Young, Bureau & Cappellari, 2008).

By inspection of the PVDs and circular velocity curves, I establish that the molecular gas reaches beyond the turnover radius in 75$\pm$6% of the ETGs. This compares well to the 71$\pm$7% of galaxies which were classified as having double-peaked or boxy single-dish spectra in Chapter 3 (and hence were assumed to reach beyond this turnover).

4.4.2 *Simulated observations*

To investigate if the observed PVDs are consistent with dynamically cold gas rotating at the predicted circular velocities, I created model observations. The models have two free parameters, controling the scaling and shape of the surface brightness profile. For the majority of galaxies, I assume that the CO is distributed in an exponential disc, with a scale length varied to match the observations. In the systems with molecular rings, I instead characterised the surface brightness profile with a Gaussian of FWHM $\approx$100 pc centred on the observed ring radius.

I assume the gas is dynamically cold, with a velocity dispersion $\sigma_{\rm gas} \approx 8$ km s^{-1}, and that it rotates at the predicted JAM circular velocity. I then project the model to the observed inclination, as derived from the JAM models (see Section 1.4.5). I impose a fixed velocity resolution (10 km s^{-1} channels) and the angular resolution of the CARMA data (Table 4.1) by binning in velocity and convolving spatially with a Gaussian beam. I then extract a PVD as described in Section 4.4.1. Two example models are shown in the right column of Figure 4.6, and models for the whole sample are shown in Appendix 4.B.

Comparing the CO PVDs to the JAM model circular velocities and modelled PVDs allows us to identify (by eye) several different classes of galaxies. In 40% (14/35) of the sample the models match well both the shape and position of the CO PVDs (these systems are marked with a "G", for good, in Figure 4.6 and Appendix 4.B). In a further 37% (13/35) of the galaxies the shape of the JAM circular velocity curve and modeled PVDs are similar to that of the observed CO PVD, but the models are systematically above the observed rotation (these systems are marked with a "O" for overestimated in the figures). In 11% (4/35) of the galaxies where the CO is disturbed (as identified in Chapter 2), the CO appears to have little coherent rotation and its kinematics are, as expected, unrelated to the JAM model predictions (these systems are marked with a "D" for disturbed in the figures). Of the remaining 11% (4/35), two galaxies (NGC 3032, NGC 2824) show signs that the assumption of a constant M/L as a function of radius is invalid, one is barely resolved in CO (PGC 029321), and one

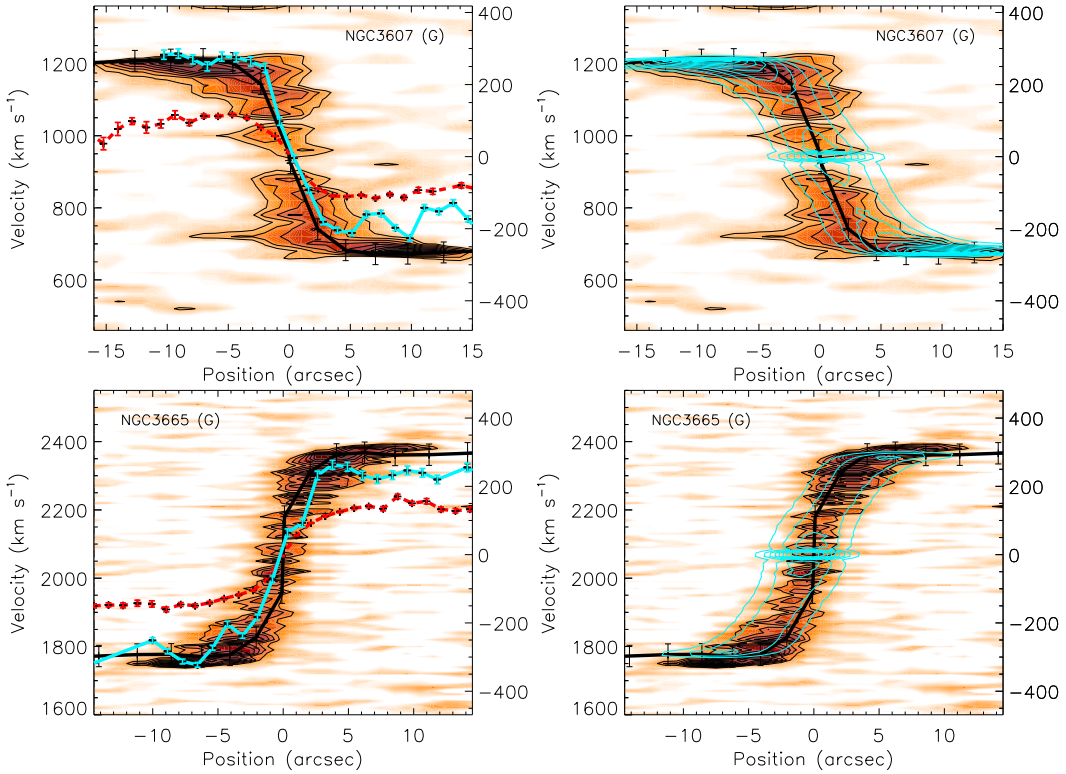

Figure 4.6: CO Position-Velocity diagrams (orange with black contours) of NGC 3607 (top) and NGC 3665 (bottom), overlaid with the JAM circular velocity curve (thick black line). On the left, these have also been overlaid with the observed stellar (red dashed line) and ionised gas (blue line) rotation curve. On the right I overlay the modeled observations of each galaxy (blue contours), created assuming that the gas is dynamically cold and rotating at the predicted circular velocity, as described in Section 4.4.2.

(NGC 0524) is so face-on that a large degeneracy exists between the model inclination and M/L (these systems are marked with a "?" in the figures).

In order to quantitatively compare the velocity of the CO at a given radius with other measures of rotation I extracted a 'trace' from the observed and model PVDs. This trace was constructed by finding the velocity of the pixel with the highest CO flux at each radius (as long as this pixel has a flux greater than three times the RMS noise in the cube). This trace will likely lie below the true circular velocity of the gas (as discussed in Section 4.5.3.1), so some offset between this measure and the other velocity tracers is expected. Given this caveat however, it is possible to use this trace as a measure of relative variations between sample members.

In Figure 4.7 I plot the average equivalent width (EW) of the Hβ emission against the average difference between the CO trace and the model trace. The average EW is

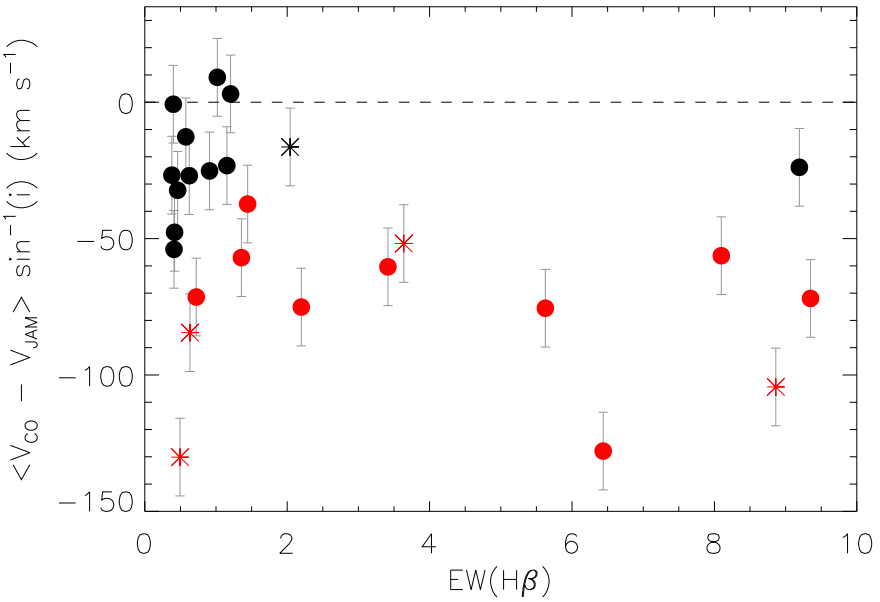

Figure 4.7: Radially averaged velocity differences between the trace of the CO and model PVD, plotted against the luminosity average equivalent width of the Hβ emission within an elliptical aperture (with the same extent, PA and axis ratio as the molecular gas). Black points denote galaxies in which the JAM model prediction of the circular velocity matches well the observed molecular gas rotation. Red points are those galaxies in which the JAM model over-predicts the CO rotation. Stars of these colours denote galaxies in which the gas kinematics are misaligned from the stellar kinematics (see Chapter 5). The dashed line indicates a velocity offset of zero.

the Hβ luminosity weighted mean of all bins within a elliptical aperture of the same extent, axis ratio and position angle (Table 4.1) as the molecular gas. Black points identify galaxies where the JAM model prediction of the circular velocity is *good*. Red points identify galaxies in which the JAM model prediction is an *overestimate* of the CO velocities. Stars of these colours denote galaxies where, in addition to the above criteria, the gas kinematics are misaligned from the stellar kinematics (see Chapter 5). The red points, where the JAM model over-predicts the CO velocity, although not selected via this diagram, have as expected larger offsets than the black points, with (de-projected) offsets $\lesssim$30 km s^{-1}. Importantly, however, almost all the galaxies with high EW(Hβ) have large offsets, and are classified as having JAM models that over-predict the true CO rotation. We discuss these findings, and why these classes arise in Section 4.5.3.1.

4.4.3 *Stellar velocities*

In the left column of Figure 4.6 and Appendix 4.B I also overplot the observed stellar rotation curves with red dashed lines. These were extracted from the SAURON IFU data, using pseudo-slits along the same PAs as those used for the CO (tabulated in Chapter 5). The observed velocity field was fitted with a surface, and the required values along the slit interpolated.

Stellar systems with large velocity dispersions rotate slower, at a given radius, than dynamically cold components like the molecular gas. The difference between the velocities is known as the asymmetric drift. One would thus expect the velocity difference between the stars and the molecular gas to be larger in higher dispersion (and thus likely more massive) galaxies. Figure 4.8 shows such a comparison, plotting the radially averaged difference between the stellar velocity profile and the CO trace against the observed stellar velocity dispersion of each galaxy (from Paper III) averaged over the slit defined above. The points in this figure are colour coded to denote the JAM model profile class. Red and black points have the same meaning as in Figure 4.7, and in addition open red squares represent disturbed galaxies and open blue squares are the remaining systems (which have known problems with the observations or models, see Section 4.4.1).

Figure 4.8 clearly shows that the difference between the molecular gas and stellar velocities increase as the velocity dispersion of the host galaxy increases, as expected. It also highlights that many of the systems which show differences between the CO rotation and the JAM prediction have a low velocity dispersion. The physics underlying this correlation is discussed more fully in Section 4.5.3.3.

4.4.4 *Ionized gas velocities*

In the left column of Figure 4.6 and Appendix 4.B, I also overplot the observed ionised gas rotation curves with a blue line. These were extracted from the SAURON IFU data, using a pseudo-slit along the same PA as used for the stars and CO (tabulated

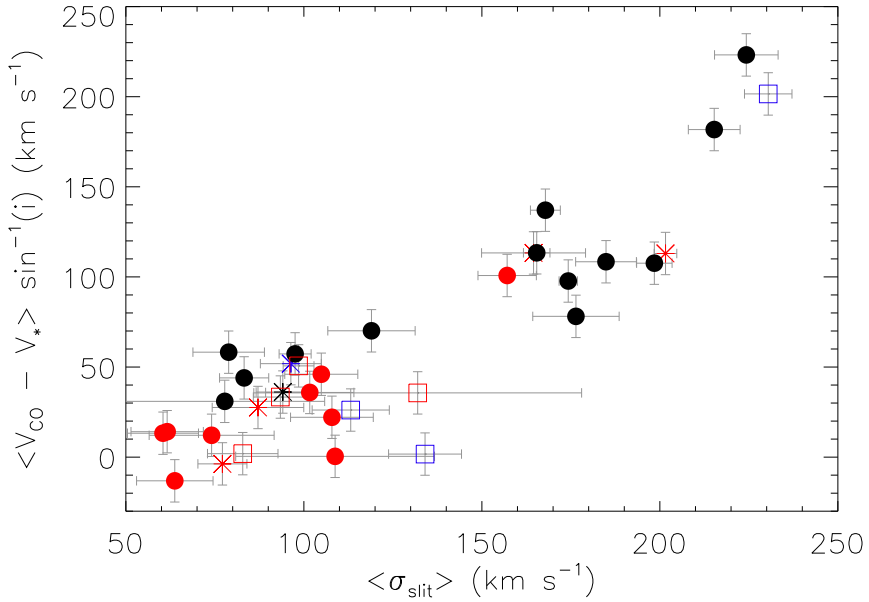

Figure 4.8: Radially averaged difference between the CO trace and the stellar velocity profile for each galaxy, plotted against the observed stellar velocity dispersion (from Paper III) averaged over a slit placed along the kinematic major axes. The points in this figure are colour coded to denote the JAM model profile class. Red and black points have the same meaning as in Figure 4.7, and in addition open red squares represent disturbed galaxies and open blue squares are the remaining systems. Stars of these colours indicate galaxies which, in addition to the above criteria, also have misaligned molecular gas. The solid line denotes zero velocity offset.

in Chapter 5). The observed velocity field was fitted with a surface, and the required values along the slit interpolated.

Ionized gas discs would normally be expected to rotate slower than the dynamically cold molecular gas, but faster than the stars. The relative velocities of the ionized gas and the CO can thus provide clues on the source and ionization mechanism of the gas emission (e.g. Young, Bureau & Cappellari, 2008).

Figure 4.9 shows the radially averaged velocity difference between the molecular and ionised gas plotted against the average EW(Hβ) (as in Figure 4.7). Galaxies with a large EW(Hβ) have ionised gas velocities close to those of the molecular gas. Systems with a low EW(Hβ) have a wide spread of velocity differences. Interestingly, these same systems have CO profiles which agree well with the JAM model prediction. These findings are discussed in more detail in Section 4.5.3.4.

Table 4.3: Surface brightness profiles and position-velocity diagram classes and model parameters for the ATLAS^{3D} ETG sample.

Galaxy	SB class	PVD class	Scale radius ($''$)	Disk/Ring
(1)	(2)	(3)	(4)	(5)
IC0676	D	O	2.0	d
IC0719	E	O	4.0	d
IC1024	E	G	2.0	d
NGC0524	D	?	2.0	d
NGC1222	E(T)	D	5.0	d
NGC1266	O	–	–	–
NGC2697	R	–	–	–
NGC2764	D	O	5.0	d
NGC2768	D	O	2.0	d
NGC2824	E(T)	?	5.0	d
NGC3032	D	?	3.0	d
NGC3182	R	O	1.5	d
NGC3489	E(T)	G	4.0	d
NGC3607	D	G	5.0	d
NGC3619	D	O	4.0	d
NGC3626	R	G	13.0	r
NGC3665	D	G	2.2	d
NGC4119	E(T)	O	3.0	r
NGC4150	D	D	1.0	d
NGC4292	D	–	–	–
NGC4324	R	G	20.0	r
NGC4429	D	G	3.0	d
NGC4435	D	G	2.0	r
NGC4459	D	G	2.3	d
NGC4476	D	G	3.5	d
NGC4477	D	G	1.0	r
NGC4526	E(T)	G	4.0	d
NGC4550	E(T)	D	1.5	d
NGC4694	E(T)	D	0.5	d

Notes: Column 1 contains the galaxy name. Column 2 lists the surface brightness profile class described in Section 4.3. "D" denotes a discy profile, "E" an excess profile, "E(T)" an excess profile with truncation, "R" a ring and "C" a composite profile. Column 3 lists the position-velocity class described in Section 4.4.2. "G" denotes a good profile, "O" an overestimated profile, "D" denotes a galaxy with disturbed gas, and "?" denotes systems with known problems. A dashes shows that the galaxy was not included in this analysis, for reasons discussed in Section 4.4.1. Column 4 shows the scale radius used to create the model PVDs described in Section 4.4.2. Column 5 shows the type of surface brightness profile used to create the model PVD: "d" denotes an exponential disc and "r" a Gaussian ring.

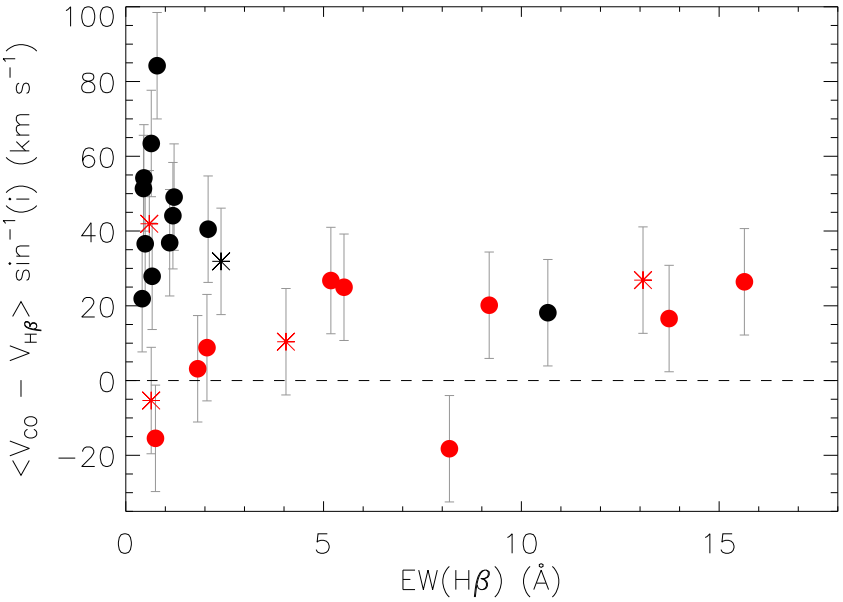

Figure 4.9: Radially averaged velocity difference between the molecular and ionised gas plotted against the luminosity weighted EW(Hβ) (as in Figure 4.7). Symbols, and their colour coding have the same meaning as in Figure 4.7. The dashed line denotes zero velocity offset

Galaxy	SB class	PVD class	Scale radius ($''$)	Disk/Ring
(1)	(2)	(3)	(4)	(5)
NGC4710	C	O	25.0	r
NGC4753	D	G	5.0	d
NGC5379	D	O	20.0	r
NGC5866	C	G	25.0	r
NGC6014	E	O	1.5	d
NGC7465	E	O	3.0	d
PGC029321	D	?	0.5	d
PGC058114	D	–	–	–
UGC05408	U	–	–	–
UGC06176	D	O	1.0	d
UGC09519	D	O	2.5	d

Table 4.3: continued

4.5 DISCUSSION

4.5.1 Molecular gas extent

4.5.1.1 ETGs and spirals

Earlier in this chapter we identified various scenarios that would result in the gas in ETGs being more compact than that in spiral galaxies. In Section 4.2.3 (Figure 4.2), I indeed found convincing evidence that the absolute extent of the molecular gas in ETGs is smaller than that in spiral galaxies. However, spiral galaxies are generally more extended (due to their discy light profiles; the average effective radius of the BIMA-SONG galaxies is 2 kpc larger than that for ATLAS^{3D} galaxies) and less luminous (by an average of 3×10^9 $L_\odot$ when comparing BIMA-SONG to ATLAS^{3D} galaxies). Figure 4.3 shows that the distribution of molecular gas extents seem to scale with the size and luminosity of the galaxy. That is, the distributions of the relative CO-extent (with respect to R_e, R_{25} and K_s-band luminosity) of ETGs and spirals are similar.

A similar correlation between the size scale of spiral discs and their large-scale CO distribution has been discussed before by several authors. Young & Scoville (1982) found that the major- and minor-axis profiles of the molecular gas in NGC 6946 and IC 342 were in good agreement with optical B-band radial profiles. Regan et al. (2001) found a similar result for a subsample of 15 BIMA-SONG spirals, for which the mean ratio of the CO to stellar scale lengths was 0.88 ± 0.14. Leroy et al. (2009) find an average CO scale-length of 0.2 ± 0.05 R_{25} for their HERACLES sample spiral galaxies. Although these parametric scale radii for the CO are not directly comparable to the (isophotal) radii used in this chapter, I do find a similar average extent $\approx$0.2 R_{25} for the ATLAS^{3D} ETGs and BIMA-SONG spirals.

Despite the large intrinsic variation in scale-length between galaxies, Regan et al. (2001) suggest that in a time-averaged sense, the stellar and molecular discs must be closely coupled. This coupling could arise from star formation associated with the molecular gas, that would over time cause the scale lengths to become equal. Alternatively, gravitational effects could exert some feedback on the molecular disc,

damping out variations and causing the molecular disc to conform more closely to the stellar potential. The fact that I find a similar relative molecular gas extent in both the ATLAS^{3D} ETGs and BIMA-SONG spirals argues that one (or both) of these processes may also be at work here. When one considers the low molecular gas mass fractions present in the ETGs (typically molecular to stellar mass ratios for our ETGs are $\approx$0.5%, as compared to $>$10% for spirals; e.g. McGaugh & de Blok 1997), gravitational processes seem more likely to be the dominant driver.

4.5.1.2 Environment and gas origin

In Section 4.2.4 I investigated the extent of the molecular gas in subsamples of the ATLAS^{3D} ETGs. I found that kinematically-misaligned galaxies (where the gas has an external origin; see Chapter 5) have a similar distribution of extents as aligned galaxies (where the gas could be from internal sources). In Chapter 5 I go on to discuss evidence that the majority of the gas in (field) ETGs could be of external origin, even when it is aligned with the stars. This would provide a natural explanation for the similarity between the two distributions. Indeed, when one restricts the sample to field galaxies only (where mergers and accretion play the largest role), the kinematically-aligned and misaligned galaxies extent distributions are still statistically indistinguishable. This is not the sole possible explanation, however, as the molecular gas (and hence likely the star formation) in spirals cover a similar proportion of the galaxy (as discussed above). Gas created from stellar mass loss (which comes predominantly from stars $<$1 Gyr old) would thus occupy a similar area in a newly transformed galaxy.

In Section 4.2.4, I also showed that the molecular gas in Virgo cluster ETGs covers only around half as much of the effective radius as the gas in an average field galaxy. This result is statistically significant at the 97% level, even given the low number of mapped galaxies in the Virgo cluster. Chapter 5 reports that all but one of these Virgo cluster galaxies have kinematically-aligned gas, and thus the molecular reservoir has either been substantially affected by the cluster environment or new gas has

been generated internally. This is despite the total molecular gas detection rate, and mass fractions being similar inside and outside of the Virgo cluster, requiring a more efficient gas regeneration mechanism. The fact that the molecular gas discs in these galaxies are more compact lends further weight to the theory that these molecular reservoirs had a different evolutionary path from those in field ETGs.

Over time it is expected that stellar mass loss from old stars and any kinematically-misaligned molecular gas would collide, reducing the velocity and angular momentum of both components and causing them to become more compact. The observation that the kinematically-aligned gas in Virgo galaxies is more compact is thus consistent with a scenario where misaligned gas is forced to align (due to the stellar potential and interaction with stellar mass loss). This process would have to be quick, however, as:

(a) very few systems in the cluster still have kinematically-misaligned gas.

(b) the molecular gas fractions observed inside and outside the cluster are similar. Assuming the galaxies entered the cluster looking like field ETGs, then star-formation would use up significant fractions of the molecular material if the timescale for the gas to relax into the equatorial plane of the galaxy were long.

If the molecular gas can be held stable against star formation (or equivalently have its star formation efficiency reduced) then this second problem may be bypassed. However the first problem remains. A quick relaxation of the molecular gas into the equatorial plane might produce observational signatures in the stellar kinematics of these galaxies, as discs of young stars misaligned from the bulk of the stellar body, but at the sensitivity of the observations no such discs are detected.

Alternatively, if the gas in Virgo galaxies were regenerated through stellar mass loss (and thus created kinematically-aligned with the stars), then this mass loss would have to come preferentially from stars at the very centre of these galaxies (perhaps because the youngest stars, which lose the most mass, are formed in a central starburst as the galaxies enter the cluster). Mass loss from the outer parts could also be swept away by ram pressure or transported inwards (e.g. by a bar).

4.5.2 *Molecular gas surface brightness profiles*

In Section 4.3 I presented the molecular gas radial surface brightness profiles of the ATLAS^{3D} ETGs, and compared them with the stellar profiles. I showed that, broadly speaking, they can be separated into four classes, discs: excess (with or without truncation), rings and composite systems. These four classes are very different, and hence it is meaningful to ask how these differences arise. For instance, ≈23% (60/260) of the ATLAS^{3D} galaxies are in the Virgo cluster, and I have shown in this chapter that they have more compact gas distributions. Do these systems show more sign of truncation (possibly by ram pressure stripping)? Or do cluster galaxies have discy molecular gas because the gas has been relaxing in the stellar potential for longer?

Molecular reservoirs with discy profiles are almost all found in galaxies where the molecular gas is co-rotating (or exactly counter-rotating) with respect to the stars (the kinematic misalignments are tabulated in Chapter 5). The exceptions are NGC 2768 and UGC 09519, where the molecular gas is in a polar disc (see e.g. Crocker et al., 2008). H I is detected in 60% of the (observed) field galaxies with discy profiles- a higher detection rate than observed in the parent population (Serra et al., in prep). This H I is often also in relaxed discs, suggesting many of these galaxies are relaxed systems even out to larger radii. This also suggests galaxies with discy profiles have not had a large merger or accretion event recently, which would disturb the molecular (and atomic) gas disc.

Just over a quarter (11/41; 27%) of the galaxies in the sample show a CO profile that does not fall off as fast as the stellar profile. These systems appear to be divided into two types, those that show truncations in their molecular gas distribution (7/11; 64%), and those that fall off regularly but with a different scale-length than that of the stars (4/11; 36%). Over half of the galaxies with truncated profiles are in the Virgo cluster (4/7), which contains only 27% (11/41) of the CO-mapped galaxies, suggesting that ram pressure stripping may have some effect on the outer edges of the molecular gas distributions (even if it does not appear to make a difference to the total molecular gas detection rate and mass fractions; see Paper IV). The other half

of truncated galaxies are either messy with signs of ongoing interaction (NGC 1222, Beck, Turner & Kloosterman 2007) or they have evidence of spiral structure in the molecular gas (NGC 2824, Alatalo et al., in prep; NGC 3489, Crocker et al. 2011).

Similarly, the galaxies which have excess profiles without a clear truncation are often messy (IC 1024, Alatalo et al., in prep; NGC 7465, Li & Seaquist 1994), counter-rotating (IC 0719, Alatalo et al., in prep) or have molecular spirals (NGC 6014, Alatalo et al., in prep). The excess galaxies (including those with and without truncation) are generally found to be low-luminosity ETGs (a Kolmogorov-Smirnov test gives a 3% chance that excess galaxies have been drawn randomly from the parent ATLAS^{3D} sample). Lower luminosity (hence presumably lower mass) galaxies have shallower potentials, are less able to retain their gas, and may require longer to force accreted molecular gas into discs with similar scalelengths as the stars. All of the excess class of galaxies in the field which were observed in H I were detected, suggesting that recent gas accretion or mergers may cause such profiles.

Galaxies with a ring may betray the presence of resonance systems, potentially caused by a bar. The molecular gas will then accumulate onto stable, non-intersecting closed orbits, as often seen in spiral discs (e.g. Combes, 1991). By inspection of the CO PVDs (Section 4.5.3), I suspect that the galaxies in the ring class generally have gas around the turnover radius (often coincident with co-rotation, i.e. inner rings; Mazzuca et al. 2011) or further out. Gas within the inner Linblad resonance (i.e. nuclear rings or spirals) is unlikely to be resolved enough to show a central dip at our surveys spatial resolution (e.g. the gas in NGC 4119 is likely to be distributed in an nuclear ring given its morphology, but this is not apparent in its surface brightness profile). In systems with no bar, it has been shown that minor mergers can also cause gas to accumulate in rings (e.g. Eliche-Moral et al., 2010).

The two systems with composite profiles are NGC 4710 and NGC 5866. These galaxies both have X-shaped PVDs, that usually arise from gas caught in the X_2 orbits and beyond co-rotation (with little gas inbetween) within barred discs (e.g. Bureau & Athanassoula, 1999; Athanassoula & Bureau, 1999). Both systems are edge on, discy fast-rotators, and NGC 4710 has a peanut-shaped bulge (typically thought of as being caused by the buckling of a bar; see Bureau & Freeman, 1999), while NGC 5866 is

thought to be unbarred with a prototypical classical bulge. If the X-shaped PVD of NGC 5866 is indeed due to material caught in barred orbits, then this interpretation would have to be revisited. It is however possible that I am seeing material in inner and outer rings, not associated with a bar, although the creation of this double-ring structure may then be difficult to explain self-consistently.

4.5.3 Velocity profiles

4.5.3.1 Circular velocities

In Figure 4.6 (and Appendix 4.B) I presented the CO PVDs of the sample galaxies, overlaid with the modelled circular velocity curve, and the stellar and ionised gas rotation curves extracted from the SAURON data. I also presented modeled PVDs, where I assumed that the JAM models correctly predict the circular velocity and inclination, and attempted to fit the observed PVDs with simple surface brightness profiles (see Section 4.4.2).

In Sections 4.4.1 and 4.4.2 I described the behaviour of the observed CO PVDs, and how they compare to the predicted JAM circular velocities. The molecular gas reaches beyond the turnover of the circular velocity curve in 75$\pm$6% of the sample ETGs, as predicted from the single-dish spectra in Chapter 5. This confirms that using the shape of the single-dish line profile is a reliable method to select galaxies with have molecular gas beyond the turnover radius.

We separated the JAM models into four rough classes based on their relation to the observed CO kinematics: those which agreed well with the observations, those in which the shape of the model was similar to the observed profile but at higher velocities, those which have disturbed gas and its kinematics are (as expected) unrelated to the model and lastly those in which I believe there are problems in the observations and/or models.

Comparison with Chapter 5 shows that in all the galaxies where the models agree well with observed CO profiles have their gas kinematics aligned with the stellar kinematics (14/16 galaxies), or exactly counter-rotating (2/16 galaxies). The CO thus

rotates in the plane in which the model predictions are valid. Over half of these systems have discy CO surface brightness distributions (Section 4.3). The JAM circular velocity curves trace the outer envelope of the CO PVD in many cases. This behaviour is reproduced by my models, and is often seen in H I PVDs. Beam smearing, non-circular motions in the gas (e.g. spiral arms), the thickness of the gas disc, and changes in the density profile of the gas all act to lower the gas (apparent) rotation velocity. In these galaxies with good models the radially averaged mean offset between the peak of the observed CO flux at each position (the PVD 'trace' introduced in Section 4.4.1) and the model PVD trace is only -0.2 km s^{-1}, with an RMS scatter of 24km s^{-1}. Thus I consider that the observed CO kinematics and the predicted circular velocity curves in these systems are consistent. The CO is thus dynamically cold and an excellent tracer of the circular velocity.

In the 31% (11/35) of CO-mapped galaxies where the shape of the JAM generated PVD is similar to that of the observed CO rotation curve but is systematically overestimated, the average offset between the CO trace and the model trace is -70$\pm$46 km s^{-1}, larger than would be expected given the effects discussed above. The CO PVDs show that the gas is regularly rotating, and over half of these systems have discy surface brightness profiles (which I argued in Section 4.5.2 are present in relaxed systems). Such large differences are thus unlikely to be caused by a dynamical disturbance. Three of these galaxies have their molecular gas rotating in the polar plane (Chapter 5), hence the disagreement with the model predictions (for rotation along the photometric major axis of the galaxy) probably simply implies that the mass distributions in these three systems are flattened. Removing these systems with polar rings/disks decreases the average offset between the CO and the model traces to -56$\pm$36 km s^{-1}. The rest of the systems with models that over-predict the true CO rotation velocity have either co-rotating (7/11) or exactly counter-rotating (1/11) molecular gas, hence the remaining disagreement between the model and observations must be due to other factors.

One would require very large molecular gas velocity dispersions ($\sigma_{CO} \approx 80$ km s^{-1}) to explain the offset of the JAM circular velocity in these systems. I however consider such large velocity dispersions to be unlikely, especially considering the average value

for cold atomic gas in nearby spirals ($\sigma_{\rm H\,I} \approx 8$ km s^{-1}; van der Kruit & Shostak 1982; Dickey, Hanson & Helou 1990).

Nearly all of the systems in which the JAM models overestimate the true gas velocity (and which are not polar rings/discs) have central CO rings, or have (single or multiple) solid-body components in their observed PVDs. Such morphological and kinematic features often betray the presence of resonance systems, potentially caused by a bar (e.g. Combes, 1991). Lablanche et al, (in prep.) have shown that the presence of a bar can produce an overestimation of the M/L of a galaxy by ≈20%. As the assumed M/L sets the normalisation of the rotation curve ($v \propto \sqrt{M/L}$), this could explain some (but likely not all) of the offsets of the JAM predictions.

One other potential cause of the remaining offsets is that the assumption of a constant M/L as a function of radius may be invalid. The systems with model PVDs that lie above the CO profiles tend to have large Hβ equivalent widths (see Figs. 4.7 and 4.9). These systems also tend to have larger molecular gas reservoirs (Paper IV). Galaxies with overestimated JAM models have a mean H_2 mass of 3×10^8M$_\odot$, nearly an order of magnitude higher than that of galaxies with good JAM model predictions (4×10^7M$_\odot$). The average galaxy with an overestimated profile has the equivalent of 2.4% its stellar mass in molecular gas, while galaxies with good profiles average only 0.7%.

The EW of Hβ is often used as a star-formation tracer in spiral galaxies (where an EW(Hβ) $\gtrsim$2Å is usually considered indicative of ongoing star-formation). One must be cautious when using EW(Hβ) to trace star-formation in ETGs, as other sources of ionisation can cause Hβ emission (e.g. old stellar populations Sarzi et al., 2010). However, in all but one of the galaxies here that have EW(Hβ) $\gtrsim$2Å the ionisation is likely from star-formation (as they have log([OIII]/Hβ) $\lesssim$ -0.2; Sarzi et al. 2010). The one galaxy where this is not the case is NGC 7465, which is a composite source, with ionisation both from star-formation, and a X-ray bright AGN.

Active star-formation would create a population gradient, with many young stars in the inner parts of the galaxy where the CO is concentrated, and older stars dominating in the gas-poor regions further out. The galaxy average M/L (and thus circular velocity) predicted by the JAM model would thus be too high in the inner

parts of the galaxy where the CO is, leading to an overestimation of the circular velocity (with a corresponding underestimation in the outer parts). The one galaxy with a JAM model that is classified as matching well the molecular gas PVD but which has a large Hβ equivalent width is IC1024. In this galaxy the CO extends over the entire disc of the galaxy, to beyond 1 R_e, and hence the variation of M/L as a function of radius is likely to be lower.

Figure 4.8 shows that many of the systems in which the JAM model over-predicts the true CO rotation are at low velocity dispersions. This trend is not driven by the polar ring/disc galaxies, as this trend persists even if these galaxies are removed. If the JAM overestimations are due to ongoing active star-formation then this naturally leads to an explanation of the low velocity dispersions of these galaxies. Even if the star-formation rate of all ATLAS^{3D} galaxies were the same, the luminosity weighted M/L in a low-mass galaxy would be more affected than in a high-mass galaxy. As I touched on above, however, the molecular gas reservoirs of these low-mass systems are much larger on average, so the situation is even more extreme. As discussed in Paper IV, this may be due to an observational bias, or is potentially simply an illustration of 'downsizing' (e.g. Cowie et al., 1996).

A last potential cause for the offsets is the effect of dust on the mass models. Many of the systems where the JAM models overpredict the CO velocity have central dust obscuration in the optical images used to create the MGEs. The models thus badly capture the light distribution in the very central parts, that are vital to set the circular velocity normalisation. The measured light profiles may become too shallow in the inner parts, and the models will require a high M/L to best fit the (steeper) rise in the stellar velocities. Assuming a fixed dust-to-molecular gas ratio, it is clear that one would expect these problems to be worse at high molecular gas masses, as observed. These problems could be overcome to some degree by utilising near-infrared imaging (less affected by dust than SDSS) in the centres of these objects when creating the MGE (as in Williams, Bureau & Cappellari 2009), but this is beyond the scope of this chapter.

We thus conclude that in the galaxies with the largest molecular masses, and highest star-formation rates, population gradients and/or dust obscuration can affect

the JAM circular velocities. The second class of galaxies identified above is thus unlikely to be physically different from the first class. The differences I highlighted above instead arise because of the difficulty of modelling actively star-forming ETGs. The magnitude of such an effect can be up to 0.6 dex in velocity, however in the context of the entire ATLAS^{3D} sample very few galaxies ($\lesssim$15%) have sufficient molecular gas, dust and star formation for this to be an issue.

In the 11% (4/35) of CO-mapped galaxies where the CO is disturbed (as identified in Alatalo et al., in prep.), its rotation (or lack thereof) is unrelated to the JAM prediction of the true circular velocity. All of these galaxies have extended surface brightness profiles, with truncations, supporting the conclusion that these profiles indicate mergers and/or recent accretion. The remaining systems have known problems with either the JAM models or the observations, hence I will not discuss them further.

4.5.3.2 The dark matter halo of NGC4753

Steiman-Cameron, Kormendy & Durisen (1992) have discussed in detail the complex, twisted dust lanes of NGC 4753, and showed that they are consistent with a disc that is strongly twisted by differential precession. They used this twisted disc to set constraints on the shape of the matter distribution, finding that the total dark and luminous mass is nearly spherically-distributed, with an ellipticity no higher than 0.16 and no smaller than 0.01. Due to a lack of kinematic information for the warped disc however, they were unable to determine if the dark matter halo is oblate or prolate. If the material in the warped disc rotates in the same direction as the stars, then the dark matter must have an oblate shape, while if it counter-rotates the halo is likely to be prolate. Assuming that the molecular gas detected in this galaxy is associated with the warped dust disc, it is possible to break this degeneracy. The molecular gas is kinematically aligned with the stars, hence I conclude that the dark halo in this galaxy is oblate, with a flattening between 0.16 and 0.01.

4.5.3.3 *Stellar velocities*

In Figure 4.6 (and in Appendix 4.B) I overlaid the stellar rotation curves extracted from the SAURON observations over the CO PVDs. The stars generally rotate slower than the molecular gas, due to asymmetric drift. I showed in Figure 4.8 that, as expected, the velocity difference between the stars and the molecular gas increases in galaxies with a higher stellar velocity dispersion.

4.5.3.4 *Ionised gas velocities*

The ionised gas in the CO-mapped ATLAS^{3D} galaxies always (within the errors) rotates at the same speed, or slower, than the molecular gas. This confirms that CO is the best tracer of the circular velocity in the inner parts of ETGs. HI should be a comparable tracer, and is much more extended on average, but due to the large angular resolution of the HI data we posses, I am unable to confirm this here.

The differences between the velocities of the CO and ionised gas give us clues about the ionisation mechanism powering the optical emission. HII regions embedded in a dynamically cold star-forming molecular disc are likely to rotate much like the disc itself, and be dynamically cold, while emission powered by shocks for instance will likely have a much higher velocity dispersion. In Figure 4.9, it is clear that the most star-forming galaxies have the smallest differences between the ionised gas and the stellar velocities. The small offset below the one-to-one relation is consistent with the observed velocity dispersion of the ionised gas. Galaxies with a smaller amount of star formation have a wide range of offsets between the ionised and molecular gas velocities, likely reflecting the variety of ionisation mechanisms powering the ionised gas emission.

4.6 CONCLUSIONS

I have investigated the extent and surface brightness profile of the molecular gas in the CO-rich ATLAS^{3D} ETGs, and compared them to spiral galaxies. I find that the molecular gas extent is smaller in absolute terms in early-type than in late-type galaxies, but that the size distributions appear to scale similary with optical/stellar characteristic scalelengths. Amongst ETGs, I find that the extent of the molecular gas is independent of the kinematic misalignment, despite the many reasons why misaligned gas might be more compact. The extent of the molecular gas does depend on environment, with Virgo cluster ETGs having more compact molecular gas reservoirs. This may be due to ram pressure stripping, or a greater prevalence of bars driving gas towards the galaxy centres.

I have identified four classes of surface brightness profiles in the CO-mapped ATLAS^{3D} ETGs. Around half have molecular gas that follows the stellar light profile, similarly to molecular gas in spirals. These galaxies appear to have relaxed gas out to large radii, suggesting that gravitational effects have had time to force the molecular gas into a profile that follows the stellar mass. A quarter of the sample galaxies show molecular gas surface brightness profiles that fall off slower than the light, and sometimes show a truncation. These galaxies often have a low mass, and either have disturbed molecular gas, suggesting that a recent merger or gas accretion may cause the excess, or are in cluster environments where ram pressure stripping and the presence of hot gas may compress and/or truncate the gas. The remaining galaxies have rings, or composite profiles, that I argue can be caused by the effects of bars or potentially minor mergers.

I also investigated the kinematics of the molecular gas using position-velocity diagrams. On to these I overlaid the JAM model circular velocity predictions and the stellar and ionised gas velocities. I find that the molecular gas reaches beyond the turnover of the circular velocity curve in $75\pm6\%$ of ATLAS^{3D} ETGs, validating previous work. The CO is also closer to the predicted circular velocity than the stars or ionised gas, validating its use as a kinematic tracer for Tully-Fisher and similar

analyses.

I found that in ≈40% of the sample galaxies the predicted circular velocity profiles and the observed CO rotation are consistent, the CO appears to be dynamically cold, and CO is an excellent tracer of the circular velocity of the system. In 31% of galaxies I found the JAM model systematically over-predicted the observed CO velocity. These galaxies have higher molecular gas masses and Hβ equivalent widths than the rest of the sample, suggesting that active star formation is causing the JAM model assumption of a constant mass-to-light ratio to break down. These galaxies also have strong dust features, that make constructing a mass model from optical imaging challenging. The ionised gas in the most star-forming galaxies appears to be dynamically colder, likely because it is associated with star formation in the molecular disc.

In conclusion, I find that the molecular gas reservoirs in many ETGs are very similar in terms of their kinematics and relative extent to those in spiral galaxies. However cluster environments and increased merger activity can lead to some systems having quite different properties. Understanding how these differences affect the gas properties, and star-formation will thus be required to correctly understand the ongoing evolution of the most massive galaxies in our universe.

APPENDIX 4.A SURFACE BRIGHTNESS PROFILES

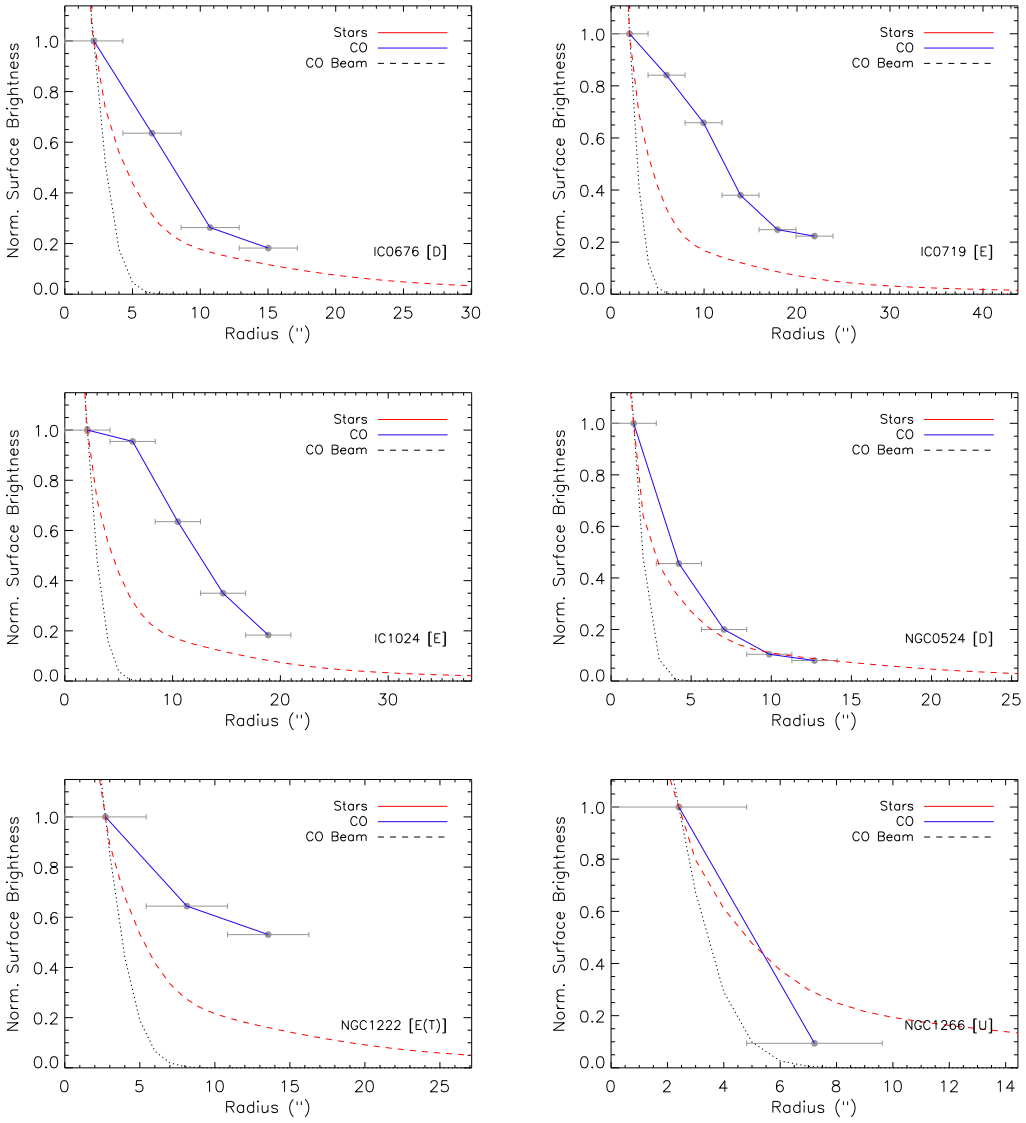

Figure 4.10: Radial surface brightness profiles of the stars (red dashed line; *r*-band) and molecular gas (blue solid line with errors) for our ATLAS^{3D} ETGs (normalized at the first CO datapoint). The CO beamsize is shown as a black dotted line. The error bars on the CO measurements denote the width of the elliptical annuli in the x-direction and the RMS noise in the elliptical annulus in the y-direction. The letter at the bottom-right corner of each plot denotes the profile class.

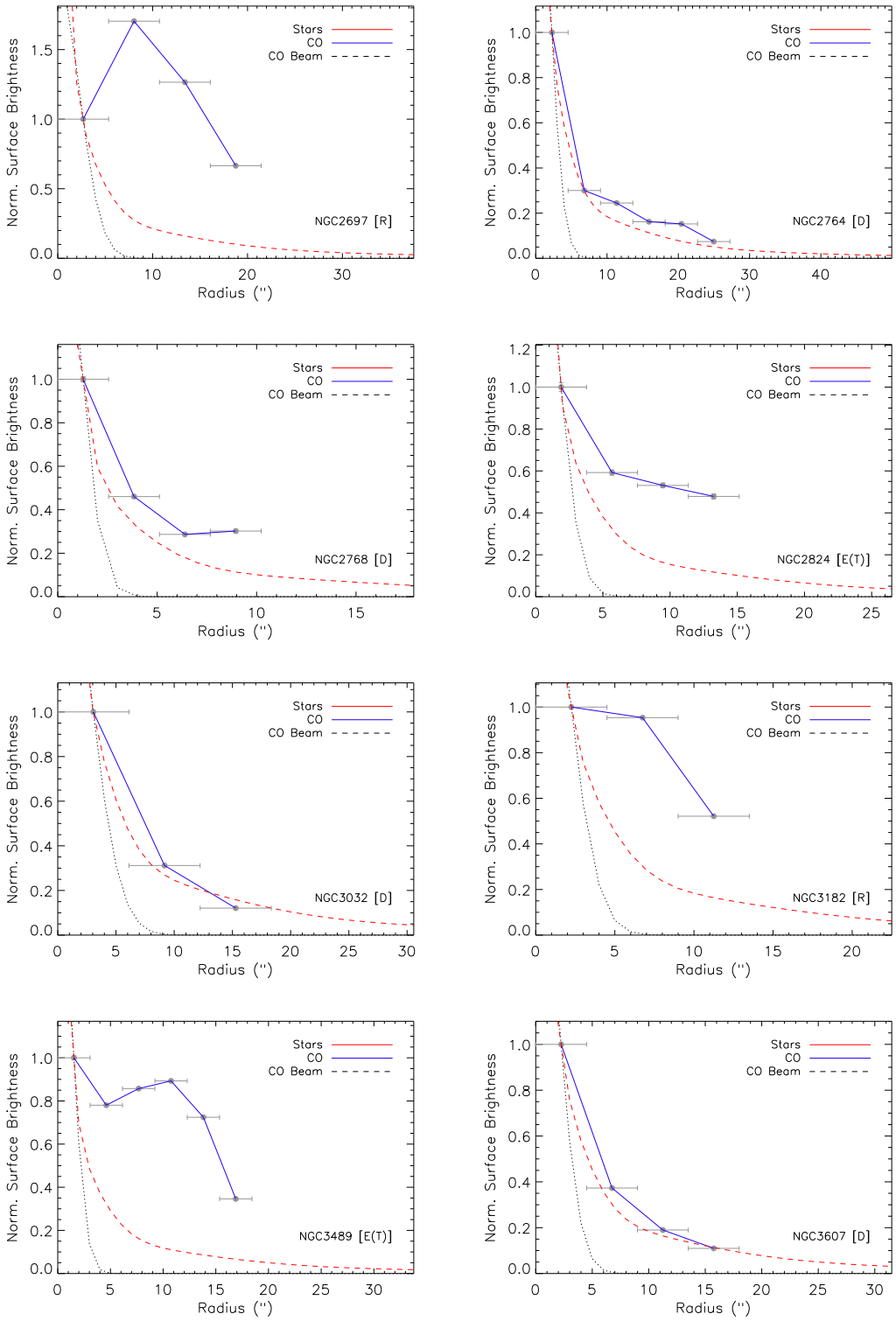

Figure 4.10 continued

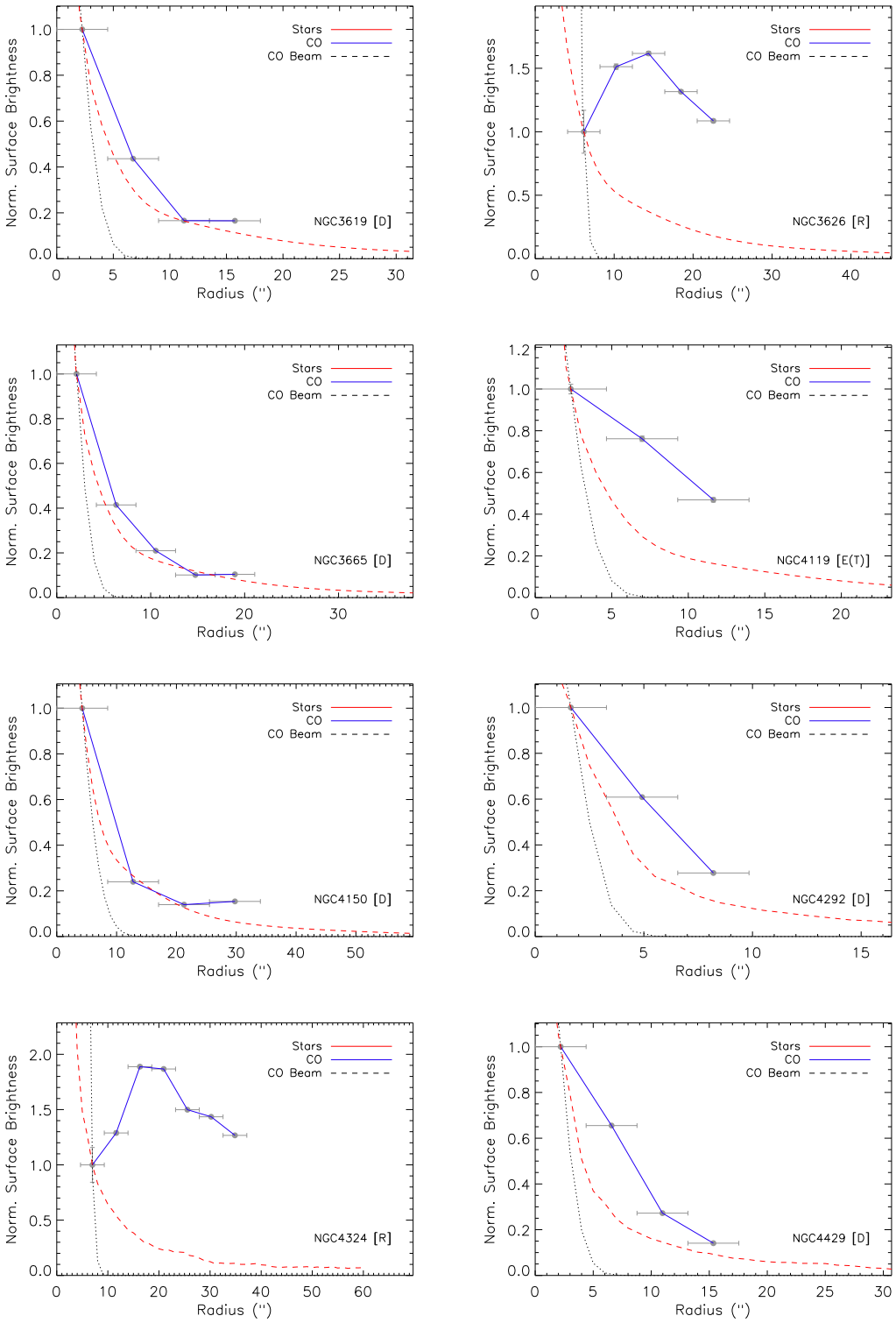

Figure 4.10 continued

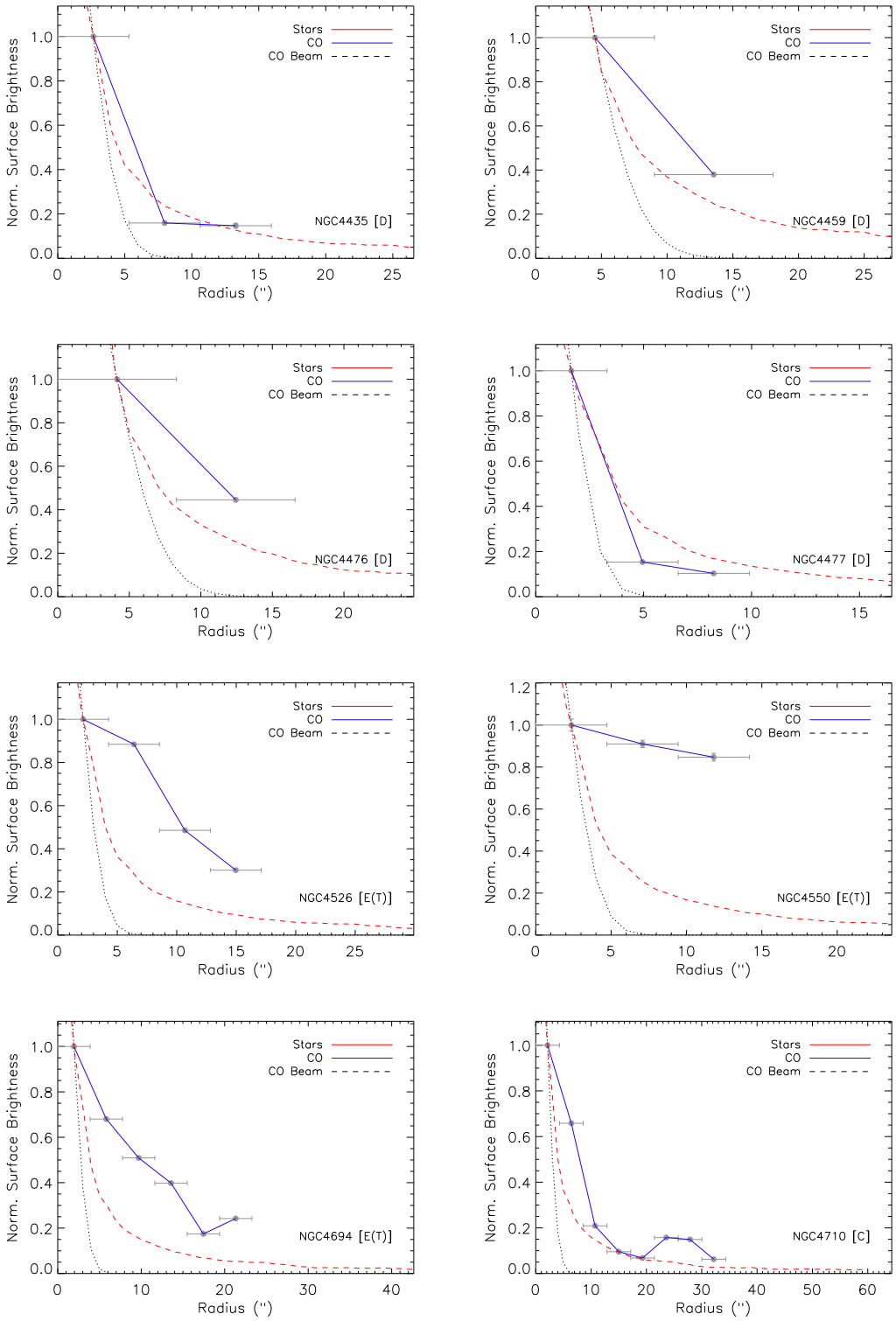

Figure 4.10 continued

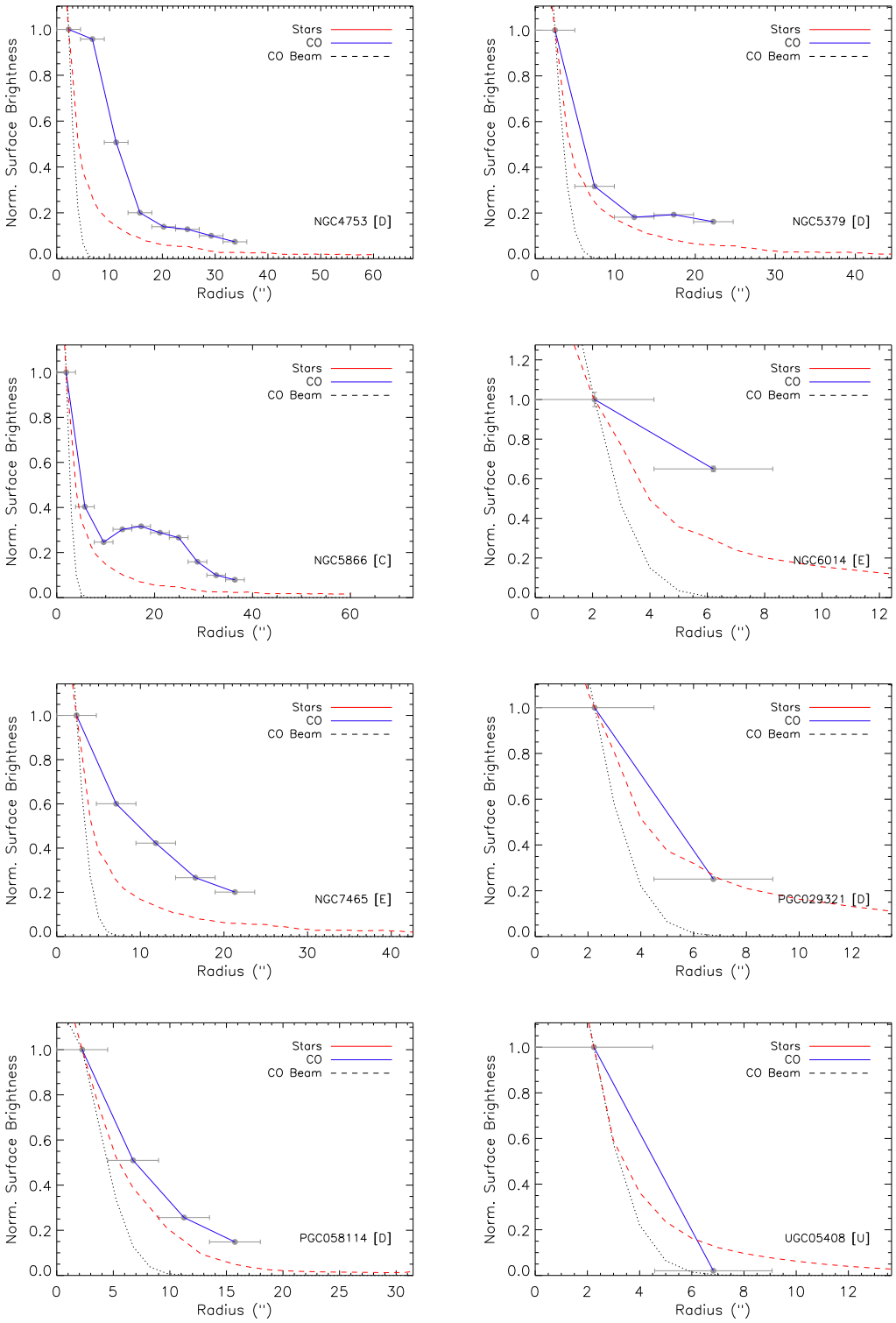

Figure 4.10 continued

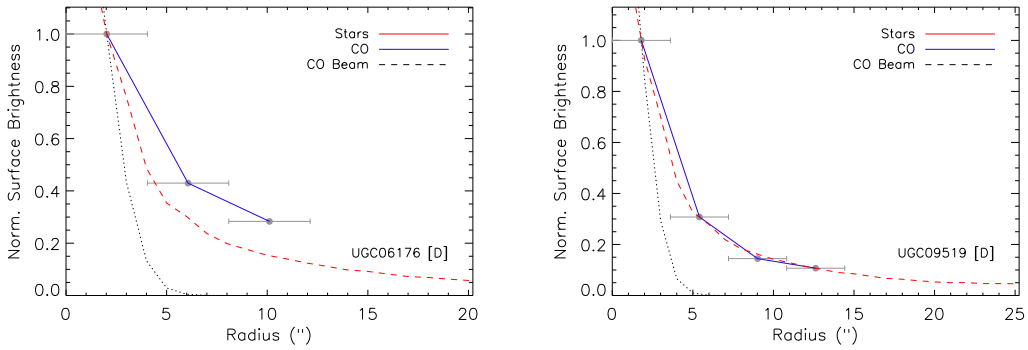

Figure 4.10 continued

APPENDIX 4.B POSITION-VELOCITY DIAGRAMS

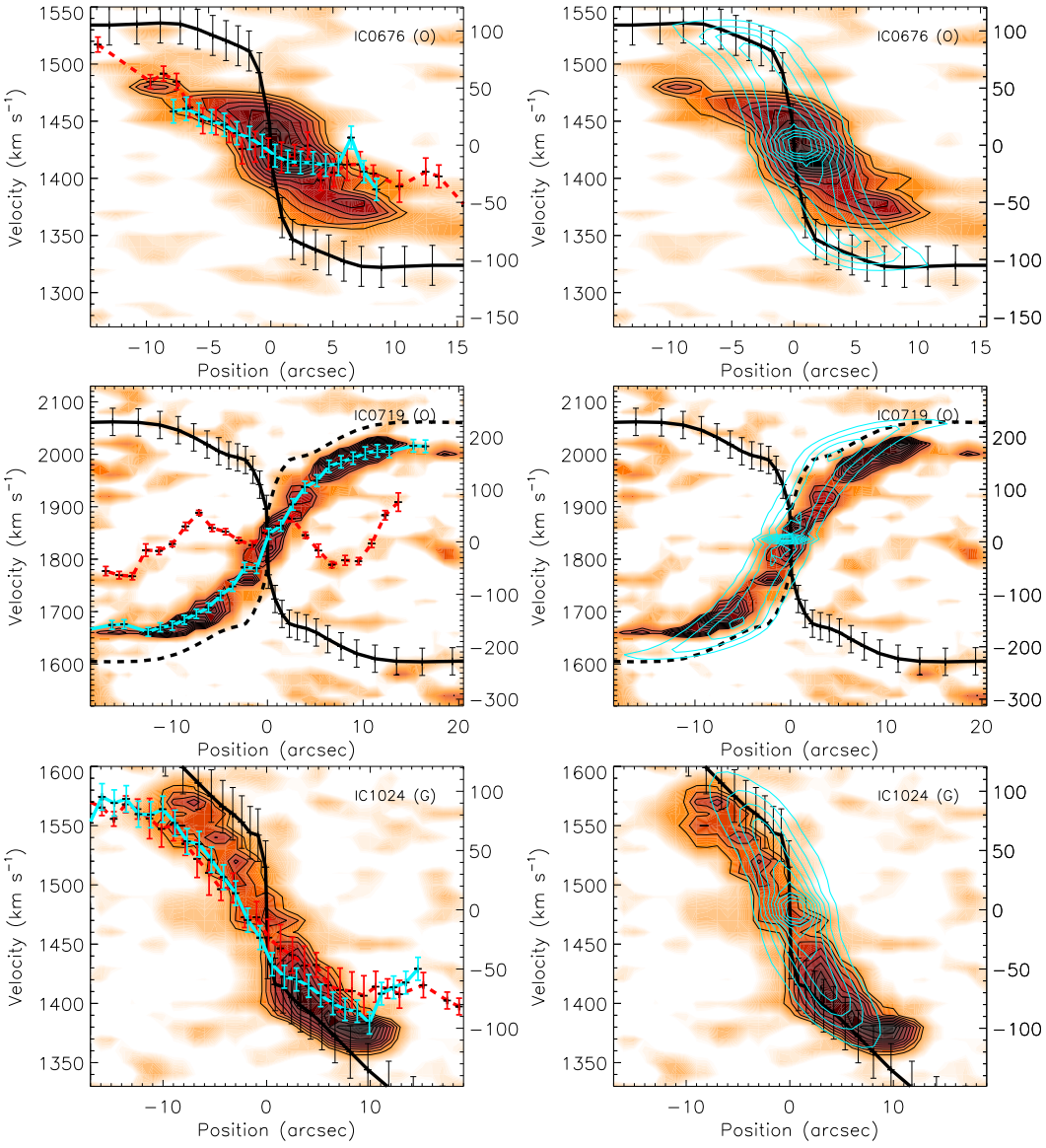

Figure 4.11: CO Position-Velocity diagrams (orange with black contours) for the ATLAS^{3D} galaxies, overlaid with the JAM circular velocity curve (thick black line). On the left, these have also been overlaid with the observed stellar (red dashed line) and ionised gas (blue line) rotation curve. On the right we overlay the modeled observations of each galaxy (blue contours), created assuming that the gas is dynamically cold and rotating at the predicted circular velocity, as described in Section 4.4.2.

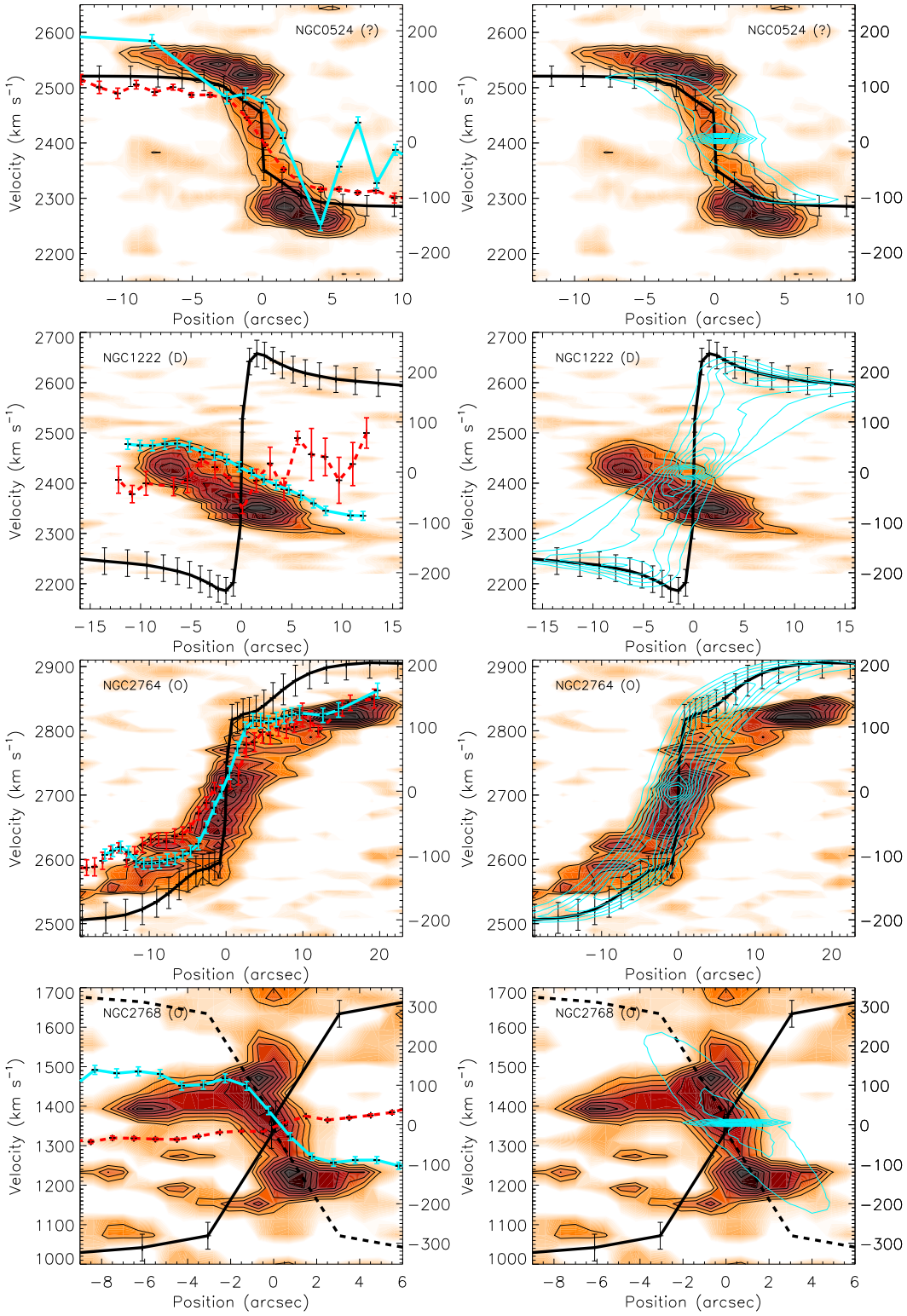

Figure 4.11 continued

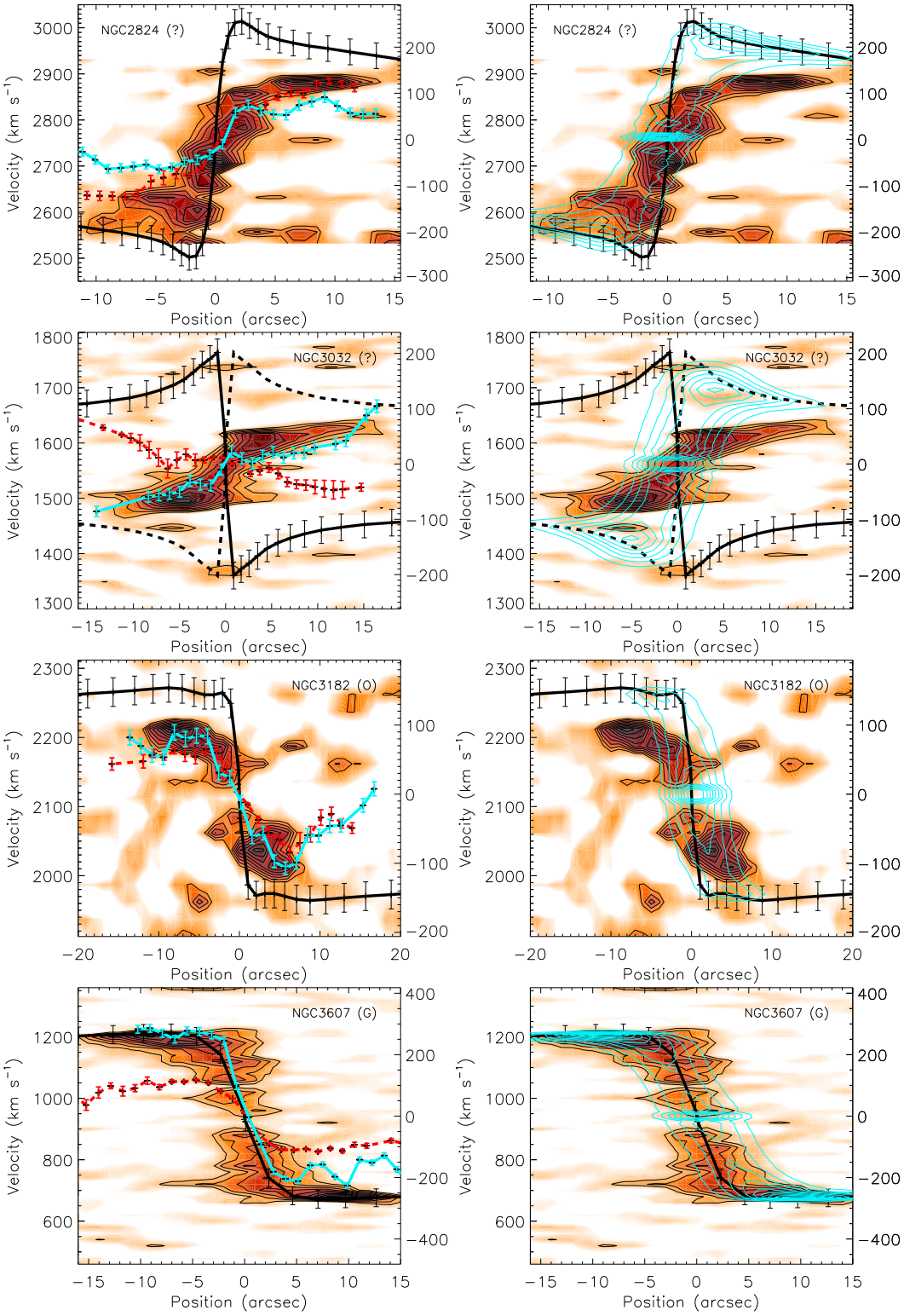

Figure 4.11 continued

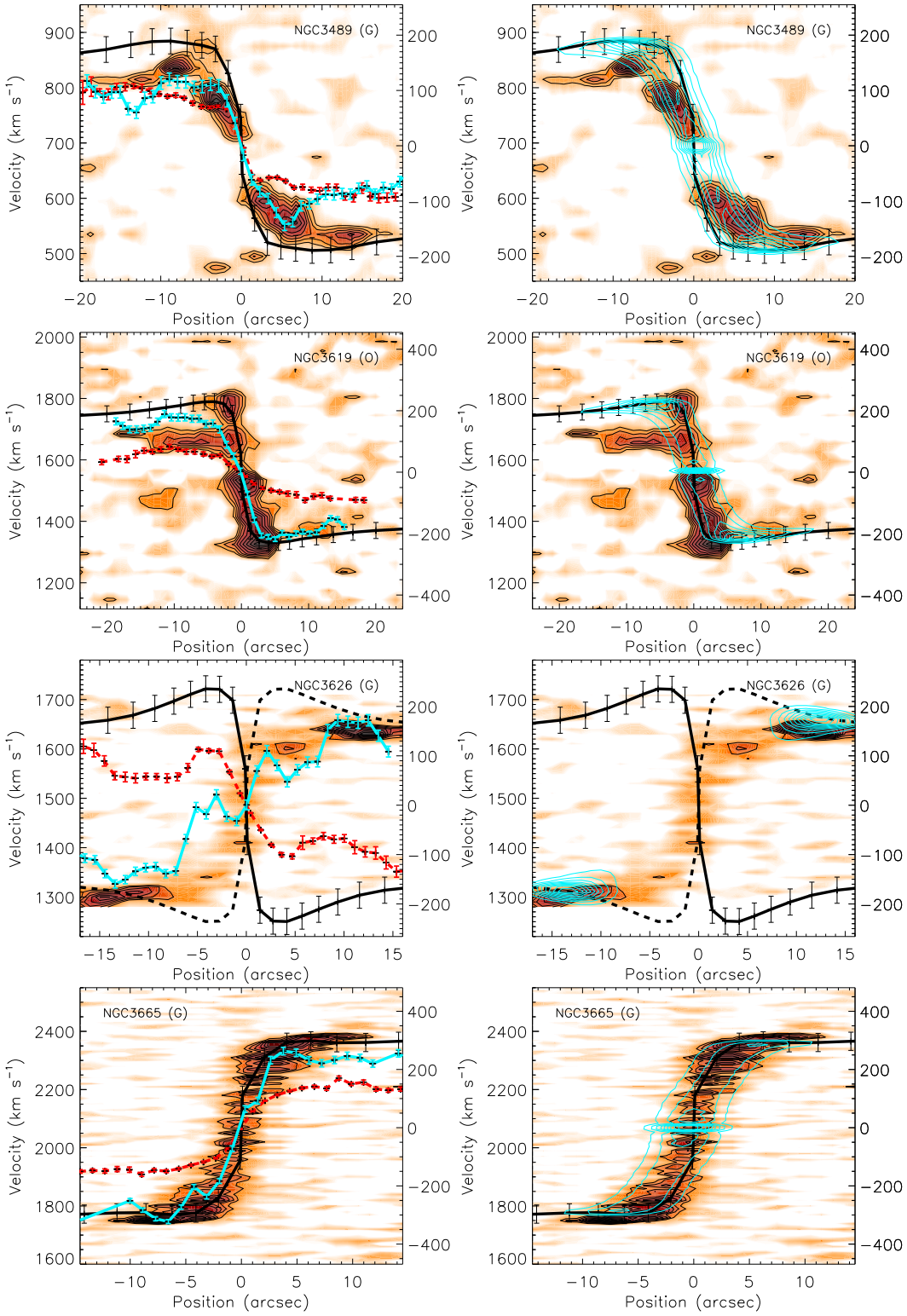

Figure 4.11 continued

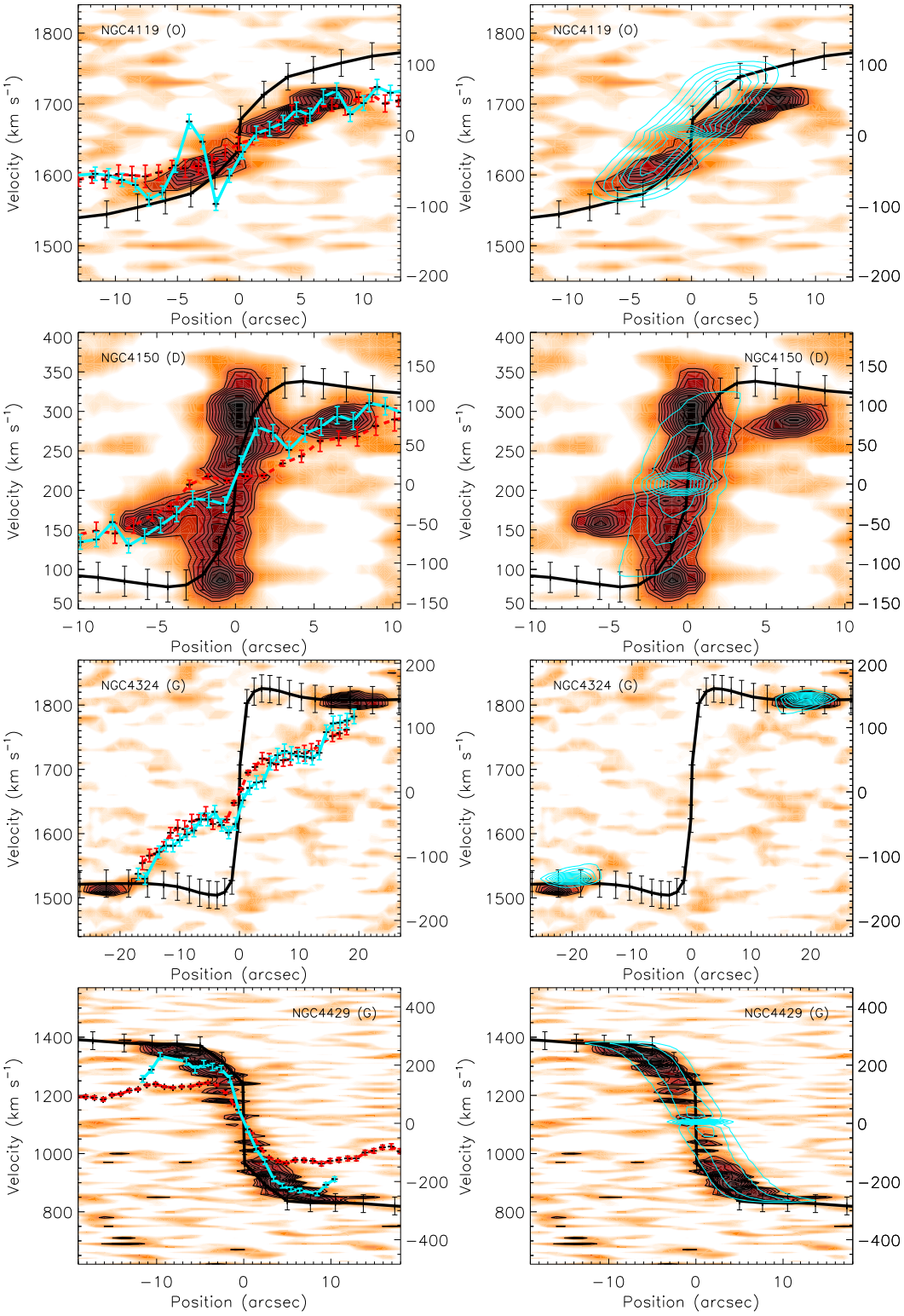

Figure 4.11 continued

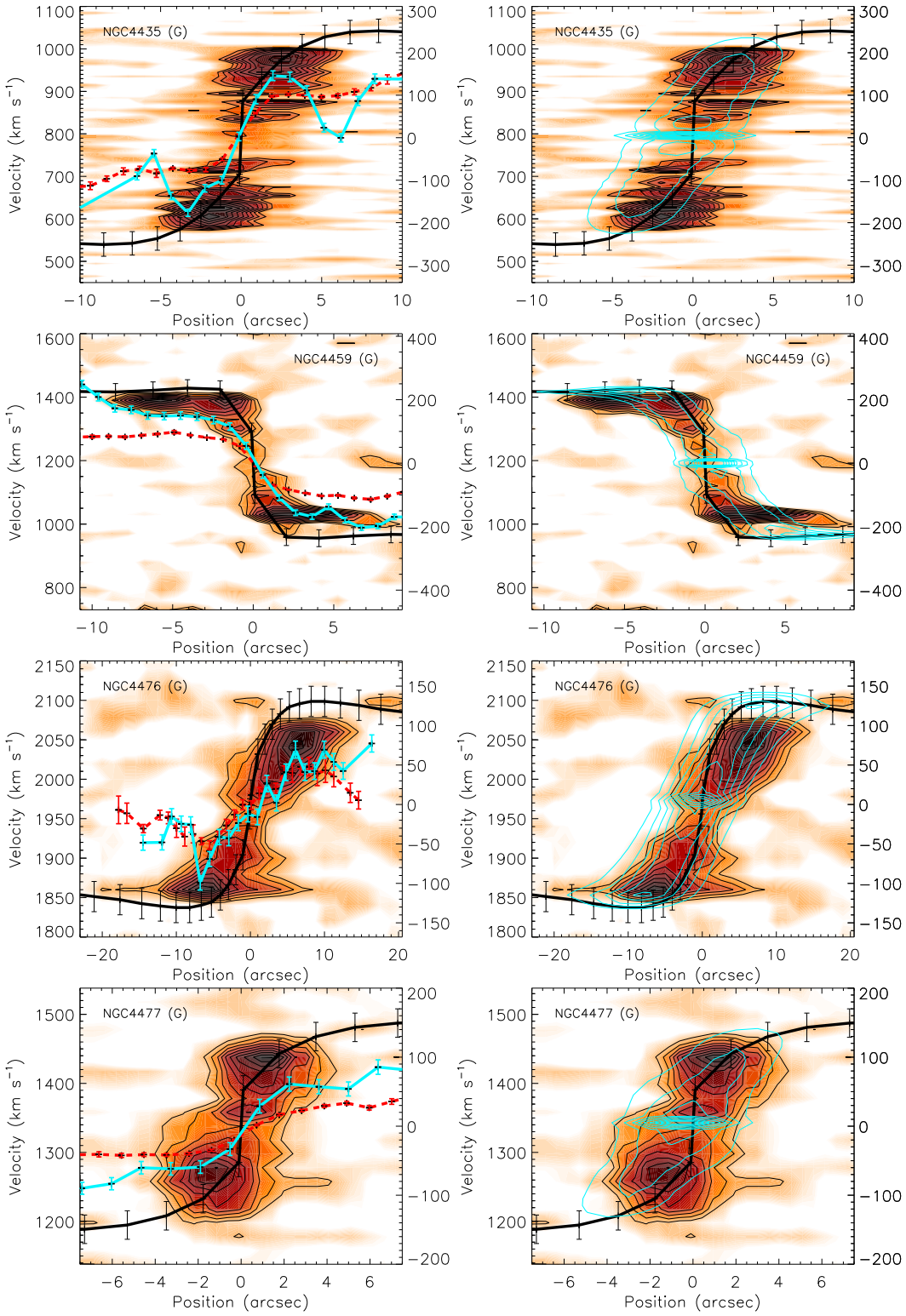

Figure 4.11 continued

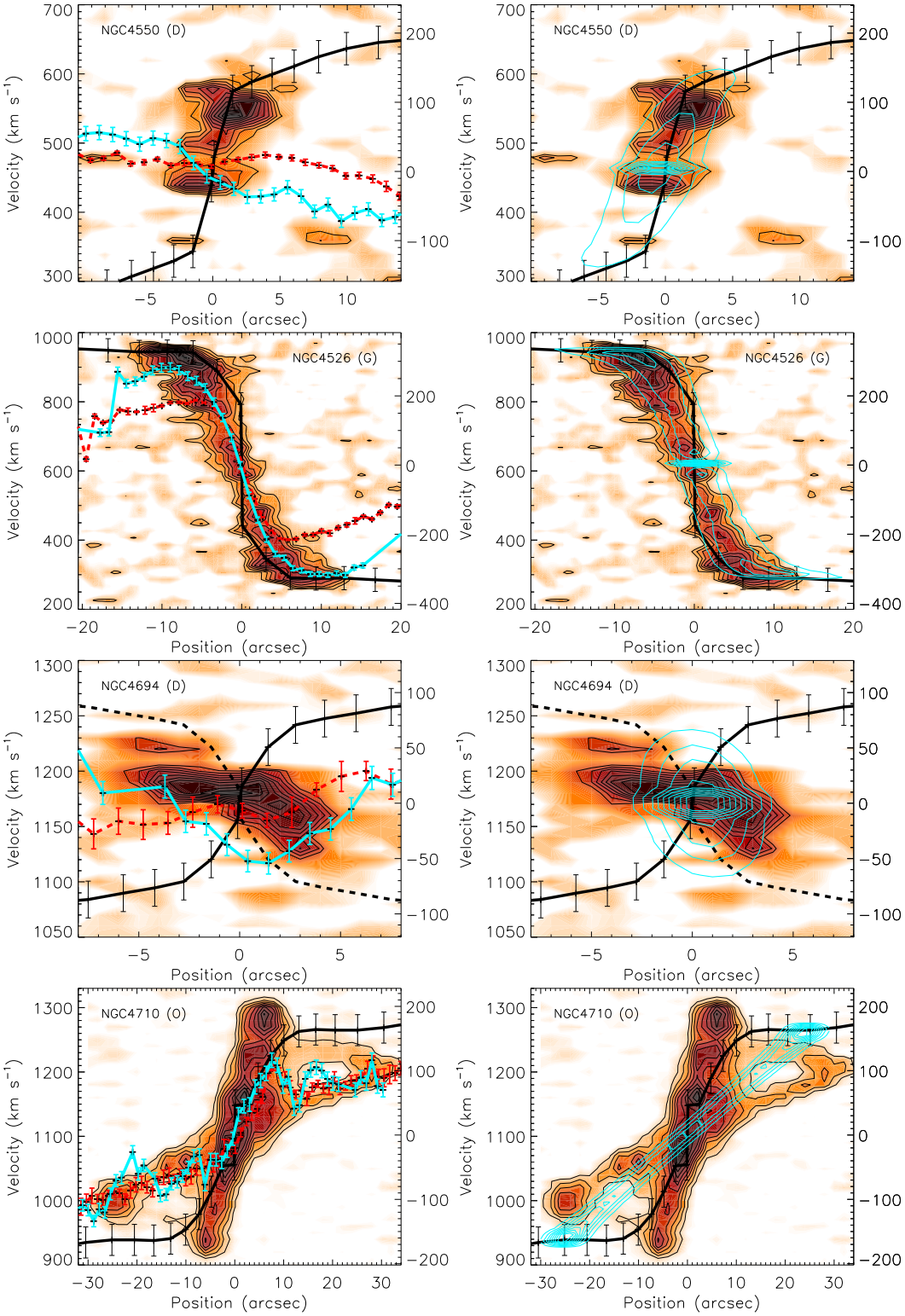

Figure 4.11 continued

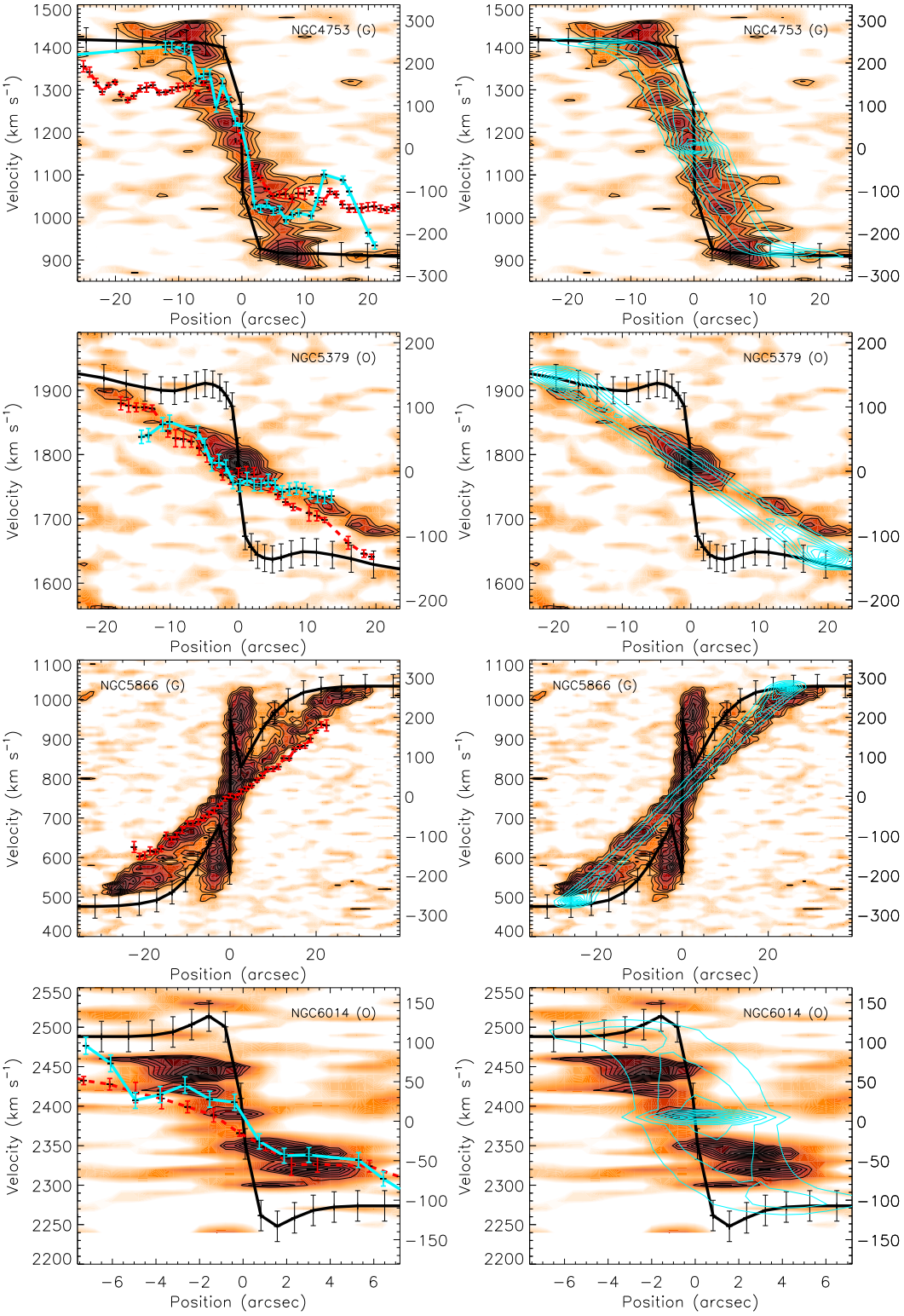

Figure 4.11 continued

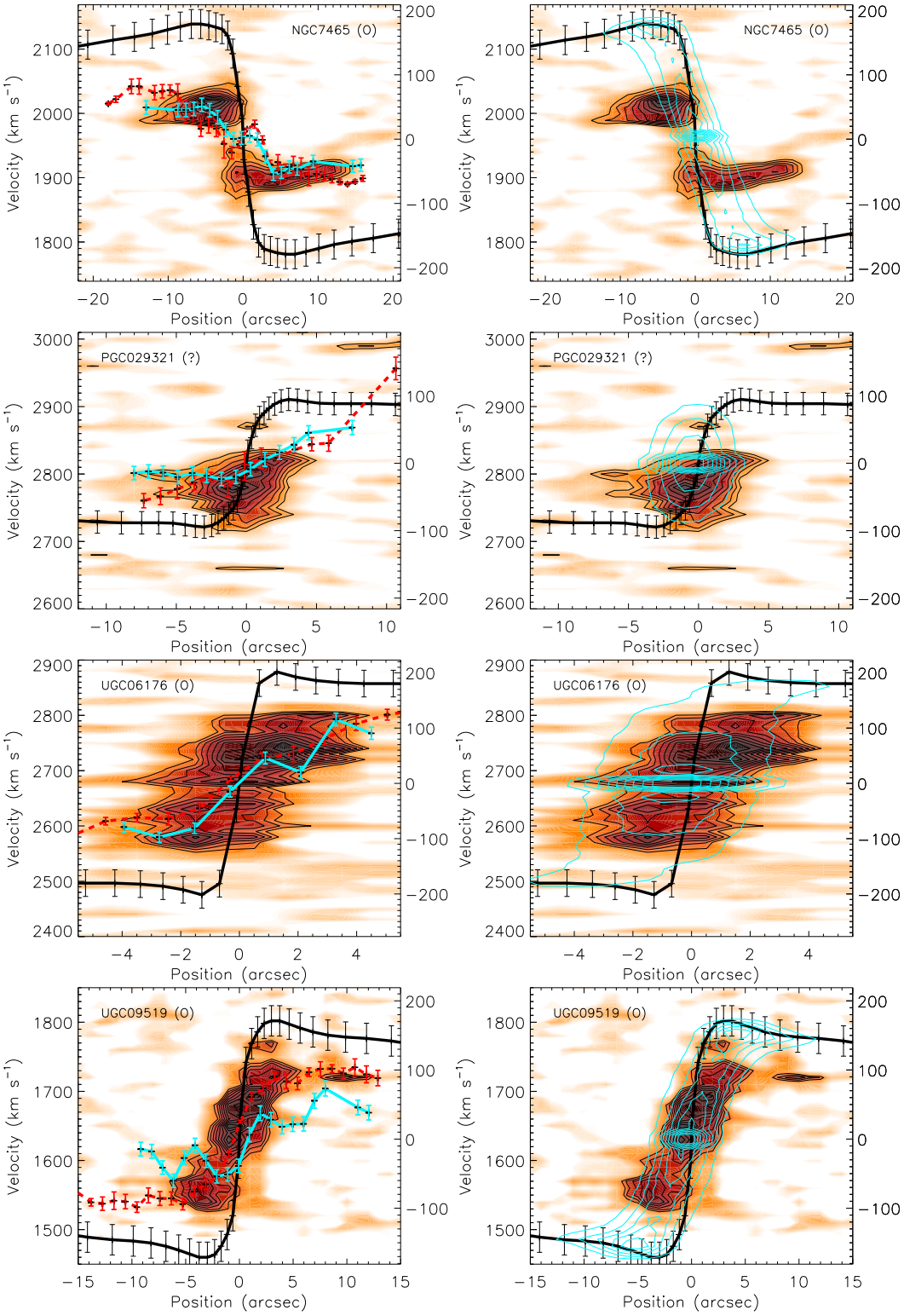

Figure 4.11 continued

5

ON THE ORIGIN OF THE MOLECULAR AND IONISED GAS IN EARLY-TYPE GALAXIES

"alert to the clay wet // fingers of dark matter // that shaped you // from the radiant death // of exhausted stars" - William Irwin Thompson

The material in this chapter has been accepted for publication in MNRAS as 'The ATLAS^{3D} project – X. On the origin of the molecular and ionised gas in early-type galaxies', Timothy A. Davis, Katherine Alatalo, Marc Sarzi, Martin Bureau, Lisa M. Young, Leo Blitz, Paolo Serra, Alison F. Crocker, Davor Krajnović, Richard M. McDermid, Maxime Bois, Frédéric Bournaud, Michele Cappellari, Roger L. Davies, Pierre-Alain Duc, P. Tim de Zeeuw, Eric Emsellem, Sadegh Khochfar, Harald Kuntschner, Pierre-Yves Lablanche, Raffaella Morganti, Thorsten Naab, Tom Oosterloo, Nicholas Scott, and Anne-Marie Weijmans (arXiv:1107.0002)

5.1 INTRODUCTION

The origin of the colour bimodality that separates the ETGs in the red sequence from star-forming galaxies, located in a 'blue cloud', has become a central question in extragalactic astrophysics. In order for galaxies to fade and join this tight red sequence rapidly enough, it is thought that the fuel for star formation must be consumed, destroyed or removed on a reasonably short timescale (e.g. Faber et al., 2007).

In the paradigm of cold dark matter with a non-zero cosmological constant (ΛCDM), it is thought that star-formation is shut-off in these galaxies by major

mergers that can funnel the cold gas into the centre of the remnant (Barnes, 2002), where it may be destroyed by an active galactic nucleus (AGN) or be used up quickly in a starburst. In massive galaxies, virial shocks (such as those discussed by Birnboim & Dekel, 2003) can also create a halo mass threshold, above which incoming gas will always shock to the virial temperature, stopping the accretion of further cold gas. Energy input from an AGN or starburst may also remove cold gas without a major merger, and keep halo gas from cooling. Galaxies in clusters and groups may also have their interstellar medium (ISM) removed by harassment, or stripped and ablated away by a hot intra-cluster medium (ICM).

Evolutionary processes like those listed above leave galaxies on the red sequence with little or no cold ISM, and thus no star formation. As discussed earlier in this thesis, it is clear that many ETGs do have cold gas reservoirs. If galaxies form in a hierarchical manner, then these observations pose a challenge to the standard view that early-type galaxies join and remain on the red-sequence due to a lack of cold gas. One must either demonstrate that it is possible to create a tight red sequence without removing all of the cold ISM, or that galaxies can regenerate or acquire cold gas after joining the red sequence.

The gas detected in these galaxies could be a remnant, left over from the progenitors that formed the ETG. Stellar population analyses (e.g. Kuntschner et al. 2006, Kuntschner et al. 2010, McDermid et al., in prep), however, show that the underlying stellar populations in these galaxies are old ($\gg 1\,\mathrm{Gyr}$). When combined with the fact that most ETGs show relaxed stellar kinematics (Paper III) and evidence from deep imaging (Duc et al., 2011; Paper IX) this suggests that the last major merger that could have formed such systems was at least several gigayears ago. Unless the remnant gas can be made stable against star-formation this thus suggests that we are seeing regenerated or newly accreted gas.

Galaxies can regenerate a cold ISM through both *internal* and *external* processes. Stellar evolution models predict that an average stellar population returns on the order of half its stellar mass to the ISM over a Hubble time (Jungwiert, Combes & Palouš, 2001; Lia, Portinari & Carraro, 2002; Pozzetti et al., 2007; Martig & Bournaud, 2010). This *internal* gas return is dominated not by cataclysmic events such as supernovae,

but by the long-term stellar mass loss from red giant branch, (post-)asymptotic giant branch stars and planetary nebulae (Parriott & Bregman, 2008; Bregman & Parriott, 2009). The majority of the ejected mass from giant stars will shock heat and join the hot gas reservoir of the galaxy (Parriott & Bregman, 2008). It may then be possible for this material to cool, recombine, fall toward the galaxy centre and eventually become molecular, regenerating the cold gas reservoir. The fraction of gas which is able to cool from the hot halo in this way is however unknown. Mass loss from planetary nebulae may avoid being shock heated, and cool from the ionised phase directly without joining the galaxies hot halo (Bregman & Parriott, 2009). Simulations have shown that this mass loss looses some angular momentum in this process, but generally it preserves the general sense of rotation of the parent star (e.g. Martig & Bournaud, 2010).

Stellar mass loss must be occurring in all ETGs at all times, at a rate depending on the number of stars present in each galaxy and its star formation history. One would thus expect many ETGs to have detectable molecular gas (assuming that some fraction of the hot gas reservoir does cool). Paper IV however found that only 22% of ETGs have detectable molecular gas, and there is no dependence of the detection rate and molecular gas mass fraction on host luminosity. It is of course possible that gas reservoirs exist in the other systems with a more quiescent recent star-formation history, resulting in low gas masses from stellar mass loss that are below the detection threshold. The lack of correlation with the host galaxy properties, however, suggests that other mechanisms must be destroying or preventing the molecular gas from forming in 78% of ETGs, and that stellar mass loss may not be the dominant method of acquiring cold gas.

Galaxies can also regain a cold ISM via *external* processes, such as (major and minor) mergers and/or cold mode accretion from the intergalactic medium (IGM). In a minor merger or cold accretion some fraction of the gas can avoid being shocked and will fall to the centre of the galaxy and cool, often producing a central disc or rings (Mazzuca et al., 2006; Eliche-Moral et al., 2010). In a major merger ejected gas can be re-accreted over the course of cosmic time. H I in ETGs has long been thought to come almost exclusively from external sources (e.g Knapp, Turner & Cunniffe,

1985). More recently deep HI observations (e.g. Morganti et al., 2006) have confirmed that almost all H I-detected field ETGs show signs of accretion, indicating an external origin for much of the atomic gas, with an average H I accretion rate of 0.1 $M_{\odot}$ yr^{-1} (Oosterloo et al., 2010). If the same is true for the molecular and ionised gas has yet to be determined.

Recent work has suggested one way to completely sidestep this problem, via 'morphological quenching' (Martig et al., 2009). In this scenario, red sequence galaxies are created not by removing all the cold ISM, but by making some fraction of it stable against gravitational collapse. The growth of a stellar spheroid via merging or secular processes increases the stellar density, and hence the epicyclic frequency and velocity dispersion in the centre of the galaxy. This can cause the Toomre stability criterion (Toomre, 1964) to exceed unity, implying that the gas is stable against gravitational collapse. As the star formation rate would be very low, this stable cold ISM would persist for many billions of years, and hence would be detectable today in red galaxies. In some ATLAS^{3D} galaxies we do indeed see large amounts of H I in a regular disk, but no corresponding young stellar population (Morganti et al., 2006). This process cannot be how every ETG transits to the red sequence, however, as such long-lived discs are not observed in all ETGs.

In summary, determining the dominant source of the cold ISM in ETGs is vital in order to understand their formation and evolution. If stellar mass loss can build up molecular reservoirs, then galaxies can transform themselves from spheroidal to disky systems over time and in isolation, and perhaps even (if morphological quenching does not intervene) evolve back into the blue cloud over cosmic timescales (e.g. Kannappan, Guie & Baker, 2009). If however mergers are the dominant source of the gas, then star-formation episodes are likely to be short-lived and possibly violent, and the gas will not accumulate and regenerate.

Observationally the origin of the gas may be addressed by comparing the angular momentum of the ISM with that of the underlying stellar population. Because of angular momentum conservation, stellar mass loss must produce gas that is kinematically aligned with the bulk of the stars which produced it. To first order, material from external sources can enter a galaxy with any angular momentum, so

many such mismatches should be observable today, the exact fraction depending on the dynamical timescales for misaligned material to relax into the equatorial plane. Even in very old systems, one might thus expect to see an equal number of galaxies with counter and co-rotating gas if external accretion and mergers are important (and if there is no preferred accretion direction).

A number of previous studies have used the misalignment of the angular momenta of gas and stars to constrain the origin of the ionized gas (e.g. Kannappan & Fabricant, 2001; Sarzi et al., 2006), and the molecular gas (e.g. Young, 2002; Young, Bureau & Cappellari, 2008; Crocker et al., 2011) in early-type galaxies. The goal of this chapter is to use the ATLAS^{3D} complete volume limited sample of 260 ETGs to constrain the importance of externally acquired gas in this way.

In Section 5.2 of this chapter I present my method for extracting kinematic position angles from the CARMA and SAURON data. In Section 5.3 I describe the misalignment distributions obtained, and I discuss them further in Section 5.4. I conclude in Section 5.5 and discuss prospects for the future.

5.2 OBSERVATIONS AND DATA ANALYSIS

To compare the orientation of the stellar and gaseous angular momenta, it is preferable to have full kinematic maps at comparable angular resolutions. Krajnović et al. (2008) have shown that many ETGs have kinematically distinct stellar substructures, that may cause confusion in long-slit spectroscopic data. Hence IFS data (such as the SAURON data we possess; see Section 1.4.3) are desirable in order to retrieve full two-dimensional maps of the kinematics of the stars and ionised gas. These also allow classification of polar and misaligned structures, instead of confining alignment measures to purely co-rotating and counter-rotating bins (as one is forced to do with only long-slit spectroscopy). These 2D maps may be combined with the mm-wave interferometry for the sample of galaxies presented in this thesis (Chapter 2), to map the cold molecular component of the ISM at similar spatial resolutions.

5.2.1 *Measuring kinematic position angles*

The apparent (projected) direction of the angular momentum vector of any tracer can be found by estimating its kinematic position angle ϕ, which lies normal to the angular momentum vector. The kinematic position angle (PA) is defined as the counter-clockwise angle between north and a line which bisects the tracer's velocity field, measured on the receding side.

One can then define the kinematic misalignment angle ψ as the difference between the kinematic PA of two galactic components. In this chapter, I will consider misalignments between the molecular gas, warm ionised gas and stellar angular momentum:

$$\psi_{\mathrm{mol-star}} \equiv |\phi_{\mathrm{molecular\,gas}} - \phi_{\mathrm{star}}|, \tag{5.1}$$

$$\psi_{\mathrm{mol-ion}} \equiv |\phi_{\mathrm{molecular\,gas}} - \phi_{\mathrm{ionised\,gas}}|, \tag{5.2}$$

$$\psi_{\mathrm{ion-star}} \equiv |\phi_{\mathrm{ionised\,gas}} - \phi_{\mathrm{star}}|, \tag{5.3}$$

These quantities are defined to lie in the range 0-180°.

In this work, the kinematic PA of the stars is taken from Paper II (Table 1, column 4 in Appendix C, and available online at http://www.purl.org/atlas3d). The molecular and ionised gas kinematic PAs are presented here for the first time, and are measured using the same method (the FIT_KINEMATIC_PA routine[1] described in Appendix C of Krajnović et al. 2006).

In this chapter I was able to measure molecular gas kinematic position angles for all the galaxies with mapped molecular gas. The values of the kinematic PA for these galaxies are listed in Table 5.1. I give two examples of CO velocity fields overlaid with their derived kinematic PA and the associated error in Figure 5.1. Ionised gas kinematic position angles were measured only on galaxies where the emission appeared coherent, with a regular velocity field, and was not very confined to the very central regions (as this is indicative of template mismatch within the GANDALF package; see Sarzi et al. 2006). These criteria were satisfied in 132 of the 260 sample galaxies (51%). Where the ionised gas is only detected over a small region, I have re-run the FIT_KINEMATIC_PA code using only this region to reduce the effect of low

[1] Available from http://purl.org/cappellari/idl

signal to noise ratio bins on the PAs determinations. Table 5.1 contains the ionised gas kinematic PA for all CO mapped galaxies in this work. Tables 5.2 and 5.3 contain the kinematic misalignment between the ionised gas and stellar components for all fast-rotating galaxies and slow rotating galaxies respectively, which were not mapped in CO, but which have a significant enough ionised gas detection to allow a kinematic PA measurement.

H I data was available for 29 fast-rotating galaxies that overlap with the CO and ionised gas sample considered in this chapter. The large difference in angular scale probed make comparisons between the extended H I and centrally concentrated molecular and ionized gas challenging, but potentially powerful. I do not extract kinematic position angles for the H I, but discuss the general trends present from visual inspection of the H I velocity fields in Section 5.3.4. More detailed analysis of the H I velocity fields and intensity maps will take place in a future paper in the ATLAS^{3D} series.

In real galaxies, there can be kinematic substructures (e.g. bars, kinematically decoupled cores) that may or may not share the same kinematic PA. In these cases, the *fit_kinematic_pa* routine returns the value applicable to the bulk of the material (as it is area, rather than luminosity weighted). Such substructures can, however, skew the measured kinematic PA, in some cases by tens of degrees. When a bar is present, Paper II has shown that the global kinematic PA of the stars is uncertain with a standard deviation of $\approx 10^{\circ}$. In general however the stellar kinematic position angle is a good estimate of the PA of the line of nodes even when a bar exists. Bars would be expected to have a stronger influence on the gaseous components than on the stars.

It is worth remembering that I always compare the kinematic PAs of the molecular gas to that of the main body of the stars. Some stellar velocity fields show a kinematically decoupled core (KDC), a stellar subcomponent with misaligned rotation from the rest of the stellar body. These KDCs generally extend only over a small central region however, and hence do not significantly affect my results.

The mm interferometric data have a poorer angular resolution than the optical data ($\approx$4-5″ vs 1-2″). In order to test how this affects the determination of the kinematic PA, I performed a Monte-Carlo simulation. A synthetic velocity field with a known

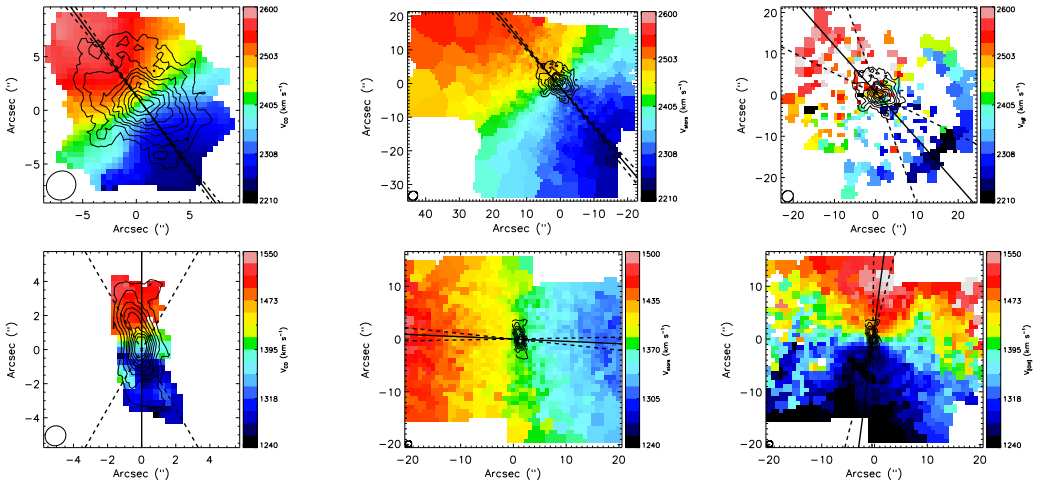

Figure 5.1: Examples of the data for one of the galaxies with the best constrained molecular gas PA (NGC 0524, top), and the galaxy with the worst constrained molecular gas PA (NGC2768, bottom). *Left:* CO velocity field (colours). *Middle:* Stellar velocity fields from the SAURON IFU (data from Emsellem et al., 2004). *Right:* Hβ emission line kinematics from the SAURON IFU (data from Sarzi et al., 2006). These are overlaid with the CO integrated intensity (black contours) and the best fitting molecular gas/stellar kinematic PA, and its associated error as calculated in this chapter (solid black line, and dashed black lines respectively). The CO moments are taken from Crocker et al. 2008 (NGC2768) and Crocker et al. 2011 (NGC0524). The SAURON IFU coverage of NGC2768 extends beyond the range of the plots shown above.

PA was created using an empirical galaxy rotation curve from Roscoe (1999). I then added Gaussian noise to simulate the average signal to noise ratio of the data. I varied the inclination, and the angular extent of the emitting material while keeping a fixed beam size (which is identical to changing the angular resolution) using a fixed spatial sampling of 3 pixels per beam, and measured the kinematic PA using the *fit_kinematic_pa* routine. Changing the inclination from edge-on to face-on had little effect of the determination on the PA, apart from very face on inclinations where the velocity range becomes comparable to the channel width. This happens only at inclinations less than 2.8 degrees for a typical galaxy with a maximum velocity of 200 km s^{-1}, and 10 km s^{-1} channel width. Varying the source size from 50 to 2.5 beams across (or equivalently 1″ to 20″ angular resolution) caused a scatter of $\approx$10° in the determined kinematic PA, with no systematic offset. The true PA was always within the 3σ error bars returned by the routine.

I also used this simulation to test the effect of signal to noise on the PA determinations. The average RMS deviation from the bi-(anti)symmetric velocity map created by

the *fit_kinematic_pa* is ≈15 km s^{-1} for the real CARMA data used in this work (with a maximum of 35 km s^{-1}). Varying the simulated RMS noise from 5 km s^{-1} to 50 km s^{-1} scattered the derived kinematic PAs by ≈10°. Once again this induced no systematic offset, and the true PA was always within the 3σ error bars returned by the routine.

The largest error on the observed molecular gas PA (as estimated by the *fit_kinematic_pa* routine) is 30°, and the average (1σ) error on the molecular gas PAs is 7°, consistent with the predicted error from the simulation. In this chapter I choose to consider kinematic misalignments between the gas and stars of $> 30°$ as being significantly misaligned. This conservative estimate ensures that I can set a robust lower limit on the importance of externally accreted material.

5.3 RESULTS

5.3.1 Molecular gas and stars

A direct comparison between the kinematic PAs of the molecular gas and the main body of the stars reveals two populations (Figure 5.2). I find 24±7% (9 out of 38 galaxies) have their molecular gas misaligned ($\Psi > 30°$) with respect to the stars, setting a lower limit on the number of galaxies where the gas is likely to have an external origin. The remaining 76±7% (29 out of 38 galaxies) have their molecular gas aligned with the stars ($\Psi < 30°$) with the stars, consistent with an internal origin. The uncertainties quoted above include only the formal binomial counting errors.

Table 5.1: Kinematic misalignment angles for the ATLAS^{3D} early-type CO mapped galaxies.

Name	ϕ_{mol} (deg)	$\Delta\phi_{mol}$ (deg)	ϕ_{ion} (deg)	$\Delta\phi_{ion}$ (deg)	$\psi_{mol-star}$ (deg)	$\Delta\psi_{mol-star}$ (deg)	$\psi_{mol-ion}$ (deg)	$\Delta\psi_{mol-ion}$ (deg)	$\psi_{ion-star}$ (deg)	$\Delta\psi_{ion-star}$ (deg)	Ref.
(1)	(2)	(3)	(4)	(5)	(6)	(7)	(8)	(9)	(10)	(11)	(12)
IC0676	16.5	10.0	348.5	26.9	2.0	15.8	28.5	29.6	30.0	29.6	1
IC0719	229.0	3.5	232.5	2.5	177.0	26.2	3.5	26.1	173.5	26.1	1
IC1024	24.5	12.8	31.5	8.2	5.0	16.7	7.0	13.6	2.0	13.6	1
NGC0524	36.5	1.8	41.5	21.9	4.0	2.7	5.0	22.0	1.0	22.0	6
NGC1222	33.0	1.5	54.5	21.5	10.0	9.4	21.5	23.4	11.5	23.4	1
NGC2685	105.0	10.0	109.5	13.8	68.5	10.3	4.5	14.0	73.0	14.0	2
NGC2697	301.5	1.8	300.0	3.1	0.0	3.6	1.5	4.4	1.5	4.4	1
NGC2764	202.5	1.8	189.5	5.2	6.5	7.0	13.0	8.6	6.5	8.6	1
NGC2768	180.0	30.0	187.5	6.1	87.5	30.2	7.5	7.0	95.0	7.0	4
NGC2824	161.5	1.8	159.5	7.5	2.0	3.3	2.0	8.0	0.0	8.0	1
NGC3032	92.5	10.0	62.5	19.1	179.0	14.9	30.0	22.0	151.0	22.0	3
NGC3182	331.5	7.2	316.5	6.0	11.0	10.0	15.0	9.2	4.0	9.2	1
NGC3489	67.5	1.8	78.5	5.3	5.0	3.3	11.0	6.0	6.0	6.0	6
NGC3607	302.5	2.5	302.5	0.5	1.0	2.9	0.0	1.6	1.0	1.6	1
NGC3619	74.5	4.2	76.0	0.5	22.5	5.2	1.5	3.0	24.0	3.0	1
NGC3626	169.5	1.8	165.0	3.2	170.0	1.9	4.5	3.3	174.5	3.3	1
NGC3665	219.5	2.0	209.5	2.2	14.0	2.8	10.0	3.0	4.0	3.0	1
NGC4119	296.0	12.0	292.5	18.6	4.5	13.6	3.5	19.7	1.0	19.7	1
NGC4150	146.0	10.0	168.5	10.1	1.5	11.9	22.5	12.0	21.0	12.0	3

Notes: Columns 2-5 list the kinematic PAs for the molecular gas and ionised gas (even columns), and their respective errors (odd columns). Columns 6-11 list the misalignments between the molecular gas, ionised gas and stars (even columns) and their respective errors (odd columns). The errors quoted on the kinematic PAs are those calculated by the FIT_KINEMATIC_PA routine. The kinematic PA of the main body of the stars for each galaxy is taken directly from Paper II (Table 1 in Appendix C, Column 4; available online at http://www.purl.org/atlas3d). Column 12 lists the data reference: (1) Alatalo et al., in prep (2) Schinnerer & Scoville (2002), (3) Young, Bureau & Cappellari (2008), (4) Crocker et al. (2008), (5) Crocker et al. (2009), (6) Crocker et al. (2011).

Table: 5.1 continued

Name	ϕ_{mol} (deg)	$\Delta\phi_{mol}$ (deg)	ϕ_{ion} (deg)	$\Delta\phi_{ion}$ (deg)	$\psi_{mol-star}$ (deg)	$\Delta\psi_{mol-star}$ (deg)	$\psi_{mol-ion}$ (deg)	$\Delta\psi_{mol-ion}$ (deg)	$\psi_{ion-star}$ (deg)	$\Delta\psi_{ion-star}$ (deg)	Ref.
(1)	(2)	(3)	(4)	(5)	(6)	(7)	(8)	(9)	(10)	(11)	(12)
NGC4324	232.0	1.8	239.0	6.8	6.0	5.5	7.0	8.6	1.0	8.6	1
NGC4429	82.0	2.0	92.5	2.0	4.5	3.2	10.5	3.2	6.0	3.2	1
NGC4435	201.0	1.8	198.6	3.1	8.5	2.5	2.4	3.6	6.1	3.6	1
NGC4459	269.0	5.0	281.5	1.5	11.5	5.6	12.5	2.9	1.0	2.9	3
NGC4476	208.0	2.5	219.0	7.5	1.5	11.8	11.0	13.7	12.5	13.7	1
NGC4477	227.0	3.0	226.5	1.6	25.5	6.0	0.5	5.5	26.0	5.5	6
NGC4526	288.0	3.0	294.5	4.7	0.5	3.5	6.5	5.0	6.0	5.0	3
NGC4550	355.0	10.0	358.5	9.7	3.5	10.3	3.5	10.0	0.0	10.0	5
NGC4694	155.5	27.5	167.0	45.0	169.0	33.6	11.5	48.9	157.5	48.9	1
NGC4710	207.0	10.0	208.5	2.2	0.5	10.7	1.5	4.4	1.0	4.4	1
NGC4753	93.0	2.8	85.5	1.5	4.5	3.8	7.5	2.9	3.0	2.9	1
NGC5379	66.0	20.0	77.0	5.0	5.0	22.4	11.0	11.2	16.0	11.2	1
NGC5866	127.0	2.5	123.0	4.5	2.0	3.9	4.0	5.1	2.0	5.4	1
NGC6014	139.5	6.2	151.5	10.2	7.5	10.5	12.0	13.3	4.5	13.3	1
NGC7465	106.0	3.8	109.5	9.5	60.5	29.2	3.5	30.5	57.0	30.5	1
PGC029321	76.0	27.5	105.5	27.2	19.5	46.1	29.5	46.0	49.0	46.0	1
PGC058114	94.5	7.0	93.1	3.1	152.5	12.2	1.4	10.5	153.9	10.5	1
UGC06176	201.0	8.5	214.0	8.5	0.5	30.2	13.0	30.2	13.5	30.2	1
UGC09519	177.5	5.5	172.0	4.5	72.0	8.0	5.5	7.3	77.5	7.3	1

Continued from previous page

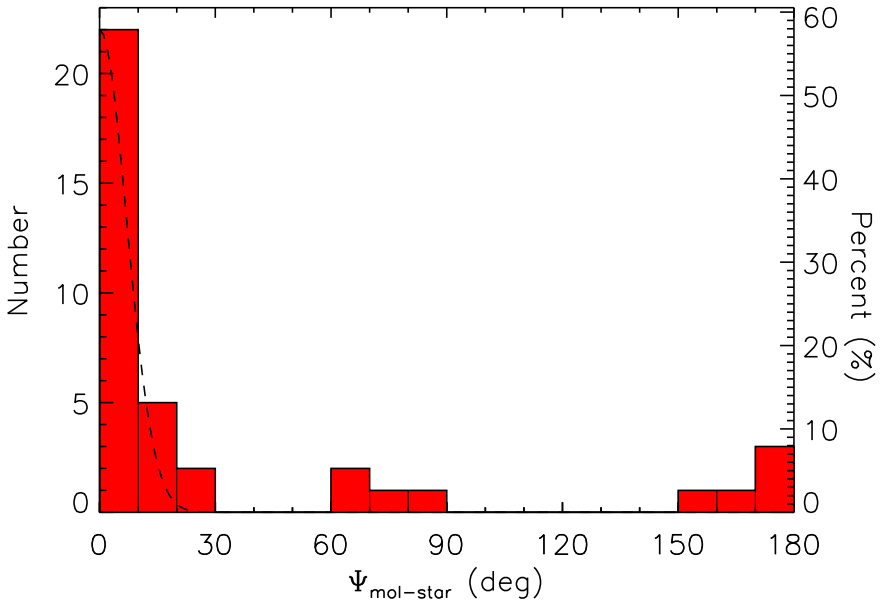

Figure 5.2: Histogram showing the kinematic misalignment angle between the molecular gas and the stars for all of the galaxies listed in Table 5.1. The dashed line overplotted is a normalized Gaussian distribution with its center at zero and a standard deviation of 7°, showing the expected scatter.

Several individual galaxies have a KDC coincident with the molecular gas. NGC 4476 is a pathological example, as it has a large stellar KDC, kinematically aligned with (and likely formed from) the molecular gas, while the stars have little sense of rotation outside this region within the SAURON IFS field of view. PPAK IFS stellar kinematics suggest that the stellar velocity field may become inverted outside the SAURON field of view (Crocker et al., in prep), hence the molecular gas could be considered to be counter-rotating with respect to the stellar body at large radii. For consistency, however, I use only the SAURON stellar kinematics in this work (probing roughly one effective radius), and hence label NGC 4476's molecular gas as co-rotating. It is worth bearing in mind, however, that the stellar kinematics in the outer parts of all of these galaxies could be different from the kinematics in the central regions. Discounting the few galaxies such as this, where the origin of the gas is hard to judge would not significantly alter my conclusions.

5.3.2 *Molecular and ionised gas*

The analysis presented in Section 5.3.1 can be repeated, comparing the apparent angular momenta of the molecular and ionised gas. This results in Figure 5.3. The molecular gas has a kinematic misalignment angle with the ionised component of less than 40° in every galaxy (and generally much better than this), and within the errors quoted all galaxies are consistent with having a kinematic misalignment angle of less than 10.5°. The overall distribution is consistent with a Gaussian error distribution with centre at zero and a standard deviation of 15°, as shown in Figure 5.3.

The galaxies which have a misalignement between 15° and 40° are IC 0676, NGC 1222, NGC 3032, NGC 4150 and PGC 029321. These small misalignments can always be understood as arising from small-scale kinematic substructures within the galaxies affecting the ionised component, that are usually unresolved at the resolution of the CO interferometry. IC 0676 has its ionised gas kinematic PA affected by a bar. NGC 1222 is a highly disturbed star-bursting system, that may be in the process of undergoing a three-way merger (Beck, Turner & Kloosterman, 2007). As discussed above, NGC 3032 and NGC 4150 have KDCs that may be affecting the gas properties (McDermid et al., 2006; Sarzi et al., 2006). The ionised and molecular material in PGC 029321 has a small angular extent, and as I showed above this can increase the error in the kinematic PA determination.

The uncertainty on ionised gas PA measurements is larger than the average 10° I have estimated for the molecular gas PAs. As discussed above, this is because the ionised gas is often patchy, has a smaller angular extent than the molecular gas, and can be less relaxed. Despite this increased uncertainty, and greater intrinsic variance due to small substructures in the galaxies, my conservative threshold for misalignment ($\Psi > 30°$) ensures that I still set a strong lower limit on the importance of externally accreted material. Despite the increased uncertainty, I only show plots of the ionised gas misalignment from here on, taking advantage of the increased number of galaxies available to improve the statistics. When one examines the molecular gas kinematic misalignments all results remain unchanged.

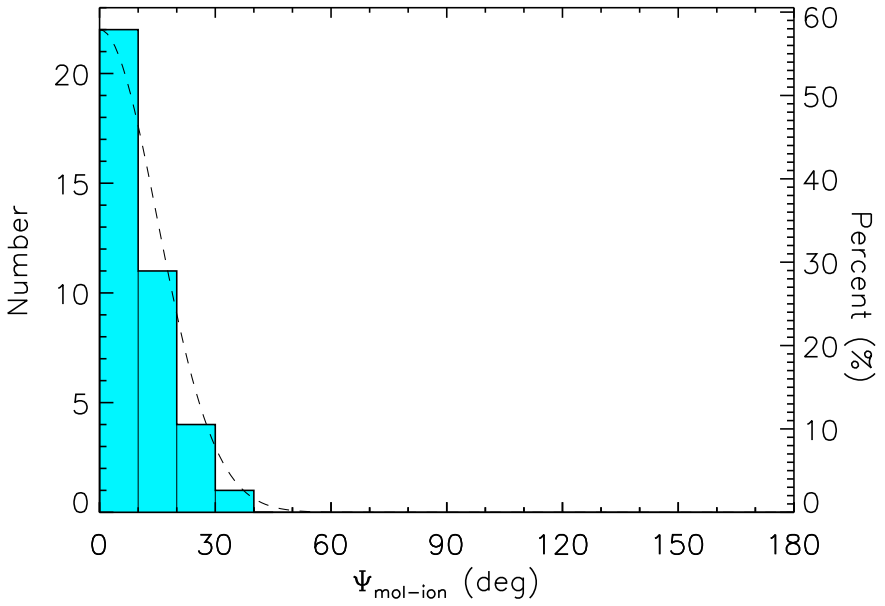

Figure 5.3: Histogram showing the kinematic misalignment angle between the molecular gas and the ionised gas for all the galaxies listed in Table 5.1. The dashed line overplotted is a normalized Gaussian distribution with its center at zero and a standard deviation of 15°, showing the expected scatter.

One galaxy (NGC 3032) has a molecular to ionized gas kinematic misalignment $\gtrsim 30°$ cut-off I have taken to denote the boundary between aligned and misaligned gas. As the distribution of misalignments closely follows the gaussian error distribution however, I suggest that this is due to observational scatter. We therefore conclude that the ionised and molecular material are always kinematically aligned with each other, even when they are kinematically misaligned with respect to the stars, strongly suggesting they share a common origin (as previously discussed in a subsample of these galaxies by Crocker et al., 2011). This is discussed further in Section 5.4.1.

Assuming 30° rather than 40° for the cut-off between aligned and misaligned gas can at most bias my results by ≈4% (this is the area under the error distribution at misalignments greater than 30°, normalized by the total area under this error distribution curve.) For the typical number of galaxies included in this analysis this can result in the misclassification of 1-2 galaxies.

5.3.3 *Ionised gas and stars*

As the molecular and ionised gas are always aligned and are likely to share a common origin, investigating the kinematic misalignment between the ionised gas and the stars can therefore also shed light on the origin of both of these gas phases in ETGs.

The ATLAS^{3D} ionised gas detection rate (above an integrated equivalent width of 0.02 Å in either Hβ or [OIII]) is $\approx$73$\pm$3% in the field, and $\approx$47$\pm$6% in the Virgo cluster. These figures are comparable with the previous SAURON survey ionised gas detection rate of 86$\pm$6% in the field and 55$\pm$12% in the Virgo cluster (Sarzi et al., 2006). I am hence able to repeat the analysis in Section 5.3.1, with the benefit of increased number statistics.

Table 5.2 contains the kinematic misalignment between the ionised gas and stars for all fast-rotating galaxies with a significant enough ionised gas detection to allow a kinematic PA measurement.

5.3.3.1 *Slow-rotators*

Slow-rotators as a class are round, massive, dispersion dominated, mildly triaxial ETGs that generally have old stellar populations, and large KDCs (Paper III). Ionised gas is detected in slow-rotators (Sarzi et al., 2006), while molecular gas almost never is (Paper IV). Ionised gas is hence the best tracer to help us understand the origin of the gas in the central parts of these systems. The stellar kinematic PA can be poorly defined in a slow-rotator, which have little or no coherent rotation by definition, and this translates to large uncertainties in the misalignments. Despite this it is possible to estimate the kinematic misalignment for 22 of the 36 slow rotating galaxies in the ATLAS^{3D} sample. The derived misalignments are listed in Table 5.3.

When slow rotators are considered by themselves (Figure 5.4), they display a flat distribution of misalignments between the ionised gas and the stars, suggesting the dominant source of (ionised) gas is external (as was seen previously with fewer galaxies by Sarzi et al., 2007). A MW-U test finds no statistically significant evidence

Table 5.2: Kinematic misalignment between the ionised gas and the stars for all the detected, fast-rotating, ATLAS^{3D} early-type galaxies.

Name	$\phi_{\rm ion}$ (deg)	$\Delta\phi_{\rm ion}$ (deg)	$\Psi_{\rm ion-star}$ (deg)	$\Delta\Psi_{\rm ion-star}$ (deg)
(1)	(2)	(3)	(4)	(5)
IC0676	348.5	26.9	30.5	29.6
IC0719	232.5	2.5	173.5	26.9
IC1024	31.5	8.2	2.0	13.6
NGC0680	26.0	2.5	26.5	4.5
NGC1266	350.5	3.5	56.0	7.8
NGC2577	88.0	2.8	16.0	3.4
NGC2764	189.5	5.2	6.5	8.6
NGC2778	50.5	4.0	5.0	6.2
NGC2824	159.5	7.5	0.0	8.0
NGC2852	188.0	2.8	32.0	5.5
NGC2859	269.0	1.8	5.0	3.5
NGC2950	97.5	2.2	16.5	4.0
NGC3182	316.5	6.0	4.0	9.2
NGC3226	36.0	1.0	8.0	6.3
NGC3245	184.0	4.8	9.5	5.6
NGC3248	302.5	4.0	179.5	9.8
NGC3412	175.0	10.5	19.0	12.1
NGC3457	339.5	4.8	5.5	38.5
NGC3499	125.0	4.2	75.0	12.7
NGC3595	99.5	7.2	99.0	7.4
NGC3599	352.5	3.2	63.0	17.6
NGC3607	302.5	0.5	1.0	2.8
NGC3610	128.0	3.8	6.5	3.8
NGC3613	96.0	0.5	3.5	1.3
NGC3619	76.0	0.5	24.0	3.0
NGC3626	165.0	3.2	174.5	4.6
NGC3648	315.0	5.2	60.5	6.0
NGC3665	209.5	2.2	4.0	3.0
NGC3694	309.5	8.0	159.5	12.2
NGC3838	137.0	5.2	1.5	6.3
NGC3941	144.0	1.2	129.0	3.7
NGC4026	343.0	2.0	18.5	3.6
NGC4036	258.0	1.5	3.0	1.8
NGC4111	197.0	1.0	47.5	2.5
NGC4119	292.5	18.6	1.0	19.7
NGC4143	155.0	1.8	165.5	2.9
NGC4179	142.8	3.1	0.7	4.4
NGC4203	198.0	1.8	3.5	6.0
NGC4251	207.0	1.2	71.5	3.2

Notes: Columns 2-5 show the ionised gas kinematic PA, error, and the misalignments between the ionised gas and the main body of the stars for all the fast-rotating ATLAS^{3D} galaxies where a kinematic PA was measurable. The stellar PA is taken directly from Paper II, and the data tables from this paper are available to download from http://www.purl.org/atlas3d. Kinematic misalignments for the fast-rotating SAURON ETGs are tabulated in Sarzi et al. (2006).

Name	ϕ_{ion} (deg)	$\Delta\phi_{ion}$ (deg)	$\Psi_{ion-star}$ (deg)	$\Delta\Psi_{ion-star}$ (deg)
(1)	(2)	(3)	(4)	(5)
NGC4255	113.0	2.8	2.0	4.3
NGC4281	118.0	0.5	33.0	1.6
NGC4324	239.0	6.8	1.0	8.6
NGC4382	29.0	9.7	8.5	10.8
NGC4417	224.0	9.5	4.5	10.4
NGC4429	92.5	2.0	6.0	3.2
NGC4435	198.6	3.1	6.1	3.6
NGC4473	101.0	9.7	9.0	10.5
NGC4474	95.5	4.5	16.5	8.1
NGC4494	186.2	3.1	1.2	6.8
NGC4521	12.5	1.8	23.5	3.3
NGC4596	112.5	0.5	12.5	4.5
NGC4612	310.3	3.1	17.7	12.0
NGC4621	307.0	10.0	14.0	11.2
NGC4643	68.0	2.5	20.0	4.9
NGC4684	292.0	7.5	87.5	9.0
NGC4694	167.0	45.0	157.5	48.9
NGC4697	218.0	0.5	29.5	2.1
NGC4710	208.5	2.2	1.0	4.4
NGC4753	85.5	1.5	3.0	2.9
NGC5103	357.0	8.0	38.5	8.9
NGC5173	93.5	6.0	174.0	17.8
NGC5273	71.5	44.5	119.0	45.0
NGC5353	297.5	0.5	24.5	1.1
NGC5355	62.0	8.5	33.0	16.4
NGC5379	77.0	5.0	16.0	11.2
NGC5422	348.5	2.0	14.5	4.2
NGC5485	264.0	4.2	5.0	8.0
NGC5493	137.5	5.2	16.0	6.5
NGC5582	23.5	2.5	6.0	3.7
NGC5866	126.5	3.2	0.0	3.5
NGC6014	151.5	10.2	4.5	13.3
NGC6017	132.5	5.2	0.0	8.4
NGC6149	218.0	7.5	17.0	8.6
NGC6278	337.0	3.0	31.5	5.6
NGC6798	313.0	1.2	174.0	6.9
NGC7465	109.5	9.5	57.0	30.5
NGC7710	154.0	21.2	20.0	46.6
PGC016060	161.5	2.8	2.5	3.4
PGC029321	105.5	27.2	55.0	46.0
PGC035754	47.0	12.0	39.0	16.3
PGC042549	242.0	5.0	1.0	7.8
PGC056772	214.0	2.8	23.0	6.1
PGC058114	93.1	3.1	153.9	10.5
PGC061468	73.0	15.2	32.0	19.1
UGC05408	122.5	10.2	27.5	19.9
UGC06176	214.0	8.5	13.5	10.7
UGC09519	172.0	4.5	77.5	6.2

Continued from previous page

Table 5.3: Kinematic misalignment between the ionised gas and the stars for all the slow-rotating ATLAS^{3D} early-type galaxies with regular gas.

Name	ϕ_{ion} (deg)	$\Delta\phi_{ion}$ (deg)	$\Psi_{ion-star}$ (deg)	$\Delta\Psi_{ion-star}$ (deg)
(1)	(2)	(3)	(4)	(5)
NGC0661	227.5	2.8	8.5	12.3
NGC1222	54.5	21.5	11.5	23.5
NGC1289	276.0	15.0	176.0	18.0
NGC3522	192.0	5.5	78.5	89.9
NGC3796	67.5	12.2	58.0	18.8
NGC4168	102.5	1.2	142.5	89.8
NGC4191	178.0	5.7	4.5	7.5
NGC4261	103.0	0.5	52.0	3.3
NGC4476	219.0	7.5	12.5	13.7
NGC4636	32.5	1.0	125.5	89.8
NGC4690	191.5	1.5	139.5	25.8
NGC5322	102.0	1.0	171.0	7.3
NGC5481	233.5	3.8	7.5	19.4
NGC5631	305.0	2.0	174.0	9.0
PGC028887	216.5	8.0	4.5	12.4

Notes: Columns defined as in Table 5.2. Kinematic misalignments for the slow-rotating SAURON ETGs are tabulated in Sarzi et al. (2006).

that the observed kinematic misalignments (in Figure 5.4) are not drawn from a uniform underlying parent distribution.

5.3.3.2 *Fast-rotators*

Figure 5.5 shows that 36±5% of fast-rotating galaxies (40 out of 111) have their ionised gas kinematically misaligned from the stars ($\Psi_{ion-star} > 30°$), consistent with the percentage of misaligned galaxies found in molecular gas (but with a smaller uncertainty). Where both the ionised gas and molecular gas are detected, the measured kinematic misalignments from the stars agree well with each other, with a 1σ scatter around the one-to-one relation of 10°. A MW-U test finds no statistically significant evidence that the molecular gas and ionised gas misalignments from the stars (Figures 5.2 and 5.5) are not drawn from the same underlying parent distribution.

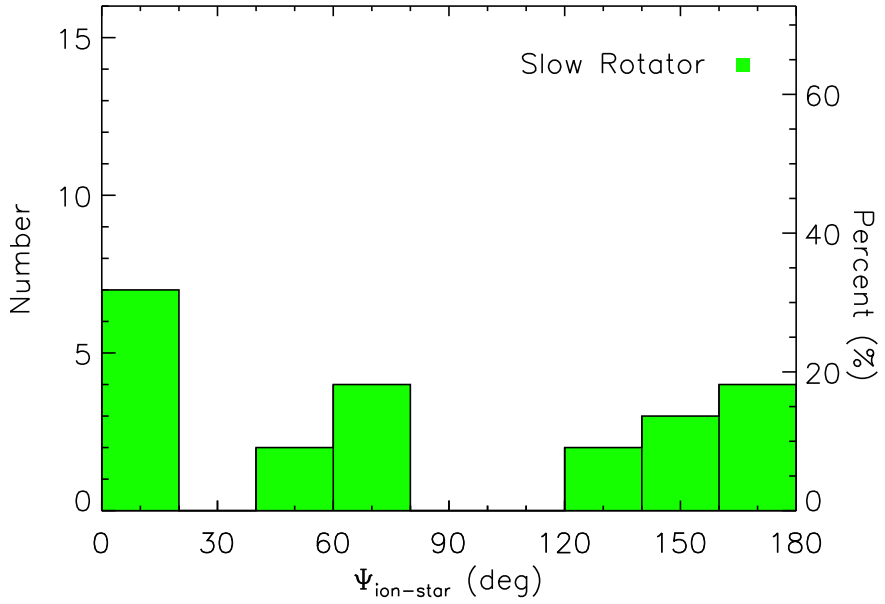

Figure 5.4: Histogram showing the kinematic misalignment angle between the ionised gas and the stars for all the slow-rotating galaxies with measurable kinematic misalignments. These systems are listed in Table 5.3.

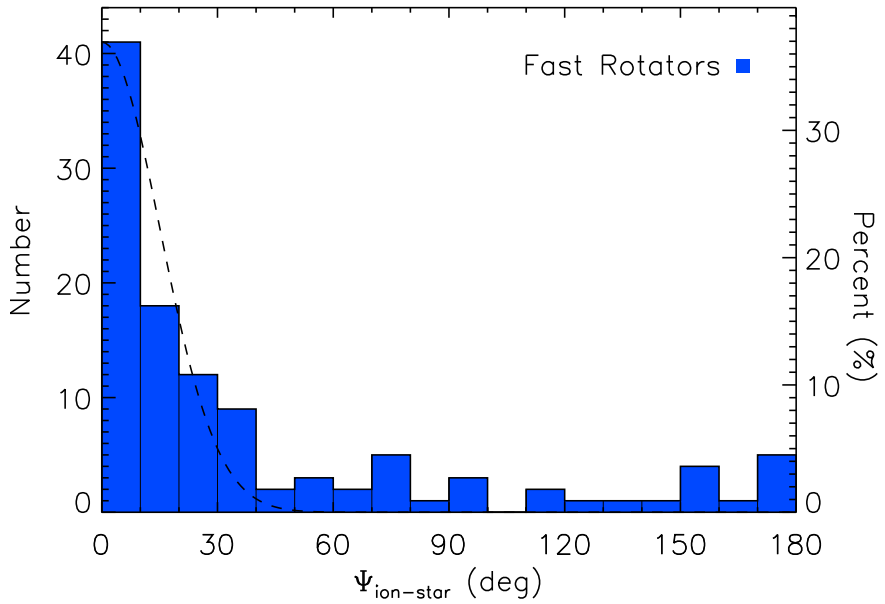

Figure 5.5: Histogram showing the kinematic misalignment angle between the ionised gas and the stars for all the fast-rotating galaxies listed in Table 5.2. The dashed line overplotted is a normalized Gaussian distribution with its center at zero and a standard deviation of 15°, showing the expected scatter.

5.3.4 *Comparison to HI*

As part of the ATLAS^{3D} survey we collected H I data for all 166 galaxies above declination +10° and further than 15 arcmin from Virgo A. Most of these galaxies were observed with the Westerbork Synthesis Radio Telescope (WSRT). Observations are described in detail in Morganti et al. (2006); Oosterloo et al. (2010) and Serra et al., in prep (see Section 1.4.7.3 for a summary). For about 20 galaxies inside the Virgo cluster we use Arecibo data taken as part of the Alfalfa survey (di Serego Alighieri et al., 2007) instead of WSRT data. We use Alfalfa data to derive an upper limit on the HI mass which is comparable to what we obtain with our WSRT observations.

This ATLAS^{3D} H I sample has 29 H I detections of fast-rotators that overlap with the molecular and ionised gas sample with measurable misalignments I consider in this chapter (13 that overlap with the interferometric CO sample, and a further 16 that overlap with the ionised gas sample). Despite the large difference in angular resolution between the H I data and the other tracers, in most cases it is possible to estimate a rough kinematic PA of the atomic gas in the region where it overlaps with the CO and ionised gas. We find that the atomic and molecular material always appear to be kinematically aligned with one another, suggesting that they share a common origin. This is in agreement with the results of Morganti et al. (2006), who find that the H I and ionised gas are always aligned in the SAURON sample (which is a subset of the ATLAS^{3D} sample).

As I have established that the ionised, molecular and atomic gas are all likely to be part of the same structure, it is interesting to use the H I data to investigate the connection with H I seen at large radii. Of the H I-detected systems that have (molecular or ionised) gas kinematically misaligned from the stars, 86% (12/14) have extended H I structures, clearly suggesting a source for the misaligned material. These systems are discussed in detail in Li & Seaquist (1994) (NGC 7465), Verheijen & Zwaan (2001) (NGC 4026), Morganti et al. (2006) (NGC 1023, NGC 2685, NGC 2768, NGC 7332), Duc et al. (2007) (NGC 4694), Oosterloo et al. (2010) (NGC 3032, NGC 4262), and Serra et al., in prep (NGC 0680, NGC 3626, UGC 09519).

Furthermore, 38% (6/16) of the H I-detected galaxies that have gas kinematically aligned with the stars also have kinematically disturbed H I at larger radii, with clear suggestions of ongoing accretion from external sources. These are discussed in Morganti et al. (2006) (NGC 4150), Oosterloo et al. (2010) (NGC 3384, NGC 3489) and Serra et al., in prep (NGC 2778, NGC 3457, PGC 028887).

5.3.5 *Environmental effects*

5.3.5.1 *Cluster environment*

The ATLAS^{3D} sample includes a range of galaxy densities, from the Virgo cluster to sparse field environments. Galaxies in clusters are often H I deficient (e.g. di Serego Alighieri et al., 2007), and it is thought that the atomic material is removed by ram-pressure stripping and interactions as the galaxies fall into the cluster potential and plough through the hot ICM (e.g. Gunn & Gott, 1972; Giovanelli & Haynes, 1983). Kenney & Young (1986) have shown that spiral galaxies in Virgo are not CO deficient, even when they are H I deficient. This is likely to be because molecular gas is denser and resides deeper in a galaxy potential well, where it will not be as affected by infall into a cluster.

To first order, the merger rate is enhanced as galaxies fall into clusters, but once the galaxies are virialized the chance of a merger drops off considerably (the large velocity dispersion within the cluster makes mergers reasonably rare; e.g. van Dokkum et al., 1999). Cluster (and group) centre galaxies are the only exceptions, which are likely to have many merging events, and are typically slow rotators (see Paper VII). Paper IV shows that ATLAS^{3D} Virgo fast-rotating ETGs are likely to be virialized within the cluster (the line-of-sight velocities are centrally peaked and consistent with being relaxed), and hence their last merger should have occurred several crossing times ago (a few gigayears).

Stripped or free-floating gas is likely to be destroyed and shock heated to the cluster virial temperature as it is captured by the cluster, joining the cluster's hot X-ray halo. The external channels by which cold gas can be acquired are therefore likely to

be shut-off once a galaxy is embedded in a cluster potential, whereas internal stellar mass loss is not impeded. This is consistent with the lack of H I detections in Virgo (e.g. Giovanardi, Krumm & Salpeter 1983; di Serego Alighieri et al. 2007; Oosterloo et al. 2010 and Serra et al., in prep) and with the steep decrease in the frequency of spirals, and increase in the frequency of fast-rotating ETGs in the Virgo cluster core (see Paper VII).

Despite this, as for spirals, the ETG CO detection rate inside the Virgo cluster is much higher than the H I detection rate, and is almost identical to that found in the field (Paper IV). The molecular gas mass fractions (M_{H_2}/L_K) of cluster and field galaxies also appear to be similar. Paper IV does however show some evidence that the H_2-richest ETGs are all low mass, and in poor environments. It is hence interesting to investigate these high- and low-density galaxy populations separately, to see if the origin of the gas is affected by the environment.

When the sample of galaxies is divided into Virgo (defined in Paper I as all the galaxies within a sphere of radius 3.5 Mpc centered on the cluster centre[2]) and field (everything else), a clear dichotomy in the kinematic misalignment distribution is apparent.

In Figure 5.6, 42±5% (38 out of 91) of the fast-rotating field ETGs have kinematically misaligned ionised gas. However, in the Virgo cluster only 10±6% (2 out of 20) of the fast-rotating galaxies have ionised gas kinematically misaligned for the stars ($\Psi_{\rm ion-star} < 30^\circ$). If this distribution of alignments in the cluster was the same as in the field one would expect ≈8 to 10 galaxies to show misalignments.

A MW-U test gives a probability that the Virgo and field galaxies are randomly drawn from the same parent galaxy population as 0.3% (≈3σ significance). The same result is found when one considers the kinematic misalignment between the molecular gas and the stars, but with lower number statistics (shown as the hatched area in Figure 5.6).

The two kinematically misaligned Virgo galaxies (NGC 4262 and NGC 4694) both lie on the outskirts of the cluster and are undergoing mergers/interactions as they

[2]Cluster membership is listed in Paper I, Table 5, Column 6, and available online at http://www.purl.org/atlas3d

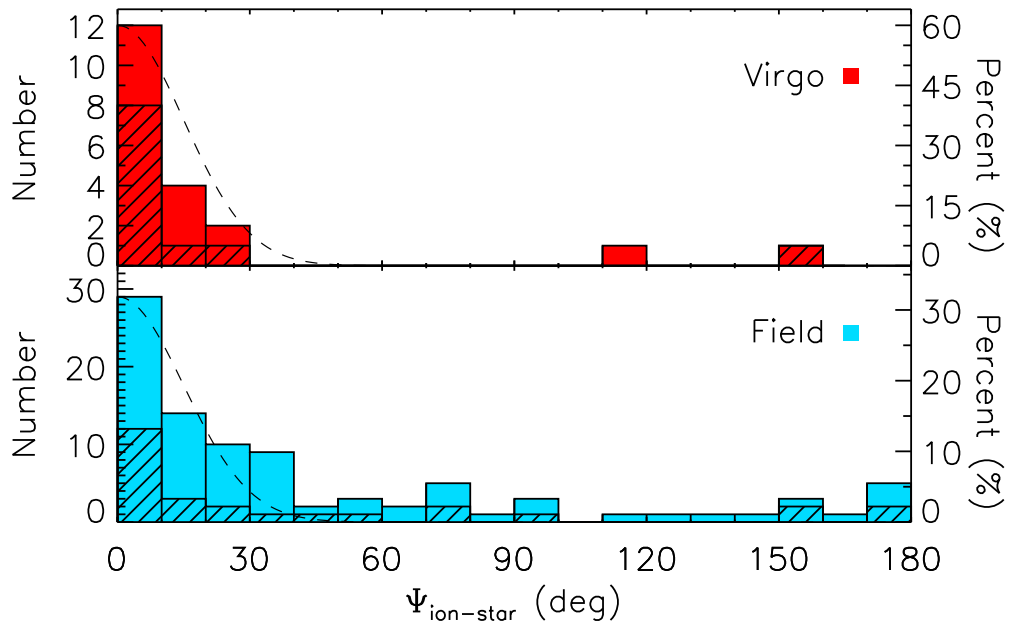

Figure 5.6: *Top:* Histogram showing the kinematic misalignment angle between the ionised gas and the stars for all fast-rotator galaxies in Virgo (defined as lying within a sphere of 3.5 Mpc centered on the cluster centre). The hatched area indicates the number of galaxies in each bin that were also mapped in molecular gas. The two outlying galaxies with Ψ >30 are NGC 4262 and NGC 4694. *Bottom:* As above, but for all fast-rotator galaxies which are not in Virgo, including galaxies in the field and small groups.

fall into the cluster. NGC 4262 may have recently undergone a close encounter with a nearby galaxy (see Vollmer, Huchtmeier & van Driel, 2005). It has a ring of H I surrounding the galaxy (Krumm, van Driel & van Woerden, 1985). This system is strongly barred, and the H I shows elliptical orbits which may be the cause of the observed misalignments. This ring may be the source of the ionised gas as the kinematic position angles appear to be similar. No CO emission was detected from NGC 4262 (Paper IV). NGC 4694 is undergoing a gas-rich major merger in the cluster outskirts. The CO and H I in this galaxy are in non-equilibrium structures offset from the stellar body, towards a dwarf galaxy (Duc et al. 2007).

5.3.5.2 *Group environments*

There is observational evidence that preprocessing (through mergers and tidal disruption) in group environments may be important in the formation of ETGs (Zabludoff & Mulchaey, 1998; Kodama et al., 2001; Helsdon & Ponman, 2003; Kautsch et al., 2008). Paper VII also shows that local environment density seems to be the most important factor in determining the fraction of spiral galaxies and fast-rotating ETGs, outside of the Virgo cluster core. However, simulations show that galaxies can enter clusters directly from the field (e.g. Berrier et al., 2009), avoiding any preprocessing in groups, and that therefore any transformation mechanism should also be able to occur in the cluster environment.

It is possible with the data I possess to examine if it is the local density or the global environment that drive the observed kinematic misalignment correlations. To do this, I utilize a luminosity surface density estimator (I_3) based on a redshift cylinder with a depth of 600 km s^{-1}, and an angular size adapted to include the 3rd nearest neighbor, as presented in Cappellari et al. (2011b) (Paper VII; Table 2, Column 7 and available online at http://www.purl.org/atlas3d). This estimator should pick out locally dense environments, such as groups, as well as substructures within the Virgo cluster. I plot this density indicator against the kinematic misalignment of the ionised gas and stars in Figure 5.7.

In the densest environments, above a critical local luminosity surface density of $\approx 10^{11.7}$ L$_\odot$ Mpc^{-2}, all fast-rotators in both the field and cluster have ionised gas kinematically aligned with the stars, while a wide range of misalignments exist at lower densities. The two misaligned systems in the Virgo cluster are below this luminosity surface density (they are thought to be recently accreted systems, still undergoing mergers in the cluster outskirts; see Section 5.3.5.1). This result does not change if one plots number surface density (Σ_3; see Paper VII, Table 2, Column 4) rather than luminosity surface density, with the critical number density being ≈ 20 Mpc^{-2}. A MW-U test gives a (a posteriori) probability of $\approx$1% that the kinematically aligned galaxies above (and all the galaxies below) this critical density are randomly

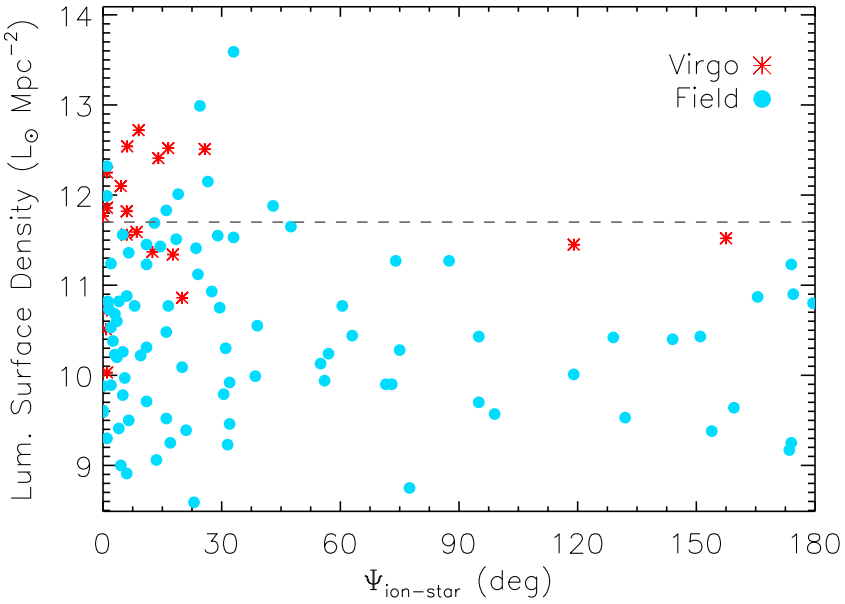

Figure 5.7: The kinematic misalignment angle between the ionised gas and the stars for fast-rotator galaxies, plotted against the local luminosity surface density within cylinders of depth 600 km s^{-1} in the redshift direction, with an angular size adapted to include the 3rd nearest neighbor. Virgo galaxies are plotted with red stars, and field/group galaxies with solid blue circles. The dashed line is a guide to the eye, at the suggested critical density of $10^{11.7}$ L$_\odot$ Mpc^{-2}. The error on each kinematic misalignment angle measurement is ≈15°.

drawn from the same parent population. If one considers the larger scale I_{10} and Σ_{10} environment indicators from Paper VII the cluster/field result discussed in Section 5.3.5.1 is recovered.

The field galaxies that exist above this critical density are NGC 0524, NGC 0680, NGC 3379, NGC 3412, NGC 5353, NGC 5355, NGC 5379 and PGC 042549, all of which are in known galaxy groups. All but one of these systems (which were observed in our H I survey) are H I poor (NGC 0680 is the exception, it is a major merger remnant, and has kinematically disturbed H I extending between several of its group members; see Paper IX and Serra et al., in prep). At least two of these groups have extended X-ray halos (NGC 524, Romer et al. 2000; NGC 5353/NGC 5355, O'Sullivan, Forbes & Ponman 2001).

5.3.6 *Mass dependence*

Whenever one sees an effect which appears correlated with environment, it is important to check if the observed relation is in fact driven by galaxy mass. The mass of a galaxy can affect the gas content in various ways. A deeper potential can allow a galaxy to retain gas that would be lost due to supernovae and galactic winds in a lower mass system. Massive ETGs can also have X-ray halos, which can prevent external gas (especially in cold flows) from entering the galaxy. Figure 5.8 shows the dependence of the ionised gas-star kinematic misalignment of fast-rotators on absolute K_s-band magnitude, an observable proxy for stellar mass. Distances to the galaxies are taken from Paper I. One can see a clear lack of misaligned fast-rotating galaxies at $M_K \lesssim -24$. The only kinematically misaligned galaxy brighter than this threshold is NGC 2768, which is a large elliptical galaxy in a relatively isolated environment, that appears to be accreting from a nearby cloud of H I (Morganti et al., 2006; Crocker et al., 2008). A MW-U test gives a ≈2% chance that the galaxies with $M_K \lesssim -24$ are drawn from the same distribution of misalignment angles as the fainter galaxies.

We re-plot Figure 5.7 with the galaxies with $M_K < -24$ mag highlighted in green (Figure 5.9). Interestingly, the fast-rotators above the proposed critical luminosity are not all the same systems identified previously as being in dense environments, in fact, most are different. This is likely to be because the brightest and most massive galaxies in dense environments are usually slow rotators (Paper VII). It seems that for fast-rotating galaxies both mass *and* environment can be important independent parameters in determining the origin of the molecular and ionised gas.

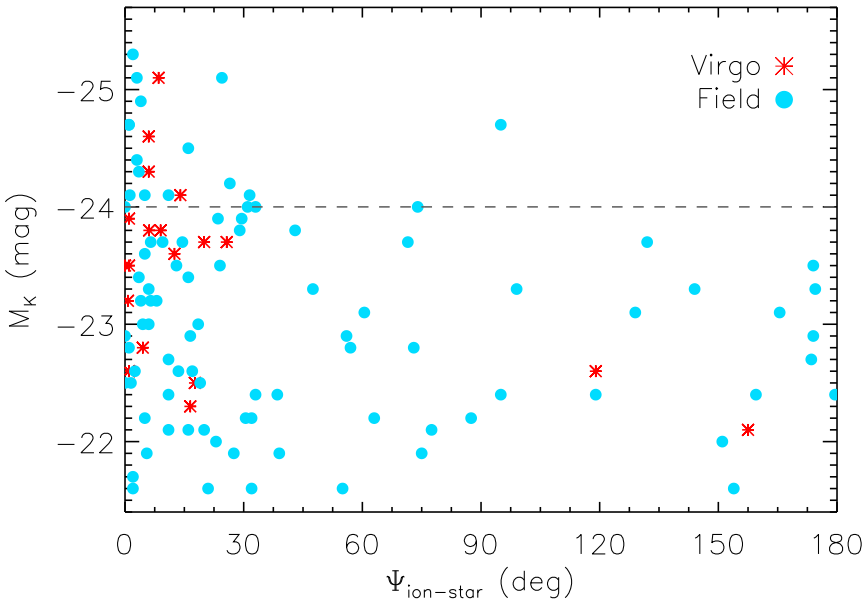

Figure 5.8: The kinematic misalignment angle between the ionised gas and the stars for fast-rotator galaxies, plotted against the total absolute K_s-band magnitude of the galaxy from 2MASS. Distances to the galaxies are taken from Paper I. Virgo galaxies are plotted with red stars, and field/group galaxies with solid blue circles. The dashed line is a guide to the eye, at the suggested critical magnitude of M_K=−24 mag. The error on each kinematic misalignment angle measurement is ≈15°.

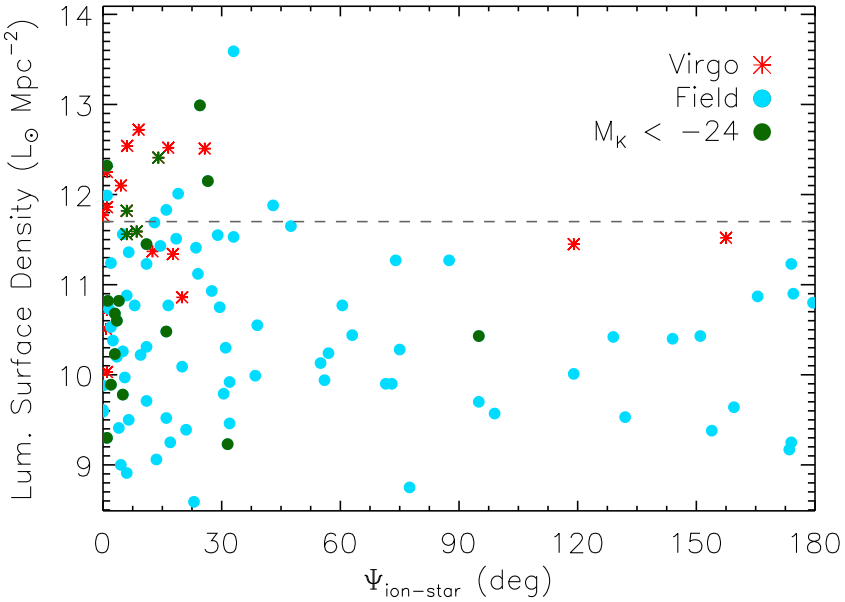

Figure 5.9: As Figure 5.7, but galaxies with $M_K < -24$ mag are plotted with dark green stars (for Virgo galaxies) and solid dark green circles (for field/group galaxies). The error on each kinematic misalignment angle measurement is ≈15°.

Table 5.4: Synopsis of the misalignment statistics for the ATLAS^{3D} galaxies.

Category (1)	Number (2)	Mol. Detection (3)	Ion Detection (4)	# Mapped Mol (5)	# Mapped Ion (6)	Misaligned Mol (7)	Misaligned Ion (8)
Fast-Rotators	224	24±3%	67± 3%	36	111	23± 7%	36± 5%
Slow-Rotators	36	6±4%	86± 6%	2	22	50±35%	68±10%
Field FR	202	22±3%	73± 3%	26	91	28± 9%	42± 5%
Virgo FR	58	21±5%	47± 6%	10	20	10± 9%	10± 6%
$I_3 < 10^{11.7}$ FR	209	22±3%	67± 3%	35	93	24± 7%	44± 5%
$I_3 \geq 10^{11.7}$ FR	51	16±5%	69±10%	1	18	0%	16± 9%
$M_{Ks} \geq$ -24 FR	191	24±3%	65± 3%	29	92	39± 9%	44± 7%
$M_{Ks} <$ -24 FR	33	27±8%	80± 7%	7	19	14±13%	5± 5%

Notes: Column 1 lists the categories of galaxies I discuss in this chapter. FR denotes fast-rotators only. I_3 is a local the luminosity surface density estimator, based on a redshift cylinder with a depth of 600 km s^{-1}, and an angular size adapted to include the 3rd nearest neighbor, as presented in Cappellari et al. (2011b) (Paper VII; Table 2, Column 7 and available online at http://www.purl.org/atlas3d). M_{Ks} is the absolute *Ks*-band total magnitude. Column 2 lists the number of galaxies from the ATLAS^{3D} survey that fall in this class. Columns 3 and 4 list the molecular gas detection rates (taken from Paper IV) and ionised gas detection rates (above an integrated equivalent width of 0.02 Å in either Hβ or [OIII]) for these subsamples. Columns 5 and 6 state the number of galaxies in this category mapped in molecular gas, and those with measurable kinematic PA's in their ionised gas maps. Columns 7 and 8 state the percentage of mapped galaxies which have misaligned molecular, and ionised gas respectively ($\Psi > 30^{\circ}$).

5.4 DISCUSSION

The results presented in the previous section shed light on the origin of the molecular and ionised gas in local ETGs, but they pose additional puzzles that require further discussion.

5.4.1 The link between the gaseous phases

Our results suggest that the molecular, atomic and ionised gas form a single structure, and have undergone a common evolution (as previously found for atomic and ionised gas by Morganti et al., 2006; Oosterloo et al., 2010) at least in fast-rotating galaxies. It would be difficult to maintain two kinematically distinct phases of the ISM for any length of time, given the collisional nature of gas (unless they were widely separated in radius, e.g. separate rings). For instance, let us consider a galaxy which has stellar mass loss ongoing, and has built an aligned gas reservoir. If this galaxy acquires misaligned gas from an external source, the two systems may interact. Collisions between two components with different angular momentum vectors should cause some of the gas to lose its angular momentum and fall to the centre resulting in a more compact gas distribution. As discussed in Chapter 4 no such signature has been found in the mapped ATLAS^{3D} ETGs.

The ionised gas in these galaxies will also be coupled to the properties of the broader ISM (due to its dissipative nature). The dominant ionisation mechanism in ETGs is thought to be irradiation by old stellar populations (e.g. post-asymptotic giant branch stars; Binette et al., 1994; Sarzi et al., 2010), which are uniformly distributed throughout the galaxy, hence ionised gas should be produced at the interface of any part of the cold ISM, and the ionised gas would have the same angular momentum as the material it is produced from.

The difference in angular resolution (and field of view) between the CO and H I observations (and to a lesser extent the ionised gas observations) could have some effect on these conclusions. For instance warps are often seen in outer H I disks

around galaxies of all types (e.g. García-Ruiz, Sancisi & Kuijken, 2002). However the agreement between the CO (and ionised gas) in the inner parts, and the H I at larger radii would be hard to manufacture by chance. Although challenging, higher resolution H I observations of the inner parts of these galaxies could be used to remove this uncertainty, and further establish the link between these phases.

5.4.2 The importance of external accretion

5.4.2.1 Slow-rotators

In slow rotators there is clear evidence that their ionised gas is primarily acquired externally. The kinematic misalignments are statistically consistent with a flat distribution, with no significant increase in the number of galaxies with exactly co- or counter-rotating gas. This suggests that accretion and mergers dominate the gas supply in slow-rotating galaxies. If the source of ionization in these galaxies is long lasting (e.g. irradiation by old stellar populations) then this gas could even be left-over from the last merger that created the slow-rotator.

Slow rotators are thought to be formed from progenitors that have undergone multiple major mergers (Paper III). Simulations suggest an average of 3 major mergers per slow-rotating galaxy, and multiple minor mergers (Khochfar et al., 2011, Paper VIII). Slow rotators are predominately massive (Paper III), and sit at the centre of their group and cluster environments (Paper VII), which is likely to enhance their merger rate (e.g. van Dokkum et al., 1999). Our results provide additional evidence that mergers and/or accretion are important in the evolution of slow rotators.

A few questions do remain. For instance there is no statistically significant evidence for any of these galaxies having generated aligned ionised gas from stellar mass loss. The stars in these systems are predominantly old (e.g. Kuntschner et al. 2010; McDermid et al., in prep), and hence the mass loss rate from the stellar population will be low. Any mass that is lost from these stars into the ISM may be kept hot by the large velocity dispersion of these pressure supported systems, and may join the X-ray halo.

Furthermore, the lack of a peak in the misalignment distribution for co- and counter-rotating gas suggests the timescale required for the ionised gas in these systems to relax into the orbital plane is long (especially as the ionised gas is likely to be long lived). This may be because these systems are in general very round (Paper III), and hence the gravitational torques will be lower than in disky systems. Slow rotators can also be triaxial (Paper II & Paper III), allowing gas in polar configurations to be stable.

5.4.2.2 Fast rotators

The molecular and ionised gas in ≈36% of the fast-rotating galaxies in the sample are kinematically misaligned from the stellar body, and hence are likely to have an external origin. There are ways in which the angular momentum of gas in the central regions of galaxies can be altered (e.g. bars which produce resonant orbits and branching; see Wada & Habe, 1995). However the kinematic alignment with the atomic gas at larger scales suggests this is not a dominant effect. In addition, 36% is likely a lower limit to the importance of externally acquired material. Assuming that gas from mergers and accretion enters galaxies isotropically then one would expect on average ≈17% of galaxies to exhibit aligned kinematics (within 30°) by chance ($30^\circ/180^\circ \approx 0.17$), despite the gas having an external origin.

The assumption that gas from mergers and accretion enters galaxies isotropically is a conservative one. In fact one can imagine scenarios where the gas accretion is not isotropic, but in fact preferential results in aligned gas. One such example would be a major merger that imparts a large amount of angular momentum to the stars in the remnant, forcing them to rotate in the plane of the merger. Gas that is thrown off in the merger may fall back into the remnant over many gigayears, and would likely fall in preferentially aligned. Some simulations have predicted that minor mergers may preferentially occur with the angular momentum vector of the accreted system aligned along the major axes of the dark matter halo (e.g. Deason et al., 2011). If such processes are ongoing, then I will underestimate the importance of external accretion

in this work. How isotropic the accretion of gas from major mergers and cold-mode accretion onto ETGs truly is could be tested further in cosmological hydrodynamic simulations.

If a large amount of external gas is present within a galaxy, the gas depletion timescale through star-formation will become larger than the relaxation time (the time it takes for gas structures to settle into the equatorial plane). In this case one would expect to find 50% of the galaxies to have co-rotating gas, and 50% to show counter-rotation. The lack of a large peak at a kinematic misalignment of 180° however suggests that this criterion is seldom fulfilled, or that relaxation into the equatorial plane is not a symmetric process.

Clemens et al. (2010) compared the dust production rate in the envelopes of evolved AGB stars with a constraint on the total dust mass in Virgo cluster ETGs (from Herschel observations). They find that passively evolving ETGs (defined by having Spitzer mid-infrared spectra consistent with passively evolving stellar populations) are not detected by Herschel, and thus the dust destruction timescale in passive ETGs must be short. They conclude that passive ETG's with dust are thus likely to have acquired it from an external source. As dust is thought to be important to shield nascent molecular clouds, and catalyze the conversion of H I into H_2 molecules (e.g. Duley & Williams, 1993), perhaps a lack of dust could prevent some of the sample galaxies from regenerating their molecular reservoirs from internal sources.

External accretion/mergers appear to only be important in the field, where at least 42% of galaxies have a significant kinematic misalignment between the molecular or ionised gas and the stars. The molecular and ionised gas are nearly always consistent with a purely internal origin in three (partially overlapping) populations: fast-rotating Virgo cluster galaxies, the densest group environments I sample, and in the highest luminosity fast-rotators.

As shown in Section 5.3.4, there is clear evidence that at least 6 of the field ETGs which are kinematically aligned have gas which is in fact externally accreted. Including this evidence increases the percentage of field galaxies which have externally accreted gas to at least 46%. Knapp, Turner & Cunniffe (1985) have shown that the H I masses of early-type galaxies are unrelated to the galaxy luminosity, unlike in spirals. This

led them to predict that external sources provide *all* the H I in field ETGs. Morganti et al. (2006) and Oosterloo et al. (2010) have also shown that in almost all cases where H I is present in ETGs, there are some signs that it has been externally accreted. As it appears that the gaseous phases are closely linked, this suggests that the molecular and ionised gas in H I-detected ETGs frequently has an external origin, even if it is kinematically aligned. Hence the true importance of external accretion is likely underestimated in field environments.

If this is so, then I am forced to conclude that mergers and accretion must not proceed isotropically, or relaxation of misaligned gas happens over a short timescale, and preferentially in a prograde direction. It is also conceivable that retrograde gas survives for a shorter length of time (due to interactions with the hot halo of the galaxy, or similar). Due to the different angular resolutions (and hence spatial scales) probed by the H I and CO data however, these conclusions require further investigation. To first order, one would expect the evidence for external H I accretion to become stronger if one were able to investigate the kinematics and morphology of the H I at higher spatial resolution. A more in depth treatment of these issues will be included in a future work in the ATLAS^{3D} series.

5.4.3 *The effect of group and cluster environments*

The striking result that galaxies in the Virgo cluster (and other dense environments) almost always have kinematically aligned gas suggests that dense environments affect the accretion and/or generation of ionised and molecular material. The challenge is thus to find a consistent theory that can explain the environmental dependence of the kinematic misalignments, while simultaneously accounting for the identical detection rates (and mass fractions) of the molecular gas in the field and clusters (Paper IV).

Paper IV has shown that the CO-detected galaxies in Virgo are virialised, and hence have been in the cluster for several gigayears. The average gas depletion timescale for field galaxies in the CO-detected sample is $\approx$1-2 Gyr, assuming that the gas forms stars at the rate predicted by either the Schmidt-Kennicutt relation of Kennicutt (1998)

or a constant star formation efficiency as in Bigiel et al. (2008) (See Alatalo et al., in prep). Recent studies have found little evidence that these ETGs deviate from these star-formation relations, and hence morphological quenching may not play a large role in the prolonging the lifetime of the gas in majority of these systems (see Shapiro et al. 2010, Crocker et al. 2011 and Alatalo et al, in prep).

If the ETGs present in clusters today were like current field galaxies when they fell in, then they should have exhausted the vast majority of their molecular gas by now (due to star formation) and should not be detectable anymore. This implies that the ETGs detected in Virgo today either must have been systematically more molecular gas-rich than is typical now when they fell in, or they must have regenerated their gas from an internal source recently. Of course, if ETGs were more molecular gas-rich in the past, then either all the gas must have been kinematically aligned (contrary to today's field ETGs) or it must have somehow re-aligned upon entering the cluster. Both possibilities however seem rather contrived, so the internal replenishment hypothesis seems more plausible. Skillman et al. (1996) showed that spiral galaxies in the inner parts of the Virgo cluster have higher gas-phase metallicities than those in the field. They suggested that these systems have been evolving as 'closed-boxes', undiluted by metal poor gas infall, providing some support for this hypothesis.

It is of course possible that the molecular (and ionised) gas in ETGs in Virgo all comes from cooled stellar mass loss. This would however require that ETGs which fall into the cluster exhaust their pre-existing gas rapidly, so that any kinematically misaligned gas is destroyed, and then that the right percentage of the ETG population regenerate a molecular gas reservoir.

Figure 5.7 suggests that high local density environments also result in aligned gas. I speculate that preprocessing in groups, before galaxies enter clusters, could perhaps be important in explaining the kinematic alignment of the gas. As galaxies fall into groups, or transit through the outskirts of clusters, merger rates are enhanced (e.g. van Dokkum et al., 1999). Starbursts triggered by these violent interactions can quickly deplete the cold molecular gas, which would rapidly remove any evidence of misaligned material. The galaxies in H I-poor groups and clusters would then be unable to re-accrete external gas as they settle into the group/cluster potential and

become virialized. Stellar mass loss can then regenerate an aligned gas reservoir over time.

The principal difficulty of this explanation is that it requires the gas generation efficiency to be higher in clusters than in field galaxies. Cluster galaxies have the same molecular gas detection rate and mass fractions as field galaxies, but all this molecular gas must be generated internally. About 11% of galaxies in the field have a substantial molecular gas reservoir kinematically aligned with the stellar component (i.e. half of the detections), while ≈20% of galaxies in Virgo have kinematically aligned gas (i.e. almost all of the detections). The ATLAS^{3D} ionised gas detection rate is ≈73% in the field, but only ≈48% in the cluster. If this ionised gas is cooling to become molecular, then it must do so with a much greater efficiency in the cluster environment.

Some studies of the formation of molecular clouds (e.g. Heitsch & Hartmann, 2008) have suggested that they are most likely to form at the intersection of gas flows or shocks, such as those found in the spiral arms and bars of disc galaxies. Conceivably, if such conditions are found more often in cluster galaxies, this could result in a higher molecular cloud formation efficiency. The morphological classification of the ATLAS^{3D} galaxies presented in Paper II reports a slightly enhanced barred fraction in the Virgo cluster (36±4% versus 27±2% in the field). Almost all of the CO-detected galaxies in Virgo and dense groups that are aligned have their molecular gas distributed in rings, spirals, or within bars (see Chapter 2). These structures associated with galaxy resonances can perhaps provide an environment with suitable gas flows or shocks, that could concentrate any diffuse gas present (from stellar mass loss) and allow it to cool and form molecular clouds. The small difference in barred fraction within the cluster is unlikely to be enough to explain the apparent enhanced molecular gas formation efficiency however.

Paper VII revisited the morphology-density relation (Dressler, 1980) for the galaxies in the sample using the kinematic classification presented in Paper III. It showed that the fraction of spirals decreases, and the fraction of fast-rotating ETGs increases as you approach a group or cluster core. This can be interpreted as circumstantial evidence that spiral galaxies can be transformed into fast-rotating ETGs as they settle into a group or cluster. Therefore, it is possible that some of the ETGs detected in the group

and cluster environments actually fell in as spirals, which were then subsequently transformed into early-types. We would then be detecting the remnant of their star-forming gas, that would naturally be co-rotating (counter-rotating molecular gas is very rare in spirals). This explanation would however require accepting that the molecular gas mass fraction is coincidentally similar inside and outside the cluster. The CO-detected ETGs in Virgo are also statistically indistinguishable from the other ETGs in Virgo in their brightness at *K*-band, specific angular momentum (λ_R, from Paper III) , dynamical mass or stellar velocity dispersion (both from Cappellari et al, in prep), alpha-element enhancement and stellar metallicities (at least in single stellar population analyses, McDermid et al., in prep). Nevertheless, I feel that this possibility is worthy of further study, as it may provide direct observational evidence of galaxies undergoing morphological change due to cluster environments.

All of the mechanisms discussed above fail to satisfactorily explain the identical detection rate and molecular gas fractions found inside and outside of Virgo. The low number of detected ETGs means that the detection rates and molecular gas fractions in the cluster may be identical by chance, and of course other clusters may be very different. Clearly observations of other clusters are required to resolve this ambiguity, and pinpoint which, if any, of the above mechanisms are dominant.

5.4.4 The effect of galaxy mass

Figure 5.8 shows that the kinematic misalignments of the molecular and ionised gas in fast-rotating ETGs also seem to be effected by the mass of the host galaxy. Furthermore, this effect appears to be independent of the environmental effect discussed above (see Figure 5.9). The processes resulting in these kinematic alignments must thus act on single galaxy scales.

Massive galaxies are better able to contain material that would normally be lost during energetic events (such as supernovae/galactic winds), perhaps resulting in a larger pool of aligned material that can later cool. This process, however, can only create aligned gas, and thus leaves us unable to explain the lack of externally accreted

gas in these massive fast-rotating galaxies.

AGN feedback is one of the possible mechanisms which could explain this lack of kinematically misaligned gas. Springel, Matteo & Hernquist (2005) have shown in simulations that galaxy mergers and accretion events that cause nuclear gas inflow can trigger AGN feedback, quenching star formation and gas accretion on a short timescale, particularly in massive galaxies. AGN feedback triggered by merging events could disrupt and destroy misaligned gas reservoirs as they form in the most massive galaxies. Gas from stellar mass loss can avoid such a fate, as it will not flow into the centre in great quantities due to angular momentum conservation, and hence will not fuel an AGN.

Massive ETGs are also known to host hot, X-ray emitting gas halos (Forman, Jones & Tucker, 1985). These hot halos can heat infalling cold gas clouds, preventing the gas from reaching the galaxy centers. In a similar way, as mentioned above, virial shocks can create a halo mass threshold, above which incoming gas will always shock heat to the virial temperature, joining the hot halo (Birnboim & Dekel, 2003). This material is virialised in the hot halo, and likely forced into an aligned configuration by interaction with the rest of the halo gas. It may then cool in an identical way to stellar mass loss, producing a kinematically aligned gas reservoir.

Both of the halo effects described above are reported to occur primarily in galaxies of mass $\gtrsim 10^{11}$ $M_\odot$, a good match to my apparent threshold ($M_K = -24$ mag, or 8×10^{10} $L_{\odot,K}$). Once again, however, the fact that the molecular gas detection rate is independent of mass makes explaining these results difficult. Massive galaxies may well retain a large reservoir of kinematically aligned hot gas (from internal or external sources), but in order to achieve a uniform detection rate as a function of mass the cooling rate from the halos would have to be enhanced by just the right amount to balance the reduction due to the lack of accretion events. It is possible that the star formation efficiency in these systems could be lower, perhaps due to morphological quenching, allowing galaxies that do have gas to be detectable for longer.

Slow-rotating galaxies in general have a similar mass to this population of aligned fast-rotators ($>3\text{x}10^{10}$ $M_\odot$; Paper III), but have gas that is mainly from external sources. This suggests, as discussed in Papers III and VIII, that slow-rotators have evolved

differently to fast-rotators, with a greater number of external events, such as mergers, shaping their properties.

5.5 CONCLUSIONS

In this chapter I have demonstrated that a large proportion of the gas found in local early-type galaxies is likely supplied by external processes. Gas kinematically misaligned with respect to the stars is common, indicating an external origin for the gas in $\gtrsim$36% of all fast-rotating ETGs. We have also shown that the ionised, atomic and molecular gas in local ETGs are linked, always having similar kinematics and thus presumably sharing a common origin. In the field, $\approx$42% of galaxies have kinematically misaligned ionised gas, confirming that mergers and accretion play a vital role in supplying gas to field ETGs. Slow rotators are not generally detected in molecular gas, but show a flat distribution of ionised gas kinematic misalignments, suggesting they obtain ionised gas primarily through mergers and/or accretion. In many cases, fast-rotating galaxies with kinematically aligned molecular and ionised gas have H I distributions that again suggest an external origin for the gas. This suggests that external gas sources dominate in the field (as has been suggested by previous authors).

In the Virgo cluster, the molecular and ionised material in fast-rotators is nearly always kinematically aligned with the bulk of the stars, pointing to gas supplied by purely internal processes. Fast-rotators in dense groups also appear to always have aligned gas kinematics, suggesting that the local environment is important in understanding the environmental dependance of the gas origins. Given the results of Paper IV, indicating similar molecular gas detection rates and mass fractions in clusters and the field, this sets constraints on potential mechanisms for generating and influencing molecular and ionised gas in cluster environments.

Molecular and ionised gas in the most massive fast-rotating galaxies also appear to always be kinematically aligned with the stars, independent of environment, suggesting that the alignment can be caused by galaxy scale processes which reduce

the probability that cold, kinematically misaligned gas can be accreted onto the galaxy (e.g. AGN feedback, the ability to host a hot X-ray gas halo, or a halo mass threshold). This also supports the picture (discussed in Papers III and VIII) that fast-rotating galaxies (which are always aligned at high mass) have a different formation mechanism to slow-rotators (who at similarly high masses mainly have externally supplied ionised gas).

We tentatively suggest that preprocessing in groups may help to explain the environmental dichotomy in the origin of the gas. Merger-induced starbursts in groups and cluster outskirts could consume any kinematically misaligned molecular gas that is present, and leftover ionised material would be ram pressure-stripped. Once galaxies settle into a cluster or H I-poor group, external gas accretion and mergers are suppressed, allowing stellar mass loss to regenerate a kinematically aligned gas reservoir. It is possible that features such as bars and rings could funnel dust and gas lost by stars to the centre of the galaxy, or collect them together, and could explain the greater efficiency with which galaxies in dense environments must recreate their dense gas reservoirs. Alternatively, we could be detecting the remnant gas left over from the morphological transformation of spiral galaxies into ETGs as they enter the cluster and group environments. Both of these possibilities, however, fail to explain why the detection rate of molecular gas (and the molecular gas mass fractions) are similar inside and outside of the Virgo cluster.

More work to pin down the mechanism(s) creating and/or aligning the gas is clearly required to unambiguously determine which, if any, of these effects is dominant.

It would also be beneficial to extend this sort of analysis to other clusters and groups, to see if the results reported hold true in yet denser environments. The Fornax cluster in the southern hemisphere and the Coma cluster in the north are obvious nearby targets, which should become accessible once new facilities such as the Large Millimeter Telescope (LMT) and the Atacama Large Millimeter/sub-millimeter Array (ALMA) come online.

6

CONCLUSIONS

"Ships and sails proper for the heavenly air should be fashioned. Then there will also be people, who do not shrink from the dreary vastness of space." – Johannes Kepler, letter to Galileo Galilei, 1609.

In this thesis I have presented details of a campaign to interferometrically map CO detected ETGs. This work was carried out as part of the ATLAS^{3D} survey. In Chapter 2 I presented ^{12}CO molecular gas channel maps, integrated intensity maps and velocity fields for 30 ETGs newly mapped with CARMA. These were combined with data from the literature to create the largest ever sample of 41 interferometrically mapped ETGs. The rest of this thesis then concentrated on exploiting this dataset to understand the origin, morphology and kinematics of the molecular gas. I summarise the main results below, before discussing ongoing work based on this data, and highlighting some future projects that could shed more light on the issues tackled in this thesis.

6.1 SUMMARY OF MAIN RESULTS

6.1.1 Morphology and surface brightness profiles of the molecular gas in ETGs

In Chapter 2, I analysed the morphology of the molecular gas in ETGs. I revealed that 55% of the sample galaxies have relaxed molecular disks, while rings and bars are present in 17.5% of ETGs. Around 17.5% of my galaxies show some form of

disturbance, and a small proportion (5%) have clear single or doubled armed spiral morphologies. This is the first time the relative abundance of different gas morphologies has been measured in a large sample of ETGs. The CO is generally spatially coincident with obscuring dust, and the two are likely strongly coupled.

In Chapter 4, I identified four classes of surface brightness profiles in the CO-mapped ATLAS^{3D} ETGs. Around half have molecular gas that follows the stellar light profile, similarly to molecular gas in spirals. These galaxies appear to have relaxed gas out to large radii, suggesting that gravitational effects have had time to force the molecular gas into a profile that follows the stellar mass. These galaxies are usually those classified morphologically as discy. A quarter of the sample galaxies show molecular gas surface brightness profiles that fall off slower than the light, and sometimes show a truncation. These galaxies often have a low mass, and either disturbed molecular gas (suggesting that a recent merger or gas accretion may cause the excess) or are in cluster environments where ram pressure stripping and the presence of hot gas may compress and/or truncate the gas. The remaining galaxies have rings, or composite profiles, that I argue can be caused by the effects of bars or potentially minor mergers.

6.1.2 The CO Tully-Fisher Relation of ETGs

In Chapter 3, I have presented the first CO Tully-Fisher relation for ETGs. I have shown that CO line widths are a reliable tracer of the circular velocity in fast-rotating ETGs, and relations derived in this way agree well with ETG TFRs derived by other authors. I showed that my CO TFR relation has a robust slope and zero point, and a comparable scatter to that of TFRs derived with other techniques.

Early-type galaxies follow a TFR that is offset by nearly one magnitude at K_s-band from that of spiral galaxies. This offset is similar to that found by previous authors. An offset ETG TFR is usually thought to be caused by passive evolution of spiral galaxies into lenticulars, after an abrupt cessation of star formation. However, the presence of molecular gas in these ETGs suggests that the majority of this sample

must have ongoing residual star-formation. This should increase the timescale to fade by the required ≈1 mag. Some models, such as those that involve a change in the size of galaxies as they transform, do not require star formation to completely cease, providing an alternative explanation that is fully consistent with my data. Unfortunately the low molecular gas fractions in these systems make drawing any firm conclusions difficult.

6.1.3 Molecular gas extent

In Chapter 4, I investigated the extent of the molecular gas in the CO-rich ATLAS^{3D} ETGs, and compared it with the extent of the gas in spiral galaxies. I find that the molecular gas extent is smaller in absolute terms in early-type than in late-type galaxies, but that the size distributions appear to scale similarly with optical/stellar characteristic scalelengths. Amongst ETGs, I find that the extent of the molecular gas is independent of the kinematic misalignment, but does depend on environment, with Virgo cluster ETGs having more compact molecular gas reservoirs. This may be due to ram pressure stripping, or a greater prevalence of bars driving gas towards the galaxy centres. The amount of molecular gas present, however, is independent of cluster membership and so on average the molecular gas in Virgo ETGs is denser than that in the field.

6.1.4 The origin of the molecular and ionised gas in ETGs

In Chapter 5, I demonstrated that a large proportion of the gas found in local early-type galaxies is likely supplied by external processes. Gas kinematically misaligned with respect to the stars is common, indicating an external origin for the gas in $\gtrsim$36% of all fast-rotating ETGs. I also shown that the ionised, atomic and molecular gas in local ETGs are linked, always having similar kinematics and thus presumably sharing a common origin. In the field, ≈42% of galaxies have kinematically misaligned ionised gas, confirming that mergers and accretion play a vital role in supplying gas to field

ETGs. In many cases, fast-rotating galaxies with kinematically aligned molecular and ionised gas have H I distributions that again suggest an external origin for the gas. This suggests that external gas sources dominate in the field.

Slow rotators are not generally detected in molecular gas, but show a flat distribution of ionised gas kinematic misalignments, suggesting they obtain ionised gas primarily through mergers and/or accretion. This also supports the picture (discussed in Papers III and VIII of the ATLAS^{3D} survey) that high mass fast-rotating galaxies have a different formation mechanism to slow-rotators.

In the Virgo cluster, the molecular and ionised material in fast-rotators is nearly always kinematically aligned with the bulk of the stars, pointing to gas supplied by purely internal processes. Fast-rotators in dense groups also appear to always have aligned gas kinematics, suggesting that the local environment is important in understanding the environmental dependance of the gas origins. Further projects concentrating on expanding our understanding of the origin of the gas in ETGs are discussed below.

6.1.5 CO as a kinematic tracer

In Chapter 4, I build on the results of Chapter 3 by investigating the kinematics of the molecular gas using position-velocity diagrams. On these I overlaid the JAM model circular velocity predictions and the stellar and ionised gas velocities. I find that the molecular gas reaches beyond the turnover of the circular velocity curve in 75$\pm$6% of ATLAS^{3D} ETGs. The CO is also closer to the predicted circular velocity than the stars or ionised gas, validating its use as a kinematic tracer for Tully-Fisher and similar analyses.

In $\approx$40% of the sample galaxies the CO appears to be dynamically cold, and thus is an excellent tracer of the circular velocity of the system. In 31% of galaxies I found the dynamical models systematically over-predicted the observed CO velocity, potentially because the assumption of a constant mass-to-light ratio breaks down. These galaxies also have strong dust features, that make constructing a mass model from optical

imaging challenging. The ionised gas in the most star-forming galaxies appears to be dynamically colder than in less star-forming systems, likely because it is associated with star formation in the molecular disc.

6.1.6 *The effect of galaxy mass*

One emerging result from the different analyses discussed above is the effect that high stellar luminosities (and hence likely high galaxy masses) have on the molecular gas properties. A change in the slope of the TFR at the high-mass end has been reported by some authors at luminosities $M_{Ks} \lesssim$-23.75 (e.g. Peletier & Willner, 1993; Verheijen, 2001; Noordermeer & Verheijen, 2007). In Chapter 3, I showed that my CO TFR is consistent with the presence of a different slope of the CO TFR above this luminosity. As I find that CO is a good dynamical tracer in these galaxies, the mass-to-light ratios (or underlying potentials) above such a mass must be different.

In Chapter 2, I showed that high mass galaxies ($M_{Ks} \lesssim -24.5 mag$) almost always have their molecular gas distributed in a relaxed disk, and the gas almost always follows the stellar light profile, similarly to molecular gas in spirals (Chapter 4). Molecular and ionised gas in the most massive fast-rotating galaxies (above a luminosity of $M_K \lesssim -24$) always appear to always be kinematically aligned with the stars, independent of environment (Chapter 5). These high mass galaxies also appear to have relaxed gas out to large radii, suggesting that gravitational effects have had time to force the molecular gas relax into the equatorial plane and adopt a profile that follows the stellar mass, and/or that a galaxy scale process is suppressing the accretion of new cold gas.

These results thus suggest that galaxies brighter than a critical *Ks*-band magnitude of ≈-24 have different molecular gas properties, and different potentials. Assuming an average V-K colour of ≈2.5 for low redshift ETGs (e.g. Tonini et al., 2009) then this critical magnitude is also where the central luminosity profiles of ETGs start to show cuspy cores (Faber et al., 1997). We suggest in this thesis that AGN feedback, the ability to host a hot X-ray gas halo, or a halo mass threshold could suppress the

accretion of cold gas and affect the molecular gas properties. Both of these halo effects are reported to occur primarily in galaxies of mass $\gtrsim 10^{11}$ $M_\odot$, a good match to my apparent threshold ($M_K \approx -24$ mag, or 8×10^{10} $L_{\odot,K}$). X-ray and radio observations could be used to distinguish between these mechanisms, and shed light on what causes these high mass galaxies to have different properties.

6.2 ONGOING WORK

I now describe ongoing projects which make use of the CARMA observations of the ATLAS^{3D} sample galaxies, which have been presented in this thesis.

6.2.1 *Star-formation laws in ETGs*

In Chapter 1, I discussed the opposing Kennicutt (1998) and Bigiel et al. (2008) formulations of the Schmidt law of star-formation (Schmidt, 1959). Several studies of the global star formation law in ETGs have been conducted, and the data are found to be consistent with either relation (Temi, Brighenti & Mathews, 2009; Shapiro et al., 2010; Wei et al., 2010; Crocker et al., 2011). It is clear that a broader study, using our large interferometrically mapped sample of ETGs would allow us to better address the question of which, if any, of the star-formation laws derived in spiral galaxies are applicable in ETGs. I am working with K. Alatalo to complete a spatially resolved study of star-formation in the ATLAS^{3D} galaxies to determine the efficiency with which gas is turned into stars in ETGs.

6.2.2 *Dense gas tracers*

Detecting other molecules besides ^{12}CO gives access to a whole raft of information on the physical conditions and excitation of the molecular gas. With A. Crocker we have surveyed the 18 brightest ^{12}CO detections from the ATLAS^{3D} survey, and detected

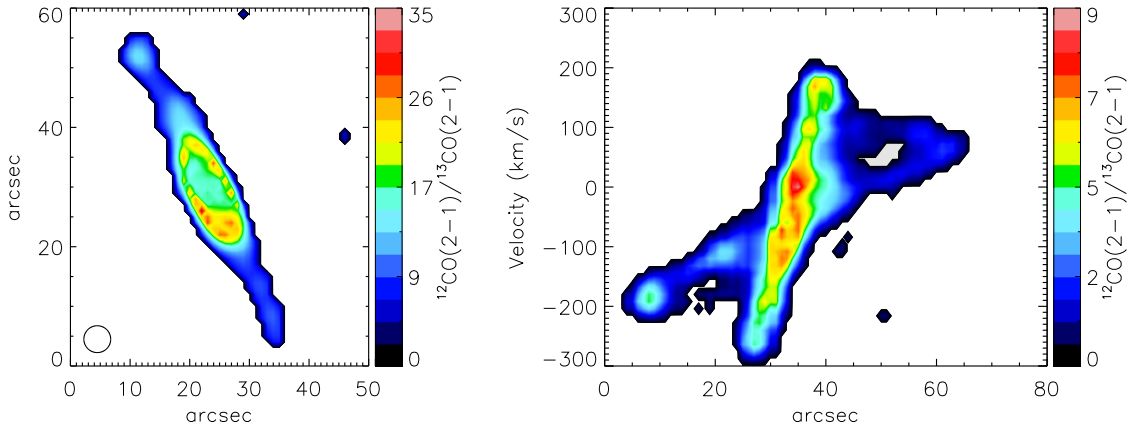

Figure 6.1: ^{12}CO(2-1)/^{13}CO(2-1) integrated intensity ratio map (left) and ratio of the position velocity diagrams (right) for NGC4710.

^{13}CO, HCN and HCO+ in the majority of systems with the IRAM-30m telescope. In collaboration with E. Bayet we have also been deriving the physical properties of the molecular gas with Large-Velocity Gradient (LVG) models. Preliminary analyses suggest that interacting and/or star-bursting early-type galaxies have more optically thin molecular gas, and that a small number of galaxies may have particularly stable molecular gas.

Following on from these single-dish detections, I am the PI on several proposals to map the dense gas emission in a few of our ETGs with CARMA and PdBI (see Fig. 6.1). To date we have mapped two galaxies in multiple molecular tracers, and S. Topal is leading efforts to derive spatially resolved maps of the molecular gas properties. We will then be able to correlate these directly with star-formation indicators, to understand how the properties of the molecular gas affect the efficiency of star-formation.

6.2.3 GMOS IFU observations of the molecular outflow in NGC1266

NGC 1266, one of the galaxies mapped as part of the ATLAS^{3D} survey, has a large molecular outflow described in detail in Alatalo et al. (2011). I have Gemini GMOS IFU data for the centre of this object, which clearly shows an ionised gas outflow, with velocities upto $\pm$700 km s^{-1} away from the galaxy systemic (Figure 6.2). This ionised

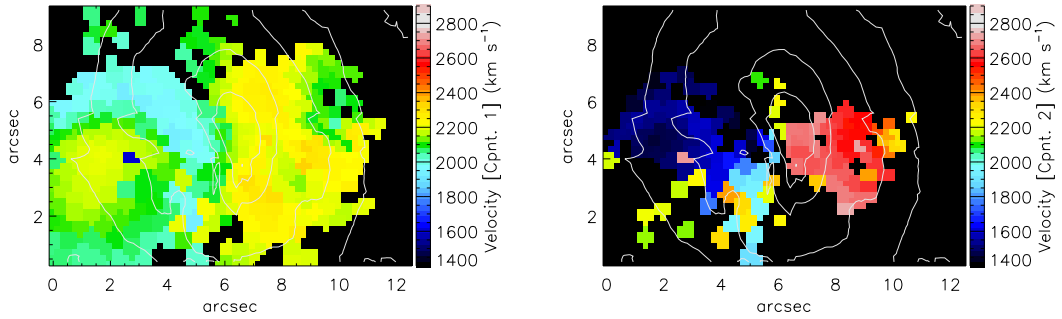

Figure 6.2: Gemini GMOS IFU velocity fields for the ionised gas nearest the systemic (left) and in the high velocity outflow (right) in NGC 1266. Overlaid in white are the optical isophotes of the galaxy.

gas outflow is spatially coincident with the molecular outflow, and radio continuum suggesting that both outflows are driven by an AGN jet. During further analysis of this data I will attempt to shed light on the processes powering this large AGN feedback event.

6.2.4 *Molecules as a tracer of gas phase metallicity*

Understanding the production of metals, and the subsequent enrichment of the ISM is crucial in many field of extragalactic astrophysics. However the current tools that allow astronomers to determine gas phase metallicities only work if the emission spectrum is powered by star-formation processes. Where strong AGN activity, old stellar populations or shocks dominate these methods are hence unusable.

Models of gas chemistry that E. Bayet and I have been running predict that the CS/HCN abundance ratio should provide a sensitive probe of the gas phase metallicity, especially in high metallicity galaxies. The power of such an indicator is two-fold: 1) it is observable at wavelengths completely free of any dust attenuation and 2) it is reliable even if star formation does not dominate the ionisation of the gas. In order to verify the predictions of our models I have obtained CS detections with the IRAM-30m telescope in a sample of ETGs which have measured HCN fluxes, and derived metallicities. Figure 6.3 shows a spectrum obtained during my recent

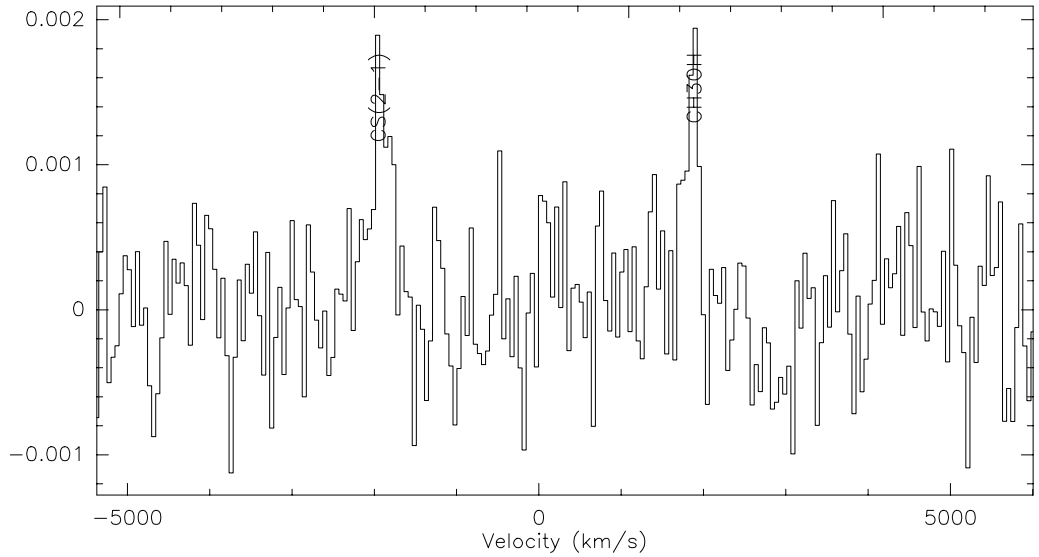

Figure 6.3: CS(2-1) and methanol in NGC4710, detected with the IRAM-30m telescope. The x-axis shows velocity offset from the frequency centre, and the y-axis is in antenna temperature (T_a^*).

observing run, showing detected CS(2-1) and methanol emission. I will use the observed line intensities to derive the fractional abundances of CS and HCN, and attempt to calibrate a new metallicity indicator for the molecular ISM.

6.2.5 Gas accretion and relaxation timescales

In Chapter 5, I discussed the kinematic misalignment distributions present in the ATLAS^{3D} ETGs. I used the presence of large gas misalignments as a simple criteria to determine if the gas had an external origin. However, the shape of the kinematic misalignment distribution encodes information on the relaxation timescale of molecular gas (as discussed in Chapter 2), and the relative frequency at which new gas is accreted onto ETGs. I have built simple analytic models which trace the accretions of gas onto simulated galaxies, its relaxation over time, and its depletion via star-formation. I plan to use these simulations to put constraints of the relaxation and accretion timescales of gas onto ETGs, and compare these with hydrodynamic and N-body simulations.

6.3 FUTURE WORK

In this Section I highlight some projects I intend to embark upon that extend the work presented in this thesis, and then finally conclude by discussing future prospects for the field as a whole.

6.3.1 *The effect of hydrostatic mid-plane pressure*

Blitz & Rosolowsky (2006) have suggested that hydrostatic mid-plane pressure ($P_{\rm ext}$) could govern the conversion of H I into H_2, and drive the formation of giant molecular clouds in spiral galaxies. If such a mechanism also is important in the formation of the gas in ETGs, this could explain the similarity between the total extent of the molecular gas in both early- and late-type galaxies. All of the quantities required to calculate the hydrostatic mid-plane pressure of the ATLAS^{3D} ETGs are available, and hence in a future work I plan to investigate how the mid-plane pressure varies across the galaxy sample, and thus how H I is converted into the molecular gas we observe.

6.3.2 *The stability of the gas in ETGs*

Recent research has suggested that the conditions present in massive, bulge dominated ETGs may increase the stability of molecular gas, and supress its star-formation efficiency (dubbed morphological quenching; Martig et al., 2009). The growth of a stellar spheroid via merging or secular processes increases the stellar density, and hence the epicyclic frequency and velocity dispersion in the centre of the galaxy. This can cause the Toomre stability criterion (Toomre, 1964) to exceed unity, implying that the gas is stable against gravitational collapse. As the star formation rate would be very low, this stable cold ISM would persist for many billions of years, and hence would be detectable today in ETGs. I intend to investigate this process by estimating the Toomre-Q parameter within the molecular gas of the ATLAS^{3D} ETGs, and correlating

these with tracers of ongoing star-formation.

6.3.3 *Gas phase metallicity and the origin of the gas in ETGs*

As mentioned in Chapter 5, kinematic misalignments alone cannot fully determine the origin of all the gas we observe. For instance, in several cases the molecular and ionised gas are aligned with the stars, consistent with an internal origin; but HI observations show clear evidence of ongoing accretion onto the galaxy. In order to disentangle the importance of external and internal processes, more information is clearly required. One way of addressing this issue is by estimating the gas-phase metallicity of the star-forming material. For instance, gas accreted from a low-mass HI rich dwarf or cold-accretion stream would be low metallicity, while gas acquired in major mergers would be more metal rich. Stellar mass-loss, on the other hand, would share the metallicity of the stars in the host. I thus plan to conduct a project to measure the gas phase metallicity in the ATLAS^{3D} star-forming ETGs to constrain the origin of the gas. A small number of the ATLAS^{3D} objects have gas phase metallicities available from SDSS, and interestingly they are all high-metallicity outliers from the usual mass-metallicity relation (see Figure 6.4).

The environmental effects mentioned in Chapter 5 are tantalising, however the low number of galaxies at high environmental densities does not allow us to draw strong conclusions. Investigating the molecular and ionised gas kinematic misalignments from the stellar kinematics in other dense local clusters would be invaluable to help us understand if the results I find in Virgo hold more generally. The Fornax and Coma clusters are obvious targets, that are only now becoming accessible as new instruments such as the Atacama Large Millimetre/Sub-Millimetre Array (ALMA) come online.

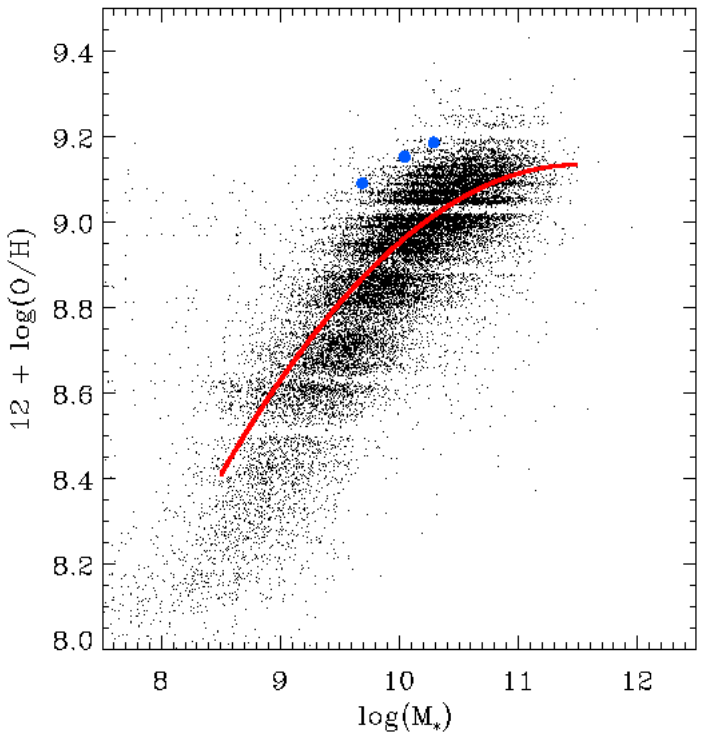

Figure 6.4: The mass - gas phase metallicity relation for the 3 ATLAS^{3D} star-forming ETGs with SDSS data (blue points) overlaid on the SDSS relation.

6.3.4 *Future prospects*

Millimetre and Sub-Millimetre astronomy are about to enter an exciting new era, with new instruments coming online over the next few years that should revolutionise the field and shed more light on the questions posed in this thesis.

ALMA is a new large mm-interferometer in Chile, which is now entering its early-science phase, and will allow us to detect much weaker emission, and achieve much higher spatial resolutions than currently possible. This will be very useful in extending the work presented in this thesis. For instance, resolving the true morphology of the molecular gas at high spatial resolutions in ETGs will become possible for the first time. This will allow us to check if the molecular gas and dust really trace each other over small scales, and thus if closely wrapped spiral patterns are common in our molecular disks. High spatial resolution will allow us for the first time to resolve individual GMC's in ETGs, and establish if the density variations within the ISM are

correlated with star-formation.

Our sample of mapped galaxies is also biased to high molecular gas masses, and ALMAs sensitivity would allow us to investigate the behaviour of lower molecular mass systems. Another benefit of ALMAs increased sensitivity will be the ability to map the molecular gas in systems at higher redshifts, indeed, one of ALMAs stated goals is to allow detection of a galaxy like the Milky Way at z$\sim$3 in less than 24 hours. Synergies between ALMA, the eVLA, and eventually the SKA will allow us access to CO lines across the redshifted universe.

New single dish telescopes, such as the Large Mexican Telescope (LMT) and eventually the Cornell Caltech Atacama Telescope (CCAT) will improve access to objects in the northern and southern skies, respectively. Such telescopes, along with existing facilities, will be vital to survey large numbers of galaxies, and select targets for the new interferometers. With these large new facilities it should be possible to directly track the mass-to-light ratio evolution of galaxies as a function of both redshift and morphological type using CO Tully-Fisher relations (such as the one presented in Chapter 3).

Our understanding of the gas chemistry and physical conditions within the molecular gas will also be improved by these new instruments. ALMAs sensitivity, for instance, will allow blind line surveys of the millimetre atmospheric windows, enabling detection of a vast array of molecular species and increasing our understanding of the ISM. With these powerful diagnostics we will be able to investigate if the physical conditions of the ISM are different in ETGs, and if this affects star-formation.

Improvements in computing power are starting to allow simulators to better trace baryonic processes, and implement gas physics into large simulations. Such simulations will allow us to explore the gas accretion and settling process, better understand gas kinematic misalignments and the global importance of minor mergers and cold gas accretion. Overall this powerful combination of new instrumentation, and better simulations should allow us to make further steps towards understand the molecular gas present in the most massive galaxies in our universe.

REFERENCES

Abazajian K. N. et al., 2009, ApJS, 182, 543

Adelman-McCarthy J. K. et al., 2008, ApJSS, 175, 297

Alatalo K. et al., 2011, ApJ, 735, 88

Athanassoula E., Bureau M., 1999, ApJ, 522, 699

Bacon R. et al., 1995, A&AS, 113, 347

Bacon R. et al., 2001, MNRAS, 326, 23

Baldry I. K., Balogh M. L., Bower R. G., Glazebrook K., Nichol R. C., Bamford S. P., Budavari T., 2006, MNRAS, 373, 469

Baldry I. K., Glazebrook K., Brinkmann J., Ivezić Ž., Lupton R. H., Nichol R. C., Szalay A. S., 2004, ApJ, 600, 681

Barnes J. E., 2002, MNRAS, 333, 481

Bauermeister A., Blitz L., Ma C.-P., 2010, ApJ, 717, 323

Baum W. A., 1959, PASP, 71, 106

Beck S. C., Turner J. L., Kloosterman J., 2007, AJ, 134, 1237

Bedregal A. G., Aragón-Salamanca A., Merrifield M. R., 2006, MNRAS, 373, 1125

Begelman M. C., Blandford R. D., Rees M. J., 1980, Nature, 287, 307

Bell E. F., de Jong R. S., 2001, ApJ, 550, 212

Bell E. F., McIntosh D. H., Katz N., Weinberg M. D., 2003, ApJSS, 149, 289

Bell E. F. et al., 2004, ApJ, 608, 752

Bender R., Saglia R. P., Gerhard O. E., 1994, MNRAS, 269, 785

Bender R., Surma P., Doebereiner S., Moellenhoff C., Madejsky R., 1989, A&A, 217, 35

Berrier J. C., Stewart K. R., Bullock J. S., Purcell C. W., Barton E. J., Wechsler R. H., 2009, ApJ, 690, 1292

Bertola F., Cinzano P., Corsini E. M., Rix H.-W., Zeilinger W. W., 1995, ApJL, 448, L13

Bigiel F., Leroy A., Walter F., Brinks E., de Blok W. J. G., Madore B., Thornley M. D., 2008, AJ, 136, 2846

Binette L., Magris C. G., Stasińska G., Bruzual A. G., 1994, A&A, 292, 13

Binney J., Merrifield M., 1998, Galactic astronomy / James Binney and Michael Merrifield. Princeton

Birnboim Y., Dekel A., 2003, MNRAS, 345, 349

Blitz L., Rosolowsky E., 2006, ApJ, 650, 933

Bloemen J. B. G. M., Deul E. R., Thaddeus P., 1990, A&A, 233, 437

Boselli A., Lequeux J., Gavazzi G., 2002, Ap&SS, 281, 127

Bottinelli L., Gouguenheim L., 1977, A&A, 54, 641

Bower R. G., Lucey J. R., Ellis R. S., 1992, MNRAS, 254, 601

Braine J., Henkel C., Wiklind T., 1997, A&A, 321, 765

Bregman J. N., Parriott J. R., 2009, ApJ, 699, 923

Bureau M., Athanassoula E., 1999, ApJ, 522, 686

Bureau M., Freeman K. C., 1999, AJ, 118, 126

Buta R., 1986, ApJS, 61, 631

Caldwell N., 1984, PASP, 96, 287

Cappellari M., 2002, MNRAS, 333, 400

Cappellari M., 2008, MNRAS, 390, 71

Cappellari M. et al., 2006, MNRAS, 366, 1126

Cappellari M., Copin Y., 2003, MNRAS, 342, 345

Cappellari M. et al., 2009, ApJL, 704, L34

Cappellari M., Emsellem E., 2004, PASP, 116, 138

Cappellari M. et al., 2011a, MNRAS, 413, 813, (Paper I)

Cappellari M. et al., 2011b, eprint arXiv, 1104, 3545, (Paper VII)

Cappellari M. et al., 2010, Highlights of Astronomy, 15, 81

Carilli C. L. et al., 2010, ApJ, 714, 1407

Catinella B., Haynes M. P., Giovanelli R., Gardner J. P., Connolly A. J., 2008, ApJL, 685, L13

Cenarro A. J., Trujillo I., 2009, ApJL, 696, L43

Chapman S. C., Smail I., Windhorst R., Muxlow T., Ivison R. J., 2004, ApJ, 611, 732

Christodoulou D. M., Tohline J. E., Steiman-Cameron T. Y., 1988, AJ, 96, 1307

Chung E. J., Rhee M.-H., Kim H., Yun M. S., Heyer M., Young J. S., 2009, ApJS, 184, 199

Clemens M. S. et al., 2010, A&A, 518, L50

Colbert J. W., Mulchaey J. S., Zabludoff A. I., 2001, AJ, 121, 808

Combes F., 1991, Dynamics of Galaxies and Their Molecular Cloud Distributions: Proceedings of the 146th Symposium of the International Astronomical Union, Eds. F. Combes and F. Casoli, 146, 255

Combes F., 1994, Proceedings of Mass-Transfer Induced Activity in Galaxies, Eds. I. Shlosman, CUP, 170

Combes F., Young L. M., Bureau M., 2007, MNRAS, 377, 1795

Condon J. J., Cotton W. D., Greisen E. W., Yin Q. F., Perley R. A., Taylor G. B., Broderick J. J., 1998, AJ, 115, 1693

Courteau S., Dutton A. A., van den Bosch F. C., MacArthur L. A., Dekel A., McIntosh D. H., Dale D. A., 2007, ApJ, 671, 203

Cowie L. L., Songaila A., Hu E. M., Cohen J. G., 1996, AJ, 112, 839

Crawford M. K., Genzel R., Townes C. H., Watson D. M., 1985, ApJ, 291, 755

Crocker A. F., Bureau M., Young L. M., Combes F., 2008, MNRAS, 386, 1811

Crocker A. F., Bureau M., Young L. M., Combes F., 2011, MNRAS, 410, 1197

Crocker A. F., Jeong H., Komugi S., Combes F., Bureau M., Young L. M., Yi S., 2009, MNRAS, 393, 1255

Daddi E. et al., 2010, ApJ, 713, 686

Davies R. L., Efstathiou G., Fall S. M., Illingworth G., Schechter P. L., 1983, ApJ, 266, 41

Davis M., Geller M. J., 1976, ApJ, 208, 13

Davis T. A. et al., 2011a, eprint arXiv, 1107, 19

Davis T. A. et al., 2011b, MNRAS, 414, 968

de Vaucouleurs G., 1948, Annales d'Astrophysique, 11, 247

de Vaucouleurs G., de Vaucouleurs A., Corwin H. G., Buta R. J., Paturel G., Fouque P., 1991, Volume 1-3

de Zeeuw P. T. et al., 2002, MNRAS, 329, 513

Deason A. J. et al., 2011, MNRAS, 415, 2607

di Serego Alighieri S. et al., 2007, A&A, 474, 851

di Serego Alighieri S., Trinchieri G., Brocato E., 1990, Windows on Galaxies eds. Giuseppina Fabbiano, John S. Gallagher, and Alvio Renzini. Astrophysics and Space Science Library, 160, 301

Dickey J. M., Hanson M. M., Helou G., 1990, ApJ, 352, 522

Dickey J. M., Kazes I., 1992, ApJ, 393, 530

Dickman R. L., Snell R. L., Schloerb F. P., 1986, ApJ, 309, 326

Djorgovski S., Davis M., 1987, ApJ, 313, 59

Dopita M. A., Sutherland R. S., 1995, ApJ, 455, 468

Dressler A., 1980, ApJ, 236, 351

Dressler A., Lynden-Bell D., Burstein D., Davies R. L., Faber S. M., Terlevich R., Wegner G., 1987, ApJ, 313, 42

Dressler A. et al., 1997, ApJ, 490, 577

Duc P.-A., Braine J., Lisenfeld U., Brinks E., Boquien M., 2007, A&A, 475, 187

Duley W. W., Williams D. A., 1993, MNRAS, 260, 37

Dutton A. A., Conroy C., van den Bosch F. C., Prada F., More S., 2010, MNRAS, 923

Ebneter K., Davis M., Djorgovski S., 1988, AJ, 95, 422

Eliche-Moral M. C., González-García A. C., Balcells M., Aguerri J. A. L., Gallego J., Zamorano J., 2010, HUNTING FOR THE DARK: THE HIDDEN SIDE OF GALAXY FORMATION. Edited by Victor P. Debattista and Cristina C. Popescu AIP Conference Proceedings, 1240, 237

Emsellem E. et al., 2011, MNRAS, 414, 888, (Paper III)

Emsellem E. et al., 2007, MNRAS, 379, 401

Emsellem E. et al., 2004, MNRAS, 352, 721

Emsellem E., Monnet G., Bacon R., 1994, A&A 285, 285, 723

Faber S. M., Dressler A., Davies R. L., Burstein D., Lynden-Bell D., 1987, IN: Nearly normal galaxies: From the Planck time to the present; Proceedings of the Eighth Santa Cruz Summer Workshop in A&A, 175

Faber S. M., Jackson R. E., 1976, ApJ, 204, 668

Faber S. M. et al., 1997, AJ, 114, 1771

Faber S. M. et al., 2007, ApJ, 665, 265

Ficarra A., Grueff G., Tomassetti G., 1985, A&AS, 59, 255

Forman W., Jones C., Tucker W., 1985, ApJ, 293, 102

Forman W., Schwarz J., Jones C., Liller W., Fabian A. C., 1979, ApJ, 234, L27

Fraternali F., Binney J. J., 2008, MNRAS, 386, 935

García-Ruiz I., Sancisi R., Kuijken K., 2002, A&A, 394, 769

Gavazzi G., 1993, ApJ, 419, 469

Gavazzi R., Treu T., Rhodes J. D., Koopmans L. V. E., Bolton A. S., Burles S., Massey R. J., Moustakas L. A., 2007, ApJ, 667, 176

Gerhard O., Kronawitter A., Saglia R. P., Bender R., 2001, AJ, 121, 1936

Giovanardi C., Krumm N., Salpeter E. E., 1983, AJ, 88, 1719

Giovanelli R., Haynes M. P., 1983, AJ, 88, 881

Gooch R., 1996, Astronomical Data Analysis Software and Systems V, Eds. George H. Jacoby and Jeannette Barnes, ASPC, 101, 80

Gregory P. C., Condon J. J., 1991, ApJS Series, 75, 1011

Grossi M. et al., 2009, A&A, 498, 407

Gunn J. E., Gott J. R., 1972, ApJ, 176, 1

Hawarden T. G., Longmore A. J., Tritton S. B., Elson R. A. W., Corwin H. G., 1981, MNRAS, 196, 747

Heitsch F., Hartmann L., 2008, ApJ, 689, 290

Helfer T. T., Thornley M. D., Regan M. W., Wong T., Sheth K., Vogel S. N., Blitz L., Bock D. C.-J., 2003, ApJSS, 145, 259

Helsdon S. F., Ponman T. J., 2003, MNRAS, 339, L29

Ho L. C., 2007, ApJ, 669, 821

Ho L. C., Filippenko A. V., Sargent W. L. W., 1997a, ApJ, 487, 591

Ho L. C., Filippenko A. V., Sargent W. L. W., 1997b, ApJ, 487, 579

Hopkins P. F., Hernquist L., Cox T. J., Di Matteo T., Martini P., Robertson B., Springel V., 2005, ApJ, 630, 705

Hubble E. P., 1926, ApJ, 64, 321

Hubble E. P., 1936, Realm of the Nebulae, Yale University Press

Jarrett T. H., Chester T., Cutri R., Schneider S., Skrutskie M., Huchra J. P., 2000, AJ, 119, 2498

Józsa G. I. G., Kenn F., Klein U., Oosterloo T. A., 2007, A&A, 468, 731

Józsa G. I. G., Oosterloo T. A., Morganti R., Klein U., Erben T., 2009, A&A, 494, 489

Jungwiert B., Combes F., Palouš J., 2001, A&A, 376, 85

Kannappan S. J., Fabricant D. G., 2001, AJ, 121, 140

Kannappan S. J., Fabricant D. G., Franx M., 2002, AJ, 123, 2358

Kannappan S. J., Guie J. M., Baker A. J., 2009, AJ, 138, 579

Kautsch S. J., Gonzalez A. H., Soto C. A., Tran K.-V. H., Zaritsky D., Moustakas J., 2008, ApJ, 688, L5

Kaviraj S. et al., 2007, ApJSS, 173, 619

Kenney J. D., Young J. S., 1986, ApJ, 301, L13

Kennicutt R. C., 1998, ApJ, 498, 541

Kent S. M., 1987, AJ, 93, 816

Khochfar S. et al., 2011, eprint arXiv, 1107, 5059, (Paper VIII)

Knapp G. R., Guhathakurta P., Kim D.-W., Jura M. A., 1989, ApJS Series, 70, 329

Knapp G. R., Rupen M. P., 1996, ApJ, 460, 271

Knapp G. R., Turner E. L., Cunniffe P. E., 1985, AJ, 90, 454

Kodama T., Smail I., Nakata F., Okamura S., Bower R. G., 2001, ApJ, 562, L9

Koribalski B., Dahlem M., Mebold U., Brinks E., 1993, A&A, 268, 14

Kormendy J., 1977, ApJ, 218, 333

Kormendy J., 1979, ApJ, 227, 714

Kormendy J., Bender R., 1996, ApJL, 464, L119

Kormendy J., Fisher D. B., Cornell M. E., Bender R., 2009, ApJS, 182, 216

Kormendy J., Kennicutt, Jr. R. C., 2004, ARAA, 42, 603

Krajnović D. et al., 2008, MNRAS, 390, 93

Krajnović D., Cappellari M., de Zeeuw P. T., Copin Y., 2006, MNRAS, 366, 787

Krajnović D. et al., 2011, MNRAS, 414, 2923, (Paper II)

Krips M. et al., 2007, A&A, 464, 553

Kron R. G., 1980, ApJS, 43, 305

Krumm N., van Driel W., van Woerden H., 1985, A&A, 144, 202

Kuntschner H. et al., 2006, MNRAS, 369, 497

Kuntschner H. et al., 2010, MNRAS, 408, 97

Lavezzi T. E., 1997, PhD Thesis, University of Minnesota, 5, publication Number: AAT 9804738

Lavezzi T. E., Dickey J. M., 1997, AJ, 114, 2437

Lavezzi T. E., Dickey J. M., 1998, AJ, 116, 2672

Leroy A. K. et al., 2011, eprint arXiv, 1102, 4618

Leroy A. K. et al., 2009, AJ, 137, 4670

Li J. G., Seaquist E. R., 1994, AJ, 107, 1953

Lia C., Portinari L., Carraro G., 2002, MNRAS, 330, 821

Magorrian J., Ballantyne D., 2001, MNRAS, 322, 702

Maiolino R., Caselli P., Nagao T., Walmsley M., Breuck C. D., Meneghetti M., 2009, A&A, 500, L1

Malin D. F., Carter D., 1980, Nature, 285, 643

Markwardt C. B., 2009, Astronomical Data Analysis Software and Systems XVIII, ASPC, 411, 251

Martig M., Bournaud F., 2010, ApJL, 714, L275

Martig M., Bournaud F., Teyssier R., Dekel A., 2009, ApJ, 707, 250

Masters K. L., Springob C. M., Huchra J. P., 2008, AJ, 135, 1738

Mathews W. G., Brighenti F., 2003, ARAA, 41, 191

Mazzuca L. M., Sarzi M., Knapen J. H., Veilleux S., Swaters R., 2006, ApJ, 649, L79

Mazzuca L. M., Swaters R. A., Knapen J. H., Veilleux S., 2011, eprint arXiv, 1107, 4959

McDermid R. M. et al., 2006, MNRAS, 373, 906

McGaugh S. S., de Blok W. J. G., 1997, ApJ, 481, 689

Mei S. et al., 2007, ApJ, 655, 144

Merluzzi P., 1998, A&A, 338, 807

Merritt D., Mikkola S., Szell A., 2007, ApJ, 671, 53

Mihos J. C., Hernquist L., 1996, ApJ, 464, 641

Morganti R. et al., 2006, MNRAS, 371, 157

Neistein E., Maoz D., Rix H.-W., Tonry J. L., 1999, AJ, 117, 2666

Nilson P., 1973, Acta Universitatis Upsaliensis. Nova Acta Regiae Societatis Scientiarum Upsaliensis - Uppsala Astronomiska Observatoriums Annaler

Nipoti C., Binney J., 2007, MNRAS, 382, 1481

Noordermeer E., Verheijen M. A. W., 2007, MNRAS, 381, 1463

Obreschkow D., Rawlings S., 2009, ApJL, 696, L129

Oemler A., 1974, ApJ, 194, 1

Okuda T., Kohno K., Iguchi S., Nakanishi K., 2005, ApJ, 620, 673

Oosterloo T. et al., 2010, MNRAS, 1397

Oosterloo T. A., Morganti R., Sadler E. M., van der Hulst T., Serra P., 2007, A&A, 465, 787

O'Sullivan E., 2002, etheses.bham.ac.uk

O'Sullivan E., Forbes D. A., Ponman T. J., 2001, MNRAS, 328, 461

Parriott J. R., Bregman J. N., 2008, ApJ, 681, 1215

Paturel G., Garcia A. M., Fouque P., Buta R., 1991, A&A, 243, 319

Paturel G., Petit C., Prugniel P., Theureau G., Rousseau J., Brouty M., Dubois P., Cambrésy L., 2003, A&A, 412, 45

Peletier R. F., 1989, Ph.D. Thesis, Rijksuniversiteit Groningen, 149

Peletier R. F., Willner S. P., 1993, ApJ, 418, 626

Phillipps S., 1989, A&A, 211, 259

Phillips T. G. et al., 1987, ApJ, 322, L73

Pizagno J. et al., 2007, AJ, 134, 945

Pozzetti L. et al., 2007, A&A, 474, 443

Regan M. W., Thornley M. D., Helfer T. T., Sheth K., Wong T., Vogel S. N., Blitz L., Bock D. C.-J., 2001, ApJ, 561, 218

Rijcke S. D., Zeilinger W. W., Hau G. K. T., Prugniel P., Dejonghe H., 2007, ApJ, 659, 1172

Roberts M. S., 1978, AJ, 83, 1026

Rogstad D. H., Lockhart I. A., Wright M. C. H., 1974, ApJ, 193, 309

Romer A. K. et al., 2000, ApJSS, 126, 209

Roscoe D. F., 1999, A&A, 343, 788

Rubin V. C., Burstein D., Ford W. K., Thonnard N., 1985, ApJ, 289, 81

Sadler E. M., Gerhard O. E., 1985, MNRAS, 214, 177

Sage L. J., Welch G. A., 2006, ApJ, 644, 850

Sage L. J., Welch G. A., Young L. M., 2007, ApJ, 657, 232

Sage L. J., Wrobel J. M., 1989, ApJ, 344, 204

Sancisi R., 2004, IAUS, Eds: S. D. Ryder, D. J. Pisano, M. A. Walker, and K. C. Freeman, ASP, 220, 233

Sarzi M. et al., 2007, New Astronomy Reviews, 51, 18

Sarzi M. et al., 2006, MNRAS, 366, 1151

Sarzi M. et al., 2010, MNRAS, 402, 2187

Schawinski K. et al., 2007, ApJSS, 173, 512

Schechter P., 1976, ApJ, 203, 297

Schinnerer E., Scoville N., 2002, ApJ, 577, L103

Schmidt M., 1959, ApJ, 129, 243

Schoeniger F., Sofue Y., 1997, A&A, 323, 14

Schoniger F., Sofue Y., 1994, A&A, 283, 21

Schreiber N. M. F., Genzel R., Bouché N., Cresci G., Davies R., Buschkamp P., Shapiro K., Tacconi L. J., 2009, ApJ, 706, 1364

Scott N. et al., 2009, MNRAS, 398, 1835

Sersic J. L., 1968, Atlas de galaxias australes, Cordoba

Shapiro K. L. et al., 2010, MNRAS, 402, 2140

Shen S., Wang C., Chang R., Shao Z., Hou J., Shu C., 2009, ApJ, 705, 1496

Silk J., Rees M. J., 1998, A&A, 331, L1

Skillman E. D., Kennicutt R. C., Shields G. A., Zaritsky D., 1996, ApJ, 462, 147

Skrutskie M. F. et al., 2006, AJ, 131, 1163

Sparks W. B., Macchetto F., Golombek D., 1989, ApJ, 345, 153

Sprayberry D., Bernstein G. M., Impey C. D., Bothun G. D., 1995, ApJ, 438, 72

Springel V., Matteo T. D., Hernquist L., 2005, ApJ, 620, L79

Sramek R., 1975, AJ, 80, 771

Steiman-Cameron T. Y., Kormendy J., Durisen R. H., 1992, AJ, 104, 1339

Strong A. W., Mattox J. R., 1996, A&A, 308, L21

Swings P., Rosenfeld L., 1937, ApJ, 86, 483

Tacconi L. J. et al., 2010, Nature, 463, 781

Temi P., Brighenti F., Mathews W. G., 2007, ApJ, 660, 1215

Temi P., Brighenti F., Mathews W. G., 2009, ApJ, 695, 1

Thomas D., Greggio L., Bender R., 1999, MNRAS, 302, 537

Thomas D., Maraston C., Bender R., de Oliveira C. M., 2005, ApJ, 621, 673

Tonini C., Maraston C., Devriendt J., Thomas D., Silk J., 2009, MNRAS, 396, L36

Tonry J. L., Dressler A., Blakeslee J. P., Ajhar E. A., Fletcher A. B., Luppino G. A., Metzger M. R., Moore C. B., 2001, ApJ, 546, 681

Toomre A., 1964, ApJ, 139, 1217

Toomre A., 1977, in Evolution of Galaxies and Stellar Populations, B. M. Tinsley & R. B. Larson, ed., pp. 401–+

Tully R. B., Fisher J. R., 1977, A&A, 54, 661

Tully R. B., Fouque P., 1985, ApJS Series, 58, 67

Tully R. B., Pierce M. J., 2000, ApJ, 533, 744

Tutui Y., Sofue Y., 1997, A&A, 326, 915

Tutui Y., Sofue Y., 1999, A&A, 351, 467

Tutui Y., Sofue Y., Honma M., Ichikawa T., Wakamatsu K.-I., 2001, PASJ, 53, 701

van den Bergh S., 1976, ApJ, 206, 883

van den Bergh S., 1990, ApJ, 348, 57

van den Bergh S., 2009, ApJL, 694, L120

van der Kruit P. C., Shostak G. S., 1982, A&A, 105, 351

van Dokkum P. G., Franx M., Fabricant D., Kelson D. D., Illingworth G. D., 1999, ApJ, 520, L95

van Dokkum P. G., Kriek M., Franx M., 2009, Nature, 460, 717

Verheijen M. A. W., 2001, ApJ, 563, 694

Verheijen M. A. W., Zwaan M., 2001, Gas and Galaxy Evolution, Eds. J. E. Hibbard, M. Rupen, and J. H. van Gorkom, ASP, 240, 867

Visvanathan N., Sandage A., 1977, ApJ, 216, 214

Vollmer B., Huchtmeier W., van Driel W., 2005, A&A, 439, 921

Wada K., Habe A., 1995, MNRAS, 277, 433

Walter F., Carilli C., Bertoldi F., Menten K., Cox P., Lo K. Y., Fan X., Strauss M. A., 2004, ApJ, 615, L17

Wang Z., Kenney J. D. P., Ishizuki S., 1992, AJ, 104, 2097

Wei L. H., Vogel S. N., Kannappan S. J., Baker A. J., Stark D. V., Laine S., 2010, ApJL, 725, L62

Weijmans A.-M., Krajnović D., van de Ven G., Oosterloo T. A., Morganti R., de Zeeuw P. T., 2008, MNRAS, 383, 1343

Welch G. A., Sage L. J., 2003, ApJ, 584, 260

Welch G. A., Sage L. J., Young L. M., 2010, ApJ, 725, 100

Wiklind T., Henkel C., 1989, A&A, 225, 1

Wiklind T., Rydbeck G., 1986, A&A, 164, L22

Wild W., Harris A. I., Eckart A., Genzel R., Graf U. U., Jackson J. M., Russell A. P. G., Stutzki J., 1992, A&A, 265, 447

Williams M. J., Bureau M., Cappellari M., 2009, MNRAS, 400, 1665

Williams M. J., Bureau M., Cappellari M., 2010, MNRAS, 409, 1330

Wilson R. W., Jefferts K. B., Penzias A. A., 1970, ApJ, 161, L43

Wrobel J. M., Kenney J. D. P., 1992, ApJ, 399, 94

Yi S. K., 2008, Hot Subdwarf Stars and Related Objects, eds. U. Heber, C. S. Jeffery, and R. Napiwotzki, ASP, 392, 3

Young J. S., Scoville N., 1982, ApJ, 258, 467

Young J. S., Scoville N. Z., 1991, ARAA, 29, 581

Young L. M., 2002, AJ, 124, 788

Young L. M., Bureau M., Cappellari M., 2008, ApJ, 676, 317

Young L. M. et al., 2011, MNRAS, 688, (Paper IV)

Zabludoff A. I., Mulchaey J. S., 1998, ApJ, 496, 39

Zwaan M. A., van der Hulst J. M., de Blok W. J. G., McGaugh S. S., 1995, MNRAS, 273, L35